
The use of interferometric spaceborne radar and GIS to measure peat subsidence in Indonesia

Thesis submitted for the degree of
Doctor of Philosophy
at the University of Leicester

by

BASHAR DAHDAL

Department of Geography
University of Leicester

2011

The use of interferometric spaceborne radar and GIS to measure ground subsidence in peat soils in Indonesia

Bashar Dahdal

Abstract

Interferometric synthetic aperture radar (InSAR) has been increasingly used to extract information about the earth's surface by exploiting the phase difference between two complex radar signals. Some significant application fields that utilize InSAR techniques are digital elevation model (DEM) generation, land use classification and land subsidence. In this thesis, by using ERS-1/2 tandem SAR images pairs, the potential implementations of SAR interferometry in tropical peatland forests in Central Kalimantan, Indonesia are described. Coherence was found to be a good tool for rapid assessment for burned and deforested areas. The coherence of burned forest area was increased by 0.2; whilst the minimum coherence was found to be than 0.35. However, many critical factors affect the quality of InSAR data and limit its applications, such as methods of InSAR data processing. This study emphasizes the impact of different processing and phase unwrapping techniques on DEM accuracy. Analyses of InSAR DEM accuracy indicate that DEMs with relative errors of less than 3 m root mean square error (RMSE) are possible in some regions in the former Mega Rice Project (Ex-MRP) area and could meet many objectives of a global mapping mission. Applying adaptive filtering many times with a decreasing window size has a strong impact to reduce the number of residues, which can increase the phase unwrapping efficiency and the final DEM accuracy. Furthermore, the differential SAR Interferometry (DInSAR) was examined to see if it can detect peatland subsidence accurately from October 1997 to January 2000 using 4-pass and complex interferogram combination methods. The subsidence rate of 2 cm per year is considered to be the best possible prediction for subsidence in the project area and between 53 and 83 Mt of peat carbon was lost for the same period of the study. The contribution of the maximum subsidence to the emission of CO₂ was estimated to be 52 tonnes per hectare per year. These results are not reliable enough for detailed planning purposes, but they provide a basis for further work by highlighting where methodological development is needed.

ACKNOWLEDGMENTS

Many thanks go out to the following individuals and organizations, all of whom played a vital part in making this research possible:

I would like to express my gratitude to my three supervisors: Dr Kevin Tansey, Dr Sue Page and Prof. Heiko Balzter for the time and constructive advices. They provided invaluable advice and fantastic support through the past four years.

Thanks go to all PhD students, staff in the Geography department for their assistance during my period of study. Thanks also go to all friends in Leicester who have mad my time here so enjoyable.

On a personal note, I would like to thank my Mum to her love and support throughout the past years. Special thanks to my Uncle Hanna and his family to their care and support.

In addition, I would to acknowledge the following:

- Damascus University, Syria for their financial support.
- CIMTROP team, University of Palangkaraya, Indonesia.
- ESA for providing ERS1/2 radar images.

*Although my father passed when I was child, I dedicated this thesis to him and my Mum.

Table of contents

1 Chapter one: Introduction

1.1 Tropical peatlands	01
1.2 Synthetic Aperture Radar (SAR)	04
1.3 InSAR applications	05
1.4 The knowledge gap	09
1.5 Aim and objectives	13
1.5 Thesis structure	15

2 Chapter two: SAR interferometry: A literature review

2.1 Introduction	17
2.2 Definition	18
2.2.1 Viewing Geometry and Spatial Resolution	18
2.3 Synthetic Aperture Radar (SAR)	19
2.4 Properties of the image phase	24
2.5. Measuring Topography	28
2.6. Terrain motion measurement using Differential Interferometry.....	32
2.6.1 Two-pass method	34
2.6.2 Three-pass method	35
2.6.3 Four-pass method	35
2.6.4 Complex interferogram combination	36
2.7 The Accuracy of DEM and DInSAR observations	36
2.8 Coherence	41
2.8.1 Coherence estimation	41
2.8.2 Applications of coherence	44
2.9 Factors affecting InSAR results	45
2.9.1 Temporal Decorrelation	46
2.9.2 Baseline decorrelation	48
2.9.3 The atmosphere and its effects on repeat-pass InSAR	49
2.10 Phase Unwrapping	53

2.10.1 Basic Measurement Principles	54
2.10.2 Residues	56
2.10.3 Phase unwrapping methods	58
3.10.3.1 Branch-Cut Concept for Phase Unwrapping	59
3.10.3.2 Minimum cost flow (MCF)	62
2.11 Persistent scatterer	63
2.12 Integrated InSAR with Global Positioning System (GPS)	66
2.12.1 Introduction to GPS	66
2.12.2 Calculating the distance to the satellite	67
2.12.3 Problems with height	68
2.12.4 Error Sources	69
2.12.5 Differential GPS	70
2.12.6 Real-Time DGPS Measuring Techniques	71
2.12.7 Limitations of GPS measurements	72
2.13 Summary	73

3 Chapter three: Characteristics of peat swamp forest ecosystem

3.1 Introduction	74
3.2 Peat subsidence	77
3.3 Causes of peat subsidence	78
3.3.1 Drainage and land clearing	78
3.3.2 Fire	79
3.4 Relationship between subsidence, groundwater level, and CO ₂ emission	81
3.5 Relationship between groundwater depth and CO ₂ emission.....	83
3.6 Burned area mapping in tropical ecosystems	84
3.7 Deforestation detection	87
3.8 measuring peat subsidence	89
3.9 Estimation of carbon emissions	91
3.10 Summary	94

4 Chapter four: Methods

4.1 Introduction	95
4.2 Study area	95

4.3 Source data and software	99
4.3.1 InSAR data	99
4.3.2 GPS observations	103
4.3.3 Burn area detection by optical remote sensing data	105
4.3.4 Software environment	105
4.4 Data processing	105
4.4.1 Co-registration	105
4.4.2 Interferogram calculation	109
4.4.3 Initial baseline estimation.....	110
4.4.4 Interferogram flattening	111
4.4.5 Coherence estimation	112
4.4.6 Interferogram filtering	114
4.4.7 Phase Unwrapping method	117
4.4.8 Precise baseline estimation	119
4.4.9 DEM Generation	125
4.5 DEM accuracy assessment	126
4.6 Differential processing	129
4.7 Statistical analysis	132
4.8 Estimate carbon loss and CO ₂ emission from tropical swamp forest.....	136
4.8.1 Carbon loss	136
4.8.2 CO ₂ emission	136
4.9 Summary	137

5 Chapter five: Coherence for change detection analysis

5.1 Introduction	138
5.2 The size of the estimation window	138
5.3 Weighting functions	140
5.4 Coherence change in Block C	145
5.5 Forest burn detection using visual interpretation	149
5.6 Forest burn detection using differential coherence	155
5.7 Coherence change in Block A	158
5.8 Deforestation detection in block A	161
5.9 Discussion	166

5.10 Limitation	174
5.11 Further work	175
5.12 Summary	176

6 Chapter six: InSAR DEM generation

6.1 Introduction	177
6.2 Phase Unwrapping	177
6.3 DEM generation	181
6.3.1 Maluku: Digital elevation model	182
6.3.2 Dadahup: Digital elevation model	186
6.4 Statistical analysis for DEMs	191
6.4.1 Maluku: Statistical analysis	191
6.4.2 Dadahup: Statistical analysis	193
6.5 Accuracy assessment and Comparison of DEMs	195
6.5.1 Maluku: Accuracy assessment of DEMs against GPS profiles	196
6.5.2 Maluku: Spatial distribution of relative assessment error.....	200
6.5.3 Dadahup: Accuracy assessment of DEMs against GPS profiles.....	205
6.5.4 Dadahup: Spatial distribution of relative assessment error.....	208
6.5.5 Maluku: Absolute assessment comparison	213
6.5.6 Maluku: Spatial distribution of absolute assessment error	219
6.5.7 Dadahup: Absolute assessment comparison	224
6.5.8 Dadahup: Spatial distribution of absolute assessment error.....	229
6.6 Discussion	235
6.7 Limitation	245
6.8 Further work	246
6.9 Summary	248

7 Chapter seven: Subsidence rates and carbon loss in peat soils

7.1 Introduction	249
7.2 Subsidence in Block C	250
7.3 Subsidence in Block A	257
7.4 Estimation of peat and carbon loss due to peat soil subsidence	261
7.5 Water table change between 1997 and 2000	267
7.6 CO ₂ emission between 1997 and 2000	270

7.7 Modelling the relationship between carbon loss, subsidence rate and water table change.....	275
7.8 Discussion	278
7.9 Limitation	292
7.10 Further work	294
7.11 Summary	296
8 Chapter eight: Conclusion	
8.1 Introduction	298
8.2 Finding: Objective 1	299
8.3 Finding: Objective 2	301
8.4 Finding: Objective 3	303
9 Bibliography	308
10 Appendices	
Appendix 1: Gamma interferometric SAR Processor (ISP) script:	
Intensity method	339
Appendix 2: Gamma interferometric SAR Processor (ISP) script:	
Orbit method	348
Appendix 3: Gamma Differential Interferometric SAR Processor (DISP) script:	
4-pass method.....	354
Appendix 4: Gamma Differential Interferometric SAR Processor (DISP) script:	
Complex interferogram combination method.....	357

List of Figures

Figure 1.1: Application of SAR interferometry	05
Figure 1.2: InSAR applications in Tropical peatland forest	11
Figure 2.1: Imaging geometry (Canada centre for remote sensing, 2007)	19
Figure 2.2: A sinusoidal function $\sin \Phi$ is periodic with a 2π radian period.....	25
Figure 2.3: Basic imaging geometry for SAR interferometry. A1 and A2 represent two antennas viewing the same surface simultaneously, or a single antenna viewing the same surface on two separate passes (NASA, 1994).....	26
Figure 2.4: A visual example that shows that main problem related to phase inconsistencies: integration of the phase values yields different results depending on the path followed. In this example, the first and the last pixels of the integration paths are common, but one path crosses a layover area, characterised by very low coherence values, and propagates significant phase unwrapping errors(Source : Ferretti,et al., 2007).....	56
Figure 2.5:(a) Visualizing residue calculation and (b) an inter-pixel network with a 2 x2 closed loop and marked inter-pixel residue.(Source: Karout, 2007).....	57
Figure 2.6: An inter-pixel network with a branch-cut between dipoles residues of opposite polarity (Source: Karout, 2007)	61
Figure 2.7:(a) Correct phase unwrapping paths avoiding the branch-cuts and (b) Wrong phase unwrapping paths cross over the branch-cuts(Source: Karout, 2007.).....	61
Figure 2.8: The relationship between Orthometric and Ellipsoidal height.....	69

Figure 3.1: Peat swamp forest in Central Kalimantan, Indonesia (Picture by B. Dahdal).....	76
Figure 3.2: Palm oil plantation in Central Kalimantan, Indonesia (Picture by B. Dahdal)	76
Figure 3.3: Burned peat surface 30x30 cm (Picture by B. Dahdal)	78
Figure 3.4: Illegal logging in Central Kalimantan, Indonesia (Picture by B. Dahdal) ...	81
Figure 3.5: Rice plantation in MRP, Indonesia.....	88
Figure 3.6: A drainage canal in MRP, Indonesia.....	89
Figure 3.7: Field measurement of peat subsidence	90
Figure 4.1: Situation of the Ex-MRP area	98
Figure 4.2: Location of the study area: Block C and block A (boundary indicated by a red cline) in the context of Ex-MRP. The two subset area (Maliku, Dadahup) are overlaid on ERS image	99
Figure 4.3: Available ERS images in the south of Central Kalimantan. Frame 4 and Frame 6 have been used further in analysis.....	100
Figure 4.4: The distribution of DGPS points in the study area	104
Figure 4.5: DGPS filed work collection	104
Figure 4.6: Schematic of steps in processing SAR data for interferometric applications	107
Figure 4.7: Interferometric phase of the ERS-1/2 tandem image pair over Frame 6 after Flattening with backscatter intensity as background	111
Figure 4.8: Coherence image derived from ERS-1/2 tandem pair acquired 22/23 October 1997 with backscatter intensity as background. Raspberry colour shows high coherence and Turquoise colour shows low coherence.....	112

Figure 4.9: Flattened and filtered interferometric phase and intensity for the ERS-1/2 tandem image pair. Each individual fringe is displayed a complete colour cycle from blue to green	116
Figure 4.10: Unwrapped phase for the ERS-1/2 tandem image pair using MCF method with backscatter intensity as background. Phase displayed as 6π per colour cycle.....	119
Figure 4.11: Distribution of GCPs that been used in precise baseline estimation.....	123
Figure 4.12: Distribution of GCPs overlaid on Maliku DEM	127
Figure 4.13: Distribution of GCPs overlaid on Dadahup	127
Figure 4.14: Frequency of DGPS check point elevation	128
Figure 4.15: Flow chart for differential interferometry processing methods	131
Figure 5.1: Coherence image of interferogram 2000 using different search windows.....	139
Figure 5.2: Histograms of the coherence values for each search window size	141
Figure 5.3 Coherence using different magnitude weighting functions	143
Figure 5.4: Histograms of of the coherence values for different magnitude weighting functions	144
Figure 5.5: Time series of coherence in frame 4.....	147
Figure 5.6 Time series of coherence in Block C within Frame 4.....	148
Figure 5.7: Coherence classification between March 1996 and January 2000 using value 0.25	151
Figure 5.8: Coherence classification between March 1996 and January 2000 using value 0.35	152
Figure 5.9: Coherence classification between March 1996 and January 2000 using value 0.5	153

Figure 5.10: Burn scar 1997 in Block C based on minimum coherence value 0.35. Crosshatch represents burn scar obtained by optical data.....	154
Figure 5.11: The change of coherence in Block C of three different time intervals compared to coherence in January 2000.....	156
Figure 5.12 Distribution of burn scars in Block C from 1997 fires using coherence change method. Crosshatch represents burn scar obtained by optical data.....	157
Figure 5.13: Time series of coherence in frame 6.....	159
Figure 5.14: Histograms of the coherence images in frame 6	161
Figure 5.15: Time series of coherence in Block A within Frame 6.....	163
Figure 5.16: The change of coherence in Block A of three different time intervals.....	164
Figure 5.17: The deforestation area in Block A as derived from ERS images based on differential coherence value of more than 0.2.....	165
Figure 5.18: Study site in Central Kalimantan, Borneo, Indonesia. Burned area derived from analysis of post-fire Landsat TM 5 and multi-temporal ERS SAR images burnt areas detected by both Landsat and ERS are indicated in red; burnt areas detected only by Landsat are shown in palevioletred; burnt areas detected only by ERS SAR and undetectable by Landsat TM 5, owing to plant re-growth are shown in moccasin (Source: Page <i>et al.</i> , 2002).....	172
Figure 6.1: The unwrapped phase maps for the interferogram generated by ERS tandem pair acquired in October 1997 in frame 4	179
Figure 6.2: DEM for the Maluku test site generated from ERS-1/2 tandem radar images using different processing techniques	183
Figure 6.3: Histograms of elevation frequency of 1997-DEMs in Maluku	184
Figure 6.4: DEM of Maluku test site generated from eight ERS-1/2 tandem radar images using intensity adaptive filter t processing technique with MCF unwrapping	

Method	185
Figure 6.5 DEM for the Dadahup test site generated from ERS-1/2 tandem radar images using different processing techniques with BC unwrapping method	187
Figure 6.6: DEM for the Dadahup test site generated from ERS-1/2 tandem radar images using different processing techniques with MCF unwrapping method.....	188
Figure 6.7: DEM for the Dadahup test site generated from three ERS-1/2 tandem radar images using intensity adaptive filter processing technique with MCF unwrapping method	189
Figure 6.8: Histograms of elevation frequency of 2000- DEMs in Dadahup.....	190
Figure 6.9: The mean elevation of Maluku DEMs	193
Figure 6.10: The elevation difference between the mean values of DEMs and the mean value of DGPS check point.....	196
Figure 6.11: Histogram of the absolute elevation differences (m) between InSAR DEMs and GCPs in Maluku using 100 points	197
Figure 6.12: RMSE change due to coherence change	199
Figure 6.13: Error distribution of check GCPs in DEM2000 in Maluku	202
Figure 6.14: Error distribution of check GCPs for four DEMs generated from eight ERS-1/2 tandem radar images over Maluku site using intensity adaptive filter processing technique with MCF unwrapping method	203
Figure 6.15: Coherence changes of GCPs in Maluku between 1996 and 2000.....	204
Figure 6.16: Histogram of the absolute elevation differences (m) between InSAR DEMs and GCPs in Dadahup using 100 points	207
Figure 6.17: Error distribution of check GCPs in DEM2000 in Dadahup using intensity and intensity adaptive filter processing technique	209
Figure 6.18: Error distribution of check GCPs in DEM2000 in Dadahup using orbit	

and orbit adaptive filter processing technique	210
Figure 6.19: Error distribution of check GCPs for three DEMs generated from six ERS-1/2 tandem radar images over Dadahup site using intensity adaptive filter processing technique with MCF unwrapping method	211
Figure 6.20: Coherence change in Dadahup between 1996 and 2000.....	212
Figure 6.21: Final DEM for Maluku using intensity processing technique with MCF unwrapping method.....	214
Figure 6.22: Spatial distribution of elevation difference between DEMs-1997 and DEM17 (reference)	215
Figure 6.23: Spatial distribution of elevation difference in Maluku between three tandem ERS image DEMs (DEM5, DEM11 and DEM23) and DEM17 (reference)...	218
Figure 6.24: Histograms of variation between Maluku reference DEM and generated DEMs.....	219
Figure 6.25: Spatial distribution of absolute elevation difference between DEMs-1997 and DEM17 (reference)	220
Figure 6.26: Spatial distribution of absolute elevation difference in Maluku between three tandem ERS image DEMs (DEM5, DEM11 and DEM23) and DEM17 (reference)	223
Figure 6.27: Final DEM for Dadahup using orbit processing technique with MCF unwrapping method	225
Figure 6.28: Spatial distribution of elevation difference between DEMs-2000 and DEM24 (reference) using BC unwrapping method.....	226
Figure 6.29: Spatial distribution of elevation difference between DEMs-2000 and DEM24 (reference) using MCF unwrapping method	227

Figure 6.30: Spatial distribution of absolute elevation difference in Dadahup between two tandem ERS image DEMs (DEM8 and DEM16) and DEM24 (reference)	228
Figure 6.31: Histograms of variation between Dadahup reference DEM and generated DEMs.....	229
Figure 6.32: Spatial error distribution of absolute elevation difference of 2000-DEMs using BC unwrapping method relative to DEM24.....	232
Figure 6.33: Spatial error distribution of absolute elevation difference of 2000-DEMs using MCF unwrapping method relative to DEM24.....	233
Figure 6.34: Spatial distribution of absolute elevation difference in Dadahup between two ERS tandem image DEMs (DEM8, DEM16) and DEM24 (reference)	234
Figure 6.35: RMSE comparison of twenty four DEM profiles against GPS height profiles in Maluku.....	238
Figure 6.36: RMSE comparisons of twenty four DEM profiles against GPS height profiles in Dadahup test site.....	239
Figure 7.1: Peat subsidence rate (cm/y) for Block C during the time period 1997-2000 using two DInSAR techniques.....	252
Figure 7.2: DInSAR derived subsidence in Block C using complex interferogram method represented in 3D view with 1000 vertical exaggeration.....	253
Figure 7.3: Profile lines along and across Maluku.....	253
Figure 7.4: Profiles comparison graph along the ESE-WNW transect line in Maluku..	254
Figure 7.5: Coherence change between 1997 and 2000 in the ESE-WNW transect line in Maluku.....	255
Figure 7.6: Profiles comparison graph along the NNE-SSW transect line in Maluku...	256
Figure 7.7: Coherence change between 1997 and 2000 in the NNE-SSW transect line in Maluku.....	256

Figure 7.8: Peat subsidence map (cm/y) for Block A during the period 1997-2000 using two DInSAR techniques.....	258
Figure 7.9: Profile lines along and across the Dadahup site.....	260
Figure 7.10: Displacement profiles along an ESE-WNW transect in Dadahup.....	260
Figure 7.11: Profiles comparison graph along a NNE-SSW transect line near Dadahup	261
Figure 7.12: Peat loss rate in Block C based on CIC differential method.....	263
Figure 7.13: Peat loss rate in Block A based on CIC differential method.....	264
Figure 7.14: The rate of carbon loss in Block C based on CIC differential method.....	265
Figure 7.15: The rate of carbon loss in Block A. based on CIC differential method....	266
Figure 7.16: Water table changes for the maximum and minimum drainage scenario in Block C based on CIC differential method using the coefficient values of the linear relationship between subsidence and water table depth change	268
Figure 7.17: Water table changes for the maximum and minimum drainage scenario in Block A based on CIC differential method using the coefficient values of the linear relationship between subsidence and water table depth change	269
Figure 7.18: CO ₂ emissions for the maximum and minimum drainage scenario in Block C based on CIC differential method using the coefficient values of the linear relationship between subsidence and water table depth change	273
Figure 7.19: CO ₂ emissions for the maximum and minimum drainage scenario in Block A based on CIC differential method using the coefficient values of the linear relationship between subsidence and water table depth change	274
Figure 7.20: Carbon loss and CO ₂ emission rate in Block C and Block A	278

List of Tables

Table 1.1: Deformation measuring techniques	09
Table 2.1: Summaries of the characteristics of some SAR sensors	23
Table 4.1: List of ERS tandem data used in this study	102
Table 4.2: General value of offset estimation used in Gamma software.....	108
Table 4.3: Programs of Gamma software used in the two different approaches.....	116
Table 4.4: Branch Cut unwrapping steps and programs	118
Table 4.5: MCF unwrapping steps and programs.....	118
Table 4.6: List of GCPs in frame 4 that have been used to estimate precise baseline..	121
Table 4.7: List of GCPs in frame 6 that have been used to estimate precise baseline..	122
Table 4.8: GCPs in radar geometry in frame 4.....	124
Table 4.9: Gamma programs used in baseline and corrected height estimation.....	125
Table 4.10: Topographic and differential interferogram	130
Table 4.11: General value of offset estimation.....	130
Table 4.12: Four-pass steps and programs.....	132
Table 4.13: Complex interferogram combination steps and programs.....	134
Table 5.1: Descriptive statistics of coherence using different search window.....	141
Table 5.2: Descriptive statistics of coherence using different weighting functions.....	144
Table 5.3: Summary of statistical parameters for coherence values in frame 4.....	146
Table 5.4: Summary of statistical parameters for coherence change in frame 6.....	160
Table 5.5: Comparison of burn scar area identified by different methods.....	171
Table 6.1: Summary of statistical parameters for phase unwrapping.....	181
Table 6.2: Descriptive statistics of InSAR DEM in Maliku site.....	192

Table 6.3: Statistic information for different DEM processing in Maliku.....	193
Table 6.4: Descriptive statistics of InSAR DEM in Dadahup site.....	194
Table 6.5: Accuracy of Maliku DEMs from DGPS check points.....	199
Table 6.6: RMSE values of Maliku DEMs against coherence	200
Table 6.7: Accuracy of Maliku DEMs from DGPS check points.....	206
Table 6.8: Descriptive statistics of DEMs 1997 in Maliku relative to DEM17.....	214
Table 6.9: Summary of statistical parameters for absolute elevation difference in Maliku between three-ERS tandem image DEMs (DEM5, DEM11 and DEM23) and DEM17 (reference)	217
Table 6.10: Summary of statistical parameters for elevation difference between DEMs 1997 and reference DEM (DEM17).....	222
Table 6.11: Summary of statistical parameters for absolute elevation difference in Maliku between three-ERS tandem image DEMs (DEM5, DEM11 and DEM23) and DEM17 (reference).....	222
Table 6.12: Summary of statistical parameters for elevation difference between 2000- DEMs and reference DEM (DEM24).....	225
Table 6.13: Summary of statistical parameters for elevation difference in Dadahup between two-ERS tandem image DEMs (DEM8, DEM16) and DEM24 (reference)...	229
Table 6.14: Summary of statistical parameters for absolute elevation difference in Dadahup between 2000-DEMs and reference DEM (DEM24).....	231
Table 6.15: Summary of statistical parameters for absolute elevation difference in Dadahup between two-ERS tandem image DEMs (DEM8, DEM16) and DEM24 (reference).....	231
Table 7.1: Statistical information about peat subsidence rate (cm/year).....	259
Table 7.2: Total carbon loss from Block C and Block A during the period between	

1997 and 2000.....	263
Table 7.3: Emission estimates of carbon dioxide (CO ₂)	272
Table 7.4: Adjust emission estimates of carbon dioxide (CO ₂)	277
Table 7.5: Peat subsidence in the north of Block C measured by CIMTROP team.....	283
Table 7.6: Peat subsidence rate along a 10 km transect between the Kahayan and Sebangau Rivers measured by CIMTROP team.....	284

Chapter 1: Introduction

1.1 Tropical peatlands

Tropical peat swamp forests (PSF) are important within the global Earth system as they have several functions that make them valuable ecosystems. Their existence depends upon specific environmental conditions and they, at the same time, influence the environment. Any changes brought about to this complicated relationship affect the natural functions of tropical peatlands and reduces their natural resource value to both the environment and human communities. Peat is an accumulation of partially decomposed organic matter, mostly of plant origin. According to the Global Peatlands Initiative (2002) peat lands cover 3% of the Earth's land area and store a large fraction of the world's terrestrial carbon resources, equivalent to one-third of global soil carbon and up to 70 times the current annual global emissions from fossil fuel burning. Peatlands are multi-functional natural resource systems that play an important role in flood mitigation, climate regulation, carbon storage, maintenance of water quality, habitats provision for plants and animals, food supply, grazing land and supplies of fuel, fibre and peat.

The area of peatlands in Indonesia alone is approximately 20 million hectares (Mha), which is nearly 11% of the total Indonesian land area (Rieley *et al.*, 1996). Large areas of tropical peatland in Indonesia are under threat from land clearance for agriculture and plantations, degradation and fire, putting their natural functions as reservoirs of biodiversity, carbon stores and hydrological buffers at risk. The current deforestation

rate of peat swamp forest in Indonesia is approximately 2.2 % per year (Page *et al.*, 2006).

Tropical peat swamp forest fires and drainage have important impacts within the peatland area affected, as well as on the surrounding areas and the global environment. PSF have been used by local people for millennia for a large variety of life support products and services. These activities include gathering, hunting, fishing, shifting, agriculture, and timber extraction. Over logging and illegal logging activities, in the PSF Central Kalimantan, Indonesia, have degraded the forest condition, making the logged forest more vulnerable to future fires (Siegert *et al.*, 2001; Cochrane and Chulze, 1999). However, the most extensive forest loss in this Province occurred following the implementation of the former Mega Rice Project (Ex-MRP) in 1995. The intensive drainage infrastructure, consisting of numerous canals, had an impact on the peatland hydrological system and increased the risk of fire. The canals allowed easier access for people into previously remote areas of peatland and their activities provided ignition sources. In addition, during the widespread fires of 1997, previously disturbed (logged) and drained peat swamp forest was heavily impacted (Page *et al.*, 2000). Severe drainage leads ultimately to collapse of the peat structure, increasing tree-fall and eventually complete loss of forest cover. Peat soils need drainage and cultivation to establish productive conditions for agriculture or plantation crops. However, this leads to irreversible shrinkage and oxidation (loss of carbon as carbon dioxide) in peat area.

Indonesian forest fires burned down millions of hectares of natural forest in 1987, 1991 and 1994, whilst very large scale fires blazed during the second half of 1997 and the first months of 1998. Many of these fires occurred in peatland forests. Central

Kalimantan province, which has about 6 million hectares of peat swamp forest, experienced some of the most severe peatland fires, with hundreds of thousands of square kilometres of both peat forest and the underlying peat burned away (Page *et al.*, 2000). The occurrence of these fires was linked to the El-Nino climate oscillation. The fires were also a result of agricultural activity that resulted in the peat soils drying out and being set on fire. Similar fires occurred in 2002. Based on a field survey reported by Page *et al.* (2002), the thickness of peat lost through combustion during the 1997 fires in degraded peatland in Central Kalimantan averaged 0.40 m. They estimated that 0.19–0.23 gigatonnes (Gt) of carbon were released to the atmosphere through peat combustion, with a further 0.05 Gt released from burning of the overlying vegetation.

Obtaining information on burn scar area, topographic information and peat subsidence rates in tropical peatland is important for further land-use management and the development of mitigation strategies to reduce peat subsidence rates, and hence, CO₂ emissions from peat mineralization, and to protect sensitive wetlands set aside for nature conservation. However the possible damaging effects of drainage and subsidence need to be known in order that they can be predicted even at the initial phase of land development. Remote sensing has been widely used to map and monitor land cover and deformation change and generate digital elevation models (DEM). The problem with optical remote sensing systems for tropical swamp forest studies was the lack of available data caused by cloud cover. Therefore, the use of Synthetic Aperture Radar (SAR) in forest application has received considerable attention over the past two decades (Kasischke *et al.*, 1994; Kasischke *et al.*, 1997; Waring *et al.*, 1995). This will be addressed in the next section.

1.2 Synthetic Aperture Radar (SAR)

Synthetic Aperture Radar (SAR) is a powerful remote sensing system, enabling observations of the Earth's surface day or night, in all weather conditions from airborne platforms and from space. Interferometric Synthetic Aperture Radar (InSAR) is a powerful technique that uses differences in reflected radar signals acquired from nearly the same antenna position (viewing angle) but at different times (Rosen *et al.*, 2000). By combining two or more SAR images of the same area, it is also possible to generate elevation maps and surface change maps with unprecedented precision and resolution. InSAR has demonstrated dramatic potential for many application including: the observation of land cover change, the creation of high accuracy DEMs and deformation monitoring of the Earth's crust with millimetre per year accuracy at very dense spatial sampling (Gabriel *et al.*, 1998; Zebker and Goldstein, 1986 and Strozzi *et al.*, 2000). These applications are illustrated by Gens (1998) in Figure 1.1, which foresee many applications of InSAR in tropical peatland ecosystems, for example, mapping out clear cuts and burn scar areas by using either the phase or the coherence information, measuring the terrain elevation and detecting land subsidence.

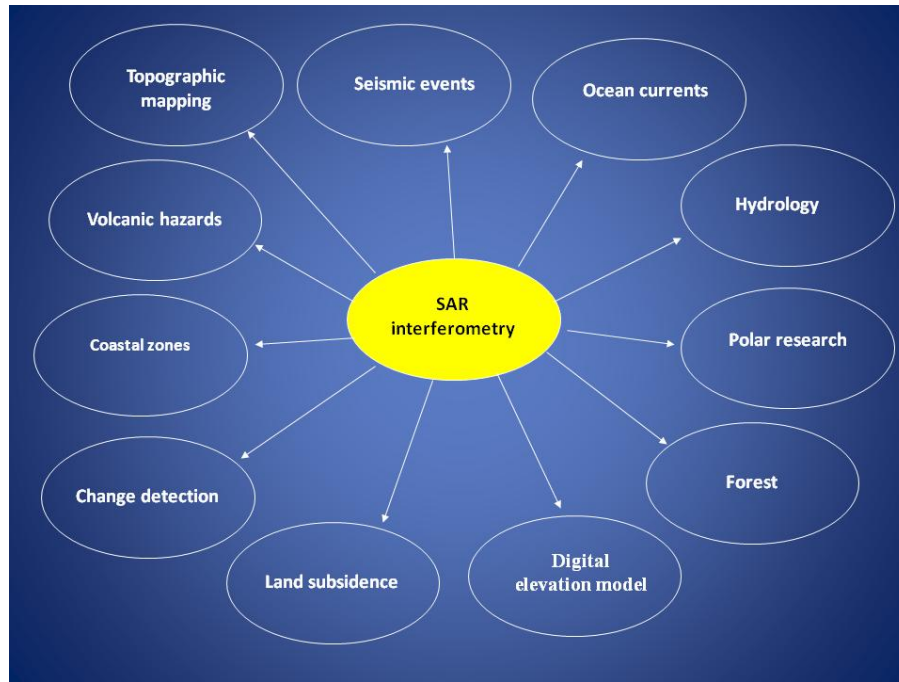


Figure 1.1: Application of SAR interferometry (Source: Gens, 1998).

1.3 InSAR applications

The SAR intensity image shows the characteristics of the scattering mechanisms of the ground surface. Coherence is another important parameter to measure the correlation between two complex SAR images taken from slightly different orbital positions; hence, it measures InSAR data quality in repeat-pass interferometry. The fact that interferometric coherence does not rely on actual backscatter from the target but random dislocation of the scatterers between the two passes, makes it an independent physical parameter that is different from the SAR backscatter. The coherence will be high if the recorded radar echoes represent nearly the same interaction with the observed target between the two images (Zebker and Villasenor, 1992). The two main effects that cause the coherence to decrease are normally referred to as temporal and volume decorrelation. The signatures of backscattering intensity and coherence have been used for land cover classification (Wegmüller and Werner, 1995) especially in forest

mapping (Wegmuller *et al.*, 1995; Balzter, 2001). SAR data has been shown to offer useful information for forestry applications, especially in cases of major forest change such as that caused by severe storms or fires. Under these circumstances, the availability of operational tools dedicated to forest monitoring is of great interest (Balzter *et al.*, 2002). Early results obtained using European Remote Sensing (ERS) repeat-pass data by Hagberg *et al.*, (1995) and Wegmuller and Werner (1995) showed that the interferometric coherence is significantly lower over forest than over open canopies, short vegetation, bare soils, burn scars, deforestation and urban areas. Subsequent studies of ERS-1/2 tandem data demonstrated in particular that the one-day repeat pass coherence is useful in land use mapping (Strozzi *et al.*, 2000).

DEMs are one of the most demanded products in the remote sensing community and have become a vital source of topographical data for the geoscientific community. In most regions where topographical data is simply non-existent or unavailable, generating DEMs from remotely sensed data can be the key to providing the required information. The InSAR system can be used to produce a highly accurate global DEM with its advantages in significantly less time and at significantly lower cost than other systems without the limitation of weather. There are a number of studies on the use of SAR interferometry data for DEM generation (Crosetto, 2002; Rocca *et al.*, 1997; Rosen *et al.*, 2000) and retrieval of terrain parameters (Zebker *et al.*, 1994a; Rufino *et al.*, 1998; Rabus *et al.*, 2003; Koch *et al.*, 2002). However, InSAR DEMs still have some problems such as vegetation cover and the near- and far-range areas where elevation data appear noisy (Jensen and Domingue, 1998). For this reason, InSAR DEMs have relatively low precision and accuracy compared to other DEM sources such as LIDAR data.

The digital description of the three-dimensional surface is important for several applications. DEMs have drastically changed the ways land surveyors and photogrammetrists collect elevation data for the production of contour maps. With the aid of DEMs, high quality contour maps can now be produced more quickly and economically. Planning and construction is one of the fields where DEMs are widely applied to different aspects, such as reconnaissance, design, construction and the maintenance of roads, railroads, airports, canals, dams, water reservoirs, pipe lines, power transmission lines and many others. Each of these applications could have different quality requirements. The quality needed for these applications is not high and their assessment methods will depend on how accurate the application needs to be (Gens, 1998). In agriculture, DEMs are mainly applicable in the design of irrigation networks, water flow management; surface modulation and in determining suitable areas for cultivation and agricultural land use management. Slope maps can be extracted from DEMs to show suitable areas for various crops and cultivation schemes.

The detection of regional-scale subsidence has historically depended on the discovery that key bench marks have moved. This has traditionally been accomplished using levelling **equipments** and more recently, Global Positioning System (GPS) surveys. Both digital level and station surveys can deliver 0.1 mm height change resolution (Table 1) while GPS can sense 5 mm changes in static and 2-3 cm in RTK modes (Ge *et al.*, 2003). However, the cost to repeat the measurement of a complete levelling network is high and is difficult to use in some places such as forest, valley or mountains. Therefore complete levelling surveys cannot be repeated often. With GPS it is time and cost effective to be considered to repeat the measurements every 2-3 years as well as

some areas can not be reached by GPS such as tropical forest areas. Differential interferometric synthetic aperture radar (DInSAR), which has emerged in the past decade, has dramatically improved the capability to detect and map land-surface deformation. DInSAR is a radar technique to detect the surface deformations by computing a differential interferogram of the same scene over two repeat-pass acquisitions (Prats *et al.*, 2008). This technique provides relative measures of the order of a few centimetres or even less (sub-centimetre) (Galloway *et al.*, 2000).

DInSAR has been increasingly used to monitor ground surface deformations due to such occurrences as underground mining and fluid extraction (Fielding *et al.*, 1998; Hanssen, 2007), earthquakes and volcanic activities (Rosen *et al.*, 1996) and land subsidence (Galloway *et al.*, 2000, Amelung *et al.*, 1999; Klees and Massonnet, 1999), such as ground-surface displacements associated with tectonic (Massonnet *et al.*, 1993; Zebker and Goldstein, 1986) and volcanic strains (Massonnet *et al.*, 1995; Rosen *et al.*, 1996; Wicks *et al.*, 1998). InSAR has also recently been used to map localized crustal deformation and land subsidence associated with geothermal fields in Imperial Valley, California (Massonnet *et al.*, 1997), Long Valley, California (Galloway *et al.*, 2000), and Iceland (Vadon and Sigmundsson, 1997), and with oil and gas fields in the Central Valley, California (Fielding *et al.*, 1998). InSAR has also been used to map regional-scale land subsidence caused by aquifer-system compaction in the Antelope Valley, California (Galloway *et al.*, 1998), Las Vegas Valley, Nevada (Amelung *et al.*, 1999), and Santa Clara Valley, California (Ikehara *et al.*, 1998).

Table 2: Deformation measuring techniques (Galloway *et al.*, 2000).

Method	Component displacement	Resolution (mm)	Spatial density (samples/survey)	Spatial scale (elements)
GPS	Vertical and horizontal	5-20	10-100	network
Spirit level	Vertical	0.1-1	10-100	line-network
DInSAR	Range	5-10	100000-1000000	Map-pixel (40-80 m ²)

1.4 The knowledge gap

The InSAR technique has not yet been tested to identify burn scar areas, clearings and generating DEMs in tropical peat swamp forest (PSF) areas. DInSAR has also not been used to measure peat soil subsidence on a large scale. Various assessments have been made of the amount of land in Indonesia that was damaged by the 1997 fire. Liew *et al.* (1998) estimated 4.5 Mha of land in Indonesia had been damaged by 1997 fires but this was subsequently increased to 9 million ha (BAPPENAS, 1998; Page *et al.*, 2002). The Centre for Remote Imaging, Sensing and Processing (CRISP) at the National University of Singapore derived estimates for Kalimantan and Sumatra by interpreting SPOT quicklooks and they calculated that approximately 3 Mha burnt in Kalimantan. The WWF Fire Project used NOAA-AVHRR in conjunction with Defence Meteorological Satellite Program (DMSP) imagery and estimated that between 1.97 and 2.3 Mha were burnt in Kalimantan between August and December 1997 (Fuller and Murphy, 2006).

An official estimate from the State Ministry of Environment (KLH) in Indonesia states that approximately 400,000 ha of forest and other land was burnt in 1997 (Dennis, 1999). The KLH report indicates that 85% of the burning was caused by oil palm plantation companies, industrial plantations and logging concessions. These widely varying estimates of total area burnt show that there is still much work required just to answer the basic question of how much was burnt. The evaluation of high resolution optical remote sensing data such as Landsat TM or Spot images are hampered by frequent cloud cover and haze during active burning. The SAR sensor is able to penetrate clouds and haze and provides the high spatial resolution (< 40 m) necessary to identify and estimate burnt areas. In boreal forests it was found that ERS backscatter strongly increases on fire scars due to an increase in soil water (French *et al.*, 1996). Interferometric coherence between image pairs has proven to be a valuable source of information in forestry (Balzter, 2001). The coherence of fire scars was found by many researchers to be lower than unburned forest before 1997 and higher after 1997, i.e. the coherence of fire scars fluctuates stronger than that of unburned forest with seasonal change. This indicates the coherence is a good indicator for identifying the fire scar in time series data. Further analyses are still needed to investigate whether or not coherence SAR interferometric images alone can be used to survey the extent and impact of 1997 forest fires in Indonesia (Figure 1.2). On the other hand, numerous tropical deforestation studies have employed multispectral remotely sensed imagery but only a limited number of tropical deforestation studies have incorporated SAR data, and even fewer have employed data acquired from orbiting satellites. Given the need for more research, and the fact that extensive cloud cover excluded the utilization of other

types of remotely sensed data, the use of InSAR coherence products in the current study is logical and warranted.

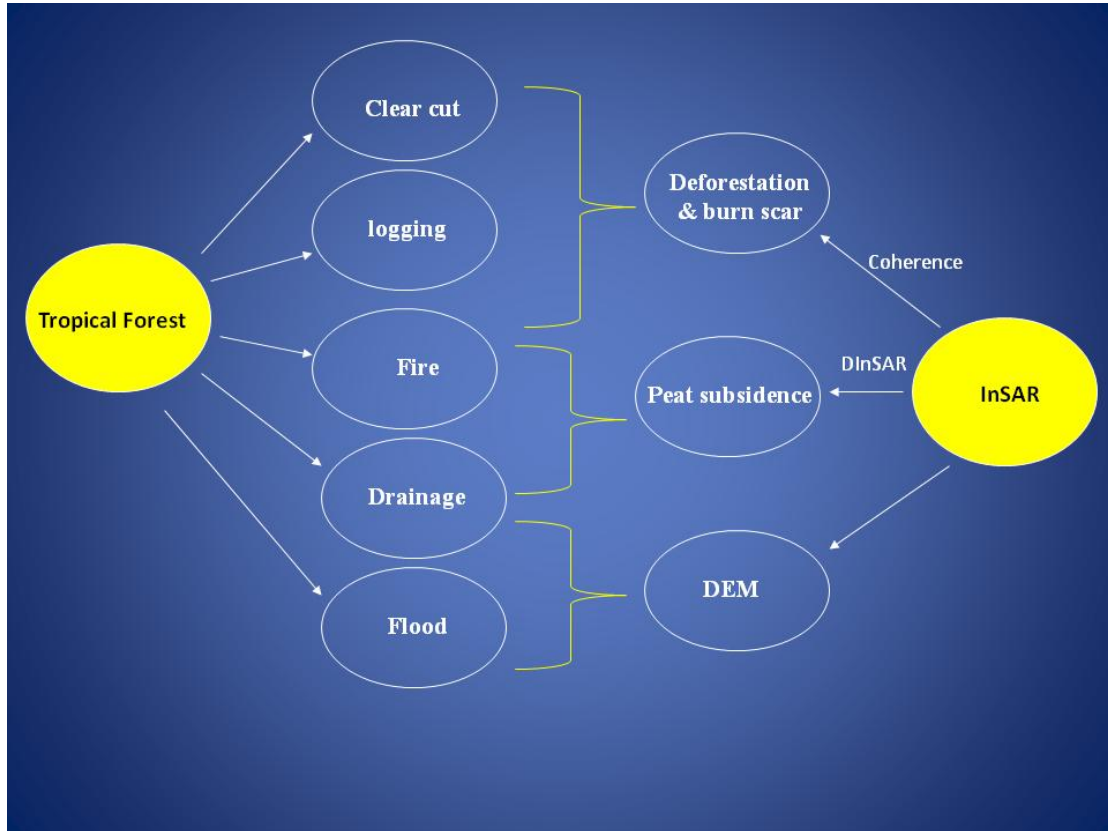


Figure 1.2: InSAR applications in tropical peatland forest.

According to previous studies on the evaluation of DEMs generated by ERS tandem pair using interferometric technique, the root-mean-square error of approximately 16.9 m (Jayaprasad *et al*, 2008), 5 m (Zebker *et al.*, 1994a), 11.3 m (Baek *et al.*, 2005), 1.7 m (Hagberg and Ulander, 1993) and 7 m (Al-Harbi, 2009) can be achieved. As a large part of Central Kalimantan is covered with tropical swamp forest, it is interesting to investigate how well an INSAR-derived DEM corresponds to the real terrain height in such areas. It should be possible to produce digital elevation models (DEM) or slope maps from repeat-pass SAR interferometry over tropical forested terrain. Such DEMs

may be useful for communication coverage, road and canal construction and flood mapping. It is also interesting to investigate how the accuracy of an ERS-derived DEM corresponds with RMS errors predicted in forest land cover to be around 18.7 m by Rufino *et al.* 1998) and 18.1 m and 5.1 m by Guritz *et al.* (1999). The quality of the produced DEMs based on ERS tandem pairs seem to be strongly affected by four issues; the offset estimation, interferogram computation, filtering and phase unwrapping methods. Little research has been carried out to reduce the errors that are caused by interferometric processing. Therefore, these four issues still need more analysis on their effects on DEM errors, especially over tropical swamp forest terrain.

Traditional methods that have been used to detect peat subsidence have used extensive sampling where by material was collected from numerous sites. These methods are not convenient in terms of either time or cost. Measuring peat soil subsidence is very difficult to achieve in tropical swamp areas due to vegetation and forest barriers. It is a big challenge to measure it with InSAR methods that are already used to measure other forms of ground subsidence. DInSAR offers the typical advantages of remote sensing techniques over classical methods used to measure subsidence deformation because, if the deformation interferogram is generated successfully: it provides data over inaccessible areas and large area coverage (for example, a scene of the ERS, covers 100 by 100 km). By comparing DInSAR with other common techniques, such as Differential Global Positioning System (DGPS) and instrumental methods, the latter can only measure ground deformations at a few discrete points, not over a wide and continuous area. However, DInSAR can potentially provide deformation measurements with a quality that is comparable with that of the traditional geodetic techniques. Although **levelling** and **surveying** instruments allow for the detection of very small

deformations, it is rather expensive and time-consuming. Because of the high temporal and spatial resolution versus relatively low costs, the interferometric use of Synthetic Aperture Radar (InSAR) is in principle a promising supplement for precise deformation monitoring. Another important advantage of the DInSAR technique is the availability of large time series of SAR images, which in the case of the ERS satellites cover more than a decade, starting from 1991, so it is possible to study the evolution of the subsidence in tropical peat soil in the last 20 years. This represents an unmatched capability compared with the traditional geodetic techniques, which might be unavailable and require long observation periods.

Measuring subsidence in peat soils can provide further information on the volume of peat soils removed over time and the amount of carbon released by fire or drainage events. By understanding the processes that cause the collapse and lowering of the peat soil surface, steps can be taken to minimise the environmental impact of land cover change in the future. Subsequent observations are required in order to determine the magnitude and rate of surface subsidence that has been caused by initial drainage or by forest fire and then combustion of the peat surface.

1.5 Aim and objectives

The aim of this project is to detect deforestation areas and generate DEMs by means of InSAR techniques. A further aim is to examine if differential SAR Interferometry can detect peatland subsidence accurately by considering the processes of peat soil compaction and oxidation or subsidence as a result of fire. Specific objectives are to:

-
1. Examine the ability of InSAR coherence to discriminate between forest and non-forest, in order to identify burn scar areas and determine areas that have been clear-cut.
 2. Examine InSAR techniques for digital elevation model generation using 14 ERS-1 and ERS-2 SAR images in tropical swamp forest and test errors that are caused by interferometric processing. Interferometric DEM generation is subject to many processing stages such as; image registration, interferogram calculation, filtering, phase unwrapping and phase-to-height transformation. This study aims to examine the accuracy of the first four processes by assessing DEM accuracy.
 3. Test the validity of the method to provide quantitative spatial information on the amount of peat soil that has subsided and determine carbon loss and CO₂ emissions. The observations will provide the first ever spatial overview of subsidence of peat soil in a tropical area. By integrating a number of observations, it should be possible to determine the amount of peat soil that has subsided due to biological oxidation or been burnt.

1.6 Thesis structure

The thesis is divided into eight chapters including the introduction chapter:

- a) Chapter 1 introduces a description of tropical peatland ecosystem and highlights the main driving forces of peat loss. This chapter foresees some applications of microwave remote sensing in tropical peatland forest. The gap of knowledge is identified and the aim and objectives of the thesis are presented.
- b) Chapter 2 gives a formal description of the Principles of SAR interferometry and explains the main theories concerning DInSAR. It also discusses the quality of interferometric results and examines the factors that can affect this quality including coherence, temporal decorrelation, baseline decorrelation, atmospheric effects and phase unwrapping.
- c) Chapter 3 outlines the importance of tropical peat swamp forest with a focus on the causes and consequences of deforestation and degradation of PSF ecosystems, particularly in the former Mega Rice Project area, Central Kalimantan, Indonesia. Peat subsidence and its causes and main characteristics are addressed.
- d) Chapter 4 gives the methods and materials used in this study, including a description of the study area and data sets. This chapter also addresses the InSAR and DInSAR processing techniques that have been used in this study to approach the research objectives.
- e) Chapter 5 provides the results of using interferometric coherence to identify burn scars and deforestation in the study area. The results are discussed in the context of relevant literature and the thesis objectives.

-
- f) Chapter 6 provides the results of an analysis of the accuracy of InSAR DEM derived from ERS-, ERS-1, and C-band spaceborne repeat-pass data using different processing InSAR techniques. It also outlines analysis of the spatial distribution of the elevation error in order to understand the error present in generated DEMs. The chapter summarises a general discussion about the suitability of the DEMs created to determine and map topographic structure.
- g) Chapter 7 illustrates and discusses the results of using the DInSAR approach to measure peat subsidence and estimate the carbon loss and CO₂ emission between 1997 and 2000.
- h) Chapter 8 draws conclusions from this study in relation to each of the three research objectives and presents further directions of research suggested by the results.

Chapter 2: SAR Interferometry: A Literature Review

2.1 Introduction

The introduction of imaging radar can be regarded as one of the most spectacular developments in remote sensing since the early 1960s. It opened a world of applications in geoscience and astronomy, and provided an alternative to the traditional optical methods of imaging, which need solar illumination and cloudless skies. Imaging radar, obtained using the synthetic aperture concept can be used for measuring spatial variations in the distance to the earth using two radar images and the principle of interferometry (Gabriel and Goldstein, 1988). This technique, known as interferometric synthetic aperture radar (InSAR), applied on board a satellite is able to image an area on earth with a typical revisit period of about 1 month. The phase difference between the two images will be determined by the path length difference between the two observation points to the resolution cell. Temporal variations in the satellite-earth distance, due to deformations such as subsidence, earthquakes and volcano dynamics, can be measured as well, with accuracies starting at the sub-cm level. The quality of an interferometric result is a function of several factors, one major influence being coherence. Interferometric radar relies on the coherence of the two signals; incoherent signals can not be used for interferometry. Other factors such as temporal decorrelation, baseline decorrelation, atmospheric effects and PU problem have a significant influence on the accuracy of delivered digital elevation model (DEM) and differential maps.

2.2 Definition

RADAR stands for Radio detection and ranging. Radar is a device which is called an "active sensor", because it emits energy in order to scan objects and areas whereupon a sensor then detects and measures the radiation that is reflected or backscattered from the target. Visible and infrared sensors are called "passive sensors" because they detect natural radiation that is emitted or reflected by the object or surrounding area being observed (Kang, 2007). Reflected sunlight is the most common source of radiation measured by passive sensors. Radar sends wave radiation in a series of pulses from an antenna, looking obliquely at the surface perpendicular to the direction of motion. When the energy reaches the target, some of the energy is reflected back towards the sensor. This backscattered microwave radiation is detected, measured and timed. Unlike instruments that look straight down such as aerial cameras and nadir pointing satellite sensors, radar data are collected looking off to the side of the spacecraft. Because radar measures the time that it takes for the signals to go from the antenna to the ground and back, this angled perspective is a necessity because this causes there to be a delay between the parts of the returned pulse that are farthest from the antenna and the parts that are closest (Massonnet and Feigl, 1998). This very small delay is measured with very high precision, these measurements are filtered using complex functions for removing noise and then time measurements are converted to a distance for every location in the radar swath resulting in a map of the surface topography.

2.2.1 Viewing geometry and spatial resolution

The imaging geometry of a radar system is different from the framing and scanning systems commonly employed for optical remote sensing. Similar to optical systems, the platform travels forward in the flight direction (A) in Figure 2.1, with the nadir (B) directly beneath the platform. The microwave beam is transmitted obliquely at right

angles to the direction of flight illuminating a swath (C) which is offset from nadir. Range (D) refers to the across-track dimension perpendicular to the flight direction, while azimuth (E) refers to the along-track dimension parallel to the flight direction. This side-looking viewing geometry is typical of imaging radar systems (Canada Centre for Remote Sensing, 2007).

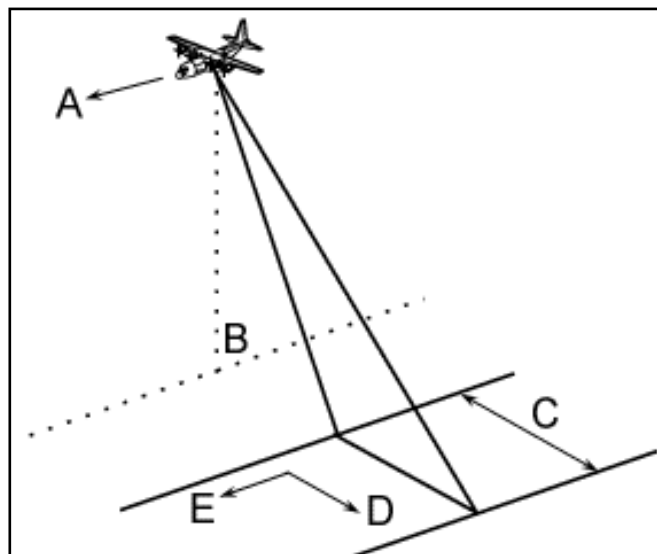


Figure 2.1: Imaging geometry (Canada Centre for Remote Sensing, 2007).

2.3 Synthetic Aperture Radar (SAR)

All radar systems send out electromagnetic radiation in radio or microwave frequencies and use echoes of that radiation to detect objects, but different systems use different methods of emitting and receiving radiation. Radar can be classified into four types named Simple pulse radar, Continuous wave radar, Phased-array radar and Synthetic aperture radar (SAR). The concept of "synthetic aperture" comes from processing techniques that can simulate a much larger antenna size. Radar resolution has two components; the "range" resolution and the "azimuth" resolution. These are determined

by the width of the synthesized antenna. The range can be achieved in synthetic aperture radar in the same manner as most other radars (Galloway *et al.*, 1998).

The other dimension is azimuth (or along track) and is perpendicular to range. It is the ability of SAR to produce relatively fine azimuth resolution that differentiates it from other radars. To obtain a fine azimuth resolution, a physically large antenna is needed to focus the transmitted and received energy into a sharp beam. The sharpness of the beam defines the azimuth resolution. Similarly, optical systems such as telescopes, require large apertures (mirrors or lenses which are analogous to the radar antenna) to obtain fine imaging resolution. Since SARs are much lower in frequency than optical systems, even moderate SAR resolutions require an antenna physically larger than can be practically carried by an airborne platform: antenna lengths several hundred meters long are often required (Strozzi *et al.*, 2001). However, airborne radar could collect data while flying this distance and then process the data as if it came from a physically long antenna. The distance the aircraft flies in synthesizing the antenna is known as the synthetic aperture. A narrow synthetic beam-width results from the relatively long synthetic aperture, which yields finer resolution than is possible from a smaller physical antenna. Achieving fine azimuth resolution may also be described from a doppler processing viewpoint. A target's position along the flight path determines the doppler frequency of its echoes; targets ahead of the aircraft produce a positive doppler offset, targets behind the aircraft produce a negative offset. As the aircraft flies a distance (the synthetic aperture), echoes are resolved into a number of doppler frequencies. The target's doppler frequency determines its azimuth position (Francesco and Benedicte, 2000).

The SAR instrument emits microwave pulses to the earth under a specific look angle (23 degrees in the case of ERS-1). These pulses are reflected at the earth's surface and a small part of this reflection can be detected again by the SAR antenna. Due to this look-angle one can record the time history of the reflected pulses. Pulses which reach the earth first are also detected first by the antenna, hereby discriminating in the ranging direction. The signal that is received by the SAR antenna contains amplitude, which is depending on the intensity of the reflection on earth and a phase. The magnitude represents how much power from the original transmitted pulse is reflected back to the antenna from a given ground pixel. The phase, or fractional wavelength of the echo, can be used to extract range information similar to what can be obtained from conventional radars, but SAR data are much more precise. Therefore, each pixel in a SAR image is represented by a complex number from which the magnitude and the phase can be calculated (Ferretti *et al.*, 2007).

The amplitude of the radar image records reflectivity, the variable ability of the terrain to send the incident energy back to the radar. Each pixel in the radar image represents the radar backscatter for that area on the ground. Bright areas are strong reflectors such as building in an urban area, while dark parts of the image represent surfaces that reflect very little or a surface that is sending the radar signal away from the satellite such as a frozen lake or flat surfaces. The amount of backscatter varies as a function of size of the scatterers in the target area, moisture content of the target area, polarization of the pulses, and observation angles. Backscatter will also differ when different wavelengths are used (Canada Centre for Remote Sensing, 2007). The backscatter is often related to the size of an object, with objects that are called rough surfaces being larger than the size of the wavelength and appear bright and objects smaller than the wavelength or

smooth objects appear dark. Backscatter is also sensitive to the target's electrical properties, including water content. Water objects will appear bright, and drier targets will appear dark. The exception to this is a smooth body of water, which will act as a flat surface and reflect incoming pulses away from a target; these bodies will appear dark (Freeman, 1994). Backscatter will also vary depending on the use of different polarization. Some radars can transmit pulses in either horizontal (H) or vertical (V) polarization and receive in either H or V, with the resultant combinations of HH (Horizontal transmit, Horizontal receive), VV, HV, or VH. Different observation angles also affect backscatter. Track angle will affect backscatter from very linear features: urban areas, fences, rows of crops, ocean waves, and fault lines (Canada centre for remote sensing, 2007).

The angle of the radar wave at the Earth's surface (called the incidence angle) will also cause a variation in the backscatter: low incidence angles (perpendicular to the surface) will result in high backscatter; backscatter will decrease with increasing incidence angles. A smooth surface acts like a mirror when the angle is small, but with angles greater than 20 degrees the amount of backscatter sharply declines because the signal bounces off the surface away from the antenna. The opposite is true for a rough surface. At steep angles (incidence angle less than 20 degrees), most of the emitted pulse is scattered in random directions so that the total backscatter measured by the antenna is lower than from a smooth surface at the same angle. By changing the incidence angle and comparing how the backscatter changes with different angles it is possible to map different types of surfaces (such as smooth vs. rough). Using different combinations of wavelength and incidence angle, the characteristics of the recorded backscatter can be

compared and interpreted (Freeman, 1994). Table 2.1 summarized the main characteristics of some SAR sensors.

Table 2.1 Summaries of the characteristics of some SAR sensors.

Characteristics	Availability	Band	Polarization	Resolution (m)	Swath Width (km)	Incidence Angle (degree)	Repeat- Cycle (days)
ERS1/2	1991- 2008	C	VV	33	100	21	35
ENVISAT/ ASAR	2002- 2010	C	VV-HH- HV	28	>100	14-45	35
JERS-1	1992- 1998	L	HH	18	75	35	44
SRTM	2002	C-X	Full	90	111	30-60	16
ALOS/ PALSAR	2006	L	Full	7-100	20- 350	8-60	46
TerraSAR-X	2007	X	Full	1-16	10- 150	20-50	11
TanDEM-X	2009	X	Full	1-16	≥30	20-50	11
SENTINEL-1	Expected in 2012	C	Full	4-20	20- 400	20-45	12
RADARSAT- 2	2007	C	Full	3	20	20-49	24

2.4 Properties of the image phase

The most important parameter that a SAR measures is phase, which equals twice the range R to the scattering centre of each pixel with 2π radian period, divided by the radar wavelength λ : $\phi = \frac{2R}{\lambda}$. The phase of a SAR image is actually the phase difference between the backscattered signal and the reference signal (Figure 2.2). The phase of the return wave depends on the distance to the ground, since the path length to the ground and back will consist of a number of wavelengths plus some fraction of a wavelength. This is observable as a phase difference or phase shift in the returning wave. The total distance to the satellite (or the number of whole wavelengths) is not known, but the extra fraction of a wavelength can be measured extremely accurately (Massonnet and Feigl, 1998).

The surface area on the ground represented by a pixel in a radar image generally contains hundreds of elementary targets. Each of these targets contributes to the pixel through a complex reflection coefficient. Therefore, the phase that is received by the SAR antenna is actually a summation of the phase of all the scattering elements so that it appears as a noisy image (Jarosz and Shepherd, 2002). Therefore, the absolute phase of pixels in a SAR image are actually quite random, and a phase plot of only one SAR image would not contain any useful information. The phases become meaningful only when some of these effects are isolated by comparing radar images. Differencing the phases may, however, isolate other contributions to the phase signal, or to its changes, by eliminating the random contribution. For this, the elementary targets must remain stable. This condition is met if the phases of images are captured with a slightly different position (e.g., two antennae on one plane acquire images simultaneously) or

with a time difference (e.g., one antenna acquires images at two distinct times) can be compared after proper image registration (Massonnet and Feigl, 1998).

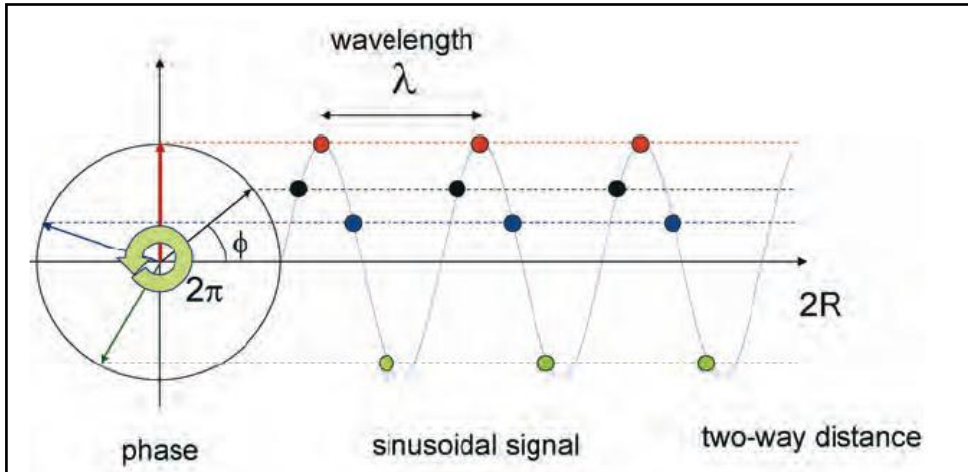


Figure 2.2: A sinusoidal function $\sin \Phi$ is periodic with a 2π radian period (Ferretti et al., 2007).

SAR data record both the amplitude and phase of the back-scattered signals from the resolution cell using a complex number. Consider two radar antennas, A1 and A2, simultaneously viewing the same surface and separated by a baseline vector B with length B and angle θ with respect to horizontal. A1 is located at height H above some reference surface. The distance between A1 and the point on the ground being imaged is the range R_1 while $R_2 = R_1 + \delta$ is the distance between A2 and the same point.

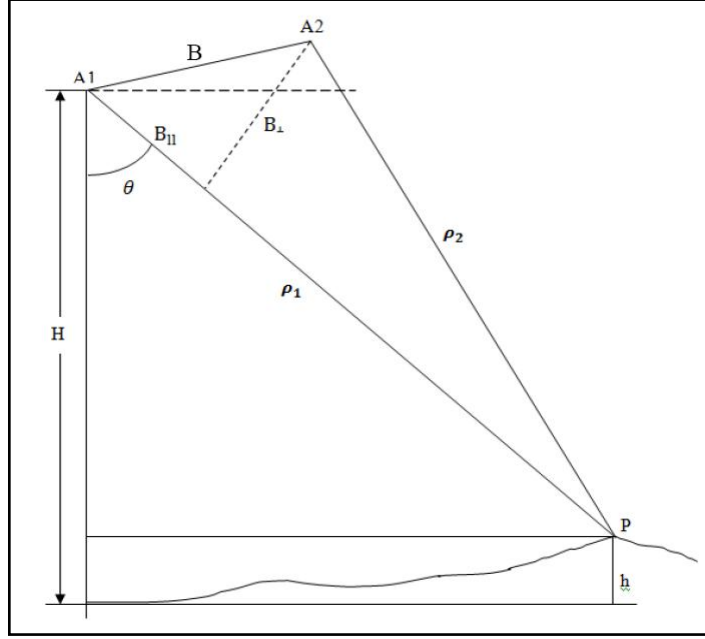


Figure 2.3: Basic imaging geometry for SAR interferometry. A1 and A2 represent two antennas viewing the same surface simultaneously, or a single antenna viewing the same surface on two separate passes (NASA, 1994).

Then, A_1 and A_2 can be represented as (2.1).

$$A_1 = |A_1| \exp(jB_1), A_2 = |A_2| \exp(jB_2) \quad (2.1)$$

The phase difference between A_1 and A_2 , so-called interferogram, can be calculated by using conjugate multiplication of A_1 and A_2 as (2.2).

$$A_1 A_2^* = |A_1| |A_2| \exp(j(B_1 - B_2)) \quad (2.2)$$

while

$$B_1 = \frac{2\pi}{\lambda} 2\rho_1 + \phi_{1scattering} \quad (2.3)$$

$$\text{and } B_2 = \frac{2\pi}{\lambda} 2\rho_2 + \phi_{2scattering} \quad (2.4)$$

$\phi_{1scattering}$ and $\phi_{2scattering}$ are the contributions of the scattering phase in both images. If A_1 and A_2 are highly coherent which means that if the summation of all these scattering elements is the same for the second image-hence the signals are correlated- the

difference between the phase in the first and the second image will vary only due to path length differences ($\phi_{1scattering}$ and $\phi_{2scattering}$ can be treated identically). The two phase values at each pixel are subtracted, leading to an interferogram that records only the differences in phase between the two original images (2.5).

$$\phi = B_1 - B_2 = \frac{4\pi}{\lambda} (\rho_1 - \rho_2) = \frac{4\pi}{\lambda} \Delta\rho \quad (\text{Ge } et \text{ al.}, 2003) \quad (2.5)$$

With the known wavelength of the emitted radiation, the record phase expresses a fraction of its wavelength and can therefore be considered as a distance measure. The resulting difference of phases is a new kind of image called an interferogram. An interferogram is an image of the complex correlation coefficient between two single-look complex images. The real and imaginary parts of this complex correlation coefficient can be mathematically expressed as the magnitude of the interferogram (which is the coherence) and the phase angle (the interferometric phase) (Franceschetti, and Lanari, 1999). The interferometric phase is given in the range from $-\pi$ to π , called modulo 2π , and is colour encoded as fringes (Gabriel *et al.*, 2001; Kampes, 1999; Massonnet *et al.*, 1993). Therefore, relative phase data from two images taken from slightly different viewing angles provide information about changes in range to targets on the ground, thus the surface topography at the resolution of the SAR image can be recovered with knowledge of the imaging geometry and enable the production of a Digital Elevation Model (DEM).

If the two images are acquired from slightly different locations, the interferometric phase is sensitive to the surface topography due to the small parallax between the two lines of sight. If the two images are acquired at two different times, the interferometric fringe is sensitive to any displacement of the ground parallel to the radar line of sight

occurring during the acquisition time interval. The sensitivity of the interferogram to topography increases with the interferometric baseline (the spatial separation of the two orbits), whereas the sensitivity to ground displacement is independent of the satellite configuration. For spaceborne systems, sensitivity to ground displacement is in general a few thousand times greater than the sensitivity to topography, allowing scientists to detect displacements of a few millimetres (Zebker *et al.*, 1994b).

2.5. Measuring topography

Interferograms are often displayed overlaying the brightness rendered in grey scale, and phase as colour, where each cycle of colour, or fringe, represents a phase change of 2π radians. Differences in range distance can be determined by multiplying the relative phase differences in units of cycles by the wavelength of the radar signal. To determine the image point's position, information is required regarding the orbit, the baseline vector separating the two imaging antenna positions and the interferometric range (Rosen *et al.*, 2000).

Estimation of topographic heights with SAR has been discussed by Zebker and Goldstein (1986), Rodriguez and Martin (1992), and Zebker *et al.* (1994a). Digital elevation models (DEMs) are regularly gridded representations of a region's topography. InSAR methods for determination of topographic DEMs vary slightly depending on the geometry of the transmitting and receiving antennas. Systems designed for topographic applications commonly use a configuration of two antennas on the same platform (Graham, 1974; Zebker and Goldstein, 1986). One antenna emits a

microwave signal whose backscattered energy is received by it and an additional antenna located at a fixed distance. Dual antennas are commonly used on aircraft mounted systems, such as NASA's TOPSAR (Topographic SAR). Most spaceborne systems rely on single-antenna satellites, such that the spacecraft must closely repeat the initial orbit to produce a second SAR image for interferometry (Rosen *et al.*, 2000).

The tandem mission of the European Space Agency (ESA) ERS-1 and ERS-2 spacecraft had the two satellites follow each other along the same orbit, so that a common area was imaged at 1-day time separation to allow for the generation of topographic maps. With the phase measurement, the known radar wavelength, and the geometry the surface elevation can be determined. Combining the physical and the geometrical relationships between the two observations generates height information. This procedure is divided into five steps:

Step 1: Physical relation

The received phase (propagation part) for the satellites is

$$\Phi_{1p} = \frac{2\pi \cdot 2\rho_1}{\lambda} \quad (2.6)$$

$$\Phi_{2p} = \frac{2\pi \cdot 2\rho_2}{\lambda} \quad (2.7)$$

Where:

ρ_1, ρ_2 are the slant ranges from satellite positions of A_1 and A_2 to the ground point P.

λ is the radar wavelength

ϕ_1, ϕ_2 are the phases of the returned signals in the two images (Hanssen and Klees, 1998a).

The interferometric phase is

$$\Phi_p = \Phi_{1p} - \Phi_{2p} = \frac{4\pi(\rho_1 - \rho_2)}{\lambda} = \frac{4\pi\delta}{\lambda} \quad (2.8)$$

The derivative of the interferometric phase is now

$$\partial\phi_p = \frac{4\pi}{\lambda} \partial\delta \quad (2.9)$$

Step 2: Geometrical relation

The path length difference δ can be expressed as

$$\delta = B \sin \psi, \text{ with } \psi = \theta - \alpha \quad (2.10)$$

Which yields

$$\delta = B \sin(\theta - \alpha) \quad (2.11)$$

The derivative of the path length difference is

$$\partial\delta = B \cos(\theta - \alpha) \partial\theta \quad (2.12)$$

Step 3: Combination of physical and geometrical relations

From the combination of steps 1 and 2 follows the relationship between an interferometric phase change and a small change in the incidence angle θ .

$$\partial\phi_p = \frac{4\pi}{\lambda} B \cos(\theta - \alpha) \partial\theta \quad (2.13)$$

or

$$\partial\theta = \frac{\lambda}{4\pi \cos(\theta - \alpha)} \partial\phi_p \quad (2.14)$$

Step 4: The height of the satellite above the zero-plane can be expressed as:

$$H = \rho_1 \cos \theta \quad (2.15)$$

And the derivative with R_1 considered constant gives the relationship of a change in incidence angle θ due to a differential height ∂H :

$$\partial H = (-) s \rho_1 \sin \theta \partial \theta (=h) \quad (2.16)$$

Step 5: Height as a function of interferometric phase

Using step 3 and 4, a relationship can be derived between a differential height ∂H , which is actually the height (h) above the zero-plane or reference-plane and the observed phase difference $\partial \phi_p$:

$$\partial H = \frac{\lambda \rho_1 \sin \theta}{4\pi B \cos(\theta - \alpha)} \partial \phi_p \text{ or} \quad (2.17)$$

$$h = \frac{\lambda \rho_1 \sin \theta}{4\pi B^\perp} \partial \phi_p \quad (2.18)$$

This relationship gives the height ambiguity-the height difference corresponding with a 2π phase shift- when $\partial \phi_p = 2\pi$ is inserted. The altitude of ambiguity h is defined as the altitude difference that generates an interferometric phase change of 2π after interferogram flattening (Hanssen and Klees, 1998a).

To conclude this evaluation, the influence of topography and surface displacement on the interferometric phase are combined using equations (2.9) and (2.17):

$$\partial \phi_p = \frac{4\pi}{\lambda} \partial \delta + \frac{4\pi B^\perp}{\lambda \rho_1 \sin \theta} \partial H \quad (2.19)$$

This implies for the case of ERS with an effective baseline B^\perp of 100 meters that a height difference ∂H of 1 meter yields an interferometric phase difference of approximately 4.5 degrees, However, in the differential case, a change $\partial \delta$ of 1 cm in the range direction, yields a phase difference of 127 degrees which is easily detectable. In principle, the higher the baseline the more accurate the altitude measurement, since

the phase noise is equivalent to a smaller altitude noise. However, it will be shown later that there is an upper limit to the perpendicular baseline, over which the interferometric signals decorrelate and no fringes can be generated. In the ERS case, such an optimum baseline is about 300–400 metres (Hanssen and Klees, 1998a).

2.6 Terrain motion measurement using differential interferometry

The phase change is determined by subtracting or “interfering” two radar scans made of the same area at different times (Galloway *et al.*, 2000). Because the phase of the radar echo is proportional to the distance travelled by the pulse, any motion of the ground surface between the two SAR scenes causes a phase difference in the interferogram. Phase differences also can be caused by propagation delays of the radar signal, such as delays owing to the variable water vapour content in the atmosphere (Zebker *et al.*, 1997).

Differential Interferometric Synthetic Aperture Radar (DInSAR) is a radar technique for detecting ground surface deformations by computing a differential interferogram of the same scene over two repeat-pass acquisitions which form a master-slave image pair and can deliver height change at a resolution of about 1 cm (Massonnet *et al.*, 1993). It can also be used for Earth deformation (subsidence, landslides) monitoring or atmosphere monitoring (Francesco and Benedicte, 2000). In such cases the following additive phase term, independent of the baseline, appears in the interferometric phase:

$$\Delta \Phi = \frac{4\pi}{\lambda} d \quad (2.21)$$

Where d is the relative scatter displacement projected on the slant range direction.

This means that after interferogram flattening, the interferometric phase contains both altitude and motion contributions:

$$\Delta \Phi = \frac{4\pi}{\lambda} \frac{B_n q}{R \sin \theta} + \frac{4\pi}{\lambda} d \quad (2.22)$$

Moreover, if a digital elevation model (DEM) is available, the altitude contribution can be subtracted from the interferometric phase (generating the so-called differential interferogram) and the terrain motion component can be measured. The DInSAR phase ($\Delta\Phi_{Dint}$) consists of the following components (2.23).

$$\Delta\Phi_{D-int} = \Delta\Phi_{int} - \Phi_{topo_sim} = \Phi_{Mov} + \Phi_{Atm} + \Phi_{Res_Topo} + \Phi_{Noise} \quad (2.23)$$

Where $\Delta\Phi_{int}$ is the InSAR phase; Φ_{topo_sim} is the topographic phase component, simulated using DEM; Φ_{Mov} is the terrain deformation component; Φ_{Atm} is the atmospheric contribution; Φ_{Res_Topo} represents the residual component due to DEM errors; and Φ_{Noise} is the phase noise (Crosetto *et al.*, 2003b). In the ERS case with $\lambda = 5.6$ cm and assuming a perpendicular baseline of 150 m (a rather common value), the following expression holds (2.24).

$$\Delta \Phi = \frac{q}{10} + 225d \quad (2.24)$$

It can be seen in equation (2.23) that the sensitivity of SAR interferometry to terrain motion is much larger than that to the altitude difference. It can be found from this equation that the 2.8 cm motion component in the slant range direction would generate a 2π interferometric phase variation.

Radar interferograms commonly contain both topographic information as well as surface motions. To separate out the contribution of topography, we need to remove

topographic fringes, either through an independently determined DEM (Massonnet *et al.*, 1993) or using InSAR to correct for the topography (Zebker *et al.*, 1994b). In the latter case, at least three images are required (three-pass method). One pair that does not include deformation is used to remove the topographic phase differences from the pair that also includes surface deformation (Gabriel *et al.*, 1989).

There are two ways of implementing differential interferometry. One is using an external elevation model (DEM) and another is using extra radar images to simulate the topography. The method using an external elevation model requires only two radar images and it is assumed that the deformation was occurred between these acquisitions; known as two-pass method. The second method does not require any other information than the radar data. The topographic reference here is created by the additional radar images, which can include a third or fourth image, called three-pass and four-pass methods. Complex interferogram combination can also be applied to get differential interferogram using two wrapped interferograms. This method requires three or four radar images. In all cases, a difference is made between the two interferograms, one image contains only topography (topographic pair) and another containing both topography and deformation (deformation pair). The result is that each differential fringe represents a half wavelength displacement in the direction of radar line of sight. By counting the fringes produced, the quantity of deformation can be determined (Massonnet and Feigl, 1998)

2.6.1 Two-pass method

In the two-pass method, a DEM is used as a synthetic interferogram simulation of topographic phase. Before subtracting from the real interferogram, which contains both

topography and deformation, the elevation model is converted to the radar slant range-azimuth coordinates and scaled using the baseline. The advantage of this method is that it does not require the unwrapping process. The only limitation is the availability of a DEM of the area of interest. This method is considered a fast one but errors in a DEM affect the deformation model. Since the measured phase is much less sensitive to topography compared to displacement, the external DEM can be of the order of 30 m accuracy (Zebker *et al.*, 1994a).

2.6.2 Three-pass method

In the three-pass method, three SAR scenes will be needed but no DEM. But three images must be acquired in such way that, in their combination, one pair contains only topographic information where its temporal separation is smaller, and another pair contains both topography and deformation information. If three images were acquired in satellite position S1, S2 and S3, and it is assumed that no movements have occurred between the two acquisitions S1 and S2 so the interferogram generated from them will be used as a topographic reference. Displacements are supposed to occur between the first and third image acquisitions (S1 and S3). To get the differential interferogram, the topographic phase of the first pair should be subtracted from the phase of the second pair, which contains both topography and deformation contributions. This method can be applied if the both the topographic pair and the deformation pair have a common image. Previous research showed that it is often difficult to find triplets of images. In the case where it is not possible to find a common image, the 4-pass method can be used (Zebker *et al.*, 1994b).

2.6.3 Four-pass method

Four-pass method is performed when there is no available data set, where the topographic and deformation pairs do not depict a common image. In four-pass method the topographic and deformation pairs are independent. They are formed from four SAR scenes acquired from four different satellite positions. This means that the SAR-scene for topographic reference interferogram can be acquired time independently with respect to the deformation pair. Then in order to subtract two interferograms with different geometry they have to be co-registered and resampled repeatedly (Derauw and Moxhet, 1996).

2.6.4 Complex interferogram combination

While the previous methods depend either on the availability of a DEM or on the successful unwrapping of the interferometric phase, the complex combination of interferograms can be done without meeting these requirements. For example, The complex combination of an interferogram with a 214 m perpendicular baseline and an interferogram with a 427 m perpendicular baseline with the wrapped phase scaled by a factor of 1 and -1, results in a differential interferogram with an effective baseline of -213m. The differential interferogram contains the differential phase components of the first pair minus the differential phase components of the second pair. Scaling of the wrapped phase leads to scaling of the phase noise as well. Therefore the approach is limited to small integer numbers and phase noise filtering of the complex interferograms before complex interferogram combination is recommended. The sensitivity of this differential interferogram to topography is therefore much smaller compared to the original interferograms but it will be much more suited for detecting the displacements than any of the original interferograms (Gamma, 2008b).

2.7 The Accuracy of DEM and DInSAR observations

InSAR is a potential technique for generating digital elevation models (DEM) by using the phase component of the complex radar signal (Madsen *et al.*, 1993; Rufino *et al.*, 1998). A properly equipped spaceborne InSAR system can be used to produce a highly accurate global DEM with its advantages in significantly less time and at significantly lower cost than other systems (Hilland *et al.*, 1998). InSAR is usually applied to construct DEMs over areas where the photogrammetric approach to DEM generation was hindered by inclement weather conditions. For example, repeat-pass InSAR was used to generate ice surface topography that determined the magnitude and direction of the gravitational force that drives ice flow and ice dynamics (Rignot *et al.*, 1995; Kwok and Fahnestock, 1996; Joughin *et al.*, 1996). In addition, volcano surface topography measurements from before and after an eruption were used to estimate the volume of extruded material Interferometric (Lu *et al.*, 1998; Pedersen and Sigmundsson, 2006). DEM generation is subject to four processing stages namely; image registration, interferogram calculation and filtering, phase unwrapping and phase-to-height transformation. Several theoretical studies have been done in the reconstruction of digital elevation models (Jayaprasad *et al.*, 2008; Koch, *et al.*, 2000; Baek *et al.*, 2005; Li, 2006; Ludwig and Schneider, 2006; Prati and Rocca, 1994; Zebker *et al.*, 1994a; Dammert, 1996; Burgmann *et al.*, 2000; Crosetto, 2002; Endreny *et al.*, 2000; Ferretti *et al.*, 1997) including analysis of co-registration (Fornaro and Franceschetti, 1995; Zou *et al.*, 2009), filtering (Fornaro and Monti Guarnieri, 2002; Goldstein, and Werner, 1998; Lee *et al.*, 1998), geocoding (Wegmüller *et al.*, 1999) and phase-unwrapping techniques (Fornaro *et al.*, 1997; Gens, 2003). The European Space Agency's ERS-1/2 satellites have provided a wealth of data that can be used for DEM generation There are a number of studies on use of ERS interferometry data for DEM generation and retrieval of terrain

parameters (Zebker *et al.*, 1994a; Rufino *et al.*, 1998; Werner *et al.*, 1993; Walker *et al.*, 2000; Tsay and Chen, 2001; Guritz *et al.*, 1999). SAR interferometry has also been applied using data from other satellites such as Seasat, SIR-B, JERS-1, SIR-C, Radarsat-1, ENVISAT ASAR, and ALOS PALSAR (Zebker *et al.*, 1996; Zebker *et al.*, 1992; Wegmüller *et al.*, 2005; Werner *et al.*, 2000). In vegetated areas, L-band SAR is considered more suitable for DEM generation because of smaller temporal decorrelation compared with C-band (Zebker and Villasenor, 1992; Rosen *et al.*, 1996; Dammert and Wegmüller, 1999).

There are many sources of error in DEM construction from repeat-pass InSAR images. These sources include inaccurate determination of the InSAR baseline, atmospheric delay anomalies and possible surface deformation due to tectonic, volcanic, or other loading sources over the time interval spanned by repeat-pass interferograms. To generate a high-quality DEM from repeat-pass InSAR images, these errors must be corrected (Lu *et al.*, 2007). The influencing parameters can be divided into three groups; the first group characterizes SAR parameters during data acquisition, the second group deals with processing steps after acquiring the raw data and the third group concerns influences of terrain characteristics (Gens and Van Genderen, 1996; Koch and Lohmann, 2000). Measurement of errors in DEMs is often impossible because the true value for every geographic feature represented in a geographic data set is rarely determinable (Garbrecht and Martz, 1999). Uncertainty, instead of error, should be used to describe the quality of a DEM. Quantifying uncertainty in DEMs requires comparison of the original elevations, such as topographic maps, with the elevation in a DEM surface. When the true values, such as ground truths are used as the reference data, the ‘uncertainty’ becomes ‘error’. Accuracy is the inverse measurement of error.

The most widely used statistical measure is the Root Mean Square Error (RMSE). It measures the dispersion of the frequency distribution of elevation between original elevation data and DEM data. Mathematically expressed as (2.20).

$$\text{RMSE} = \sqrt{\frac{1}{n} \sum_{i=1}^n (Z_{\text{DEM}} - Z_{\text{Ref}})^2}$$

(2.20)

Where: Z_{DEM} is the elevation value measures on DEM surface;

Z_{Ref} is the corresponding original elevation (Reference)

N is the number of elevation points checked.

The accuracy of a DEM can be defined as the average vertical error of all potential points interpolated within the DEM grid. In other words, it is the vertical root-mean-square accuracy of all points interpolated in the DEM grid. The accuracy of InSAR derived DEMs can be determined by comparing them with reference DEMs, which can be taken from other sources (Rosen *et al.*, 2000) such as existing topographic maps, aerial photogrammetry, Light Detection and Ranging (LIDAR) and direct ground measurements using Global Position System (GPS) and the terrestrial method. Kamaruddin *et al.* (2003) investigated the relationship between the accuracy of InSAR DEM, polarization mode, and the nature of ground surface cover. They noted that the RMSE of LIDAR DEMs and L-band DEMs over non-vegetated areas were equal (RMSE=1 m).

Although a qualitative use of the DInSAR results seems to be sufficient for the purposes of some geophysical applications, this is not the case for some other important

applications such as the deformation control in urban areas, which need to be characterised by high quality standards like those usually achieved by the geodetic techniques. In general, three important quality aspects are typically considered: the precision, accuracy and reliability of the estimates.

The errors associated with the DInSAR observations are similar to DEM errors and it includes the unwrapping-related errors, the residual topographic component due to DEM errors and the atmospheric artefacts. The unwrapping-related errors usually occur in low coherence areas, where the interferometric phase noise is high. In order to avoid these areas, the phase unwrapping for sparse data can be used. However, if the coherence is too low, the density of the good pixels may not be sufficient to guarantee a correct sampling of the deformation signal. The residual topographic component can represent an important error source if large baselines are used. Finally, the atmospheric artefacts represent a very important error source, which can strongly degrade the quality of the DInSAR observations. All these error sources represent a strong limitation of the DInSAR technique based on a single interferogram (Crosetto *et al.*, 2003a).

On the other hand, these errors cannot be fully controlled and the deformation estimates cannot support a quantitative monitoring of the deformations. A fully quantitative DInSAR monitoring may only be achieved by using multiple interferograms, i.e. multiple observations of the phenomenon under analysis. However, this is just a necessary condition, which is not sufficient to yield high quality DInSAR results. Two other conditions have to be fulfilled. Firstly, very careful DInSAR processing has to be implemented. The quality of all major processing steps (e.g. image focussing, image registration, interferogram filtering, phase unwrapping, etc.) must be controlled through

automatic or semi-automatic procedures. Note that the control of some steps, like the phase unwrapping may be time consuming. Secondly, suitable data modelling and analysis procedures have to be employed. In particular, an appropriate statistical treatment of the DInSAR observations is required (Crosetto *et al.*, 2002).

The key factor to achieve a quantitative DInSAR deformation monitoring is the number of available interferograms (i.e. observations). The classical DInSAR configuration is based on a single interferogram, derived from a pair of complex SAR images. This is the simplest DInSAR configuration, which is often the only one that can be implemented, due to the limited data availability: the results of most DInSAR applications are derived using a single interferometric pair. This is a zero redundancy configuration. With such a configuration it is not possible to check the presence of the different errors that may affect the interferometric observations: the deformation estimates are not reliable. Note that the same occurs for the digital elevation models derived with single InSAR pairs.

2.8 Coherence estimation and its applications

2.8.1 Coherence estimation

In SAR interferometry, coherence is defined as a measure of the degree of resemblance of radar phase between two SAR images of the same area and the degree of correlation that exists between the two SAR images is called the complex degree of coherence. Coherence provides a useful measure of the interferogram quality and the capability of applying efficiently phase unwrapping procedures (Rodriguez and Martin, 1992; Zebker *et al.*, 1992). Coherence is obtained from the cross-product of the two registered SLCs.

The correlation between two complex signals S_1 and S_2 is generally expressed by the correlation coefficient (2.25).

$$C = \frac{\langle S_1 S_2^* \rangle}{\sqrt{\langle S_1 S_1^* \rangle \langle S_2 S_2^* \rangle}} \quad (2.25)$$

Where, S_1, S_2 are complex values in SAR images and S^* is the conjugate of S . the braces($\langle \rangle$) indicate local spatial averaging around an individual multi-looked pixel (Bingyuan *et al.*, 2008).

The value range of C varies between zero and one, where a zero value means no interference, which implies that there will be no interferometric fringes. That is to say regions exhibiting a high level of coherence are composed of ground cells whose backscattering responses have changed very little over the intervening period between the two SAR image acquisitions. Such stable ground surfaces include dry, bare rock regions and built-up urban areas.

The two main effects that cause the coherence to decrease are normally referred to as temporal and volume decorrelation. Temporal decorrelation arises when the backscattering characteristics of the target change between the acquisitions as a result of changing moisture conditions or other environmental effects. Over forested terrain, temporal decorrelation due to wind-induced movement of scatterers (needles, branches) near the tree-tops between one acquisition to the next may be significant (Sarabandi and Wilsen, 2000). Since temporal decorrelation is normally quite strong, it is advantageous

to choose a short repeat-pass interval and thus the ERS-1/2 tandem data have become the preferred data source for forest applications.

Volume decorrelation arises when the amplitude of the return depends on the electromagnetic structure of the target and therefore the coherence is mostly related to its mechanical stability. For instance, in open vegetated fields, the level of the coherence is approximately linearly related to the biomass and the height of the crops (Moeremans and Dautrebande, 1999). Other causes of coherence loss should be properly taken into account, for example, the force of the wind could be considered, using meteorological information (Ranson *et al.*, 1997). Wagner *et al.*, (2003) found that the rainfall before and between ERS-1/2 tandem acquisitions can result in a significant loss of correlation. However, regions of high coherence can remain so for many years, this usually happens only for those areas having particularly favourable characteristics, such as poor vegetation and dry and no windy climate. This area with high coherence could usually obtain reliable interferometric measurements.

Low coherence is a feature of surfaces whose backscattering responses fluctuate to a high degree and provide little similarity, or correlation, across an InSAR pair of radar images. Notable examples include dense vegetation and water bodies, which merely yield speckled, incoherent noise in the interferogram (Weydahl, 2001). Fast growing vegetation or forests are generally not suitable for InSAR monitoring unless corner reflectors are used to provide high coherence points. Water bodies have low coherence because their surfaces are constantly moving; they therefore appear black in coherence images (Massonnet and Feigl, 1998). Motion and change in vegetation also affect

coherence. Leaf motion will usually cause a total loss of coherence, but this does not imply that areas of vegetation will always appear with zero coherence: radiation will often penetrate the foliage, at least partially and can be backscattered by the terrain underneath or by the trunk and branches of the trees, which are mechanically much more stable and will therefore contribute to the coherence (Siegert and Kuntz, 1996). In general, deciduous trees will show high coherence during winter when there are no leaves and less coherence in summer due to foliage effects. Similarly, different types of vegetation will show different one-day coherence values, depending on the height of the plant and on the lengths of the leaves: short leaves could be practically transparent to the C-band radiation of ERS satellites (Engdahl *et al.*, 2001). Coherency loss can be minimized by selecting interferometric pairs with a minimal orbital baseline. This imposes additional constraints on the archive selection.

2.8.2 Applications of coherence

The coherence measures the correlation between master and slave images, which means the changes between two image acquisitions. The complex correlation coefficient is affected by environmental conditions which depend much on time observation including the season and time separation between observations. Longer time separation will degrade the coherence between images, especially in tropical region that is characterized by high humidity and highly dense vegetation. Multi-temporal interferometric analysis of the coherence and amplitude of the backscatter can contribute to the detection and classification of forests and of vegetation in general (Tansey *et al.*, 1999; Koskinen *et al.*, 2001; Ranson *et al.*, 2003; Siegert and Kuntz, 1999). Early results obtained using ERS repeat-pass data by Hagberg *et al.* (1995) and Werner and Wegmüller (1995) showed that the interferometric coherence is

significantly lower over forest than over open canopies, short vegetation, bare soils and urban areas. Subsequent studies of ERS-1/2 tandem data demonstrated in particular that the one-day repeat pass coherence is useful in land use mapping (Strozzi *et al.*, 2000, Strozzi *et al.*, 1999, Kuntz *et al.*, 2010) and estimation of stem volume in forests (Koskinen *et al.*, 2001; Santoro *et al.*, 2010; Smith *et al.*, 1998). Hyypä *et al.* (2000) found that, compared to the JERS intensity images, the ERS tandem coherence was best suited to predicting height, basal area and stem volume over a 600 ha boreal forest site in southern Finland. Tansey *et al.* (2004) and Schullius *et al.* (1998) used both ERS tandem coherence and JERS backscatter data to classify the boreal forest in Siberia while Thiel *et al.* (2009) used ALOS PALSAR coherence to monitor large-area forest in Siberia during the winter season.

Coherence provides information on the temporal stability of the sub-resolution scatter structure and therefore is an important feature for many applications such as geological, agricultural, ice dynamics, soil moisture land cover classification and burn scar monitoring (Askne and Smith 1996, Borgeaud and Wegmüller 1996; Stebler *et al.*, 1996, Wegmüller and Werner, 1997b; Wegmüller *et al.*, 1995; Siegert and Ruecker 2000). One of the applications of coherence is forested/non-forested area segmentation such as finding the extent of forest fires. In addition, seasonal effects can be appreciated, using the regular series of ERS images available in selected locations (Wegmüller and Werner, 1997b). Thus, multi-temporal techniques make it possible to identify the periodicities of the coherence that are connected to plant growth and to the visibility of the terrain in the background. They lead to segmentation techniques with results not so far from those obtainable with optical techniques in good weather (Askne *et al.*, 1997; Dammert *et al.*, 1999).

2.9 Factors affecting InSAR results

The phase noise term is obtained from various factors including thermal noise, image misregistration, processing artefacts, temporal and baseline decorrelation (Zebker and Villasenor, 1992). All these noise sources increase the dispersion of the interferometric phase value ϕ and thus the InSAR DEM. Temporal decorrelation caused by rainfall, vegetation growth or random motion during the period of the two passes have effects on phase correlation and hence the quality of the interferogram. There is also a limit for the baseline separation. The usable perpendicular baseline separation can be up to several hundred metres for ERS-1/2 radar and one to two kilometres for JERS-1. On the other hand, the earth's atmosphere has an influence on the propagation of radar waves. The atmospheric conditions vary with changes in height, geographical location and time. A localised model of troposphere effects estimated from GPS observations is therefore essential to correct the interference from atmosphere (Atlantis, 2002; Mendes *et al*, 1995).

Some possible baseline errors are neglected and it is assumed that the interferometric phase has been compensated for the flat-Earth term (i.e. the interferogram has been flattened). However, when more than one interferogram is available, the local topography can be estimated, and the DEMs obtained from each image pair can be combined. It is then possible to combine properly the DEMs by means of a weighted average. The resulting DEM is more reliable, since the uncorrelated atmospheric and noise phase contributions coming from single interferograms are averaged, thus reducing the elevation error dispersion. The key issue is proper weight selection in order to give a positive bias to the most reliable interferograms.

2.9.1 Temporal Decorrelation

Probably the most important limiting factor in the application of InSAR is temporal decorrelation of the ground between the interferometric acquisitions, and hence a loss of meaningful phases in relation to corresponding pixels in an image pair. Temporal decorrelation usually results from changes in the complex reflection coefficient of the imaged surface as a result of changing moisture conditions or other environmental effects.

The amount of temporal decorrelation depends on the soil and vegetation type of the target area, as well as the weather conditions between the radar passes. Thus, decorrelation times can be as long as months to years for arid terrain and as short as several hours to several days for rainy and/or forested areas. Sparsely vegetated terrain can have decorrelation times between several days to several months (Zebker and Villasenor, 1992). In the case of a water basin or densely vegetated areas, the scatterers change totally after a few milliseconds, whereas exposed rocks or urban areas remain stable even after years. Of course, there are also the intermediate situations where the interferometric phase is still useful even if corrupted by change noise. Over forested terrain, temporal decorrelation due to wind-induced movement of scatterers (needles, branches) near the tree-tops between one acquisition to the next may be significant (Sarabandi and Wilsen, 2000). Since temporal decorrelation is normally quite strong, it is advantageous to choose a short repeat-pass interval, and thus the ERS-1/2 tandem data have become the preferred data source for forest applications.

Since C-band radar has a wavelength similar to the size of small-scale vegetation characteristics such as crop structure, foliage and tree canopy structure, SAR images at C-band are dependent on the variations of these features, which often occur on a daily or weekly timeframe. In contrast, longer wavelength L-band radar has a wavelength on the scale of tree trunk and branch structures, which generally change over a much longer timeframe. Thus, in vegetated areas, the longer wavelength SAR provides the possibility of obtaining useable interferometric pairs over longer timeframes than provided by C-band SAR (Zebker and Villasenor, 1992).

2.9.2 Baseline decorrelation

The spatial extent of the baseline is one of the major performance drivers in an interferometric radar system. If the baseline is too short the sensitivity to signal phase differences will be undetectable; if the baseline is too long then additional noise due to spatial decorrelation corrupts the signal. It can be shown that coherence decreases approximately linearly with the increase in baseline length (Rodriquez and Martin, 1992).

For DEM creation applications, image pairs with short temporal baseline are optimal, so that there is just a short time for the decorrelation, deformations and atmospheric changes to occur. In addition, the correlation gets worse as the temporal baseline gets longer. For deformation mapping applications, the temporal baseline must be set carefully in order for the images to be correlated enough and in order for the deformations to occur. In this case, the perpendicular baseline should be as large as possible in order to reach a low height ambiguity and therefore a high height accuracy of the DEM. This maximum separation is called the critical baseline and is dependent

on the radar wavelength, the sensor-target distance, the range resolution and the incidence angle. The critical baseline length refers to the length of the baseline for which the attainable coherence is zero, which occurs when the change in look angle between the interfering images is sufficient to cause backscatter from each pixel to become completely uncorrelated. The critical baseline length for ERS-1/2 interferometry on flat terrain is approximately 1100 m (Rufino *et al.*, 1998). The effect of baseline decorrelation may be reduced by the use of spectral filtering during interferometric processing. The upper limit of the spatial baseline is about 2 km; for such a long spatial baseline, the two scenes may be too different to allow co-registration. Typical values for maximum usable baseline separation are less than 600 m for DEM generation, between 50 – 150 m for the coherence application and 0 – 100 m for differential interferometry.

On the other hand, the temporal baseline should be as short as possible in order not to allow too much decorrelation and deformations and to reduce the topographic signal in the interferogram as much as possible. Even if the interferogram contains the topographic signal and a DEM must be used in order to eliminate it, a higher height ambiguity means worse accuracy requirements for the DEM (Ferretti *et al.*, 2007).

2.9.3 The atmosphere and its effects on repeat-pass InSAR

Phase distortion due to atmospheric effects has gained increasing attention (Goldstein, 1995; Zebker *et al.*, 1997; Hanssen, 1998; Ferretti *et al.*, 1999), since it can seriously compromise InSAR DEM quality, especially for those pass pairs with low normal baseline values. InSAR technology has many limitations. One of the most intractable is the effect of the atmosphere on repeat-pass InSAR. It is well known that electromagnetic waves are delayed (slowed down) when they travel through the

troposphere. Atmospheric effects are usually due to refraction and different atmospheric delays, which depends on the humidity or ionosphere and can be limited by data selection with respect to weather conditions at the time of acquisition. The effect often introduces significant errors to repeat pass InSAR measurements. Massonnet *et al.* (1994) first identified such effects. Since then, some intensive research has been carried out aiming to better understand and mitigate the effects. Zebker *et al.* (1997) reported, for example, that spatial and temporal changes of 20% in the relative humidity of the troposphere could lead up to 10 to 14 cm errors in the measured ground deformations and 80 to 290 m errors in derived topographic maps for baselines ranging from 100 m to 400 m in the case of the SIR-C/X-SAR. A number of researchers have concluded that the tropospheric effects are a limiting factor for wide spread applications of repeat-pass InSAR.

Atmospheric artefacts in SAR interferograms are mainly due to changes caused by the atmospheric pressure, temperature and water vapour (Hanssen and Feijt, 1996). In most cases, the spatial variations of pressure and temperature are not large enough to cause strong, localized phase gradients in SAR interferograms. Their effects are generally smaller in magnitude and more evenly distributed throughout the interferogram when comparing with that of the water vapour, and sometimes difficult to be distinguished from errors caused by orbit uncertainties (Tarayre and Massonnet, 1996). Water vapour is mainly contained in the near-ground surface troposphere (up to about 2 km above ground), where a strong turbulent mixing process occurs. It should be noted that although water vapour is often considered the most important parameter causing the tropospheric delays, pressure is also important. For example, in regions with strong

topography, changes in pressure between two acquisitions can generate a bigger tropospheric delay signal than humidity variation.

Clouds are formed when the water vapour in the air condenses into visible mass of droplets or frozen crystals. Clouds are divided into two general categories, layered and convective. These are named stratus clouds and cumulus clouds respectively. The liquid water content in the stratiform clouds is usually low so that they do not cause significant range errors to SAR signals. The liquid water content in the cumulus clouds can however range from 0.5 to 2.0 g/m³ and cause zenith delays of 0.7 to 3.0 mm/km, significant to InSAR measurements (Hanssen, 1998).

Due to the propagation delay of radar signals, in repeat-pass SAR interferometry systems, the phase measurements become:

$$\Phi_1 = \frac{4\pi}{\lambda} (L_1 + \Delta L_1) \quad (2.26)$$

$$\Phi_2 = \frac{4\pi}{\lambda} (L_2 + \Delta L_2) \quad (2.27)$$

Where ΔL_1 and ΔL_2 are atmospheric propagation delays of radar signals corresponding to the first and the second acquisitions. This gives the interferometric phase:

$$\Phi_1 - \Phi_2 = \frac{4\pi}{\lambda} (L_1 - L_2) + \frac{4\pi}{\lambda} (\Delta L_1 - \Delta L_2) \quad (2.28)$$

Where $\frac{4\pi}{\lambda} (L_1 - L_2)$ are topography and surface deformation induced interferometric

phase, and $\frac{4\pi}{\lambda} (\Delta L_1 - \Delta L_2)$ is the atmosphere induced interferometric phase.

From equation 2.28, it is clear that the atmosphere induced phase errors are easily interpreted as topography or surface deformation. Therefore, equation 2.28 shows that it is the relative tropospheric delay ($\Delta L_1 - \Delta L_2$) that causes errors in InSAR measurements. If the atmospheric profiles remain the same at the two acquisitions, the relative tropospheric delay will disappear. In addition, if $\Delta L_1 - \Delta L_2 = \text{constant}$ for all the resolution cells in an area of interest, the atmospheric effects will also be cancelled out. The two conditions are, however, next to impossible to occur in practice. First, the troposphere, especially the tropospheric water vapour, varies significantly over periods of a few hours or shorter. It is, therefore, highly unlikely to have the same atmospheric profiles even over currently the shortest revisit interval of one day (for ERS-1/ERS-2). Second, it is also rather rare for the relative tropospheric delays to be constant for all the resolution cells due to local tropospheric turbulences, which affect flat terrain as well as mountainous terrain and to vertical stratification which only affects mountainous terrain (Massonnet and Feigl, 1998).

Electromagnetic waves travelling through the ionosphere interact with the electrons and the magnetic field with the result that the polarization vector of the electric field is rotated by an angle, which is called the Faraday rotation angle (Davies, 1965). Other effects of the ionosphere include propagation delays of the radar echoes, ray bending, radio-wave scintillation, and phase changes (Thompson *et al.*, 1986). These ionospheric effects have only minimal effects on C-band radiation but become more significant in L-band imagery and would be very important for a spaceborne P-band SAR.

A SAR interferogram is a superposition of information on the topography, the surface deformation between the two SAR acquisitions, the differential atmospheric

propagation delays between the two SAR acquisitions and various noise (Tarayre and Massonnet, 1996). The contribution from the topography can be removed by using a reference elevation model from which the surface deformation can be neglected or removed if the surface deformation of the study area between the two SAR acquisitions is insignificant or the deformation is known. In addition, multi-looking operations and careful interferometric processing can help to suppress the noise. Therefore, an interferogram that contains only the atmospheric signature can be obtained (Hanssen, 1998). The atmospheric signature thus obtained is very useful for studying the properties of atmospheric effects on InSAR. Besides, the atmospheric signals can be used to derive various atmospheric products. For example; Hanssen and Klees (1998b) used atmospheric signals derived from SAR interferograms to map high-resolution water vapour.

The variation due to atmospheric effects can be isolated from multiple interferograms. This is also the approach in using interferometric stacks and in permanent scatterers analysis. In particular, for large numbers of interferograms, the atmospheric effects can be identified as a random process over time and thereby separated from other contributions to the interferometric phase.

2.10 Phase unwrapping

Two-dimensional phase unwrapping (PU) is the problem of deducing unambiguous “phase” only from known values of modulo 2π . Phase unwrapping consists of determining the correct multiple of 2π to add to each point in the interferogram such that integration of the phase between any two points is path independent (Ferretti *et al.*, 2007). PU has been a research area for more than two decades and hundreds of papers

have been published aimed at solving the PU problem (Costantini *et al.*, 1999; Fornaro *et al.*, 1996; Gens, 2003; Massonnet *et al.*, 1996; Rosen *et al.*, 1994; Zebker and Lu, 1998; Fornaro *et al.*, 1997a; Fornaro *et al.*, 1997b). Many PU algorithms have been suggested and implemented. The reason for such interest in PU is due to many applications in applied optics that require an unwrapping process. Many PU algorithms have been developed only for data from a particular application. There is no universal PU algorithm that can solve wrapped phase data from any application. Moreover, PU algorithms are generally a trade off between accuracy of solution and computational requirements. Even so, the most robust PU algorithm cannot guarantee successful or acceptable unwrapped results without a good set of weights. Existing quality or weighting maps are not problem-specific to PU. They are general and do not specifically aid PU all the time. Unfortunately, there is no standard objective method of defining weights that guarantee good PU (Ferretti *et al.*, 2007). In this section, the PU process will be defined and explained in detail. Two methods for PU will be presented and be compared. Advantages and disadvantages in existing PU methods applicable for tropical forest and low coherence will be discussed later in chapter six.

2.10.1 Basic measurement principles

Since the interferometric phase is only known in terms of modulo 2π and the maximum height variation in the area of interest can give rise to hundreds of cycles, an unwrapping procedure is necessary in order to estimate the local topography. If the phase contribution due to an ideally flat Earth has been properly estimated and compensated for, PU allows one to pass from the fringe pattern, to a phase field proportional to the local topography. In most cases this is the major obstacle to be overcome in the processing chain for InSAR DEM reconstruction and often cannot be

performed in a totally automatic way. The reasons for this become evident once we state the problem more precisely and analyse it from a mathematical point of view (Ghiglia and Pritt, 1998).

PU is a technique used on wrapped phase images to remove the 2π discontinuities embedded within the wrapped phase (φ) map. It detects a 2π phase jump and adds or subtracts an integer offset of 2π to successive pixels following that phase jump based on a threshold mechanism, thus the unambiguous phase value ψ can be finally obtained for each image pixel:

$$\psi = \varphi \pm 2\pi \cdot n \quad (2.29)$$

In Interferometric Synthetic Aperture Radar (SAR) the actual phase values cannot be extracted directly from the physical signal, since phase influences the signal through its principal values that lie between $\pm \pi$ radians. Only the wrapped phase is given and the phase values forced into the interval $[-\pi, \pi)$ by a modulo 2π operation. The unwrapping process is aimed at providing an estimation of the actual phase function, ψ given the wrapped function 2π . This turns out to be a difficult problem.

As a result, many PU algorithms have been developed in an attempt to solve these problems. However, the variety of forms, shapes and densities of noise that might be found in real wrapped phase maps makes the problem of PU complex and difficult to solve,. Since phase residues merely mark the endpoints of the ‘discontinuity lines’, the true problem is their complete identification. Discontinuities are essentially due to two independent factors: phase noise and steep terrain slopes (Figure 2.4)

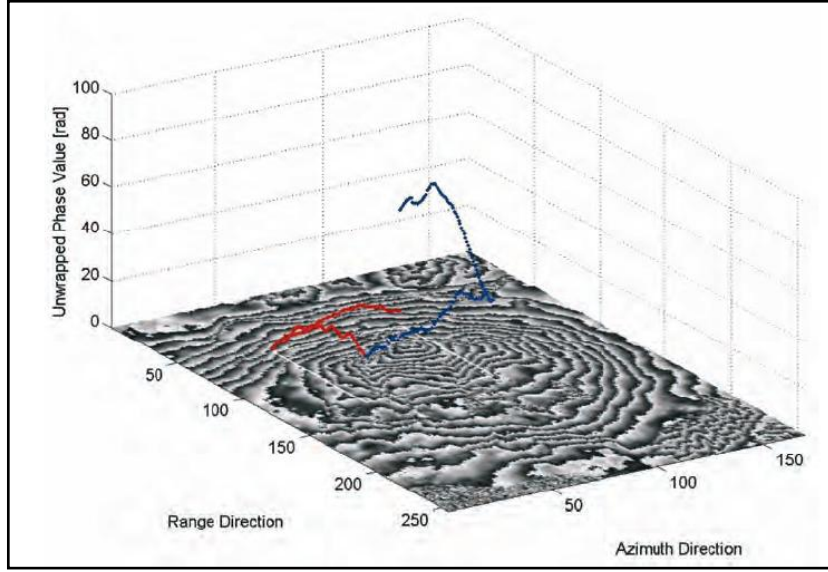


Figure 2.4: A visual example that shows that main problem related to phase inconsistencies: integration of the phase values yields different results depending on the path followed. In this example, the first and the last pixels of the integration paths are common, but one path crosses a layover area, characterised by very low coherence values, and propagates significant phase unwrapping errors (Source: Ferretti *et al.*, 2007).

2.10.2 Residues

Residues are defined to be local inconsistencies, which mark the beginning and end of 2π discontinuities (Karout, 2007). A gradient field must be irrotational, which means that the curl of $\nabla\varphi$ should be zero everywhere. Whenever the sum is not zero, a residue is said to occur (Goldstein *et al.*, 1988). Its value is usually normalised to one cycle and it can be either positive ($n=1$) or negative (-1) as it shown in equation (3.6)

$$\sum_i^M \nabla\Phi(p_i) = 2\pi n \quad (2.30)$$

However, residues have two forms of discontinuity. One is a positive polarity when n in equation (2.30) is $+1$; the other form is a negative polarity when n is -1 . In the case of a

residue is present; the result of equation (2.30) is always a +1 or -1 because the 2×2 closed path cannot encircle more than one residue. A summary of how to identify residues in the wrapped phase map is shown in Figure 2.5.

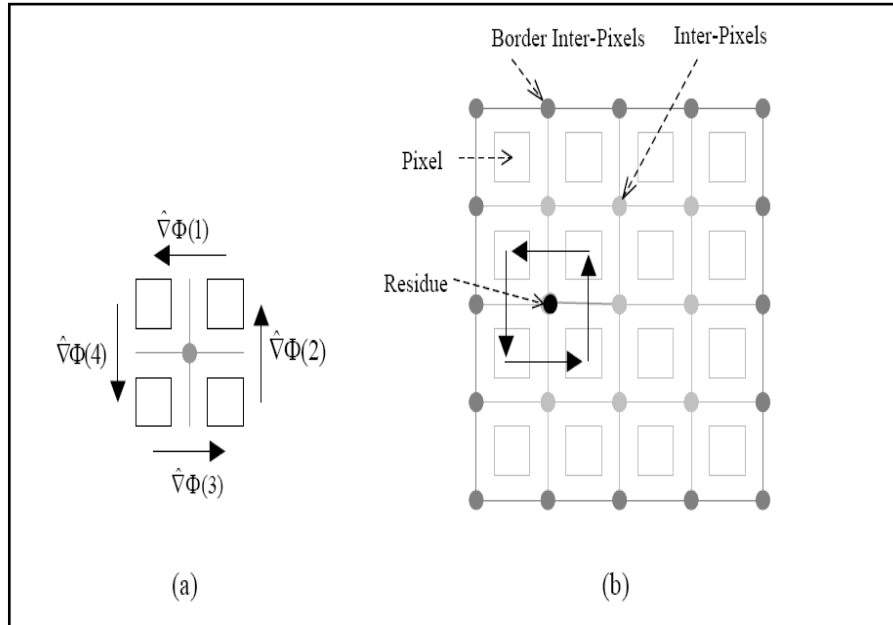


Figure 2.5:(a) Visualizing residue calculation and (b) an inter-pixel network with a 2×2 closed loop and marked inter-pixel residue (Source: Karout, 2007).

Many different kinds of residues may exist in a wrapped phase map caused by phase noise, spatial under-sampling of phase, object discontinuity. Moreover, residues can be of two forms: dipole residues and monopole residues. Dipole residues are those that exist in pairs of two opposite polarity states or charges and monopoles that are single value residues for which no corresponding opposite-sign partner exists in a wrapped phase map (Gutmann, 1999). Furthermore, the dipole residues are caused by the random fluctuation of phase due to noise, which results in the wrapped phase gradient exceeding $|\nabla\Phi| > \pi$. Each pair of dipole residues generated in this case often lay close to each other (generally one pixel apart). This kind of residue can be easily identified and isolated in the phase map (Karout, 2007).

Localization of the phase discontinuities through PU technique does not have a unique solution. There are many ways to connect the residues, however there is uncertainty as to which is best. Criteria have been proposed including minimization of the total length of branch cuts (Costantini, 1997), but this in practice is not optimal because it ignores the physical characteristics of the SAR images. As stated before, the two main difficulties facing SAR unwrapping algorithms are regions of shadow and layover. Madsen and Rosen (1993) suggested the use of the non-charged points (neutrons) that act as residues to guide tree growth, but do not affect the net tree charge. Neutrons do not contribute to the total charge of the current tree, but serve to reduce the size of the search region. Placing neutrons in regions of layover encourages the growth of branches in those areas. Algorithms have been proposed for the deployment of neutrons based upon the second derivative of the phase, the phase gradient and radar backscatter intensity (Bone, 1991). All of these methods aim to localize the branch cuts to lie within areas that are prone to unwrapping errors or where the correlation is low. Rosen *et al.* (1994) used SAR backscatter to determine the neutron locations by comparing the intensity of each pixel to a threshold. The threshold was chosen to generate a fixed percentage of neutrons regardless of contrast in the scene. In high contrast scenes the neutrons will congregate in layover regions, and improve tree structure by reducing the overall maximum length of cuts.

2.10.3 Phase unwrapping methods

Many PU algorithms were developed during the last twenty years to overcome the pixels affected by noise. These algorithms calculate a gradient estimate by evaluating the difference between two consecutive pixels, then if the absolute value of the gradient

estimate is greater than π , then an offset of $+2\pi$ or -2π is add to correct the phase (Fornaro *et al.*, 1997). Because of the presence of corrupted regions within the image, this step cannot be performed unless an integration step is performed. The PU process is an integration process that could be performed by local pixel-to-pixel integration or by global integration or could even be performed in a hybrid form which employs both local and global integrations. The local integration technique could be termed the “path-following method”, whilst, the global integration technique is usually referred to as the “minimum-norm method” (Fornaro *et al.*, 1997). Two examples of these integration techniques will be explained in the following sections.

2.10.3.1 Branch Cut Concept for Phase Unwrapping

The Branch Cut (BC) technique is a powerful method that has the potential of providing correct PU without any solution approximations. The tree Branch Cut placement method is one of the earliest branch-cut methods introduced by Goldstein *et al.* (1988) who was first to propose the Branch Cut technique. This method relies on the fact that the summation of the gradient estimate of any closed path in the wrapped phase map must be equal to zero. This principle is defined in equation (2.31) for any closed loop path $\{P\}$ in the wrapped phase maps:

$$\sum_i^M \nabla\Phi(p_i) = 0 \quad (2.31)$$

Where $\Phi(p_i)$ is the wrapped phase value at pixel $p_i \in \{P\}$, $\nabla\phi(p_i)$ is the wrapped phase gradient and M is the number of pixels in a path $\{P\}$.

This principle is applicable to noise free wrapped phase maps. However, in the presence of noise in the wrapped phase map, this principle will be violated in areas which mark the start and the end of a 2π discontinuity. However in dealing with most real data, it is often found that equation (2.31) is not respected at all points. This can occur due to real discontinuities in the underlying field variable or because of noise in the phase. Whatever causes the violation of equation (2.31); it must be identified and localized. Summation of the phase differences around a closed path taking the closest multiple of 2π gives an inconsistent result around these points, which are termed “residues”. Positive residues have a residual “charge” of $+2\pi$ and negative residues -2π for a clockwise path. Connection of the residues by “branch” cuts to create neutralized “trees” localizes the phase jumps to occur across the cuts. Branch-cuts restrict the unwrapping path from passing through corrupted areas and achieve a balance between the phases of opposite residues to satisfy the condition of equation (2.31). Ideally these branches lie in regions that will be excluded from unwrapping (Karout *et al.*, 2007). Once branch-cuts are placed between all residues in a phase map as shown in the example of Figure 2.6, the unwrapping path can take any independent path in the phase map that respects the branch cut barriers and this will result in a correct phase unwrapping which is consistent with the condition laid down in equation (2.31) as shown in Figure 2.7(a).

However, the wrong PU path is generated whenever the unwrapping path crosses the branch-cut barriers as shown in Figure 2.7(b). This creates 2π discontinuities in the unwrapped phase map.

The algorithm begins by searching for an unvisited residue to form the start of a tree. A sequential search following this search around each of the tree residues drawing cuts to other residues until the tree is neutralized. At each stage the region surrounding each residue is searched up to a certain distance. Once all the residues in the current tree have been searched, the size of the search distance is increased and areas around all members of the tree are rescanned. This process continues until the tree is neutralized, or the size of the search region exceeds a predetermined boundary. When the algorithm is finished with a tree, it searches for a new unvisited residue and the process of growing a tree repeats. The edges of the patch are problematical because the residue structure is unknown beyond the edge. Connections to the edge to discharge a tree are permitted after the size of the search region exceeds a specified threshold. The unwrapped phase close to the edge may contain small residual errors because the cut was arbitrarily drawn. The algorithm effectively excludes regions of high residue density related to low SNR or layover by creating a dense network of interlocking cuts. These regions may also be excluded by estimation of the correlation coefficient and setting a threshold for unwrapping. Once the PU trees have been constructed, the phase is unwrapped by simple integration of the phase differences. A region growing algorithm is used to perform the integration and rapidly fills the image plane beginning at a single point called a “seed”.

3.10.3.2 Minimum cost flow (MCF)

The latest most efficient method of branch-cut placement is the minimum cost flow (MCF) or the cost guided minimum discontinuity method. This method was first

introduced by Costantini (1998). The algorithm minimises the integer number of cycles to be added to the phase variations (i.e. the data $\Delta w\phi$) to make them consistent. In the Minimum Cost Flow (MCF) approach, the PU problem is equated to a general network flow problem (Costantini, 1998). This reformulation of the PU problem allows the use of powerful techniques developed for network optimisation (Ahuja *et al.*, 1993). It uses a network of flows which defines the placement of every segment of the branch-cut guided by a cost factor and a global minimization strategy.

This method minimizes the global sum of integer multiples of $\pm 2\pi$ added to the original gradient estimate at every pixel before integration. Costs define where the branch-cuts are likely (low cost), or unlikely (high cost) to be placed (Costantini, 1998). In essence, finding the best possible branch-cut placement aids the minimization criteria to achieve a global minimum value. Costs in this method are weighting factors, which if they are constant then the minimum cost flow minimizes the total length of branch-cuts. However, costs in this method are usually defined by either user defined weights or quality maps on the local interferogram such as: coherence, correlation coefficient, pseudo-correlation, phase gradient variance, maximum gradient, residue density, flatness or smoothness of the unwrapped phase. MCF algorithms are truly phase unwrapping programs, since they merely add an integer number of cycles to every wrapped phase value.

2.11 Persistent scatterer

If the phase caused by terrain elevation can be removed from an interferogram, the targets movements in the line-of-sight direction can be obtained (Hanssen, 2000). The main limitations of InSAR applications are the geometrical and temporal de-correlations. Even though the coherence of two radar signals is high enough, the

atmospheric phase screen differences between SAR images still reduce the achievable accuracy. Persistent scatterer (PS)-InSAR overcomes these restrictions of conventional InSAR technique. PS-InSAR identifies certain natural point-like stable reflectors, i.e. persistent scatterer (PS), from long temporal series of interferometric SAR images. The coherence of these PS is good enough to obtain digital surface models (DSM) in sub-meter accuracy and millimetric terrain motion (Ferretti *et al.*, 2001; Ferretti *et al.*, 2007; Crosetto *et al.*, 2010). PSI represents the most advanced class of DInSAR techniques, which started with the so-called Permanent Scatterers technique proposed by Ferretti *et al.* (2000). Ferretti *et al.* (1999) demonstrated a different process by examining a stack of differential interferograms and looking at the temporal evolution of phase-stable pixels. This technique was called the Permanent Scatterer Technique. Because this technique needs phase-stable (persistent) pixels it is especially good for use over urban areas, where temporal decorrelation effects are minimised due to the high number of stable reflective structures (buildings, bridges, etc). Since 1999 other techniques have been suggested following similar processing lines, and have been reported to measure deformation to accuracies of millimetres per year (Ferretti *et al.*, 2001; Berardino *et al.* 2002; Pepe *et al.*, 2005; Crosetto *et al.*, 2008). Even though these techniques were initially named “Permanent Scatterers techniques”, now all of them, including the original Permanent Scatterers technique, are called “PSI techniques”.

There are two main differences between DInSAR and PSI techniques: the first one is the number of processed SAR images (PSI uses large series of SAR images, typically more than 20), and the other one is the implementation of suitable data modelling and analysis procedures that allow one to get the following key products such as the time series of the deformation, the average displacement rates over the observed period, the

atmospheric phase component of each SAR image, and the so-called residual topographic error. This parameter is important for modelling purposes, and for geocoding purposes. The main products of any PSI analysis are given by the map of the average displacement rates, and the deformation time series of each measured Persistent Scatterer (Warren *et al.*, 2006).

The first key limit of PSI is related to the capability of temporally sampling the deformation phenomena, which basically depends on the revisiting time capabilities of the SAR satellites (e.g. 35 days for ERS and Envisat, 11 days for TerraSAR-X) and their data acquisition policies. The temporal SAR sampling directly impacts the temporal resolution of PSI, which can typically monitor slow deformation phenomena which evolve over several months or years. The actual spatial sampling of PSI represents a second important limit. PSI is an “opportunistic deformation measurement method”, which is able to measure deformation only over the available PSs, that is the points where PSI phases are good enough to get reliable deformation estimates. PS density is relatively high in urban areas (for instance densities up to 1000 PS/km² can be achieved with ERS and Envisat data), whilst it is usually low in vegetated and forested areas, over low-reflectivity areas (very smooth surfaces) and steep terrain. It is worth underlining that the location of the PSs cannot be known prior to the PSI processing. The spatial density limitation is particularly evident for the ERS, Envisat and Radarsat sensors, whilst for the higher resolution ones, like TerraSAR-X, PS density should considerably improve. A third limit of PSI is the line-of-sight (LOS) measurements capability. The deformation measurements coming from PSI and all DInSAR techniques are made in the LOS of the used SAR sensor. Therefore, given a generic 3D deformation, PSI provides the estimate of the LOS component of this deformation (i.e.

the projection of the 3D deformation in the LOS direction). By using ascending and descending SAR data one can retrieve the vertical and approximately the east-to-west horizontal components of deformation (Warren *et al.*, 2006).

2.12 Integrated InSAR with Global Positioning System (GPS)

GPS field observations have been used to improve the accuracy of InSAR derived DEM and for the accuracy assessment (Ge *et al.*, 2000). On the other hand, the best way to investigate the differential process is an integrated survey which improves the qualitative and quantitative analysis of the vertical displacements. The use of differential SAR interferometry and GPS measurements allows the investigation of the critical areas in real time, allowing the evolution of displacements to be tracked (Wegmüller *et al.*, 1999).

2.12.1 Introduction to GPS

The Global Positioning System (GPS) is a satellite-based navigation system that was developed by the U.S. Department of Defence in the early 1970s (Hoffmann- Wellenhof *et al.*, 1999). GPS was used by the USA military system and later on was available to civilians. GPS encompasses three segments: space, control, and user. The space segment includes the 24 operational NAVSTAR satellites that orbit the earth every 12 hours at an altitude of approximately 20,200 kilometres, which provides continuous position and timing information. To ensure continuous worldwide coverage, GPS satellites are arranged so that four satellites are placed in each of six orbital planes. With this constellation geometry, four to ten GPS satellites will be visible anywhere in the world, if an elevation angle of 10° is considered; only four satellites are needed to

provide the positioning. Each satellite contains several high-precision atomic clocks and constantly transmits radio signals using a unique identifying code (El-Rabbany, 2002).

One Master Control Station, five Monitor Stations, and Ground Antennas comprise the control segment. The Monitor Stations passively track each satellite continuously and provide this data to the Master Control Station. The Master Control Station calculates any changes in each satellite's position and timing. These changes are forwarded to the Ground Antennas and transmitted to each satellite daily. This ensures that each satellite is transmitting accurate information about its orbital path.

The user segment, comprised of both civilian and military users worldwide, acquires signals sent from the satellites with GPS receivers. The GPS receiver uses these signals to determine where the satellites are located. With this data and information stored internally, the receiver can calculate its own position on earth. This positional information can be used in many applications such as mapping, surveying, navigation, and mobile GIS.

2.12.2 Calculating the distance to the satellite

The problem with GPS is that only pseudo-ranges and the time at which the signal arrived at the receiver can be determined. Thus there are four unknowns to determine; position (X, Y, Z) and time of travel of the signal. Observing four satellites produces four equations that can be solved, enabling these unknowns to be determined. In order to calculate the distance to each satellite, one of Isaac Newton's laws of motion is used:

$$\text{Distance} = V \cdot T \quad (2.32)$$

GPS requires the receiver to calculate the distance from the receiver to the satellite. The V is the velocity of the radio signal. Radio waves travel at the speed of light, 300,000 km/s. T is the time taken for the radio signal to travel from the satellite to the GPS

receiver. The GPS receiver is matching or correlating the incoming satellite code to the receiver generated code in order to calculate the time taken for the radio signal to travel from the satellite to the GPS receiver.

2.12.3 Problems with height

The nature of GPS also affects the measurement of height. The ellipsoid used by GPS is known as WGS84 or World Geodetic System 1984. All heights measured with GPS are given in relation to the surface of the WGS84 ellipsoid. These are known as ellipsoidal heights. Existing heights are usually orthometric heights measured relative to mean sea level. Mean sea level corresponds to a surface known as the geoid which is shown in Figure 2.8. The Geoid can be defined as an equipotential surface, i.e. the force of gravity is a constant at any point on the geoid. The geoid is of irregular shape and does not correspond to any ellipsoid. The density of the earth does however have an effect on the geoid, causing it to rise in the more dense regions and fall in less dense regions. The relationship between the geoid, ellipsoid and earth's surface is shown in the graphic below. As most existing maps show orthometric heights (relative to the geoid), most users of GPS also require their heights to be orthometric. This problem is solved by using geoidal models to convert ellipsoidal heights to orthometric heights. In relatively flat areas the geoid can be considered to be constant. In such areas, use of certain transformation techniques can create a height model and geoidal heights can be interpolated from existing data.

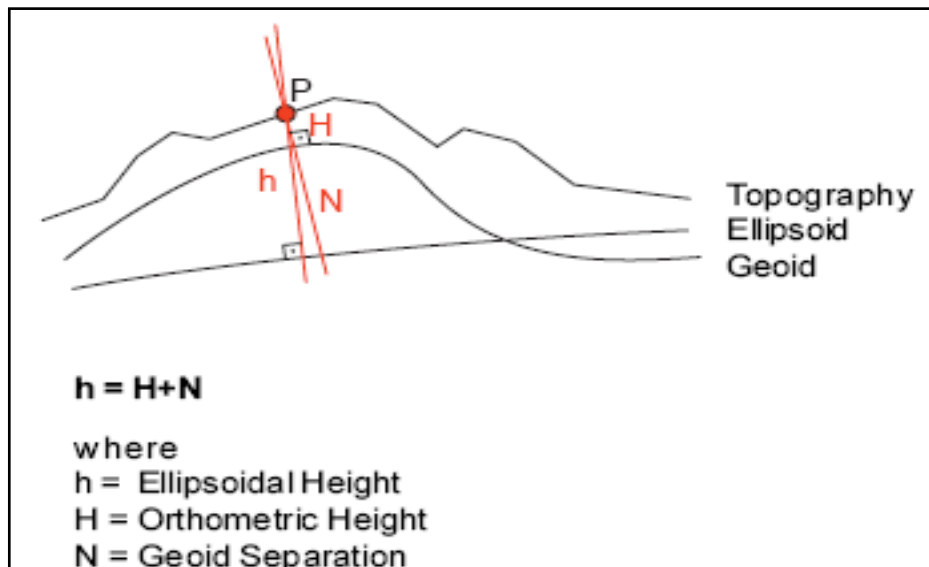


Figure 2.8: The relationship between Orthometric and Ellipsoidal height (source: Leica, 1999).

2.12.4 Error Sources

GPS receivers calculate distances by using the time it takes for signals to travel from satellites. This work needs signals from at least four satellites. Each of these signals has some errors due to different factors like disturbances in the atmosphere. These errors can have a cumulative effect in the final result the GPS gets. There are several sources of error that degrade the GPS position from a theoretical few metres to tens of metres. These error sources are: ionospheric and atmospheric delays; satellite and receiver clock errors; multi-path; dilution of precision; selective availability and anti spoofing. Further information about these error sources can be found in Leica (1999), Kaplan and Hegarty (2006) and Seeber (2003).

2.12.5 Differential GPS

Differential GPS (DGPS) is a land-based technology that works to improve the accuracy of GPS navigation. Differential GPS improves the accuracy to within two meters of the actual position for moving objects and even better for stationary situations (Ge *et al.*, 2000). This is achieved by removing the errors in the position measured by a GPS receiver due to errors such as atmospheric, satellite and receiver clock. By averaging the corrected position as a static point for about 3 - 5 minutes, the position obtained is usually within 3 m of the actual position. The errors that are left after applying corrections are random. Differential GPS takes GPS to a much higher level; it becomes a tool for positioning things on a precise scale. Wells *et al.* (1986) indicated that relative positioning DGPS acquired more accurate altitude or height than the absolute positioning. They showed that height (Z) data would have 2-5 times less accurate than the horizontal (x,y) data. This could be because of one-sided geometry.

Differential GPS works through two receivers, one of which is stationary and the other moves around making position measurements. The stationary (reference) receiver is placed at a point that has been very accurately marked and surveyed. This station is considered to receive the same GPS signals with the same amount of error as the moving receiver. Because it is on a known point, the reference receiver can estimate very precisely what the ranges to the various satellites should be. The reference receiver can therefore work out the difference between the computed and measured range values. These differences are known as corrections. The reference receiver is usually attached to a radio data link which is used to broadcast these corrections. The stationary receiver repeats this process for all the visible satellites; encodes the information into a standard format and then relays the information to the moving

receiver. The moving receiver is thus able to make appropriate corrections. The rover receiver has a radio data link attached to it that enables it to receive the range corrections broadcast by the reference receiver. The rover receiver also calculates ranges to the satellites. It then applies the range corrections received from the reference. This lets it calculate a much more accurate position than would be possible if the uncorrected range measurements were used. A limit of a differential GPS is that it can eliminate only those errors that are common to both the stationary and moving receivers.

2.12.6 Real-time DGPS measuring techniques

There are several different methods for obtaining a position using GPS. The method used depends on the accuracy required by the user and the type of GPS receiver available. Static surveying was the first method to be developed for GPS surveying. It is a relative positioning technique that employs two or more stationary receivers simultaneously tracking the same satellites. Two GPS receivers are used to measure a GPS baseline distance. The line between a pair of GPS receivers from which simultaneous GPS data have been collected and processed is a vector, referred to as a baseline. The station coordinate differences that are calculated in terms of a 3D earth-centred coordinate system that utilizes X-, Y-, and Z-values based on the WGS 84 geocentric ellipsoid model. These coordinate differences are then subsequently shifted to fit the local project coordinate system.

The real time kinematic (RTK) technique is typically used for detail surveying, recording trajectories etc. The technique involves a moving rover whose position can be calculated relative to the reference. Firstly, the rover has to perform what is known as an

initialization. This is essentially the same as measuring a rapid static point and enables the post-processing software to resolve any ambiguities. The reference and rover are switched on and remain absolutely stationary for 5-20 minutes, collecting data. The actual time depends on the baseline length from the reference and the number of satellites observed. After this period, the rover may then move freely. The user can record positions at a predefined recording rate, can record distinct positions, or record a combination of the two. This part of the measurement is commonly called the kinematic chain. A major point to watch during kinematic surveys is to avoid moving too close to objects that could block the satellite signal from the rover receiver. If at any time, less than four satellites are tracked by the rover receiver, you must stop, move into a position where 4 or more satellites are tracked and perform an initialization again before continuing.

2.12.7 Limitations of GPS measurements

In order to operate with GPS it is important that the GPS antenna has a clear view to at least 4 satellites. Sometimes, the satellite signals can be blocked by tall buildings, trees etc. Hence, GPS cannot be used indoors. It is also difficult to use GPS in town centres or woodland. The GPS signal may bounce off nearby objects causing another problem called multi-path interference. Due to this limitation, it may prove more cost effective in some survey applications to use an optical total station or to combine the use of such an instrument with GPS.

2.13 Summary

SAR interferometry provides data that contain information relating to the phase and coherence components of the backscattered radar signals. This section presents the use of phase information to derived digital elevation models and map deformation. Differential interferometric techniques and DGPS have been addressed and illustrated. The most important products from interferometric SAR are the coherence image, DEMs and deformation maps. This chapter discusses the quality of these three products and their associated errors including interferometric processing parameters and environmental parameters such as the loss of coherence, temporal and baseline decorrelation, the unwrapping-related errors, and the atmospheric artefacts.

Chapter 3: Characteristics of peat swamp forest ecosystem

3.1 Introduction

The area of peatlands in Indonesia is approximately 20 million hectares (Mha), which is nearly 11% of the total land area (Rieley *et al.*, 1996). Peat material is either fibric, hemic, or sapric. Fibric peats are the least decomposed, and comprise intact fiber. Hemic peats are somewhat decomposed, and sapric are the most decomposed (Richardson and Vepraskas, 2000). The vast majority of peatland are lowland, ombrogenous systems, which dissolved nutrients from rainfall and other precipitation as opposed to watercourses or below-ground drainage, that support a natural vegetation of peat swamp forest on top of peat that ranges from 0.5 m to more than 10 m thick (Rieley and Ahmad-Shah, 1996). Approximately 50% of these peatlands exceed 2 m in thickness (Anderson, 1983). Almost all of Indonesia's peatland is located in three islands, Borneo (Kalimantan), New Guinea (Irian Jaya) and Sumatra. Central Kalimantan province contains about 3 Mha of peatland and studies have been carried out on the ecology and environmental importance of the peat of this area since 1993 (Page *et al.*, 2000).

Forested tropical peatlands in South East Asia (Figure 3.1) store at least 42,000 Mt of soil carbon, of which 35,000 Mt is stored in Indonesian peatlands (Hooijer *et al.*, 2006). This carbon store is now being released to the Earth's atmosphere through two mechanisms, rapid land use changes (deforestation, drainage) and fire. Fire risk is increased following drainage and lowered water tables. Surface biomass fires on

tropical peatland have increased greatly in recent years owing to land clearance for development, property maintenance and vandalism. There are major additional impacts through CO₂ emissions to the atmosphere, loss of dissolved organic carbon from degraded peatland catchments and high concentrations of fire-derived pollutants which contribute to the so-called smoke 'haze' that affects much of the SE Asian region on an annual basis. As a result of these losses, it is estimated that the current extent of developed peatland in Indonesia alone puts it at third place in global CO₂ emissions. A failure to account for the loss of stored carbon from tropical peatlands could lead to underestimates of future rates of increase in atmospheric greenhouse gases and the extent of human induced climate change (Page *et al.*, 2002).

There is also a threat to the remaining biodiversity in South East Asia because the peatlands are an important habitat for many endangered species, including Orange Utan in Borneo and Sumatran Tiger in Sumatra. Increasingly, the peatlands of South East Asia have been drained to provide land for plantation agriculture. One important plantation crop is palm oil (Figure 3.2) which, among a myriad of other uses, is increasingly being used as a biofuel in Europe; the other plantation crop is Acacia which is grown on a short-rotation cycle to provide the raw material for pulp and paper manufacture. Scientists have been aware of the link between peat land development and CO₂ emissions for some time, but policy makers and governments are still insufficiently aware of the global implications of local and national peatland management strategies and actions (Page *et al.* 2006). Therefore, prediction of the rate of subsidence is an essential component of any reclamation scheme because subsidence is one of the important consequences of reclamation which influences future land-use (Rieley and Page, 2005).



Figure 3.1: Peat swamp forest in Central Kalimantan, Indonesia (Picture by B. Dahdal).



Figure 3.2: Palm oil plantation in Central Kalimantan, Indonesia (Picture by B. Dahdal).

3.2 Peat subsidence

Peat soils show characteristically different subsidence behaviour from mineral soils such as clays and sands. Over time, subsidence of mineral soils stops, first with sands and then with clays. Subsidence of peat soils, however, continues over time, albeit in some cases at decreasing rates. Subsidence of peat soils occurs mainly through decreasing volume by shrinkage and oxidation above the water table and by compression below (Schothorst, 1977). Peat soils are subject to subsidence and surface elevation loss when drained. Stephens *et al.* (1984) stated that soil subsidence and the resulting loss of surface elevation are due to six processes: shrinkage due to desiccation; consolidation by loss of the buoyant force of groundwater; compaction by tillage; wind erosion; burning and biogeochemical oxidation. Each of these six phases represents a characteristic behaviour of peat and has different practical consequences for its agricultural use and the environmental issue of CO₂ emissions. The initial rapid subsidence occurs because of consolidation. It results in compression of permanently saturated peat layers without a permanent loss of peat. The subsidence rate slows down after the first two years of rapid subsidence (Rieley and Page, 2005). Oxidation and burning (Figure 3.3) are considered the dominant forces and are irreversible. These two processes show a loss of volume due to an increase in the bulk density of the peat material. Peat subsidence occurs in the natural situation, but it is balanced by the growth of peat. In drained peat this balance is lost; the subsidence processes are orders of magnitude greater and peat surface and carbon store decline rapidly.



Figure 3.3: Burned peat surface: 30X30 cm (Picture by B. Dahdal)

3.3 Causes of peat subsidence

3.3.1 Drainage and land clearing

Most peat soils shrink when dried but swell when re-wetted, unless water content falls below a threshold value beyond which irreversible drying occurs (Andriess, 1988). Over drainage can cause irreversible drying and shrinkage. Irreversible drying of the peat soil from Central Kalimantan in Indonesia occurred at mean critical water contents ranging from 27.9 to 17.9%, 34.7 to 22.0%, and 5.5 to 3.5% for fibric, hemic and sapric peats, respectively (Haris *et al.*, 1998). Shrinkage values can be expressed as specific volumes of peat soil (Price and Schlotzhauer, 1999). Specific volumes of peat soil from Central Kalimantan ranged between 2.7 and 6.5 cm³/g and these decreased significantly with cultivation and fire damage, especially in the top 0-30 cm (Rieley and Page, 2005).

The reclamation, or conversion, of tropical peatland for agriculture involves drainage and land clearing, which, apart from causing loss of biodiversity, inevitably produce changes in the physical, chemical, and biological properties of the peat soil, introducing constraints for cropping. In addition, subsequent cultivation practices will also have an influence on these properties. In terms of physical properties, drainage results in rapid peat subsidence within the first 4-10 years, followed by a slowing down to a somewhat constant rate thereafter. With subsidence and compaction, various changes occur to soil physical properties, including increased bulk density, and decreased total porosity, oxygen diffusion, air capacity, available water volume and water infiltration rate (Radjagukguk, 2000).

3.3.2 Fire

Under natural circumstances peatland fires are extremely rare but, when damaged by logging and drainage, tropical peatlands become susceptible to fire. Fires are most severe during El Niño periods, as in 1997/98 when about 2.4-6.8 million ha of peatlands burnt in Indonesia (Page *et al.*, 2002). Furthermore, peatlands burnt once are more likely to burn again (Siegert *et al.*, 2001; Cochrane, 2003; Langner *et al.*, 2007). This positive feedback cycle leads to progressive forest degradation and continuous release of CO₂.

In Central Kalimantan, there is a dry season of usually three or four months between May/June and September. Rain still falls in dry seasons but the frequency and intensity of events are greatly reduced. During the 1997 ENSO event, the dry season, spanned eight months from March to December, during which there was hardly any rainfall (Page *et al.*, 2000). The greatly reduced rainfall during the 1997 ENSO event led to a very marked drop in the level of the peat water table. At a peat water table monitoring station in peat swamp forest in the upper catchment of Sebangau River, the water table fell to 98 cm below the surface in mid-November, 1997. Even so, this area was unaffected by forest fires.

In comparison, the water table at this location in 1995 and 1996 remained close to the peat surface throughout the dry season with a maximum drawdown of only 20 cm. After the drought ended in December 1997 the peat water table responded very rapidly to rainfall events and returned to its normal wet season level within one month (Boehm and Siegert, 2001).

The majority of large fires in 1997 were small and deliberate that rapidly got out of control in the dry conditions and escaped into areas of degraded swamp forest. Various assessments have been made of the amount of land in Indonesia that was damaged by the 1997 fires. Initial estimates indicated that approximately 4.5 Mha were affected (Liew *et al.*, 1998), but this was increased subsequently to 9 Mha (BAPPENAS, 1998). The causes of these fires were mainly the activities of illegal loggers and fishermen, and the burning for development of transmigration schemes. Transmigration developments that started in the late 1970s have created a fire-prone landscape. The extensive network of drainage canals not only opened up access to the area but also lowered the water table in the surrounding swamp forests, increasing fire incidence and susceptibility. Illegal logging (see Figure 3.4 for illustration) in the swamp forests surrounding the transmigration areas increased rapidly in the 1980s. In combination with legal logging, these illegal activities severely degraded the swamp forests to the point where fire can easily get out of control. In addition to social and biophysical conditions that predisposed these forests to fire, the confusion over land status and the absence of formal management also provided no incentives to stop the spread of the fires in these open access areas. Another source of fire in some small parts of the area was the preparation of land for swamp rice cultivation, oil palm, industrial timber, and rubber plantations (Applegate *et al.*, 2001). The impact of fires on the peat ecosystem can be

assessed through estimating the area burnt, the depth of the peat fire and the frequency of fires over a long-term period. Information is available for the whole area in the major fire episode of 1997/98 (Page *et al.* 2002) and for the period of 1973-2005 for Block C (Hoscilo, 2009).



Figure 3.4: Illegal logging in Central Kalimantan, Indonesia ((Picture by B. Dahdal).

3.4 Relationships between subsidence, groundwater level, and CO₂ emission

The relationship between subsidence and the groundwater level is an important tool for converting optimal groundwater levels, as dictated by different land use options, into subsidence rates (Price and Schlotzhauer, 1999). The major causes of peat subsidence are water loss and biological oxidation. Water loss leads to a decrease in the soil volume through shrinkage and eventually, to the subsidence of the peat layer. The first layer is also the site of active organic matter decomposition which has been favoured by the

oxidizing conditions of this layer. Although the oxidation of organic matter has beneficial effects, i.e. the release of nutrients by mineralization, the process leads to a decrease in soil volume hence promoting subsidence (Dradjad *et al.*, 1986). It should be noted however, that it is not the depth of the water table itself that affects conditions but rather the moisture content of the peat, of which the water level is an expression. For a given site with specific peat characteristics, there is a fixed relation between water table depth and the soil moisture profile in the unsaturated zone above it, although this relation varies with wetting and drying cycles (Hooijer *et al.*, unpublished).

There is a direct relationship between depth of the water table and rate of subsidence and the combination of subsidence and the groundwater level makes it possible to evaluate the sustainability of various cultivation practices on peat soils. For example, the rate of subsidence of peat under sago cultivation with an optimal water table depth of 25 cm is only half the rate of subsidence of peat under oil palm cultivation with an optimal water table depth of 50 cm. When applying these considerations it is important to know the average surface water level in order that when estimating subsidence due to mechanical processes, the extent of subsidence is measured only from that depth.

The relationship between subsidence and groundwater level follows the equation:

$$\text{Peat subsidence rate (cm/y)} = 0.x \cdot \text{Depth of the water table (cm)} \quad (3.1)$$

The actual co-efficient value (0.x) depends on the peat characteristics and it has been found to vary from between 0.1 – 0.04 in peat soils in Sarawak and Western Johore (Wösten *et al.*, 1997). The equation can be used as a tool for converting the optimal groundwater levels, as dictated by the different land-use options, into subsidence rates. The rate of subsidence has been predicted using various formulae and simulation

models for measuring physical ripening have also been devised by many scientists (Dradjad *et al.*, 2003).

3.5 Relationship between groundwater depth and CO₂ emission

The relationship between CO₂ gas emission monitoring and water depth have been discussed in many studies (Jauhiainen *et al.*, 2008; Melling *et al.*, 2005; Ali *et al.*, 2006). Other studies focussed on long term monitoring of peat subsidence in drained peatlands, combined with peat carbon content and bulk density measurements to separate the contribution of compaction from the total subsidence rate; the remainder is attributed to CO₂ emission (as reviewed by Wösten *et al.*, 1997; Wösten and Ritzema, 2001).

The relationship between peat CO₂ emission and depth of the water table is non-linear since the aerobic decomposition rate cannot increase indefinitely as the water table falls. This approach has been generally applied to describe the peat surface CO₂ respiration–water table depth relationship in some studies of tropical peatlands (Jauhiainen *et al.*, 2008; Hirano *et al.*, 2009). The upscaled regional assessments of drainage-related peat emissions from SE Asian tropical peatlands made by Hooijer *et al.* (2006, 2010) and Uryu *et al.* (2008) applied only linear relationships between peat respiration and water table depth. Hooijer *et al.* (2010) contend that the linear relationship is the best estimate currently available for determining CO₂ emissions at water table depths between 50 and 100 cm, which covers the range of most common groundwater depths of drained peatlands in SE Asia. They also concluded the regression relationship CO₂ gas emission monitoring and water depth can be expressed by this formula

$$\text{CO}_2 \text{ emission} = 91 \cdot \text{WT} \quad (3.2)$$

Where CO₂ emission is expressed in t/ha/y and groundwater depth is the average depth of the water table below the peat surface, expressed in metres.

This linear relation implies that every 10 cm water table drawdown will result in an increase in CO₂ emission rate of 9.1 tCO₂/ha/y. Using this relationship, the CO₂ emission from all geographical units can be calculated as follows:

$$\text{CO}_2 \text{ emission} = \text{LU Area} \cdot \text{D Area} \cdot \text{WT} \cdot \text{CO}_2 \text{ 1m [t/y]} \quad (3.3)$$

Where:

LU Area = peatland area with specific land use [ha]

D Area = drained area within peatland area with specific land use [fraction]

WT = average groundwater depth in drained peatland area with specific land use [m]

CO₂ 1m = CO₂ emission at an average groundwater depth of 1m = 91 [tCO₂/ ha/y]

(Hooijer *et al.*, 2010).

Peat carbon content is obtained by combining the area of peatland with the bulk density of and carbon concentration in peat. The carbon “density” of Southeast Asian peat that has been used in this calculation is based on a mean peat dry bulk density of 100 kg/m³ and average carbon concentration of 60% (Wösten *et al.*, 2010; Rieley *et al.*, 2008).

3.6 Burned area mapping in tropical ecosystems

To quantify the role of peatland fires in peat subsidence, it is important to identify the burn scar areas. Until the early 1990s researchers focused on using optical or thermal sensors to detect fires and resulting scars using measured changes in temperature during the fire and the vegetation changes immediately after (Kasischke *et al.*, 1993; Chuvieco, and Martin, 1994). Michalek *et al.* (2000) also reported on the utility of Landsat Thematic Mapper (TM) data for assessing stand density and fire severity in Alaska. The majority of satellite-based methods for burn area mapping utilise an alteration of

spectral signals recorded from affected surface before and after a fire event. Several studies have explored changes in the Normalised Difference Vegetation Index (NDVI) and have been widely used to detect burn areas in temporal and boreal forest. Recently, several studies have argued for the superiority of the Normalised Burn Ratio (NBR) over other indices in the context of burned area mapping and burn severity analysis (Escuin *et al.*, 2008). Tansey *et al.* (2008) used Landsat TM data to derive the burnt area and explore the relationship between hotspot data and burned area for a region of degraded tropical peat swamp forest in Central Kalimantan, Indonesia.

Few studies using radar imagery for tropical peatland monitoring have been published so far. According to Kasischke *et al.* (1992), burned areas were not distinguishable from unburned forest using JERS data but they found ERS data could be used to detect fire scars in the boreal forest because the scars were 3–6 dB brighter than the rest of the landscape. This brightness is a result of physical changes that occur due to fire, including increased surface roughness, removal of tree canopies and alteration of soil moisture patterns. French *et al.* (1996) reported strong changes to backscatter in ERS-1 SAR images in burn scars in Alaskan boreal forests that correlated to changes in soil moisture. They suggested that radar backscatter in recent fire scars is influenced by the moisture content of the soil, the level of damage to the vegetation and the amount of plant re-growth after. Therefore, the analysis of multi-temporal processed ERS-1 and an ERS-2 image acquired before and during the fire season allows the detection of burn scars at a high spatial resolution due to a significant reduction in the backscatter signal after burning, no matter what kind of vegetation was affected.

However, if multi-temporal SAR data of an area of interest are acquired, clearings or burning of forests/vegetation can be detected by an observed change in coherence of the area. Unlike optical/infrared sensors, SAR is unable to detect hot spots or smoke plumes directly associated with fire. It is thus not able to tell whether the clearings are due to fire or other means. However, if fires have been known to occur in an area of interest, the extent of fire affected areas can be mapped using SAR backscattered intensity and interferometric coherence signatures. These characteristics were used to map areas of burnt forests in Kalimantan and to assess the level of fire damage (Siegert and Ruecker 2000; Siegert *et al.*, 2001). Liew *et al.* (1998) used Interferometric SAR imagery acquired during the ERS-1/2 tandem missions in April/May 1996 and October 1997 over the southeast corner of Kalimantan to detect and delineate areas affected by fires during the 1997 fires. The study area was covered by four ERS scenes of about 100 km cover the study area by 100 km each. The possible fire burn scars were characterized by a low interferometric coherence in 1996 and an increase in coherence between the 1996 and 1997 imagery. About 15% (550,000 ha) of the total area surveyed was found to have been affected by fires, with most of the burnt areas occurring in the ERS scene adjacent to the town of Banjarmasin. Page *et al.* (2002) used a combination of Landsat TM/ETM and multi-temporal, synthetic aperture radar (SAR) to estimate the extent of peatlands, pre-fire land cover types and burnt area after the severe 1997 El Niño event in the Mega Rice Project (Ex-MRP) area in Central Kalimantan. The combined evaluation shows that 32.0% (796,907 ha) of the investigation area was burned, 91.5% (729,500 ha) of which was peatland and 70.0% of fragmented peat swamp forest were destroyed by fire. Of this fire-damaged peatland area, 47.4% (377,814 ha) was peat swamp forest (pristine, logged and fragmented) and the rest was degraded and deforested peatland. Ballhorn *et al.* (2009) used light detection and ranging (LIDAR)

aerial remote sensing to obtain spatial measurements on burn depth across large fire scars in Central Kalimantan, Indonesia. Their results demonstrated that LIDAR had the ability to collect sufficiently accurate and spatially representative measurements of the burn scar depths in peat over large areas in very inaccessible terrain. The determined average burn depth of 33 cm correlated well with field measurements that have been recorded in the same year at locations near the LIDAR transects.

3.7 Deforestation detection

The primary challenge in deriving accurate forest cover change information is choosing the time interval and the accuracy of remote sensing methods that maximize the signal-to-noise ratio (SNR). Coppin and Bauer (1995) tested two; four and six-year intervals for canopy change detection and found that a two-year cycle was optimal to study Aspen establishment and storm damage in the Great Lakes region with Landsat Thematic Mapper (TM) imagery. Their four and six year cycles performed best for human-induced and natural canopy disturbances such as thinning, cutting and dieback. Thiel *et al.* (2006) assessed the feasibility of forest cover mapping and the delineation of deforestation using JERS-1 SAR data. The assessment was carried out at five test sites in Europe using time series of SAR images, taken from the period 1992–1998. These images were classified into forest, non-forest and deforested areas and the overall accuracy of the derived forest cover map was 90% compared to field measurement. Forest clear-cut detection with ERS interferometry was studied by Smith and Askne (2001) and found to be feasible but dependent on weather conditions during and between image acquisitions.

In the 1990s, drainage of peat for rice expansion (Figure 3.5) was a major reason for peat destruction, particularly through the Ex-MRP in Central Kalimantan, Indonesia. A decrease in hydro-period, which is the number of days per year that an area of land is dry, will accelerate soil oxidation, rate of subsidence and frequency of peat fires (Applegate *et al.*, 2001). In recent years, the expansion of oil palm and timber plantations, together with illegal logging have been identified as the driving forces of the destruction and of deforestation over Ex-MRP area. ENVISAT satellite monitoring in 2002 revealed that most of the fire hotspots were on plantation land, and fire is routinely used by oil palm plantation owners to clear land (Dennis *et al.*, 2005). Hoekman (2007) shows that continuous radar observations are very useful for determining and mapping certain degrees of tropical peatland damage following the construction of drainage canals (Figure 3.6).



Figure 3.5: Rice plantation in Ex-MRP, Indonesia (Picture by B. Dahdal).



Figure 3.6: A drainage canal in Ex-MRP, Indonesia (Picture by B. Dahdal)

3.8 Measuring peat subsidence

Peat subsidence can be measured manually using a pipe with total length exceeding the depth of peat and anchored in the underlying mineral soil (Figure 3.7). The pipe is set in the peat soil throughout the observation period. The intersection of the pipe with the peat surface is marked and the length between it and the top of the pipe is measured. After the time of observation is finished, the length between the top of the pipe and the peat surface is measured again and the accumulation or the subsidence of the peat soil can be obtained. Driessen and Soepraptohardjo (1974) reported that for an organic soil from South Kalimantan having a peat layer ± 1 m thick, the subsidence was 0.15- 0.2 m/y following land reclamation. Subsequent studies indicated a cumulative reduction in the thickness of the peat layer by 0.15 m/y. The high abnormal trend in the rate of subsidence that have been found by Dradjad *et al.* (2003) could not be attributed to any of the mechanisms mentioned earlier, but it was suspected that fire occurring during a distinct dry spell may have destroyed much of the peat material.

Wösten *et al.* (1997) analyzed long-term subsidence recordings for a project area in peninsular Malaysia to quantify the relationships between subsidence and time as well as between subsidence and water management. The average subsidence rate for the area was found to be 2 cm/y. The oxidation and shrinkage components of total subsidence were quantified and the contribution of subsidence to the emission of CO₂ was estimated to be 27 t/ha/y.

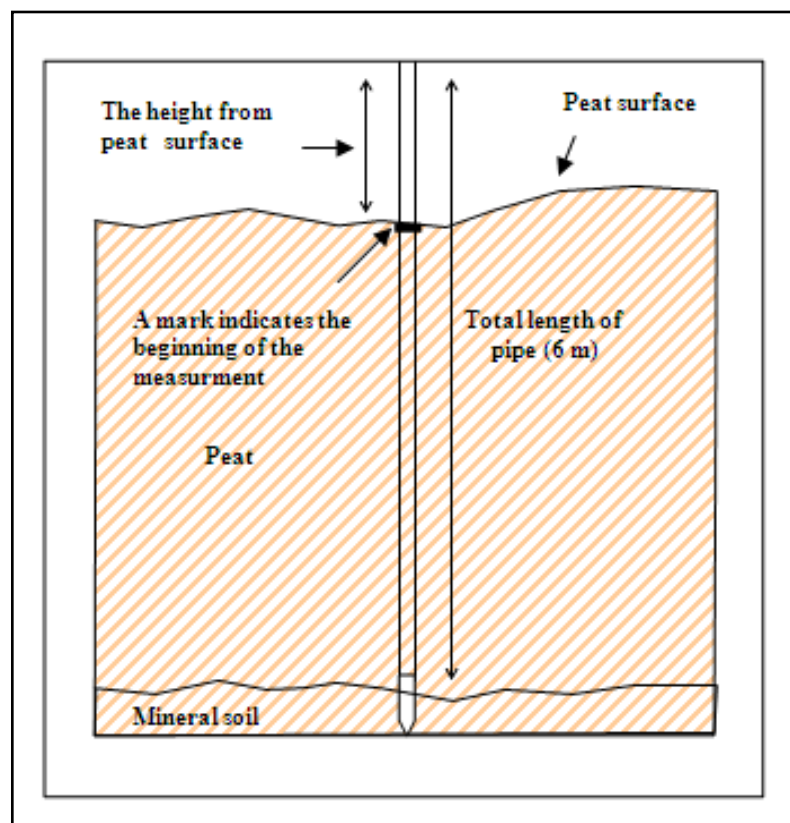


Figure 3.7: Field measurement of peat subsidence.

Dradjad *et al.* (2003) studied the rate of subsidence and its impacts on the characteristics and quality of peat soils in Barambai, south Kalimantan, based on data collected from 1972 to 1974. Measurements were taken at 16 observation points having initial peat thickness ranging from 18-63 cm. Two methods for determining subsidence were used in their research. The first method was using actual measurements based on the

measurements of the depth of the peat layer, while the second method included calculations using a soil shrinkage formula and Fokkens' formula for mechanical consolidation. They reported that the average annual subsidence ranged from 1.6 to 3.2 cm/y except some plots where cultivation was intensive. A method for calculating the rate of subsidence which takes into account the respective contributions of shrinkage and consolidation correlated well with actual field measurements. Biological oxidation, particularly that which occurred during burning, was an equally important determinant of subsidence but it was a poor parameter for estimating subsidence. In addition their study stressed the need for appropriate methods for characterizing peat soils.

Hooijer *et al.* (2008) have taken very few measurements of peat subsidence in Ex-MRP in Central Kalimantan, Indonesia. Available measurements suggested a subsidence rate in highly decomposed (sapric) peat and degraded peatland well away from canals with relatively high groundwater tables of at least 1cm/y. Rates will be higher where peat is less decomposed, unburnt or has lower groundwater tables. Furthermore, no relation was found between subsidence and average groundwater depth while they found an apparent relation between subsidence and minimum groundwater depth and they suggested that the average groundwater depth is probably a poor descriptor of the soil moisture regime that controls peat decomposition and subsidence.

3.9 Estimation of carbon emissions

The CO₂ sequestering function of peatland ecosystems is threatened by drainage and land use change that leads to organic matter oxidation and increased emission of greenhouse gases (Couwenberg *et al.*, 2010). This problem is particularly acute at the present time on tropical peatland in Southeast Asia where fires on natural and degraded

peatlands result in a rapid release of large amounts of CO₂ to the atmosphere, contributing to global climate change processes (Page *et al.*, 2002). Recent climate model simulations suggest there will be a rise in mean global surface air temperature by about 0.2 °C per decade over future decades owing to the increasing concentrations of greenhouse gases (mainly CO₂) in the atmosphere, resulting primarily from fossil fuel use and land use changes (IPCC, 2007). Therefore, recognition of tropical peatlands, monitoring impacts upon them and restoring degraded peatlands to as near their former natural condition as possible are not only of regional but also of global importance.

To quantify the role of peatland fires in the release of carbon, it is important to know how much of the peat layer is consumed by a fire. Since most peatlands in Indonesia are highly inaccessible, very few field measurements have been made to date, as this would require either knowing the fire affected area in advance or igniting peatland on a larger scale intentionally. Due to these constraints, previous peat fire carbon emission estimates were based on a very limited number of spatially non-representative field samples (Ballhorn *et al.*, 2009). Carbon emissions from drained tropical peatlands (other than from fires) have received limited attention in analyses of emissions from land use and forestry. There is the difficulty of obtaining an estimate of CO₂ losses from the drained soil. The problem arises from the fact that not all CO₂ released from the peat is a result of oxidative wastage. There are two major sources of carbon dioxide emissions from the peat surface: root respiration and breakdown of organic matter. The first process occurs under all conditions, in every landscape covered by living vegetation. The rate of the second process is increased when peat is not saturated with water and it occurs at high rates especially in drained peatlands. Distinguishing between the two processes is difficult as it requires exclusion of vegetation roots and few studies

to date that have truly achieved this (Hooijer *et al.*, 2010). Hooijer *et al.* (2010) apply peat surface carbon dioxide emission detection method based on infra-red gas analysis for instantaneous measurement of carbon dioxide concentrations from peat surface with instantaneous readouts. They concluded that peat decomposition emissions in Acacia plantations in Sumatra are in the range of 50 to 100 t/ha/y, and root respiration emissions around 50 t/ha/y.

A study carried out by Page *et al.* (2002), in Central Kalimantan, Indonesia, found that the CO₂ emissions due to peat fires in Indonesia in 1997 was between 810 and 2470 Mt. This number is supported, amongst others, by the fact that 1997 has had the largest annual jump in global atmospheric CO₂ on record. They also found that the minimum average CO₂ emission of 1418 Mt/y and a maximum of 4324 Mt/y.

Ballhorn *et al.* (2009) estimated that within the 2.79 million hectare of burned area determined from satellite imagery, between 26.81 to 49.15 megatons of carbon were released during the 2006 El Niño episode. This represented 10–33% of all carbon emissions from transport for the European Community in the year 2006. These emissions, originating from a comparatively small area (approximately 13% of the Indonesian peatland area), underlined the importance of peat fires in the context of green house gas emissions and global warming.

Hooijer *et al.* (2010) presented the first geographically comprehensive analysis of CO₂ emissions from the decomposition of organic matter from drained peatlands in Southeast Asia with particular reference to lowland peatlands. Present and future emissions from drained peatlands were quantified using data on peatland extent and peat thickness, present and projected land use, water management practices and

decomposition rates. The estimation of the carbon dioxide (CO₂) emissions resulting from drainage of lowland tropical peatland was between 355 Mt/y and 855 Mt/y in 2006 of which 82% came from Indonesia, largely Sumatra and Kalimantan. They also indicated that if current rates and practices of peatland development and degradation continue, CO₂ emission is expected to peak at 745 Mt/y in 2015.

3.10 Summary

This chapter shows that peat subsidence has been occurred mainly through fire and drainage which had taken place in Central Kalimantan, Indonesia. The relationships between peat subsidence, water table depth and CO₂ emission have been illustrated. Measuring peat soil subsidence is very difficult to achieve in tropical swamp areas due to vegetation and forest barriers and it is usually calculated using manual methods. Remote sensing imaging system has been shown to be a good tool to differentiate burnt and deforested forest from healthy forest.

Chapter 4: Materials and Methods

4.1 Introduction

This section presents the study area and the methodological approach used to generate coherence images, digital elevation models and displacement maps in two different areas in Central Kalimantan, Indonesia. The methods were chosen based on a review of relevant published methods, data type and availability.

4.2 Study area

Indonesia is spread across a chain of thousands of islands between the Indian Ocean and the Pacific Ocean in Southeast of Asia with a total area of 1.9 million square kilometres and a population of 225 million. The climate is tropical, hot and humid and 67% of the land is forest and woodland (The World Fact Book, 1995). Borneo is the largest island (539,460 square kilometres) in the Malaysia-Indonesia region (Figure 4.1). The region has a humid tropical climate, with high temperature and precipitation. Central Kalimantan is the biggest province on the island, covering 153,800 square kilometres (Figure 4.1).

The total peatland area in South East Asia is calculated at 271,000 km². Indonesia alone has 12 % of its land area as peatland, which is 83% of the SE Asian peatland area. Peat thickness in Indonesia (Sumatra, Kalimantan and Papua) ranges from less than 1 metre to over 12 m. It is estimated that 42% of the peatland area in Indonesia is over 2 m thick and these thicker peat deposits store 77% of the total peat deposits (Hooijer *et al.*, 2006). It is expected that a similar distribution applies for the remaining peatlands of SE

Asia. Average peat thicknesses in Malaysia and Brunei are estimated to be 3 m (Gorham, 1991; Immirzi *et al.*, 1992).

The research was carried out in two regions within the area of the former Mega Rice Project (Ex-MRP) in Central Kalimantan, Indonesia, that was launched through Presidential Decree No. 82/1995 on 26th December 1995. Roughly two-thirds of Ex-MRP area (927,000 ha) consists of peatland. Almost half of the peat area is over 3 m deep (447,000 ha) and in some places up to 11 m deep (Hooijer *et al.*, 2008). The purpose of the Ex-MRP was to develop wetland, mostly peatland, for rice crop production. The Ex-MRP covers an area of 1.5 Mha that is bounded by S. Sebangau in the west, Java Sea in the south, S. Barito in the east and the Main Parent Channel in the north. Therefore, the project area has been divided into five Blocks (Figure 4.1). Part of this area, called Block C, is located between Sebangau River in the west and Kahayn River in the east. The other part of Block A is located in the north of Kapuas city, the second largest city in Central Kalimantan province.

A macro-network of drainage and supply canals was designed to improve water management conditions. Construction of the canal system resulted in a 187 km long main canal connecting the Barito River (at Mangkatip) and the Kahayan River (near Palangka Raya) and 958 km of primary canals in Block A, B, C and D (Figure 4.1). In Block A, an additional 973 km of secondary canals, 900 km of tertiary canals and 1515 km of quaternary canals were constructed. Drainage interventions in the Ex-MRP over the last decade have not considered the vulnerable nature of peatland but have led to forest clearance, fire, over-drainage and subsidence and as a result are clearly

unsustainable. Fires in the Ex-MRP area have contributed to regional haze problems and carbon emissions that contribute to climate change (Hooijer *et al.*, 2008).

Two test sites were selected in Block C, and Block A respectively to generate DEM and analyze DEM accuracy (Figure 4.2). The first test site (29 x 24 km) is located in the south of Block C near Maluku village on the right bank of the Kahayan River. Soils are mainly (potentially acid) mineral soils and shallow peat. The soil and water conditions are poor, acid, and drainage and water circulation is insufficient. This site was chosen due to forest fires that have burned down millions of hectares of natural forest in 1987, in 1991 and in 1994. Very large scale fires blazed throughout Indonesia during the second half of 1997 and in the first months of 1998 and hundreds of thousands of square kilometres of peat swamp forests were burned and a lot of peatland was lost.

The second test site (30 x 19 km) was chosen in the north western part of Block A in the north west of Dadahup village. During the 1970s and 1980s large-scale government-sponsored transmigration to this area occurred by opening up the swamp interior, as the riverbanks were already occupied. The transmigrants, mainly of Javanese origin, did not have prior experience in the management of tidal lands, (potential) acid sulphate soils and organic soils. The hydraulic design of the Ex-MRP transmigration sites in Block A is based on improved concepts of drainage, leaching and flushing and includes double connected canals and structures to improve the circulation of water. Dadahup is facing flooding from the Barito River as the supply canals established by Ex-MRP were crossing elevated peat domes in a complex hydrological environment between the non-tidal Barito and the (semi) tidal Kapuas Rivers. Heavy drainage and clearing activities were carried out over this area to develop wetland, mostly peatland, and convert

thousands of hectares of wetland to rice cultivation to support nearly a quarter of a million families. Although the forest was harvested selectively, in many areas logging has left severely degraded forests with little prospect of natural recovery. Many of the naturally abundant tree species have disappeared, and large areas are dominated by shrubs and a dense ground cover of ferns and sedges as a result of over-exploitation and subsequent fires.

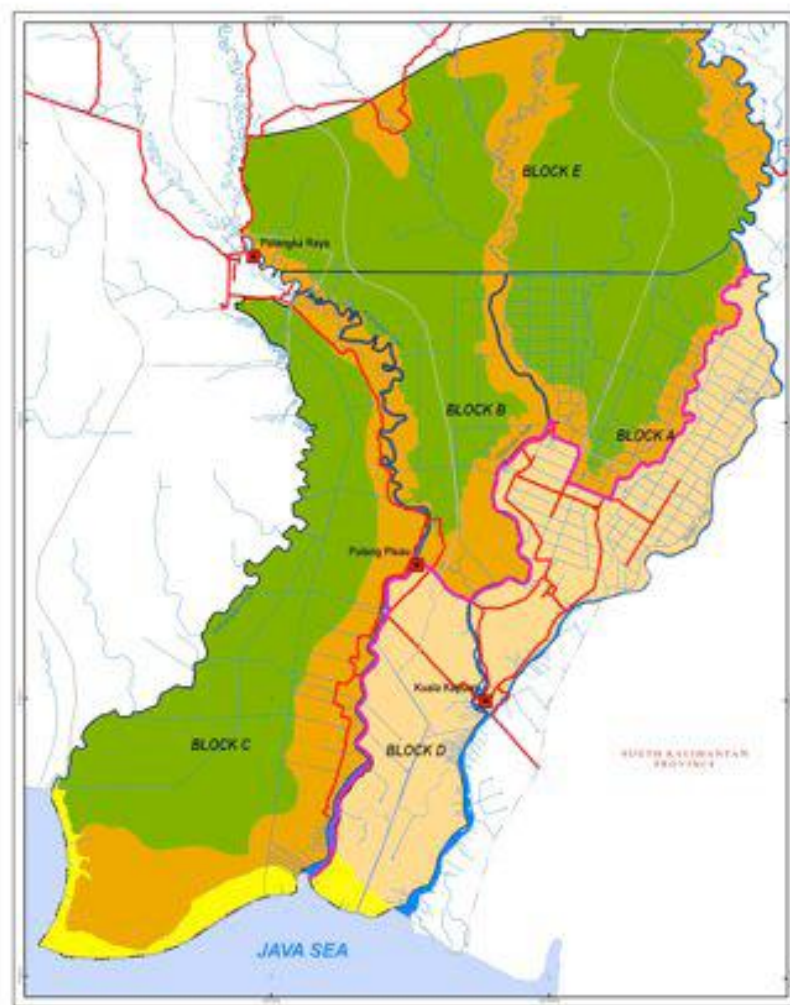


Figure 4.1: Situation of the Ex-MRP area (Hooijer et al., 2006).

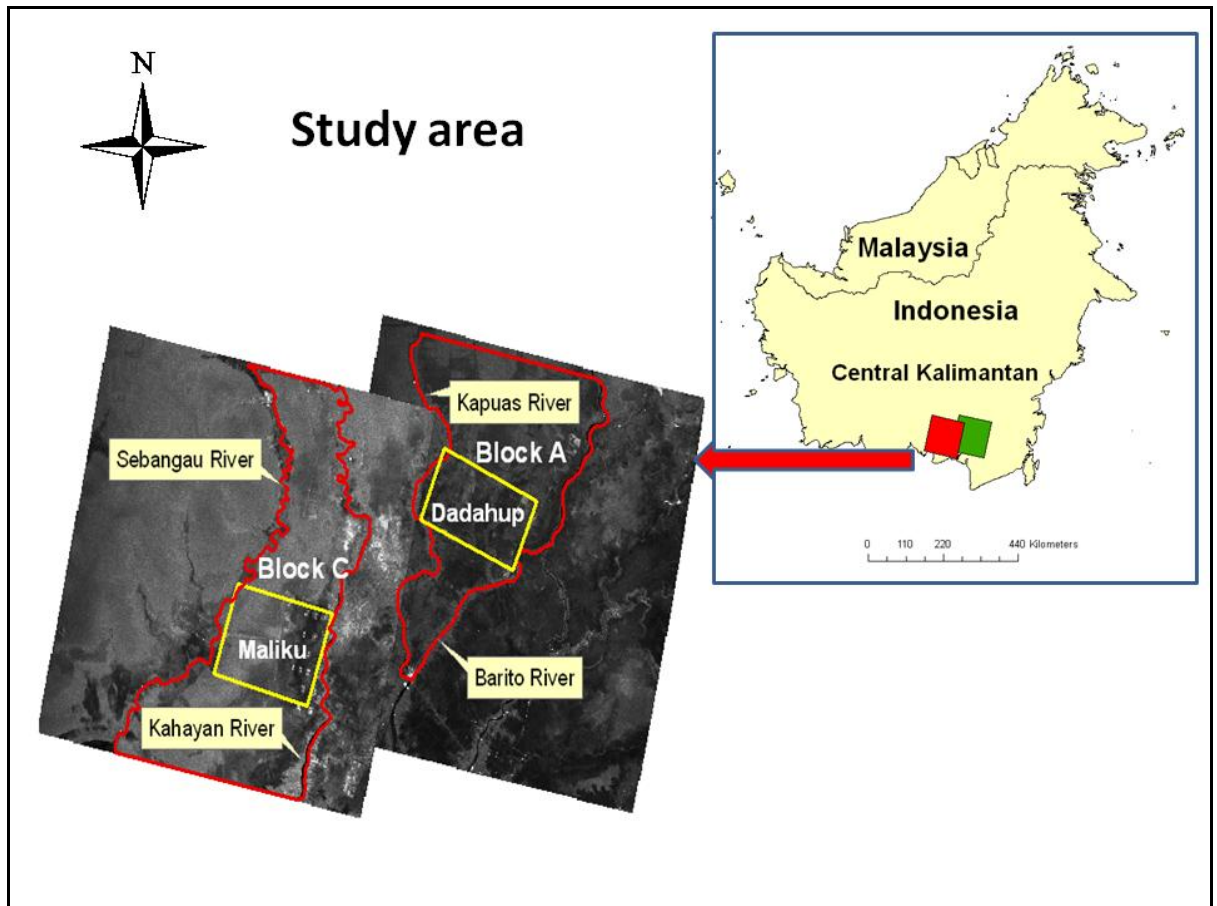


Figure 4.2: Location of the study area: Block C and Block A (boundary indicated by a red line) in the context of Ex-MRP area. The two study areas (Maliku, Dadahup) are overlaid on ERS image.

4.3 Source data and software

4.3.1 InSAR data

The primary sources of available data for analysis in this paper were from the European Space Agency (ESA). Fifty two ERS-1 and ERS-2 SAR data were acquired over Central Kalimantan from March 1996 to December 2000 covering six frames as is shown in Figure 4.3. Only 14 ERS images were chosen in this study covering frame 4 and frame 6 which covers the Ex-MRP area. To analyse coherence, height and subsidence changes, eight images in frame 4 were acquired at the beginning, during and after the fire season between March 1996 and January 2000 (113.614° E to 114.263° E; -2.188° N to -3.380° N), whilst six images acquired between April 1996 and January

2000 were used to evaluate deforestation rate in Frame 6 (114.316° E to 115.181° E; - 2.188° N to -3.339° N).

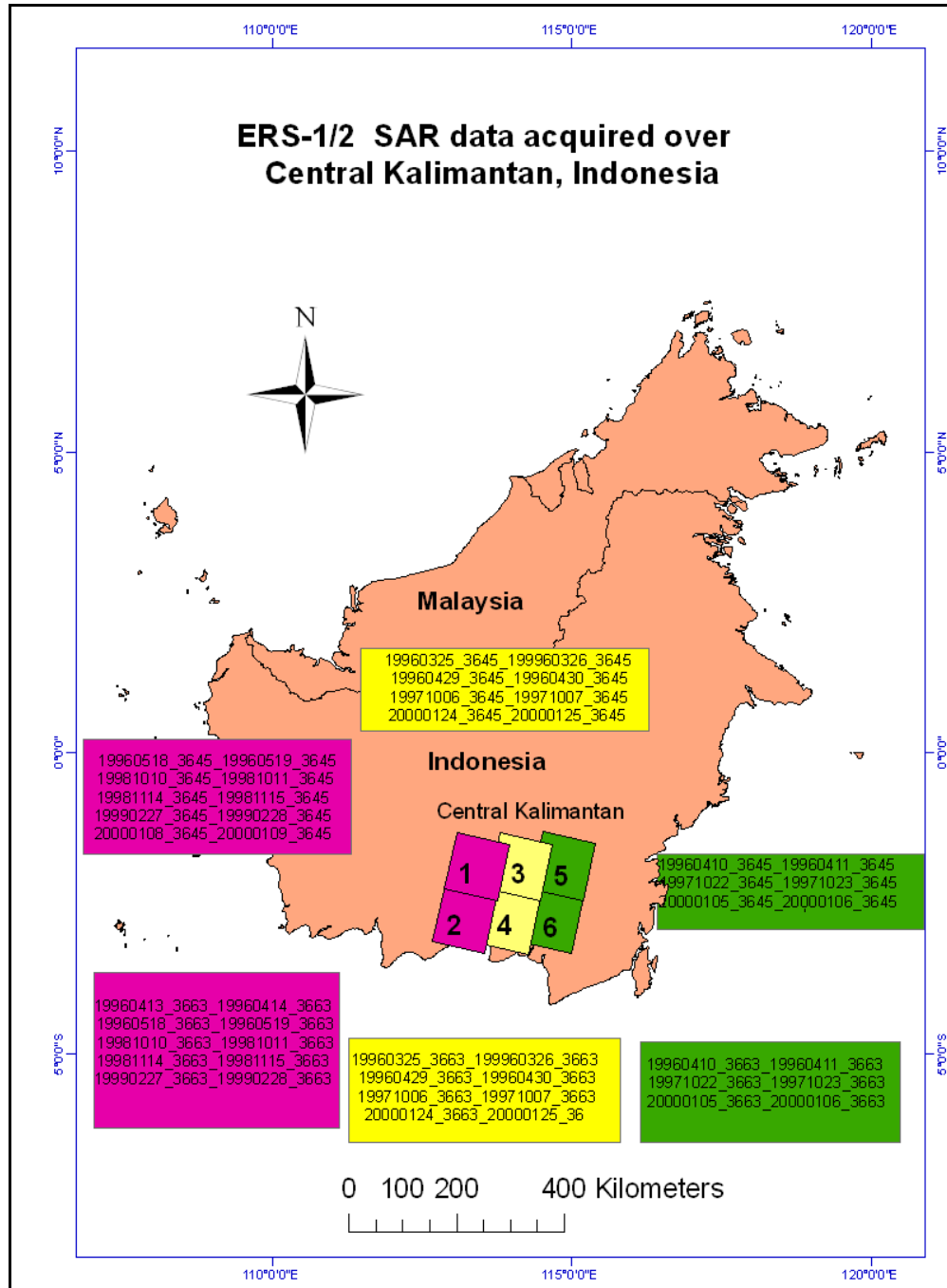


Figure 4.3: Available ERS images in the south of Central Kalimantan. Frame 4 and Frame 6 have been used further in analysis.

The ESA first sun-synchronous polar-orbiting mission, ERS-1 made 45,000 orbits, acquiring more than 1.5 million individual Synthetic Aperture Radar (SAR) scenes. From launch On 17 July 1991, until the satellite's retirement on 10 March 2000, ERS-1 monitored the study area almost continuously. The accuracy of its altimeter range measurements has been estimated to be a little less than 5 cm. ERS-2, the successor of ERS-1, was launched on 21 April 1995. Until the retirement of ERS-1 the satellites orbited in the same orbital plane, with all instruments simultaneously operating. ERS-2 is similar to ERS-1 and carries very similar instruments, with the addition of the GOME instrument (MIMAS, 2007). With respect to the Earth, the ERS-1 and ERS-2 satellites go through 35-days cycles of orbits which mean that the satellite returns to the same position every 35 days (Dow *et al.*, 1996).

The tandem operation of ERS-1 and ERS-2 satellites is the first space mission aimed at SAR interferometric coverage on a global scale and with a short temporal baseline (Rufino *et al.*, 1998). During tandem operation, the two satellites fly in the same orbital plane at the same mean altitude and the orbit phasing is adjusted to make ERS-2's ground track be coincident with that of ERS-1 24 h earlier. As a consequence, any point on the ground can be revisited after one day and re-observed in strip mode under identical conditions such as altitude, incidence, local time, etc (Duchossois and Martin, 1995). The availability of tandem data certainly deserves great interest because several authors have pointed out the need of spaceborne missions for global topographic mapping by means of SAR interferometry and the problems connected to accurate digital elevation model (DEM) production when temporal decorrelation effects are significant (Zebker and Villasenor, 1992).

By examining the data in Table 4.1, it is clear that there is only a one day difference between the two acquisitions of the ERS-1/ ERS-2 pair. This small temporal difference gives advantages of high coherence, good height accuracy and low sensitivity to show land deformation.

Table 4.1: List of ERS tandem data used in this study.

Area	Sensor	Date	Track	Orbit	Frame	Parallel baseline	Perpendicular baseline
Frame 4	ERS1	19960325	003	24540	3663	-50	-109
	ERS2	19960326	003	04867	3663		
	ERS1	19960429	003	25041	3663	-53	-98
	ERS2	19960430	003	05368	3663		
	ERS1	19971006	003	32556	3663	194	383
	ERS2	19971007	003	12883	3663		
	ERS1	20000124	003	44580	3663	58	209
	ERS2	20000125	003	24907	3663		
Frame 6	ERS1	19960410	232	24769	3663	-46	-87
	ERS2	19960411	232	05096	3663		
	ERS1	19971022	232	32785	3663	96	370
	ERS2	19971023	232	13112	3663		
	ERS1	20000105	232	44308	3663	59	204
	ERS2	20000106	232	24635	3663		

4.3.2 GPS observations

A field survey was conducted in July 2009 in order to acquire ground truth points. Differential GPS (DGPS) measurements were provided by two Leica SR20 GPS receivers. The SR20 GPS receiver can be used as a high accuracy land surveying device, a powerful GIS data collector, or even a reference station. When collecting real-time data, the line of sight to the satellites can be blocked or a satellite can be so low on the horizon that it provides only a weak signal, which causes spikes in the data. Reprocessing real-time data removes these spikes and allows real-time data that has been used in the field for navigation or viewing purposes to be made more reliable before it is added to a GIS. The files from the base and rover are transferred to the Leica Geo Office software, which computes corrected positions for the rover's file compared to reference station (static). For this measurement, ground control points (Figure 4.4) were divided into two sets of points, the first used as ground control points to calibrate the generation of DEMs during the processing steps (17 points in Frame 4 and 39 points in Frame 6) and the second set of points are independent check points (100 points) for accuracy assessment of the DEM after the processing steps are complete. Most of DGPS points were collected from the roads and stable areas (Figure 4.5) where the heights have not changed between the time of image acquisition and the time of field data measurement.

The distribution of DGPS points was not perfectly distributed in terms of covering most of the study area, due to accessibility problems. Many areas were unreachable due to forest, heavy plantation or bad infrastructure facilities in the area. The reference station crashed many times during the work due to high temperature and the data was lost and

could not be corrected. However, the area where the signal and accessibility were available resulted in hundreds of static points and thousands of rover points.

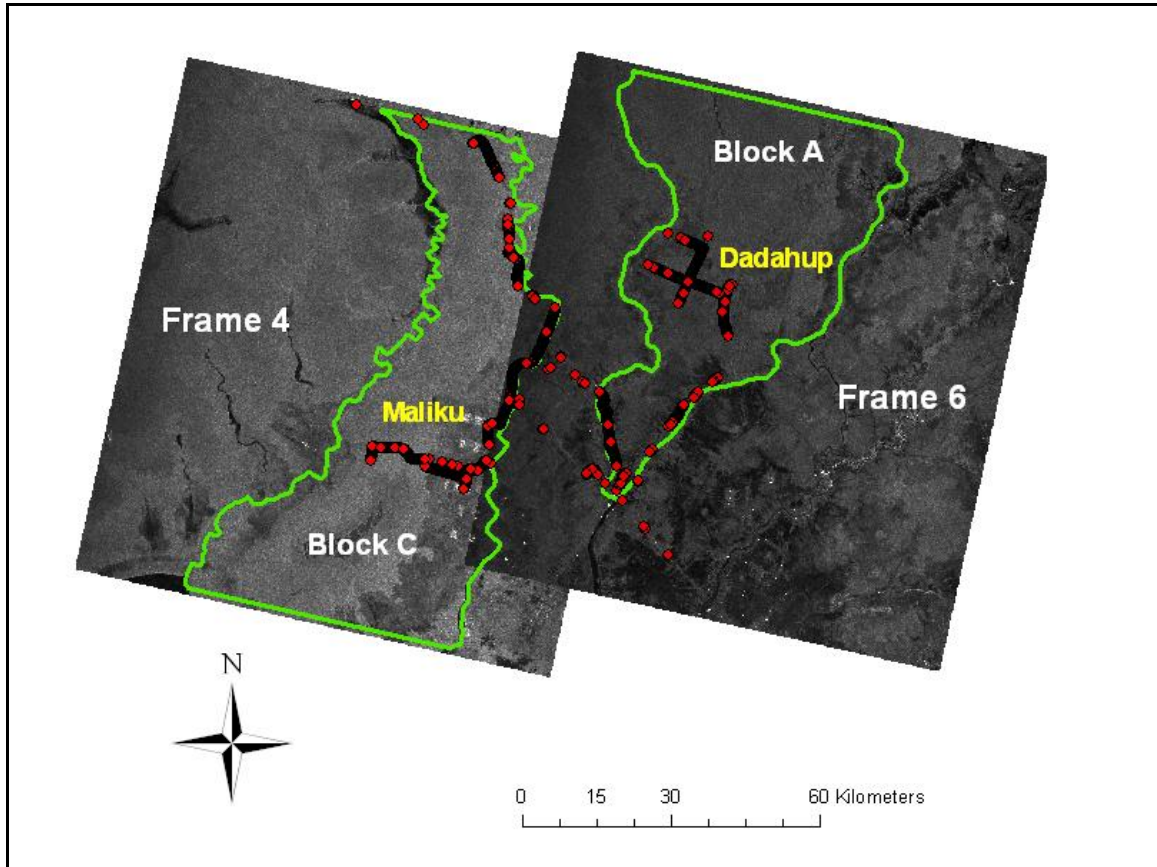


Figure 4.4: The distribution of DGPS points in the study area.



Figure 4.5: DGPS field work collection.

4.3.3 Burn area detection by optical remote sensing data

Burn scar areas were detected by Hoschilo (2009) using a time series of satellite images obtained from several sensors, including the Landsat MSS, TM, and ETM+. The Tropical Ecosystem Environment Observation by Satellite (TREES) classification scheme was used to classify the land cover area and extract burn scars for the fires that occurred in Block C in Ex-MRP, which is located in the south and south east part of Central Kalimantan, Indonesia.

4.3.4 Software environment

Gamma software, a product of GAMMA Remote Sensing and Consulting AG, supports the entire processing from ERS raw data to products such as DEMs, displacement maps and coherence maps (Wegmüller and Werner, 1997a). GAMMA conducts SAR and interferometric processing, which is adapted for ERS-1/2, SIR-C/X-SAR, RADARSAT, ENVISAT ASAR (Gamma, 2007). ArcGIS 9.2 software by Environmental Systems Research Institute (ESRI) and ERDAS 9.1 software were used for further analysis.

4.4 Data processing

4.4.1 Co-registration

Raw data were processed and transformed into a Single Look Complex (SLC) image format by ESA before distribution of SLC images. The entire InSAR process is outlined in Figure 4.6. The first part shows the processing of registration which consists of computation of offsets in range and azimuth between the two SLCs by generating an offset parameter file, using the Gamma program called *create_offset* (programs are thereafter shown in italic). Initial offsets are calculated as a process of guiding the precise estimation of the offsets.

The offsets between the SLC images can be computed by using either orbit data or correlation of images or by intensities or fringe visibility. These offsets can be computed by using two steps; estimation of the local offsets for a number of small areas throughout the image and generation of a polynomial that allows the resampling of the slave image to match with the reference image. Based on the estimated vectors, the 2d-polynomial model of required degree of correlation is computed. The least square method is used to determine the final solution. A high quality co-registration can be achieved by having sufficient tie-points. Sometimes, the number of tie-points automatically generated by the Gamma program is sufficient (Ge *et al.*, 2003).

To compute offsets between the two images, several programs are available depending on whether an initial estimate or a precise estimate has to be computed. Two programs were used to calculate the initial estimation of offset; *init_offset* and *init_offset_orbit* and both programs compute a constant offset in range and in azimuth. *init_offset* uses cross-correlation between two images extracted from the SLCs to determine the initial estimate of the offset (Gamma, 2008a).

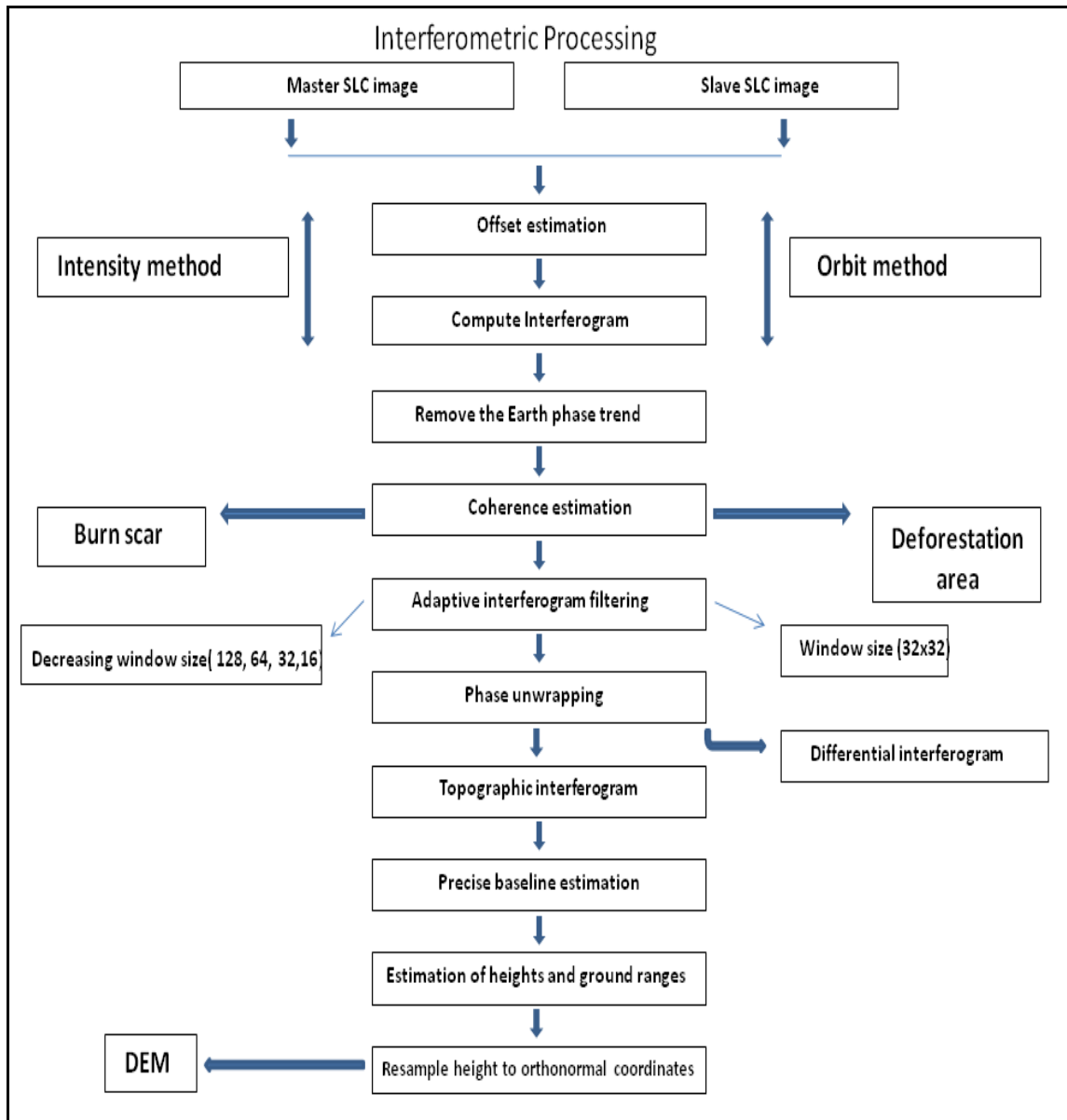


Figure 4.6: Schematic of steps in processing SAR data for interferometric applications.

The correlation signal-to-noise (SNR) was given a value (7.0) which is the default value in Gamma software. SNR provides a measure of the confidence in the offset estimate. If the SNR is greater than 7.0, this indicates a co-registration of better than 1 pixel between the two images to be co-registered (Gamma, 2008a). *Init_offset_orbit* uses the orbital information in the state vectors provided with the images and it is recommended to be used in the case of large registration offsets or any kind of problems with the

registration. With *init_offset_orbit* a first guess of the offsets can be obtained based on orbital information. This first guess can then be improved with *init_offset* which determines the initial offsets based on the cross-correlation function of the image intensities (Gamma, 2008a). The fringe visibility offset method was not good enough to create interferograms for many SLC images and therefore it was not used in this study.

A field of estimates of the offsets can be obtained with *offset_pwr* which considers the cross correlation of the real valued image intensity and is known as intensity tracking. For a large number of image segments, this method searches for the range and azimuth offsets resulting in the maximum level of intensity correlation. The method requires at least a minimum of image contrast. It does not depend on the level of coherence between the two SLC images and is computationally efficient. The more important parameters for the search are number and size of the offset estimation windows in range and azimuth, and the offset estimation threshold. In the method, the general values that have been used are illustrated in Table 4.2

Table 4.2: General value of offset estimation used in Gamma software (Gamma, 2008a).

offset_estimation_range_samples	32
offset_estimation_azimuth_samples	32
offset_estimation_window_width	64
offset_estimation_window_height	64
offset_estimation_threshold	7.0

4.4.2 Interferogram calculation

The complex interferogram is obtained using two different approaches. The first approach is implemented in the program *interf_SLC* which calculates the normalized interferogram and the registered intensity images from the two (non-registered) SLCs (Gamma, 2008a). This approach will be called the intensity method because it used the offset calculated by employing correlation of image intensities. The main advantages of this method are the lower disk space used and the higher computational efficiency achieved by the combined application of the interpolation and spectral filtering in one step.

The second method provides a simple way to register multiple SLC to the same geometry using a program called *SLC_interp*. Then the two co-registered SLCs are used to create the interferogram by the program called *SLC_intf*. This approach is called the orbit method because it benefits from the offset calculated by using orbit data. The advantage of using this approach is that the co-registered SLC is saved to a file and therefore can be compared to the reference SLC.

The result of the two approaches is an interferogram that consists of magnitude and phase. The visibility of fringes represents the correlation between the two images and indicates how accurate the phase information is. If the correlation is low then the phase is noisy. The InSAR phase is a combination of several contributions such as curved earth, topography, surface displacements, atmospheric delays and phase noise shown in equation 4.1:

$$\Phi = \Phi_{\text{flatEarth}} + \Phi_{\text{topography}} + \Phi_{\text{displacement}} + \Phi_{\text{delay}} + \Phi_{\text{noise}} \quad (4.1)$$

The InSAR phase has values between 0 and 2π which means the phase is wrapped in this interval.

4.4.3 Initial baseline estimation

The next step is to determine an estimate for the baseline. Estimation of the baseline is required for a number of operations: common band filtering, flattening of the interferogram, phase unwrapping and derivation of interferometric heights from the unwrapped phase. The baseline, which is the distance between the two SAR antennas in space when they image the same object on the ground, is difficult to measure because it requires perfect knowledge of the satellites position and altitude as they travel along their orbit. The baseline can be decomposed into components. A reference system is the local coordinate system called TCN (Track, Cross-track, and Normal) coordinates. The parallel baseline is the component along the radar's line of sight, whilst the perpendicular baseline is the component perpendicular to the line of sight (Gamma, 2008a). The baseline can be estimated using three methods; the orbit state vectors, the SLC registration offsets and the interferogram fringe rate.

Two programs were used to estimate the baseline. The first program *base_orbit*, which calculates the baseline from the orbital information, has been used in the orbit method. The second program *base_init*, has been used for the intensity method and includes the first program as well as another method, estimates the baseline from the fringe rate of the normalized interferogram using Fast Fourier Transform (FFT).

4.4.4 Interferogram flattening

Flattening of the interferogram consists of removing the phase component due to the variation of the range distance across the image ($\Phi_{\text{flat Earth}}$) and leaving fringes only related to changes in elevation, noise, atmosphere and surface displacement. This operation assumes the surface of the earth to be curved (ellipsoid) without topographic features. Flattening is performed by computation of the fringe rate across the images in order to take into account the variations of slant range distance, incidence angle and the perpendicular component of the baseline. This is done in order to facilitate consecutive filtering, averaging and phase unwrapping. The phase trend can be removed from the interferogram using the program *ph_slope_base*. It generates a phase trend using a spherical earth and a baseline model. The generated phase is then subtracted from the original interferogram (Figure 4.7).



Figure 4.7: Interferometric phase of the ERS-1/2 tandem image pair over Frame 6 after flattening with backscatter intensity as background.

4.4.5 Coherence estimation

Coherence was used to estimate how much two SAR images are correlated with each other. It represents the similarity of two complex SAR images and defined as the magnitude of the complex correlation coefficient (Haynes, 2007). Coherence is estimated using the program *cc_wave* (Figure 4.8). The size of the estimation window is a crucial factor determining the coherence estimate. In areas of low coherence, Wegmüller *et al.* (1998) suggested larger estimation windows. For increasing window size, the estimation bias, estimation uncertainty and spatial resolution of the coherence image decreases. Four search windows (3x3, 5x5, 7x7, and 9x9) have been used in this study in order to detect burn scar areas in Block C and clearing area in Block A. The results of different search windows were compared in order to choose the most accurate estimation and spatial resolution.

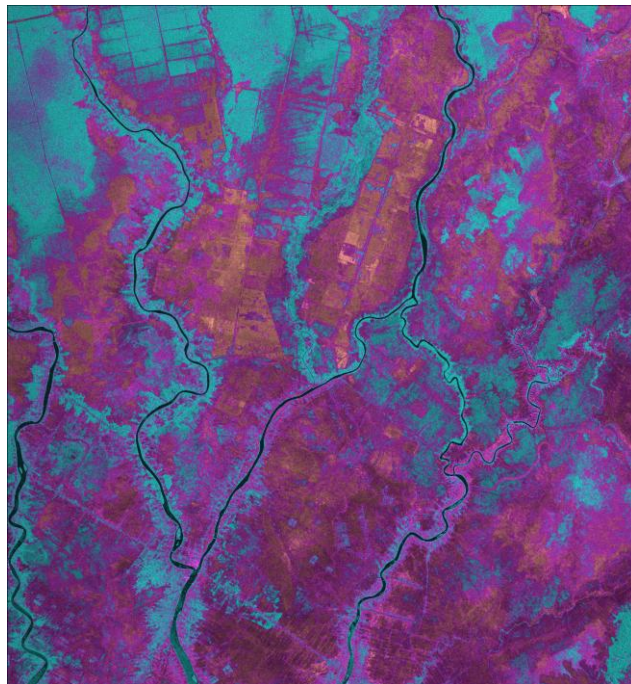


Figure 4.8: Coherence image derived from ERS-1/2 tandem pair acquired 22/23 October 1997 with backscatter intensity as background. Raspberry colour shows high coherence and Turquoise colour shows low coherence.

To decrease the effect of resolution loss due to the windowing operation, weighting functions can be applied within the window. In this way, pixels further away from the centre of the window have less weight on the estimate. Four magnitude weighting functions (constant, phase only, Gaussian and triangular) have been applied for coherence estimation. The coherence obtained by these function have been analysed in order to choose the best weighting functions for this study.

The results of the backscatter analysis suggested that the most suitable image pairs for burned scar and clearing identification were the ones with both images acquired under dry weather conditions, where differences between burned and unburned areas were most pronounced (Siegert and Ruecker, 2000). In this study, just one pair was taken in dry weather, whilst other pairs were acquired in the wet season. To eliminate the impact of seasonal effects on land cover change, the two image pairs for burned area and deforestation area have been chosen from the same seasonal condition which is the wet season.

After choosing the search window and weight function, the coherence was classified into two classes: coherence values more than or equal to 0.35 and less than 0.35. This value has been chosen as the best fit of coherence values to differentiate burn scars that have been identified by optical data from other forest areas. This classification depends on assumptions that the high coherence in tropical swamp forest should not be more than 0.35. To identify the burn scar area in Block C, two coherence images have been used, the first one represents the coherence in March 1996 before the big fire in 1997

and the second image was obtained from January 2000 after three years of the occurrence of fire. To identify the burn scar area, the similar height coherence (more than 0.35) in both coherence images was excluded from the calculations and only height coherence in 2000 were chosen. These results were compared with burn scar areas that have been mapped by optical data for the same area. The same technique was applied to Block A to identify clearing areas between April 1996 and January 2000.

Another approach was used to identify the change of land cover in Block C and Block A due to fire and heavy drainage activities. In each study area, the coherence before these activities had been subtracted from the most recent coherence (2000). This approach allows the user to notice the degree of change in coherence between two periods and applies this change as a parameter for further studies. The results from these two approaches were compared with optical data results.

4.4.6 Interferogram filtering

Filtering an interferogram has the objective to reduce phase noise, thereby reducing the number of residues and therefore making the phase unwrapping simpler, more robust and more efficient. In the design of the filter function, it should be considered that the interferometric phase cannot be assumed to be constant across the filter window.

One way of filtering that has been used in this study is multi-looking the complex interferogram. Multi-looking the interferogram reduces the standard deviation of the interferometric phase. Multi-looking in range (2-looks) and azimuth (10-looks) is applied in the interferogram computation. The main advantages of multi-looking are highly effective reduction of the phase noise, increased efficiency and the ability to

unwrap very large data sets, with the last two resulting from the reduction of the data set sizes. The main limitation of multi-looking is that the reduction in the sampling may cause under-sampling in the case of higher phase gradients. Consequently, multi-looking is generally more appropriate for relatively smooth phase surfaces.

Adaptive filtering is the second method that has been used for filtering the InSAR phase. The aim of the adaptive filtering step is to reduce phase noise thereby reducing the number of residues without losses in spatial resolution (Gamma, 2008a). The adaptive filtering program *adf* is based on local fringe spectrum (Figure 4.9). It reads the complex valued interferogram, computes locally the interferogram power spectrum, designs a filter based on the power spectrum, filters the interferogram, estimates the phase noise coherence value for the filtered interferogram and writes out the filtered interferogram and coherence map. Estimation of the local fringe quality after filtering is necessary for the phase unwrapping method.

To estimate the effect of filtering on phase unwrapping, adaptive filtering was applied for the two methods mentioned above (intensity, orbit). The program ran several times with a smaller coefficient and decreasing window size (128, 64, 32, 16) and the results were compared with interferograms that have been filtered using only one window size of 32. The terms ‘intensity adaptive filtering’ and ‘orbit adaptive filter’ will be used further to refer to interferograms that have been generated by running the filtering several times with decreasing window size (128, 64, 32, 16) and can be distinguished from other interferograms, which have been filtered only by one run using a (32x32) window search size. At this point of the processing, the programs that have been used are listed in Table 4.3.

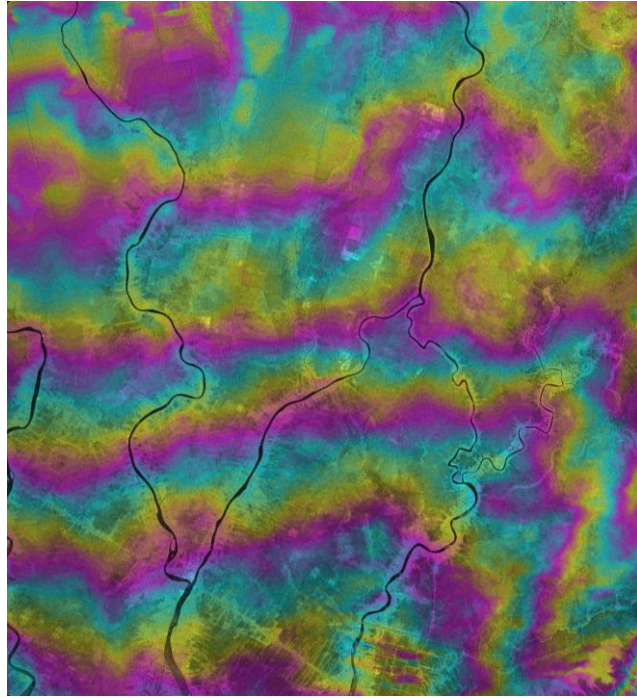


Figure 4.9: Flattened and filtered interferometric phase and intensity for the ERS-1/2 tandem image pair.

Each individual fringe is displayed a complete colour cycle from blue to green.

Table 4.3: Programs of Gamma software used in the two different approaches.

	Intensity method	Orbit method
offset parameter file	create_offset	create_offset
initial offset estimation	init_offset	init_offset_orbit
Offsets estimation	offset_pwr,offset_fit	offset_pwr,offset_fit
Compute interferogram	interf_SLC	SLC_interp, SLC_intf
Initial baseline estimation	base_init	base_init
flattening	ph_slope_base	ph_slope_base
coherence estimation	cc_wave	cc_wave
adaptive filtering	adf	adf

4.4.7 Phase Unwrapping method

The next step is the Phase Unwrapping method. Since the interferometric phase is wrapped modulo 2π , an integer number of 2π has to be added to recover the absolute phase difference. This can be done by adding a correct multiple of 2π to the interferometric phase for each pixel in order to obtain sequential phase values across the entire image. The fundamental assumption implicit in the phase unwrapping procedure is that the surface is relatively smooth and hence there should be an absence of jumps of the unwrapped phase, which means that phase differences are smaller than π between adjacent samples. The actual phase jumps do occur for many reasons such as phase noise, phase undersampling and phase discontinuities.

Two approaches have been used in this study and are supported by Gamma software. The first method is based on the Branch Cut (BC) region growing algorithm. This method detects inconsistencies in the phase data, which cause errors in phase unwrapping. Critical areas such as areas of very low coherence or residues are identified and avoided in the phase unwrapping since the phase values are inaccurate and not useful for estimation of heights or displacements. The branch Cut algorithm consists of the following steps; masking low correlation areas, generation of neutrons to exclude regions of layover by generation of dense cuts, determination of residues, connection of residues through neutral trees, and unwrapping of interferometric phase. These steps and programs that have been used are illustrated in Table 4.4. Unwrapping can be continued in areas that have been disconnected from the already unwrapped areas by construction of bridges between disconnected regions and then unwrapping disconnected areas.

Table 4.4: Branch Cut unwrapping steps and programs.

Processing steps	Program
Masking low correlation areas	corr_flag
Masking neutron areas	neutron
Determination of residues	residue
Connection of residues through neytral trees	tree_cc
Unwrapping of interferometric phase	grasses

The second method uses Minimum Cost Flow (MCF) techniques and a triangular irregular network (TIN) (Figure 4.10). This approach is a global optimization technique to the phase unwrapping problem. The gaps in input data such as very low coherence areas are considered. This method consists of the following steps; generation of phase unwrapping validity mask, adaptive sampling reduction for validity mask, unwrapping of interferometric phase, weighted interpolation to fill gaps in unwrapped phase image and use of interpolated unwrapped phase as a model to unwrap the initial interferogram. The basic sequence and related programs are shown in Table 4.5.

Table 4.5: MCF unwrapping steps and programs.

Processing steps	Program
Generation of phase unwrapping validity mask	rascc_mask
Adaptive sampling reduction for validity mask	rascc_mask_thinning
Phase unwrapping algorithm	mcf

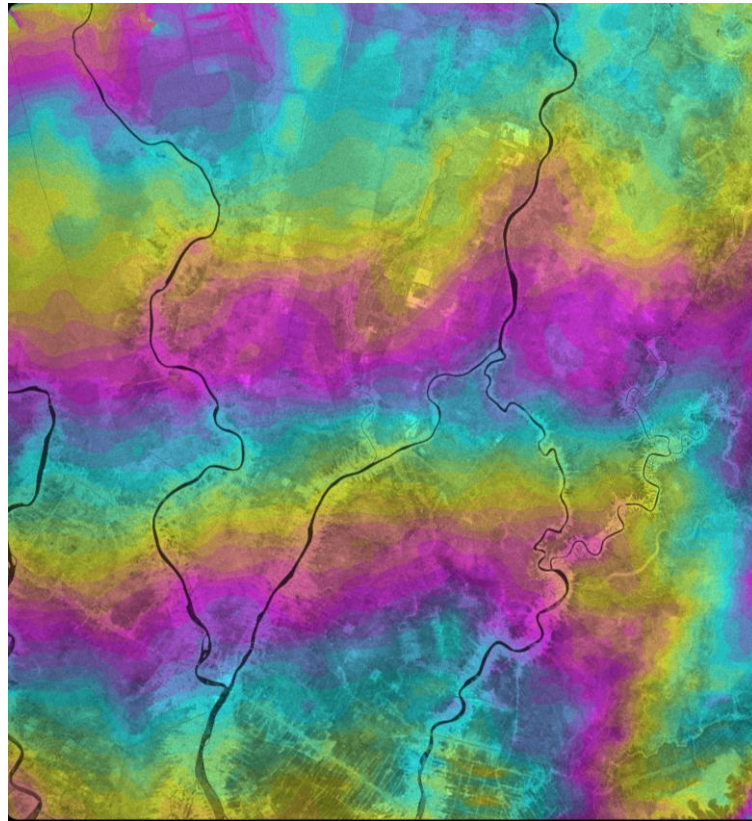


Figure 4.10: Unwrapped phase for the ERS-1/2 tandem image pair using MCF method with backscatter intensity as background. Phase displayed as 6π per colour cycle.

4.4.8 Precise baseline estimation

The baseline information should be accurate if the unwrapped phase is to be used for the derivation of a height map. A first estimate of the baseline was done using orbit data or the average interferogram fringe frequency. The first estimate was sufficient for the subtraction of the curved earth phase trend carried out to facilitate the filtering of the interferogram and the coherence estimation. This estimate is not accurate enough to convert the unwrapped interferometric phase to topographic heights. Therefore, refined baseline estimation is required using least squares fit for a number of ground control points, which have been selected by a program called *gcp_ras*. At least a dozen ground control points are required in order to estimate the baseline. The elevations of GCPs that

have been used in frame 4 and frame 6 are shown in Table 4.6 and Table 4.7 respectively.

Ground control points must be chosen in flat areas and should be spread over the entire image. Sometimes poor initial baseline estimation and poor selection of GCPs can lead to a non converging estimation. Figure 4.11 shows the distribution of the ground control points that have been used in frame 4 and frame 6 to improve the estimate of the interferometric baseline. Unfortunately, the distribution of the GCPs is not perfect due to limited access to many parts in Central Kalimantan, Indonesia. The field work covered most of all the accessible areas. After selecting ground control points, the corresponding unwrapping phase can be determined and be extracted from the unwrapped interferogram using the program *gcp_phase*. Table 4.8 shows an example of the GCPs in frame 4 in slant range/azimuth coordinates with their equivalent unwrapping phase. Once the height information and unwrapped phases are determined, the least squares estimate of interferometric baseline could be obtained by a program called *base_ls*.

Table 4.6: List of GCPs in Block C that have been used to estimate precise baseline.

ID	Lat	Long	Height(m)
1	-2.97923	114.0876	46.8252
2	-2.95533	114.1496	48.6405
3	-2.95244	114.0402	48.7313
4	-2.93175	113.942	49.1269
5	-2.89792	114.254	44.8542
6	-2.89051	114.1578	47.1715
7	-2.84863	114.1922	46.5147
8	-2.81306	114.3279	40.8967
9	-2.76599	114.2852	47.991
10	-2.67816	114.2763	48.4042
11	-2.62206	114.2067	48.6389
12	-2.56812	114.1921	48.7561
13	-2.5487	114.1918	47.8451
14	-2.48659	114.1941	52.1694
15	-2.43909	114.1746	52.1004
16	-2.37374	114.1424	52.357
17	-2.34223	114.0367	50.6893

Table 4.7: List of GCPs in Block A that has been used to estimate precise baseline.

ID	Lat	Long	Height(m)	ID	Lat	Long	Height(m)
1	-2.63979	114.5497	49.7759	21	-2.89792	114.254	42.5687
2	-3.00797	114.389	47.9757	22	-2.85391	114.2106	44.2355
3	-2.9387	114.4479	46.8478	23	-2.76599	114.2852	47.991
4	-2.54972	114.5042	47.3749	24	-2.79791	114.3129	46.6902
5	-2.63541	114.5977	48.807	25	-2.81379	114.33	51.4594
6	-2.63541	114.5977	48.961	26	-2.97903	114.3339	46.8223
7	-2.84064	114.5287	49.9792	27	-2.98337	114.4005	47.2574
8	-2.88897	114.4854	49.6796	28	-2.96373	114.3878	47.9718
9	-2.81129	114.5618	49.9648	29	-2.91975	114.3764	48.0959
10	-2.54661	114.5538	48.1192	30	-2.82853	114.356	47.8986
11	-2.56682	114.5455	48.1765	31	-2.99201	114.4266	49.377
12	-2.54018	114.4814	49.2587	32	-3.0738	114.4361	47.733
13	-2.72898	114.5902	48.3374	33	-3.12496	114.4812	48.5463
14	-2.66514	114.5842	47.9621	34	-2.98333	114.4002	47.7564
15	-2.64786	114.5691	48.8563	35	-2.61496	114.4823	47.9101
16	-2.67646	114.2766	47.7451	36	-2.64987	114.509	48.5756
17	-2.72146	114.2611	47.5074	37	-2.66961	114.5003	48.1421
18	-2.84596	114.1927	47.7847	38	-2.62834	114.518	48.1887
19	-2.99715	114.3676	41.962	39	-2.55365	114.5138	48.4486
20	-2.97065	114.3429	43.6274				

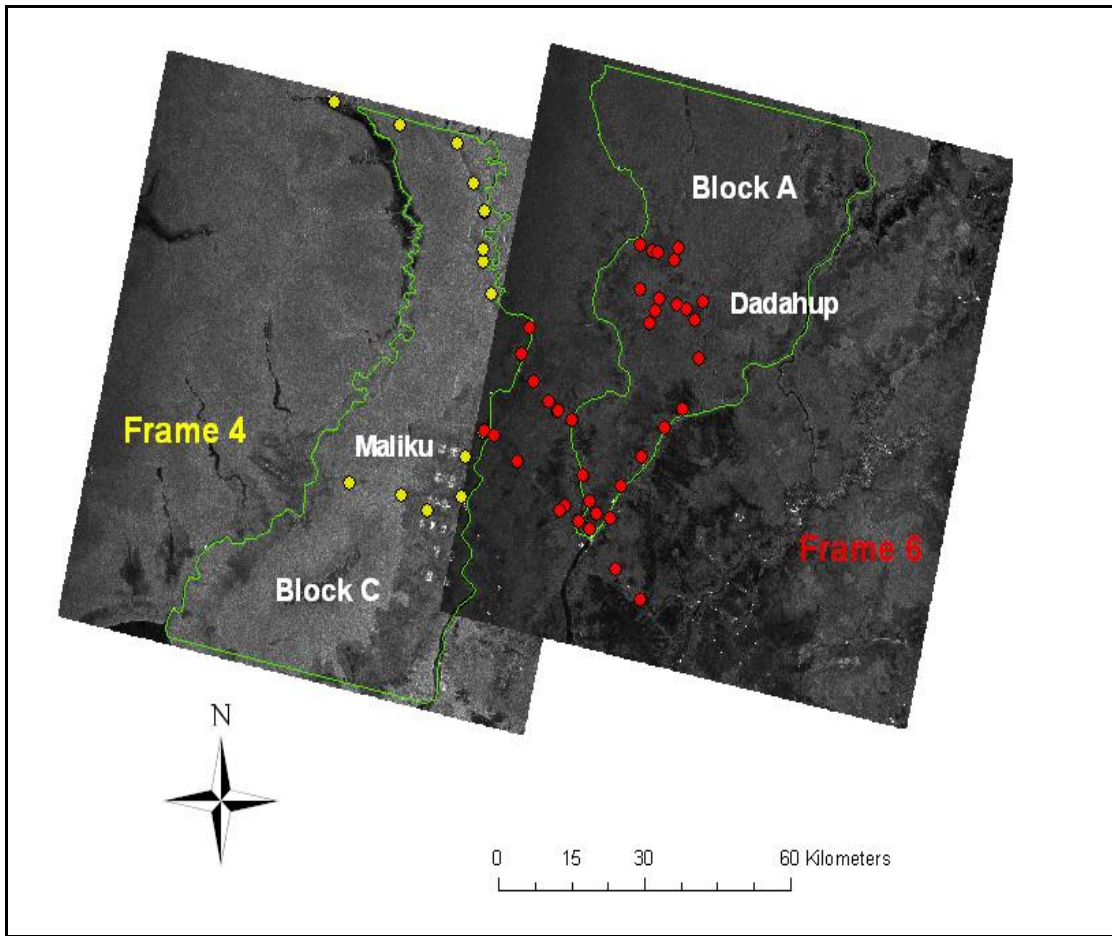


Figure 4.11: Distribution of GCPs that been used in precise baseline estimation.

Table 4.8: GCPs in radar geometry in frame 4.

Point	X	Y	Height(m)	GCP unwrapping phase(rad)
1	645	1718	46.82	-6.99715
2	471	1626	48.64	-4.35634
3	750	1667	48.73	-3.504
4	1015	1684	49.13	-6.29998
5	223	1435	44.85	-1.40626
6	473	1449	47.17	-4.56861
7	419	1322	46.51	-1.89827
8	119	1130	40.89	0.85482
9	230	1038	47.99	3.96207
10	311	789	48.4	8.76412
11	495	683	48.63	9.80734
12	574	556	48.76	14.56579
13	571	510	47.84	14.85722
14	603	339	52.17	17.73367
15	697	228	52.1	20.59836
16	722	106	52.34	23.60175
17	954	130	50.69	25.27479

4.4.9 DEM Generation

Assuming that the interferometric phase is related to topography only, the unwrapped interferometric phase, together with the accurate baseline, is then used to derive the topographic heights and true ground ranges using a program called *hgt_map*. The result is a height map in slant range/azimuth coordinates. The heights in SAR image coordinates were resampled to orthonormal coordinates (along track, cross track) using a program *res_map*. At this point of the processing, the programs that have been used after phase unwrapping are listed in Table 4.9.

Table 4.9: Gamma programs used in baseline and corrected height estimation.

Processing steps	Program
Selection of GCPs	<i>gcp_ras</i>
Extraction of GCPs unwrapped phase	<i>gcp_phase</i>
Least square estimation of baseline	<i>base_ls</i>
Estimation of heights	<i>hgt_map</i>
Resampling height to ground range	<i>res_map</i>

These images were imported to ERDAS software and a geometric correction was applied to correct the spatial distortion using the Landsat images and all resulting images were stored in the Universal Transverse Mercator (UTM) projection system, zone 50 south. In addition to the height, other products such as the coherence map are also imported and geocoded. Finally, the DEMs were extracted by two subsets; the first one is Maluku area in frame 4 and the second subset is Dadahup location in frame 6. Six different DEMs of Maluku and eight DEMs of Dadahup were the results of applying the

previous different processing of generating interferograms, adaptive filtering and phase unwrapping methods.

4.5 DEM accuracy assessment

One way to assess the quality of a digital elevation model is performed by using ground control points (GCPs). This approach is also a part of the standards for DEMs proposed by the United States Geological Survey (USGS, 1997). According to the National Digital Cartographic Data Base (NDCDB), a minimum of 28 points (20 interior and eight edge points) needs to be measured to determine the root mean square error (RMSE). The accuracy is computed by comparison of linear interpolated DEM elevations with the corresponding known elevations. In order to be suitable for this study, the test points have to fulfil the following requirements. They should be well distributed and representative for the terrain. Their accuracy has to be well within the DEM accuracy

To compare the heights that were obtained by InSAR technique and DGPS check points, height profiles in each area were extracted from every DEM at the same locations where Kinematic GPS positioning sample were taken. Figure 4.12 and Figure 4.13 present the routes from which two GPS height profiles were extracted in Maluku and Dadahup, with the DEM of the site as background. The accuracy assessment of the DEMs has been carried out using 100 DGPS survey points in Maluku and Dadahup and the frequency of check points are illustrated in Figure 4.14. The maximum, minimum, mean, median and RMSE errors were calculated for all the resulting DEMS and have been compared.

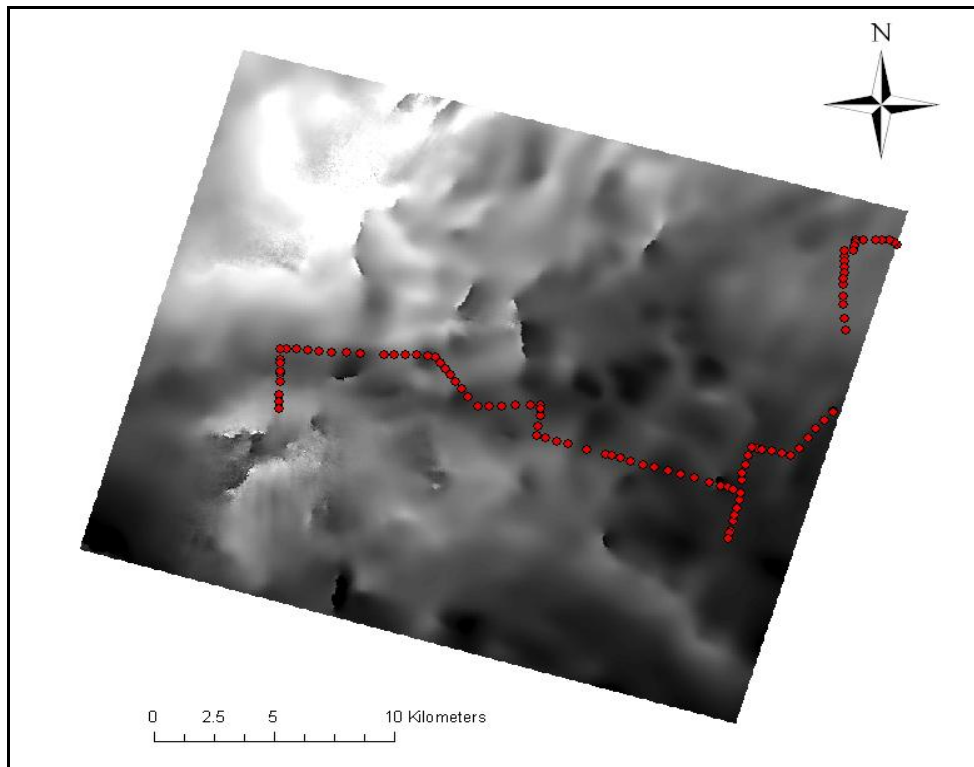


Figure 4.12: Distribution of check GCPs overlaid on Maliku DEM

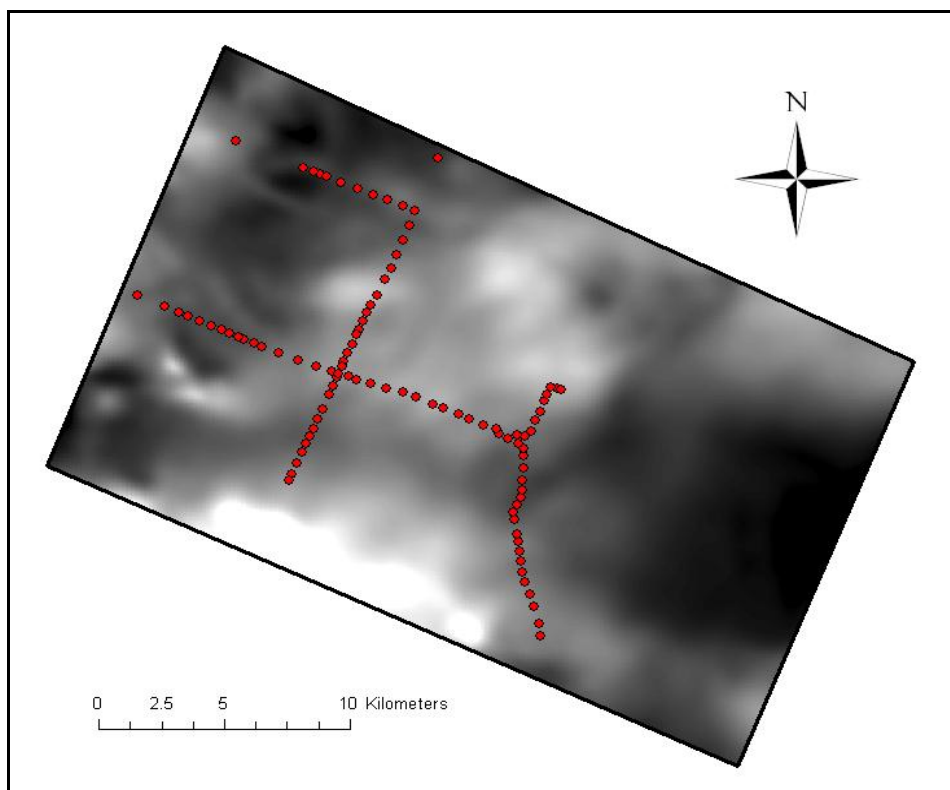


Figure 4.13: Distribution of check GCPs overlaid on a Dadahup DEM.

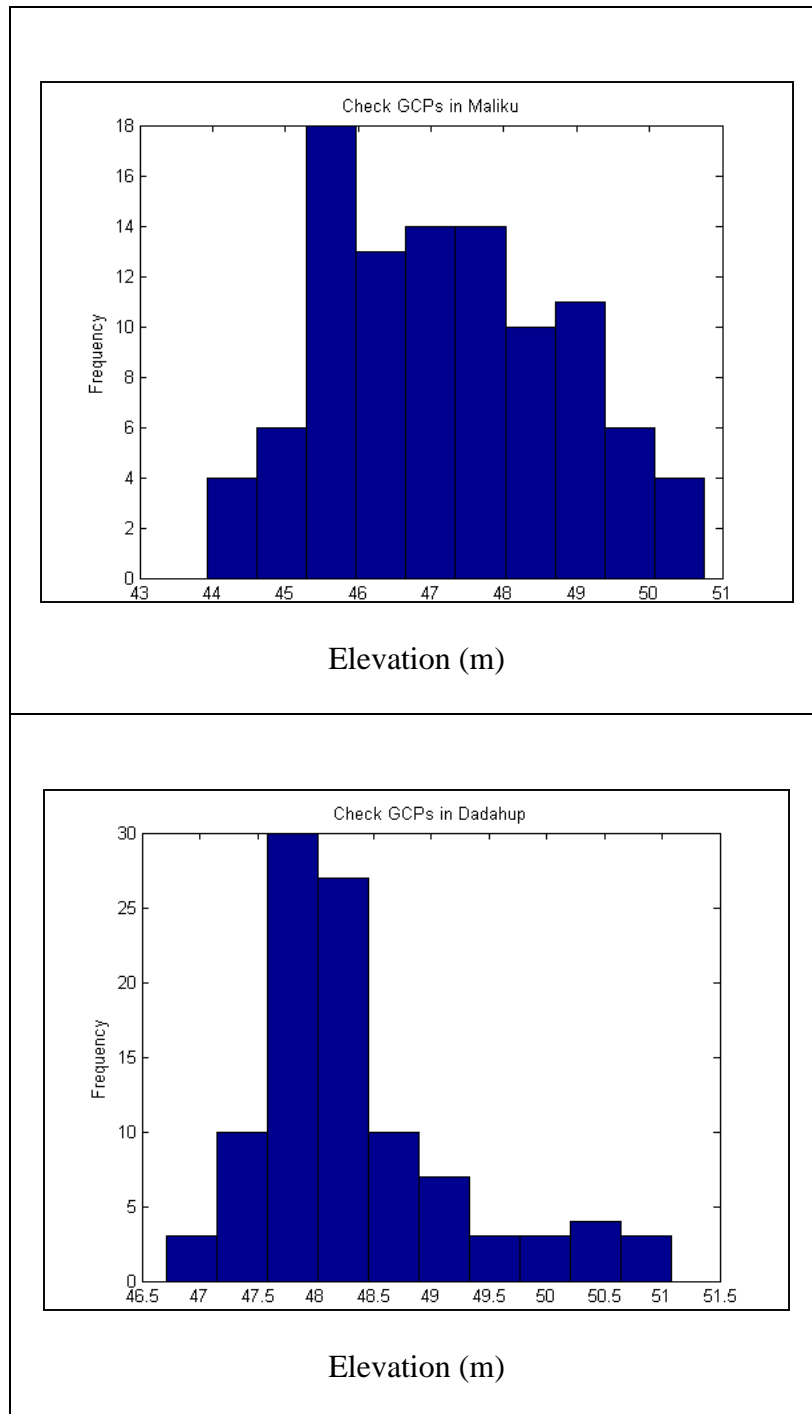


Figure 4.14: Frequency of DGPS check point elevation.

4.6 Differential processing

The differential interferogram generation process begins in this step by separating the topographic and displacement components and identifying only the displacement component (Galloway *et al.*, 2000). Any inaccuracies in the generating interferograms will directly translate into errors in the displacement measurement. Therefore, only high accuracy interferograms in 1997 and 2000 have been used to generate displacement maps.

There are four methods used to produce a differential interferogram: two pass, three pass, four pass and complex interferogram combination. These techniques were described in the literature review in chapter 2. Two pass methods could not be used in this study due to the unavailability of external DEM. Three pass methods were unsuccessful to generate interferograms with a long repeat-pass interval. The overall coherence in the images was so low that a sufficient interferogram could not be generated and then used to produce a coherence map or a DEM. Therefore; only two methods were implemented in this study; four pass method and complex interferogram combination.

Four-pass DInSAR requires two original interferograms of the study area taken at two different times. The first interferogram contains the topographic information and referred to as ‘topographic pair’. The very short repeat-pass period should imply that no significant deformation occurred between the acquisitions. The second interferogram, referred to as a differential pair, contains the topographic information and the ground deformation formed between the acquisition of topographic pair and differential pair’

(Tsay and Lu, 2001; Ge *et al.*, 2003). Interferograms that have been used in this process in frame 4 and frame 6, with 2.3, 2.15 years temporal separation respectively, are shown in Table 4.10. Figure 4.15 illustrates the two different processing methods for differential interferometry that have being used in this study.

Table 4.10 Topographic and differential interferogram.

	Frame 4	Frame 6
Topographic pair	19971006_3663_19971007_3663	19971022_3663_19971023_3663
Differential pair	20000124_3663_20000125_3663	20000105_3663_20000106_3663

Both interferograms are unwrapped interferograms that have real values obtained after phase unwrapping. The topographic pair was resampled to the geometry of the differential pair by generating a parameter file and calculating the offsets between two interferograms. The program *creat_diff_par* generates a parameter file for the differential interferogram (Gamma, 2008b). The general values that have been used are illustrated in Table 4.11.

Table 4.11: General value of offset estimation.

Number of offset measurements in range, azimuth	16
Search window sizes	256
Minimum matching SNR	7.00

The initial offset estimation between two geometries is done with the program *init_offsetm* using the correlation between the MLI intensity images. The programs

offset_pwrn and *offset_fitm* have been used to estimate the offsets and generation of the offset polynomials respectively (Gamma, 2008b). Resampling any image in the differential pair geometry to the topographic pair geometry can be done with a program *interp_real*.

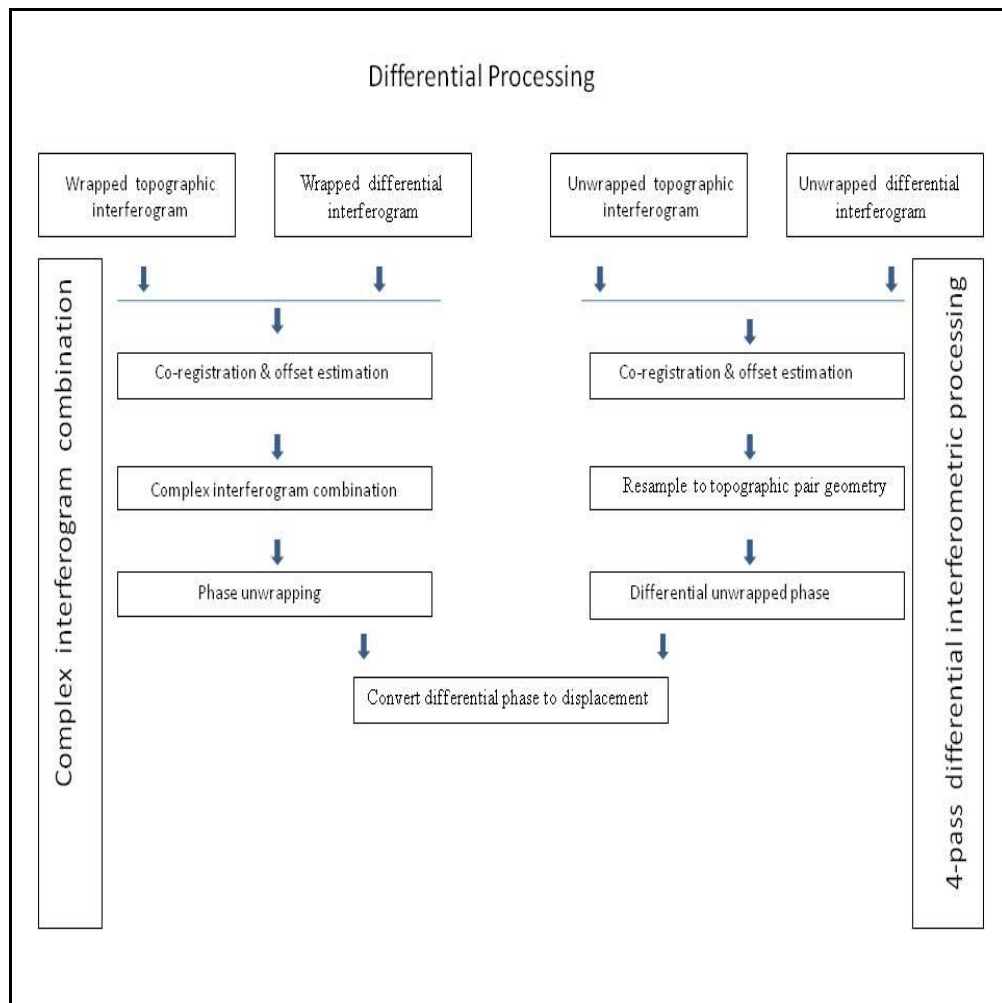


Figure 4.15: Flow chart for differential interferometry processing methods.

As there are many areas with a null value, the nearest neighbour resampling is preferred over the interpolation approach. The least squares fit approach in the program *diff_ls_fit* has been used to determine the scaling factors for phase. Using the phase scaling factors, the unwrapped differential interferogram can be created using the program

diff_ls_unw. To obtain the displacement map from the unwrapped differential phase image the program *dispmap* can be used (Gamma, 2008b). A complete phase cycle (2π radian phase difference) or fringe represents radar line-of-sight ground displacement of $\lambda/2$, where λ is the radar wavelength being used. In this case of C-band radar ($\lambda= 5.6$ cm), each fringe represents 2.8 cm radar line-of-sight displacement. The programs that have been used in 4-pass method are listed in Table 4.12.

Table 4.12: Four-pass steps and programs.

Processing steps	Program
Differential parameter file creation	create_diff_par
Initial registration offset estimation	init_offsetsm
Detailed registration offsets estimation	offset_pwrsm
Derivation of registration offset polynomials	offset_fitm
Resampling differential pair to topographical pair geometry	interp_real
determine the scaling factors for phase	diff_ls_fit
Generate the differential interferogram	diff_ls_unw
Conversion of differential phase to displacement	dispmap

Complex combination of interferograms is the second method which has been used to obtain the differential interferograms. In this method, both interferograms are wrapped flattened interferograms. Co-registration offsets between the two interferogram pair and resampling of the topographic pair to differential pair are done in the same methods that have been used in 4- pass method. The only difference is using the program *interp_cpx* in resampling of the interferogram because the interferograms are in complex format (wrapped interferogram).

Once the two interferograms have the same geometry, the complex interferogram combination can be obtained by using the program *comb_interfs*. The differential interferogram contains the differential phase components of the first pair minus two times the differential phase components of the second pair. The effective interferometric baseline for the differential interferogram can be used to remove the remaining phase trend with the program *ph_slope_base*. After the phase subtraction, complex differential interferogram have been unwrapped using MCF unwrapping method and converted to displacement with the program *dispmap*. The differential interferogram (19971006_07_20000124_25) for example, corresponds to an interferogram with (214-427=-213 m) perpendicular baseline and (-12-44=-56 m) parallel baseline and 2.3 years time interval. A summary of the processing sequence with related programs that have been used in this approach can be found in Table 4.13.

Resulting images from both differential methods were imported into ERDAS software and geocoded and stored in the Universal Transverse Mercator (UTM) projection system, zone 50 south. The displacement maps then have been extracted by Block C and Block A and the subsidence rate was calculated for the two different locations. Two transects have been generated in Maluku as well as in Dadahup to analyze the change of subsidence over the area.

Table 4.13: Complex interferogram combination steps and programs.

Processing steps	Program
Differential parameter file creation	create_diff_par
Initial registration offset estimation	init_offsetsm
Detailed registration offsets estimation	Offset_pwrsm
Derivation of registration offset polynomials	Offset_fitm
Resampling differential pair to topographical pair geometry	Interp_cpx
Complex interferogram combination	comb_interfs
Removal of residual phase trend	ph_slope_base
Phase unwrapping algorithm	mcf
Conversion of differential phase to displacement	dispmap

4.7 Statistical analysis

Once the coherence images, DEMs and subsidence maps are generated, the comparative, descriptive and special analyses for each InSAR products area was applied to summarize and asses the general characteristics of the dataset. The mean, standard derivations, minimum and maximum were examined to explain the characteristic of each product. All statistical analysis was performed using Matlab (R2010a) software.

The most widely used statistical measure is the Root Mean Square Error (RMSE). It measures the dispersion of the frequency distribution of elevation between original elevation data and DEM data. Mathematically expressed as:

$$\text{RMSE} = \sqrt{\frac{\sum (Z_{\text{DEM}} - Z_{\text{Ref}})^2}{n}} \dots\dots\dots (4.1)$$

Where: Z_{DEM} is the elevation value measures on DEM surface;

Z_{Ref} is the corresponding original elevation (Reference)

n is the number of elevation points checked.

The accuracy of a DEM can be defined as the average vertical error of all potential points interpolated within the DEM grid. In other words, it is the vertical root-mean-square accuracy of all points interpolated in the DEM grid.

In addition, Standard deviation is a statistical term that provides a good indication of volatility and measures the spread of the data about the mean value. It measures how far all measurements are from the mean by squaring each one and adding them all up. The result is called the variance, then the standard deviation calculated by taking the square root of the variance (Milton and Arnold, 1995).

$$\text{Std.Dev} = \sqrt{\frac{\sum [(Z_{\text{DEM}} - Z_{\text{Ref}}) - \text{ME}]^2}{n-1}} \dots\dots\dots (4.3)$$

Where ME is the mean elevation error:

$$\text{ME} = \frac{\sum (Z_{\text{DEM}} - Z_{\text{Ref}})}{n} \dots\dots\dots (4.4)$$

Therefore, a set of values that are closely clustered near the mean will have a low standard deviation, a set of numbers that are widely apart will have a higher standard deviation and a set of numbers that are all the same will have a standard deviation of zero. There is also varying degrees by which this measure is considered accurate. For each standard deviation, there is an increasing level of reliability as shown here:

- 1 Standard Deviation = 68.27 % reliability
- 2 Standard Deviation = 95.45 % reliability
- 3 Standard Deviation = 99.73 % reliability

4.8 Estimation of carbon loss and CO₂ emissions

The carbon loss rate and CO₂ emission can be calculated by using subsidence rate in Block C and Block A where large burn scars and deforestation areas are located in the period between 1996 and 2000.

4.8.1 Carbon loss

Peat loss volume can be calculated by multiplying the area of each cell (1600 m²) by the subsidence value. By applying values of 57% for peat carbon content and 0.10 g cm⁻³ for peat bulk density, the loss of carbon can be estimated:

$$\begin{aligned} \text{Carbon loss rate (t/y)} &= \text{subsidence rate} \cdot \text{Area} \cdot \text{carbon content} \cdot \text{peat} \\ &\text{bulk density} \dots\dots\dots(4.3) \end{aligned}$$

Where: subsidence rate [m/y] and Area [ha]

4.8.2 CO₂ emission

To estimate the carbon emission due to peat loss, the water table change should be calculated first over Block C and Block A respectively. The linear relationship between water table change and subsidence rate introduced by Wösten *et al.*, (1997) was used to map the water table change (WT) over the study area.

$$\text{Peat subsidence rate (cm/y)} = \text{XO} \cdot \text{WT (cm/y)} \quad (4.4)$$

$$\Leftrightarrow \text{WT (cm/y)} = \text{Peat subsidence rate (cm/y)} / \text{XO} \quad (4.5)$$

The actual co-efficient value (XO) depends on the peat characteristics and it has been found to vary between 0.1 – 0.04. The maximum and minimum co-efficient values have been used to calculate the highest and lowest water table levels.

The relationship between CO₂ gas emission monitoring and water depth have been discussed by Hooijer *et al.* (2010) who concluded that the relationship between CO₂ gas emission monitoring and water depth can be expressed by the following equation:

$$\text{CO}_2 \text{ emission} = 91 \cdot \text{WT} \quad (4.6)$$

Where CO₂ emission is expressed in t/ha/y and groundwater depth is the average depth of the water table below the peat surface, expressed in metres. By using the water table change in equation (4.5), the CO₂ emission in equation (4.6) can be estimated.

$$\text{CO}_2 \text{ emission} = 0.91 \cdot \text{Peat subsidence rate (cm/y)} / \text{XO} \quad (4.7)$$

4.9 Summary

In this chapter both ERS1/2 data and DGPS field measurements were presented and the nature of the test site was described. In addition, this chapter described the methodology used to estimate coherence images, generate DEMs and produce deformation maps using InSAR and DInSAR techniques. Two interferogram calculation methods namely; intensity and orbit, have been used with two phase unwrapping techniques: Branch Cut and Minimum Cost Flow. Adaptive filtering has been applied one and many times for these methods to test its influence on unwrapping methods and final DEM accuracy. The coherence change values have been used to identify burn scar and deforestation area in Block C and Block A respectively. The assumptions related to carbon loss estimation from peat soil have been introduced and the CO₂ emissions have been estimated. The next three chapters will focus on the results of applying InSAR methods to approach the research objectives.

Chapter 5: Coherence for change detection analysis

5.1 Introduction

This chapter presents the results and discussion of the estimation of coherence change of ERS tandem pairs for each test area in Ex-MRP. The first part shows the results of applying a number of different factors that affect coherence, such as the size of search window and the weighting functions. The burn scar and deforestation area have been detected in the second part based on coherence values changes and have been analyzed and compared with other research findings.

5.2 The size of the estimation window

The size of the estimation window is a crucial factor determining the coherence estimate. For increasing window size the estimation bias, the estimation uncertainty and the spatial resolution of the coherence image are decreased. In areas of low coherence, larger estimation windows are used (Wegmüller *et al.*, 1998). Quantitative investigation of the coherence as related to search window size changes was performed in this study. Figure 5.1 shows a comparison between four coherence images obtained with four different size windows using a constant weight function. The images have been acquired for the same area over frame 4 in 24/25 January 2000.

On the resulting coherence image red corresponds to high coherence whereas green corresponds to low coherence. The histogram of the coherence values shows quite similar frequency of the coherence for all search window size.

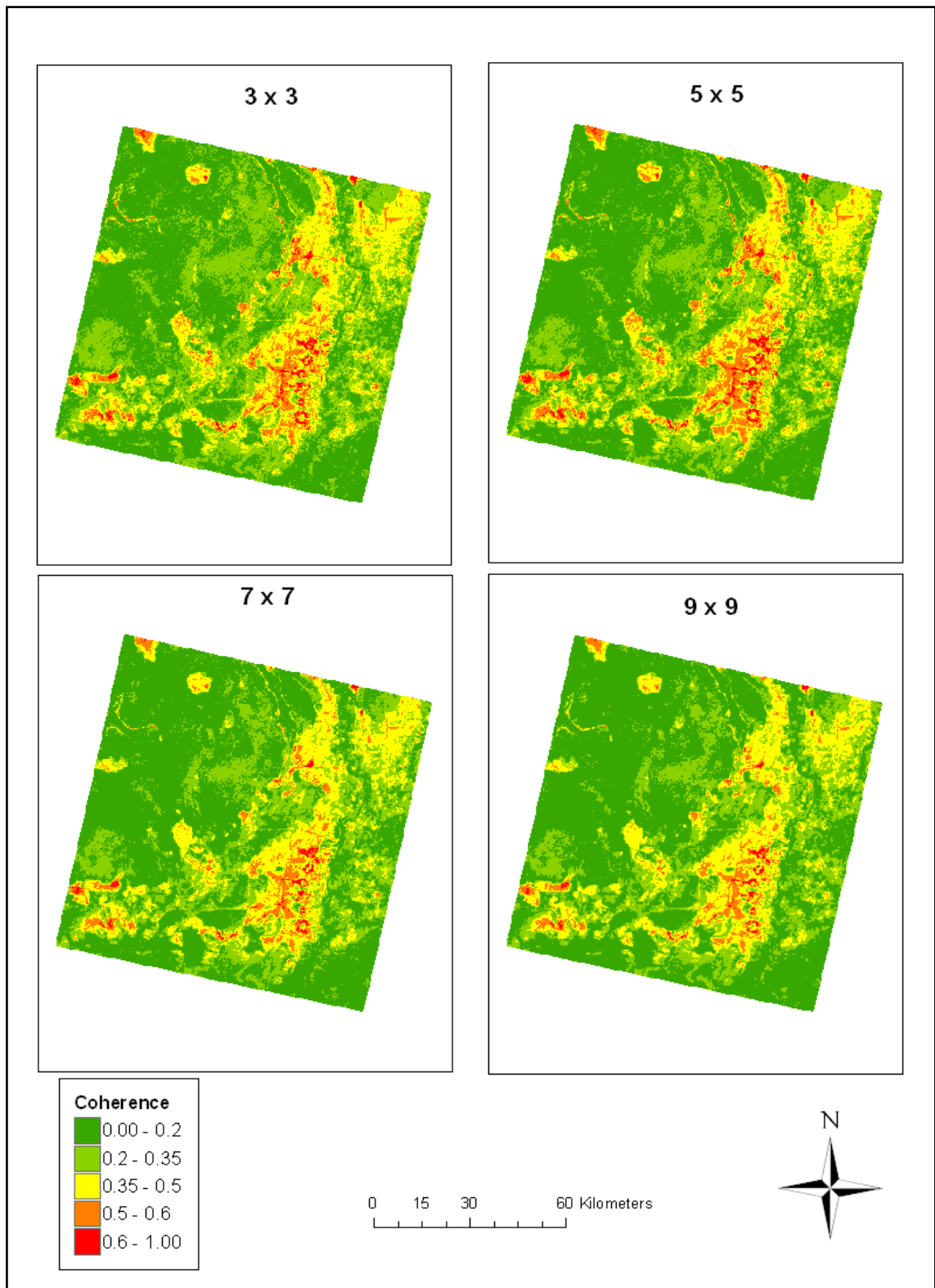


Figure 5.1: Coherence image of interferogram 2000 using different search windows.

The global coherence histograms of the whole interferometric pair in Frame 4 using four search windows are shown in Figure 5.2. The different histograms indicate that the distributions peak on the left with a longer tail on the right (positively skewed) over the

image. However, the mean value of each one (respectively, 0.26, 0.25, 0.23 and 0.23) indicates the mean and maximum coherence has decreased whilst the search window size has increased. Note that the coherence estimator has exactly the same statistics for all search window size and the difference is almost negligible. As the resulting coherence in Table 5.1 looks almost similar in the four search window size coherence maps, the change in coherence using these search windows will not have a big influence in the burn scar coherence change in further analysis.

5.3 Weighting functions

Coherence is typically computed using a sliding window. For each pixel, the coherence is obtained by applying a coherence equation to the window sliding from pixel to pixel. To decrease the effect of resolution loss due to the windowing operation, weighting functions such as constant, Gaussian, none (phase only) and triangular (linear) can be applied within the window. In this way, pixels further away from the centre of the window have less weight on the estimate. For example, if the triangular weight function is used, the weight decreases linearly with increasing distance for the central pixel. The type of weights to be applied depends on the nature of the objects in the scene. If the scene includes distributed targets, weighting plays a minor role. On the contrary, if the scene is populated with small-size point targets, it is recommended to use small windows and strong weighting functions to preserve the coherence of each of the point targets. Figure 5.3 illustrates a comparison between four coherence images obtained with four different weighting approaches. The images have been acquired during the ERS1/2 tandem mission over block C, Central Kalimantan, Indonesia using 5x5 window sizes.

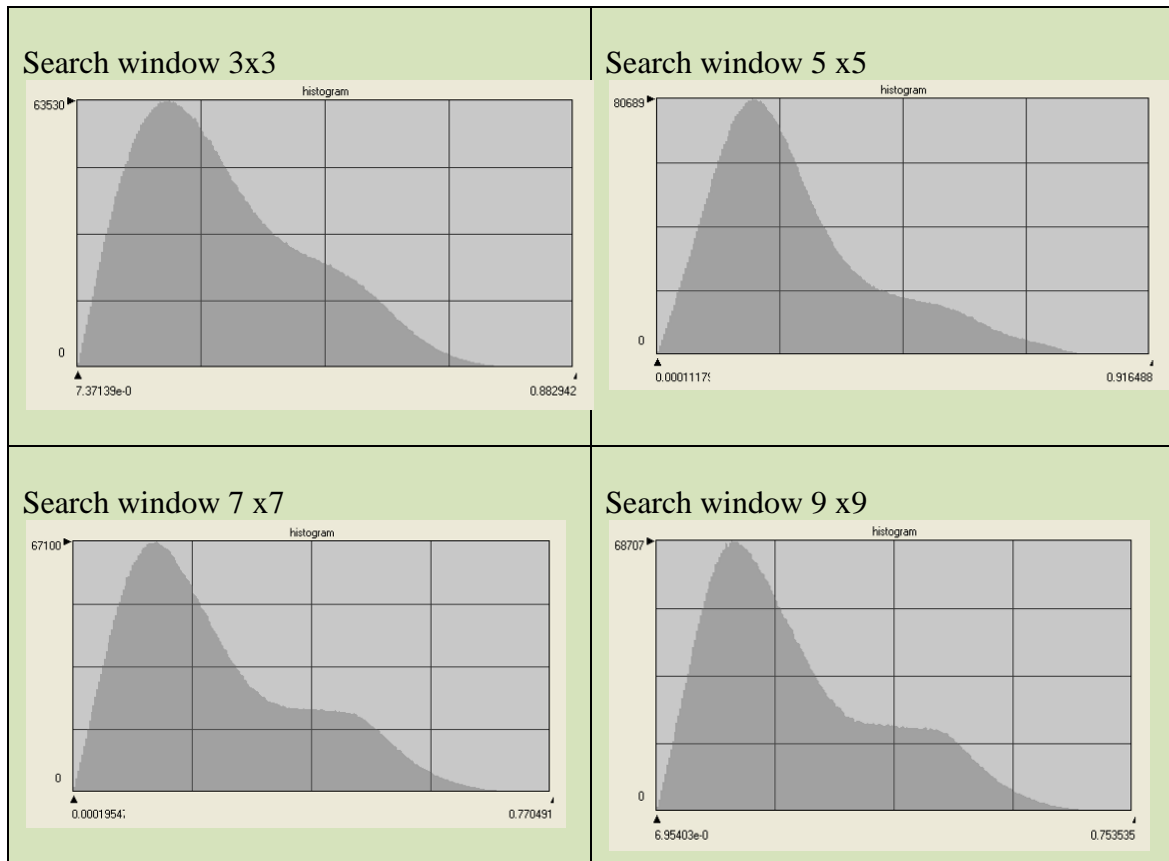


Figure 5.2: Histograms of the coherence values for each search window size.

Table 5.1: Descriptive statistics of coherence using different search window.

Search window	Min	Max	Mean	Median	Std.Dev
3x3	0.00	0.88	0.26	0.23	0.15
5x5	0.00	0.92	0.25	0.21	0.15
7x7	0.00	0.77	0.23	0.19	0.14
9x9	0.00	0.75	0.23	0.19	0.14

The exponential coherence histograms of the whole interferometric pair in frame 4 are shown in Figure 5.4. The different histograms indicate a similar frequency and distribution of the coherence (positively skewed) over the image while the histogram of the coherence using no weight function (phase only) is more likely to have a Gaussian

curve distribution. The coherence estimation and its uncertainty are increased when no weight function is used and that leads to inaccurate coherence values for most of the study area.

Comparison between the above estimators in Table 5.2 indicates that three of them are slightly better for coherence estimation compared with a non-weight estimator. Their mean coherence values are approximately half of that of non-weight estimation. However, no evidence of weighting function effects were observed on the coherence images in three cases. It was also shown that non-weight overestimates the coherence for more than 0.25 degrees over most of the area. This study provided evidence that using weighting over the search window should give more accurate coherence estimation in forested areas. The search window (7x7) with constant weighting function have been adopted in this study to examine the coherence change in order to detect burn scar and deforestation area in Block C and Block A in Ex-MRP in Central Kalimantan, Indonesia.

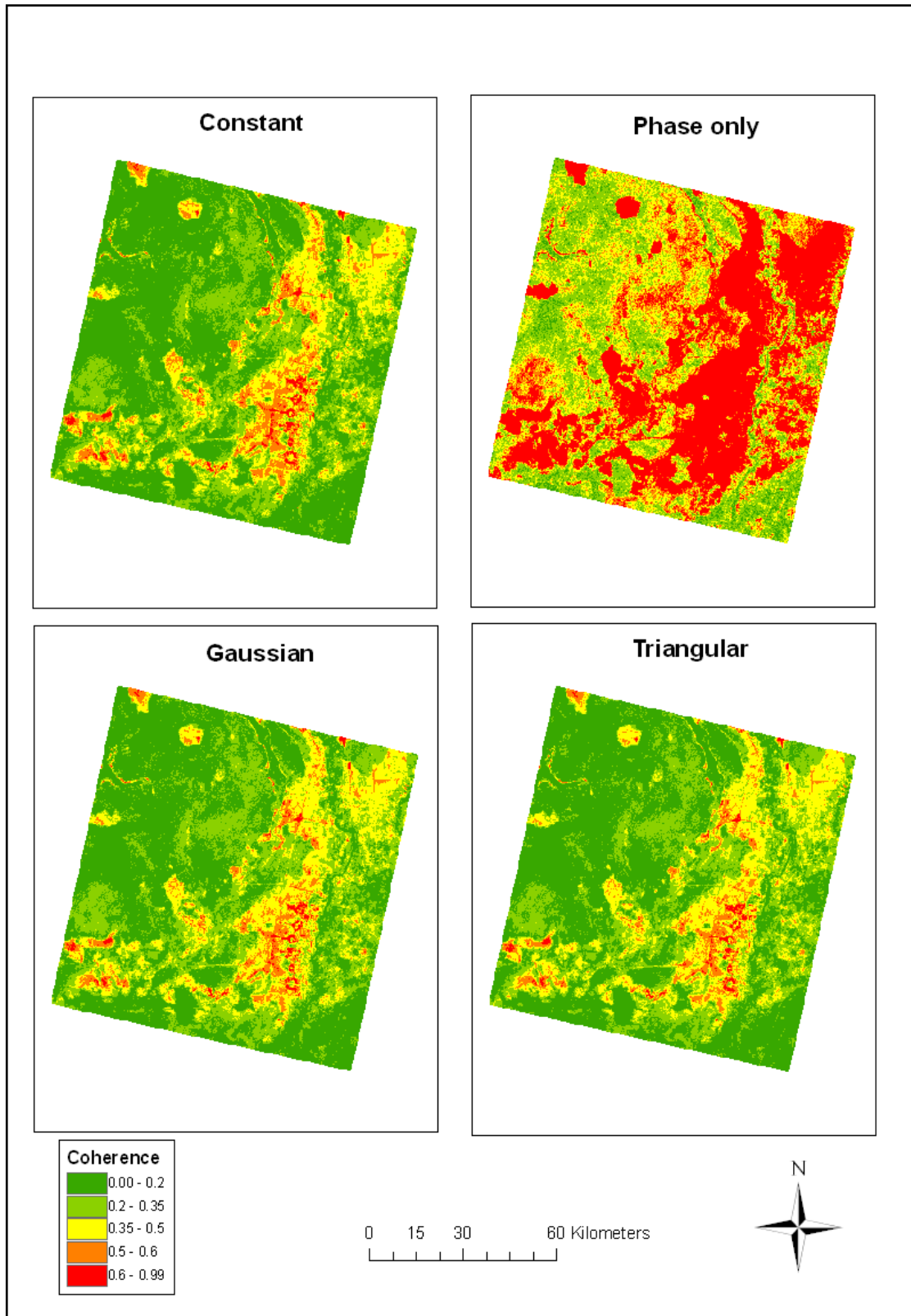


Figure 5.3 Coherence using different magnitude weighting functions.

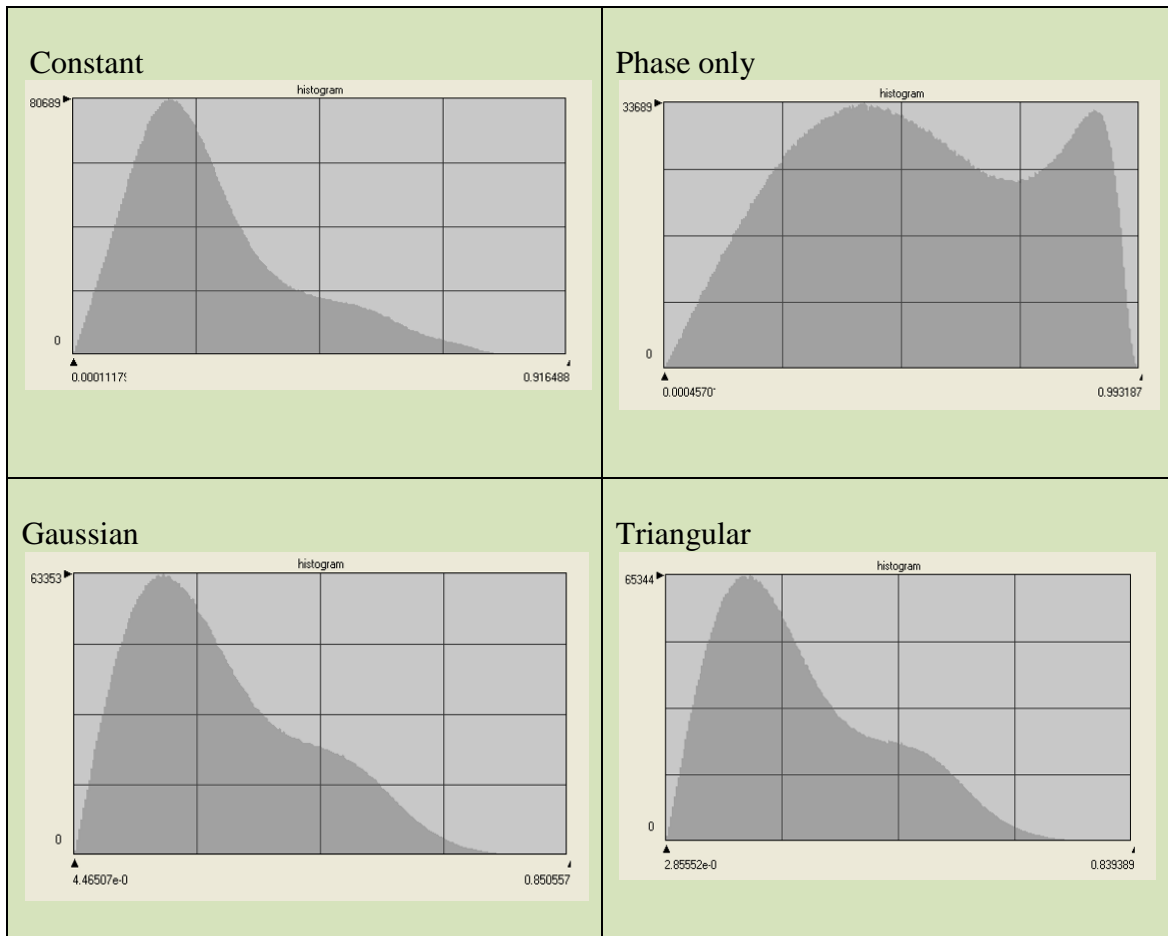


Figure 5.4: Histograms of of the coherence values for different magnitude weighting functions.

Table 5.2: Descriptive statistics of coherence using different weighting functions.

Magnitude weighting function	Min	Max	Mean	Median	Std.Dev
Constant	0.00	0.92	0.25	0.21	0.15
Phase only	0.00	0.99	0.53	0.52	0.25
Gaussian	0.00	0.85	0.25	0.22	0.15
Triangular	0.00	0.84	0.25	0.21	0.15

5.4 Coherence change in Block C

Coherence image in Figure 5.5 shows a wealth of information about landscape and land-use features such as rivers, agricultural land and forest boundaries, which could be clearly distinguished at a good spatial resolution (40 m). Between March 1996 and January 2000, marked changes in coherence were found in large parts of the study area. There is an increase of coherence in the January 2000 data with respect to March and April 1996. This change is most likely due to the fire in 1997 and occurs mainly in areas with degraded forest or plantations whilst the forested areas are relatively well conserved. Usually, the reason for poor coherence may be the long time of separation between the two images used to compute the interferogram. In this study, the temporal difference between the two images is only a day, so the coherence is independent of time separation.

Table 5.3 depicts the highest coherence and shows the pair of images which have been taken in dry season (October 1997). The baseline of 427 m of the high coherence image (October-1997-tandem) initiated an idea to test the influence of the baseline on the coherence (see Table 4.1). If the baseline is too short, the sensitivity to the signal phase differences will be undetectable, whilst if the baseline is too long, then additional noise due to spatial decorrelation corrupts the signal. Rodriguez and Martin (1992) have shown that coherence decreases approximately linearly with the increase in baseline length. The longer the baseline is, the worse the coherence. This is because the change of the look angle may cause different backscattering characteristics over the study area. The coherence of the two acquisitions will decrease linearly, becoming zero when the baseline reaches critical value (1100 m for ERS case). The situation here is different. The high coherence images have a longer baseline. The temporal effects, which follow from physical changes in the surface over the time period between observations and seasonal weather, are affecting the coherence more than baseline length. In the dry

season, zero rainfall and weak wind increases the backscatter and suppresses the corresponding volume scattering effect. In the agricultural area, the response of coherence dramatically increases in all four tandem acquisitions as the volume scattering effect decreases. However, the coherence of the two pairs in 1996 is still largely lower than the other two pairs due to heavy forest cover compared to 1997 and 2000 pair images.

Table 5.3: Summary of statistical parameters for coherence values in frame 4.

	Min	Max	Mean	Median	Std.Dev
March 1996	0.00	0.92	0.20	0.16	0.14
April 1996	0.00	0.92	0.26	0.22	0.16
October 1997	0.00	0.99	0.45	0.40	0.26
January 2000	0.00	0.92	0.25	0.21	0.15

In addition to the forest cover and baseline length change; the type of crops is also one of the factors that can enhance the volume scattering effect. For example, in rubber plantation, the signal is similar to that of the forest for both C and L bands. In this area rubber plantations are often mixed with other trees, constituting a rubber tree jungle, which is quite similar to secondary forest. Therefore the signal is temporally stable and presents a low coherence at 1 day intervals. Moreover, the backscattered intensity of the mature oil palm plantation is higher than that of the forest for ERS, mainly due to the palm leaf size, which is large compared to the wavelength (5.6 cm). Note that the coherence images are the full ERS scene with coverage of 100 km x 100km, or 1 million hectares. Therefore, as the area of interest is located in Block C, the coherence of block C was extracted from the whole ERS coherence map and shown in Figure 5.6.

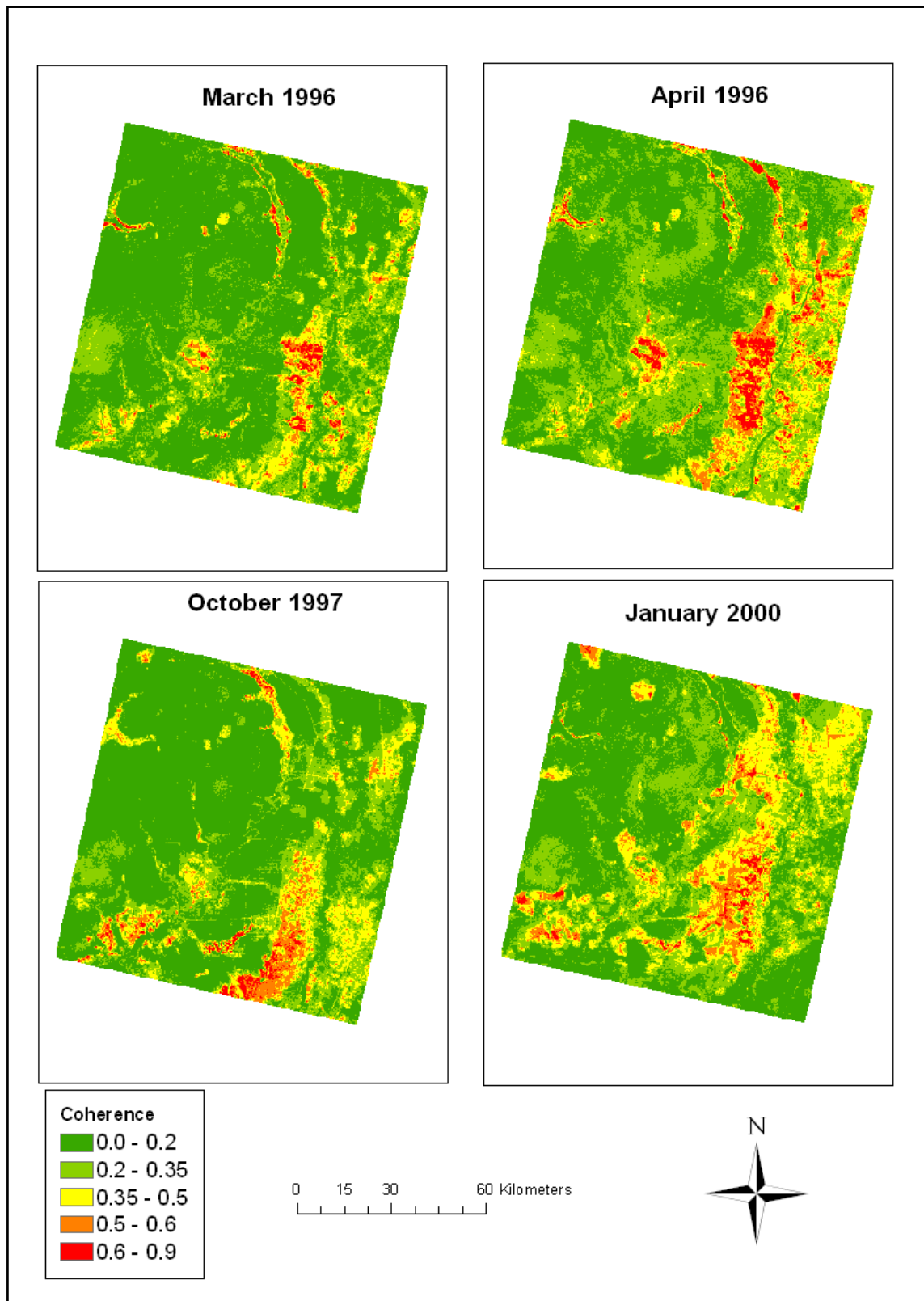


Figure 5.5: Time series of coherence in frame 4.

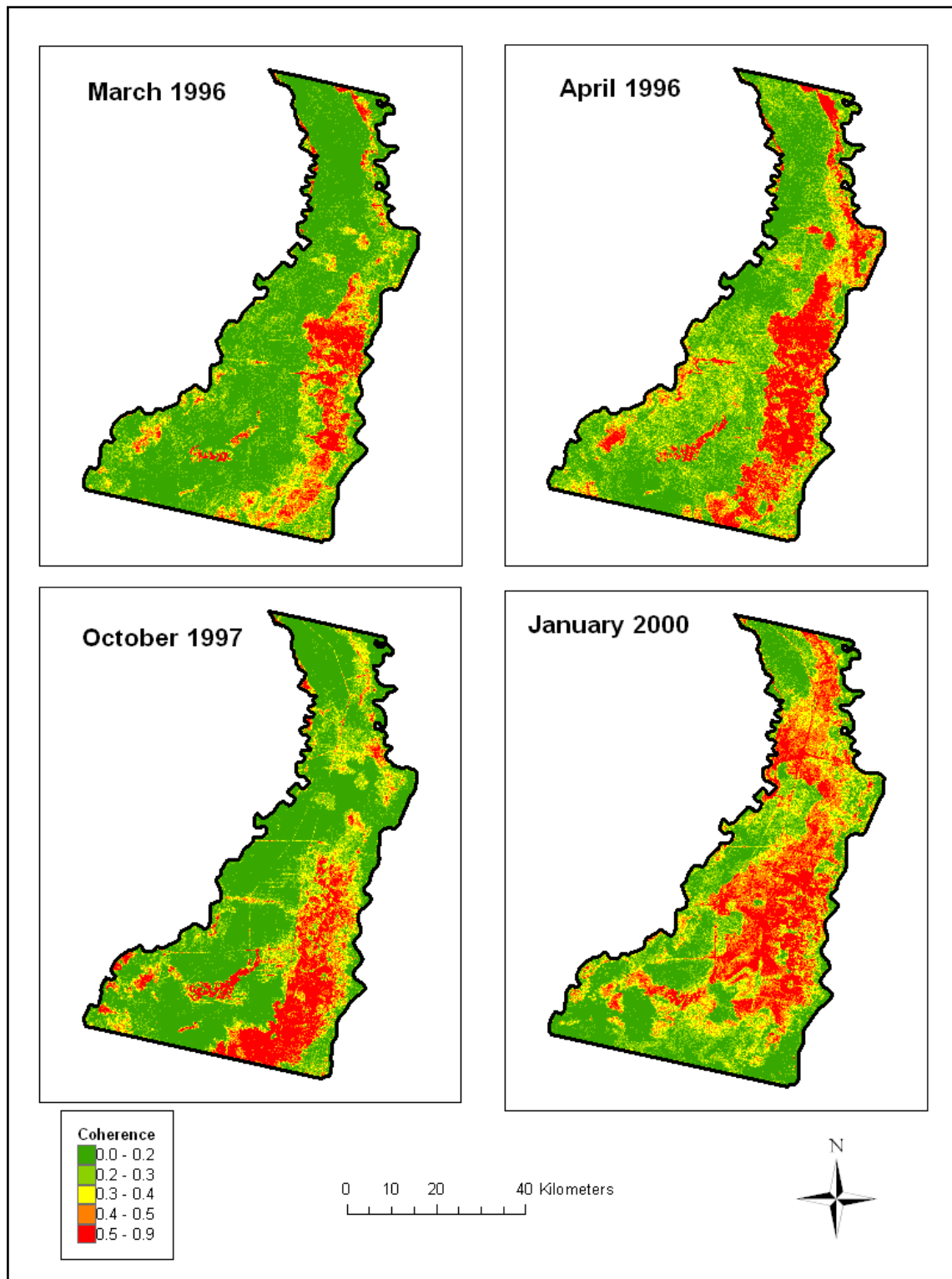


Figure 5.6: Time series of coherence in Block C within Frame 4.

5.5 Forest burn detection using visual interpretation

The basic methodology for using SAR data to detect forest burn scars relies on change detection, comparing data acquired after a fire with reference data obtained beforehand.

With this objective, applications relying on SAR data traditionally based on amplitude images may be fruitfully extended by exploiting interferometric techniques. A benefit of repeat-pass SAR interferometry is the feasibility of exploiting coherence information as well as the usual backscattering coefficient information and backscattering coefficient variation between the two acquisition times. In this study, only the 1-day coherence image produced during the interferometric processing of the multi look complex images are used for forest-burn and forest-clearing classification. The results of the signature analysis carried out by Siegert and Ruecker (2000) suggested that the most suitable image pairs for burn scar identification were the ones with both images acquired under dry weather conditions, since differences between burnt and unburned areas were most pronounced. In this study, only one tandem SAR image, taken in October 1997, which is in a dry season, was available. Therefore, the two image pairs that have been used for burn scar identification were acquired in the wet season. Two methods were employed for the detection of burnt areas, both based on the Multi-temporal evaluation of the changes that occur between two ERS over-passes before and after the fires. Both methods aim to highlight the changes and to separate this information from unchanged backscatter signals.

The first method relies on the visual inspection of coherence images classification and comparing it with burn scar areas that were identified by optical data. Here, the focus is on the results of the period from March 1996 to January 2000, where the detection of coherence changes between the two coherence images are most likely to be due to fire in 1997. The two coherence images were chosen to be taken at the same time of the year to decrease the seasonal effects on coherence estimation. Therefore, the coherence in the dry season in October 1997 was not used to derive the burn scar classification. The two

coherence images were processed by the same search window size (7x7) and with a constant weight function.

To obtain some quantitative results, an attempt was made to classify the coherence images. Figures 5.7, 5.8 and 5.9 show the simple classification using different threshold values (0.2, 0.35, and 0.5) on each coherence images on different dates. It was shown that the coherence threshold from 0.35 is generally appropriate to differentiate between burnt and non-burned areas in the coherence image compared to burn scar generated by optical data. Burnt areas that appear in red in coherence 2000 show low coherence in the March 1996 image and appear in green. Areas that have been burnt before March 1996 or urban areas appear in red in both coherence images. All coherence values which are greater than 0.35 will be considered as a selective parameter to detect burn area. In addition, there is a limitation of this method: urban or vegetation areas were classified as burned due to high coherence. Therefore, the areas that remained the same in both coherence images were excluded from the classification and the burn scar area were identified as shown in Figure 5.10. In the burn scar image, the red areas are areas with new forest clearings and non-vegetated areas that also remained unchanged, while green areas are forest and vegetated areas that remain unchanged. Green areas might be areas that have been burnt but now show re-growth, which could increase the coherence and lead to the area being classified as a burnt area.

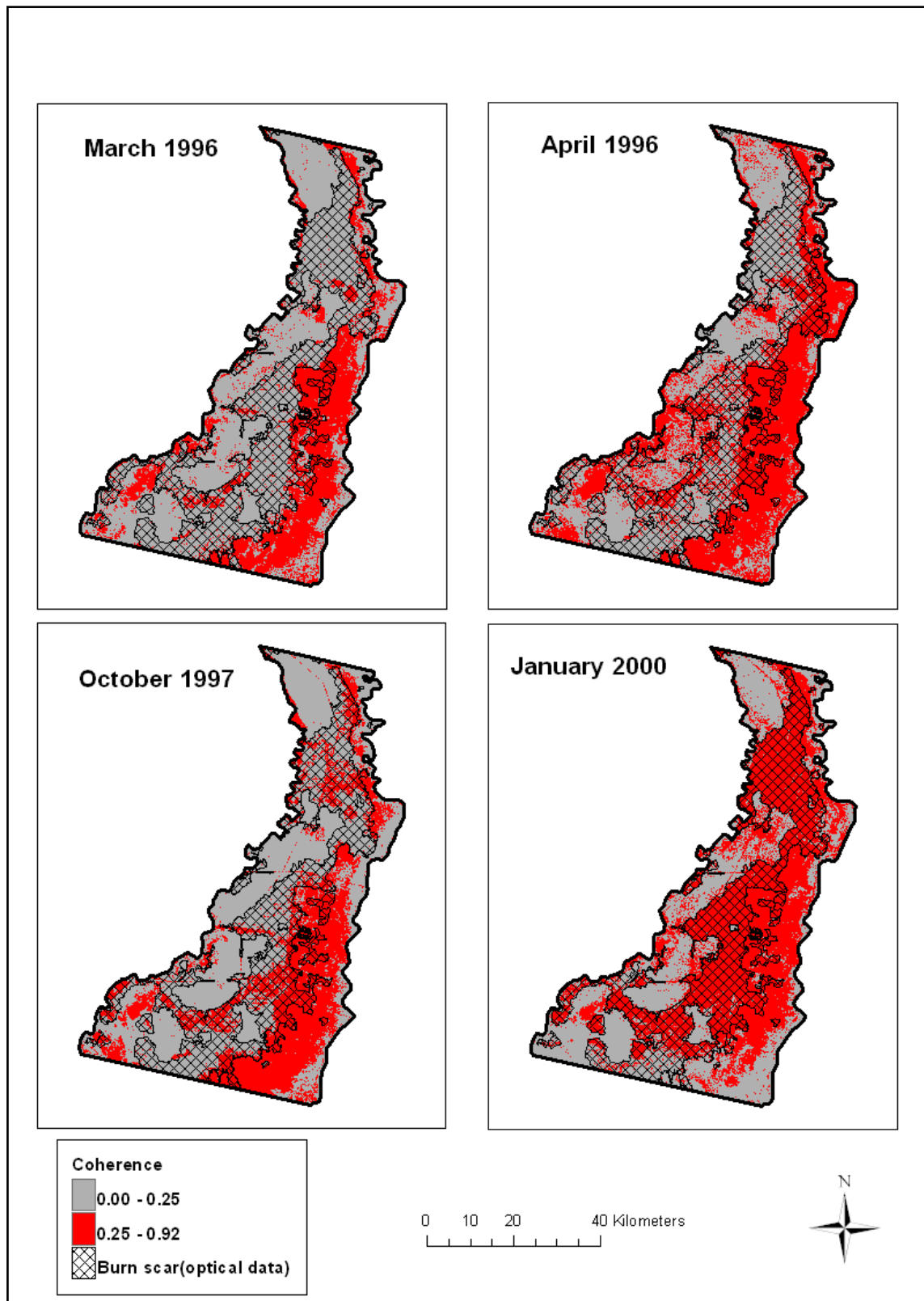


Figure 5.7: Coherence classification between March 1996 and January 2000 using value 0.25.

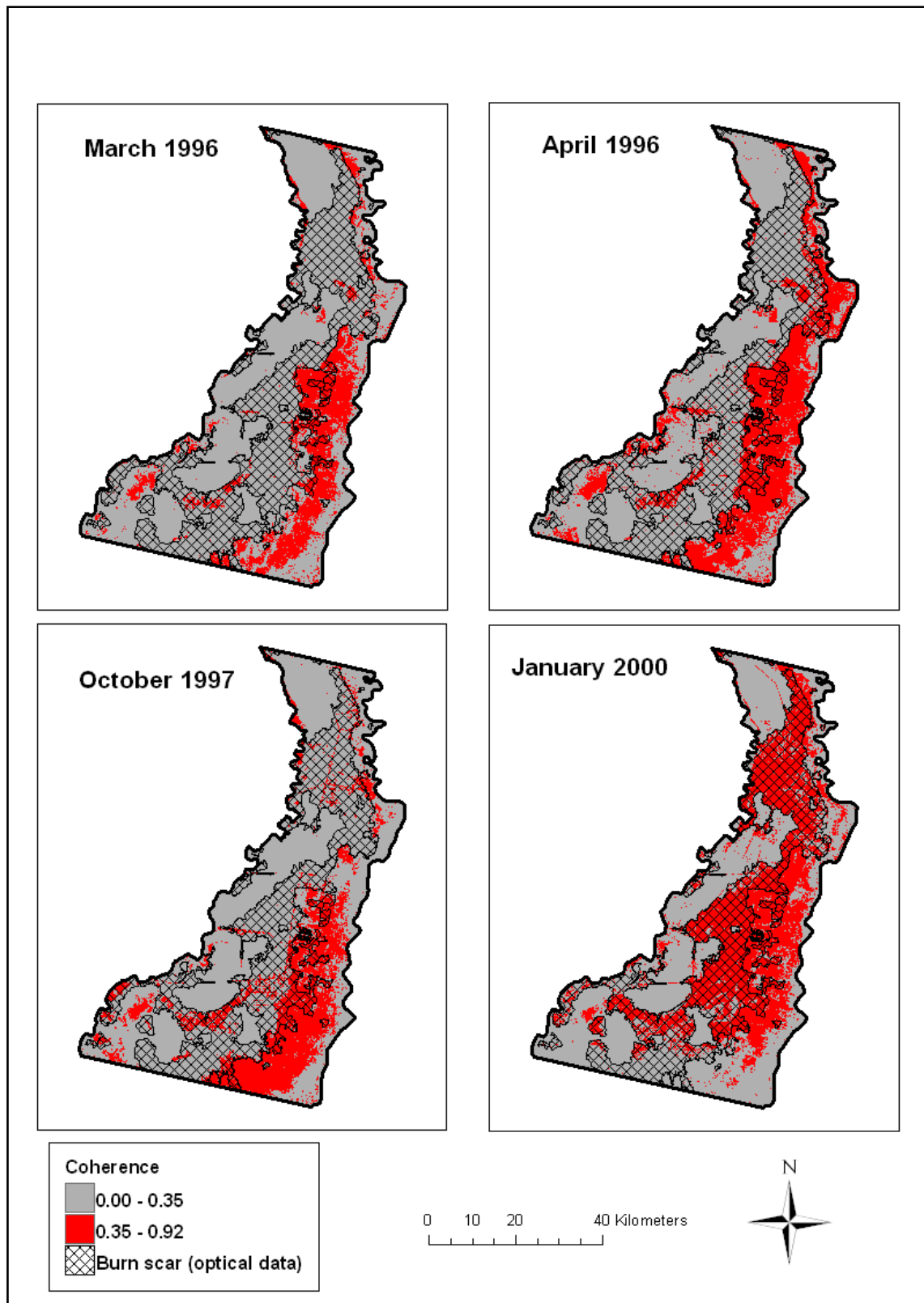


Figure 5.8: Coherence classification between March 1996 and January 2000 using value 0.35.

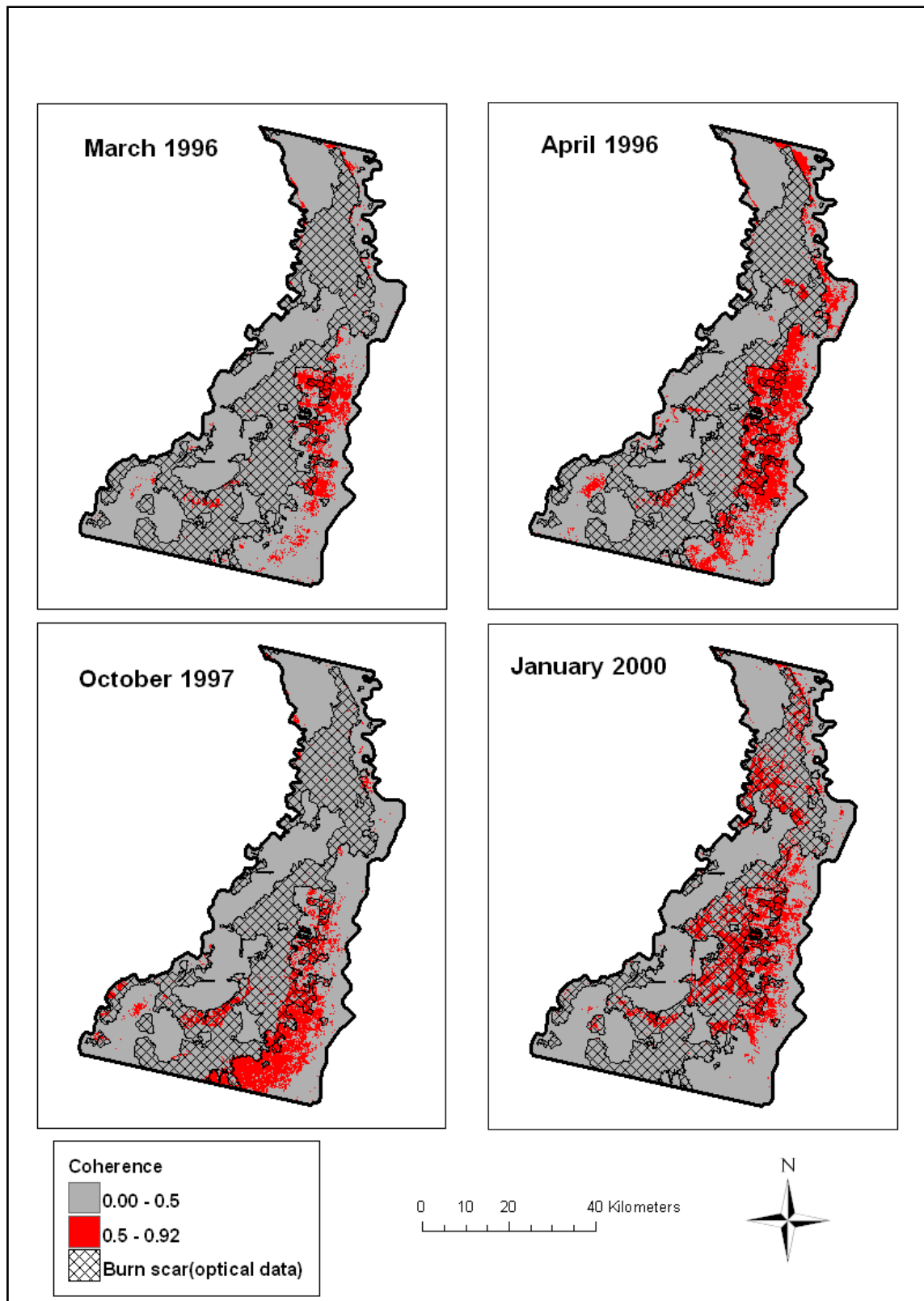


Figure 5.9: Coherence classification between March 1996 and January 2000 using value 0.5.

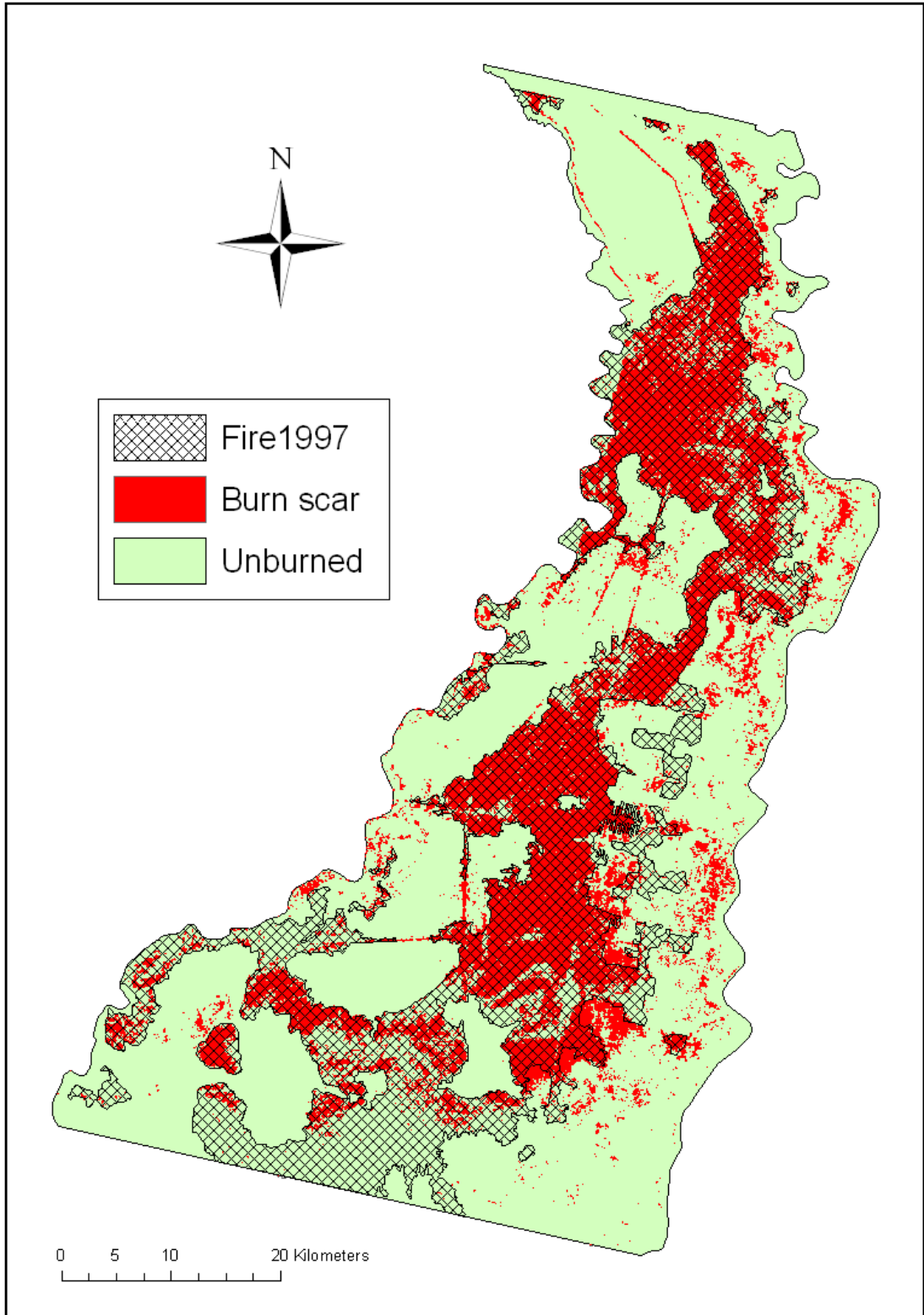


Figure 5.10: Burn scar 1997 in Block C based on minimum coherence value 0.35. Crosshatch represents burn scar obtained by optical data.

5.6 Forest burn detection using differential coherence

A simple way to analyse the changes between the two datasets is by differencing similar components of the two datasets. The coherence maps reported in Figure 5.11 allow the investigation of three different time intervals: from March 1996 to January 2000, from April 1996 to January 2000 and from October 1997 to January 2000. Only the differences between the coherence images of 1996 and 2000 datasets have been analyzed. In this difference image, it is obvious that the burn scar have been estimated by optical remote sensing data have coherence difference more than 0.2. Therefore, Burn scar areas have been chosen as the differential coherence is more than 0.2.

Figure 5.12 show burn scars in block C, which occurred between March 1996 and January 2000. Burn scars are visible as red and indicate high coherence change; unburned vegetation appears as yellow. Block C is one of the most fire-affected areas in the Ex-MRP area. Fires are found outside of the forest area and along the canals in the rest of the area. The middle south of block C has had many fires along the canals in areas with location permits for plantations and along the roads running from the Kahayan River to the west. As this is an almost uninhabited and mostly inaccessible area, fires can last for days and even weeks, out of reach of any fire suppression capacity (Hooijer *et al.*, 2008).

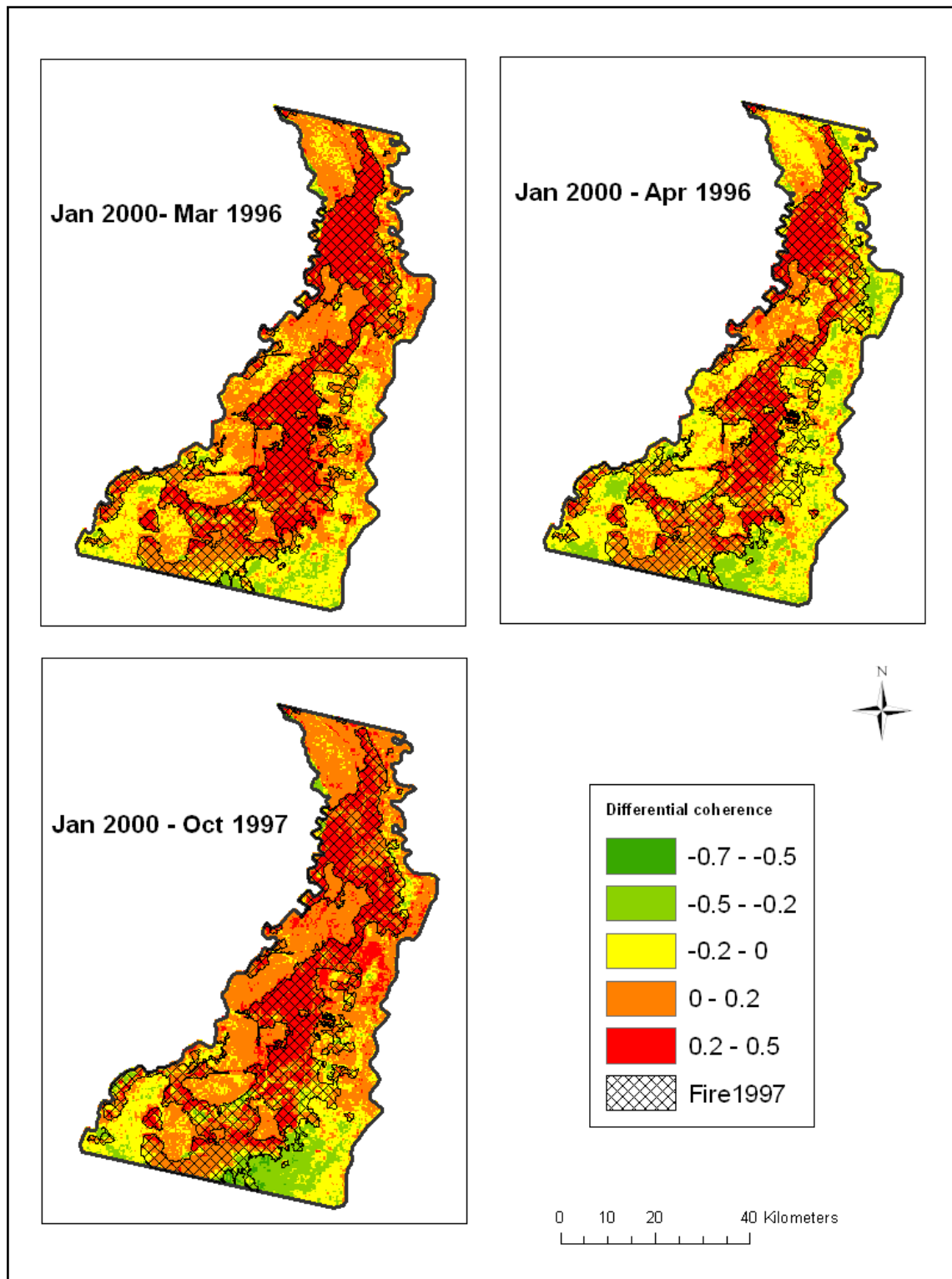


Figure 5.11: The change of coherence in Block C of three different time intervals compared to coherence in January 2000.

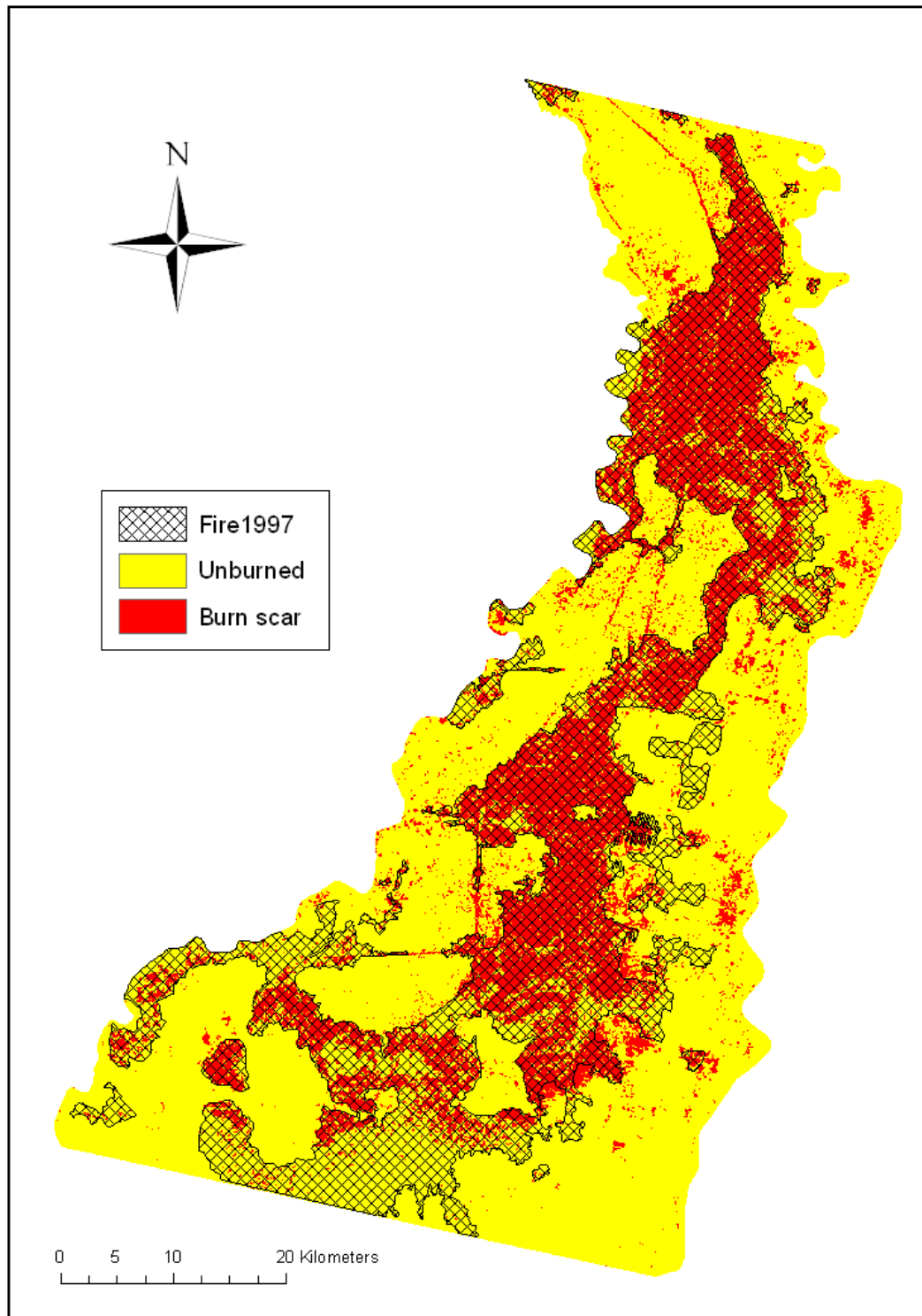


Figure 5.12 Distribution of burn scars in Block C from 1997 fires using coherence change method.

Crosshatch represents burn scar obtained by optical data.

5.7 Coherence change in Block A

Peat swamp forests in Indonesia have been subjected to intensive illegal logging that threatens the integrity and long-term stability of the peat swamp forest ecosystem. The illegal logging in Kalimantan shows some signs of abating, largely because the timber resource has almost disappeared. Large areas of forest continue to be logged and damaged however, reducing Indonesia's timber resource, threatening the survival of many species of plants and animals and depressing local economies. Based on the latest evaluation on the forestry information system at the Indonesian Ministry of Forestry (Anonymous, 1997), the Directorate General of Forest Utilization uses remotely sensed data such as aerial photographs for considering the annual allowable cutting. However, cloud cover has caused delays in acquiring aerial photographs. Therefore, SAR coherence for forest cover mapping and the delineation of deforestation has been tested in block A.

Figure 5.13 shows coherence images for the frame 6 site. The images were generated using the 1996, 1997 and 2000 tandem pairs. Between March 1996 and January 2000, remarkable changes in coherence were found in large parts of the study area. These changes occur mainly in areas with degraded forest or plantations whilst the tropical swamp forests remain relatively well preserved. Of the resulting coherence, low coherence (green) values were recorded for areas with forest and vegetated area whilst the red areas are indicative of high coherence associated with burn scars and clear cut areas. Previous deforestation and urban areas should have high coherence in both 1996 and 2000 images. For grassland, if the grass grew over the three years, a decrease in coherence may be expected. Areas that appear low in April 1996, but high in January 2000 are therefore new clearings of vegetation and candidates for recent forest clear cut and burn scars.

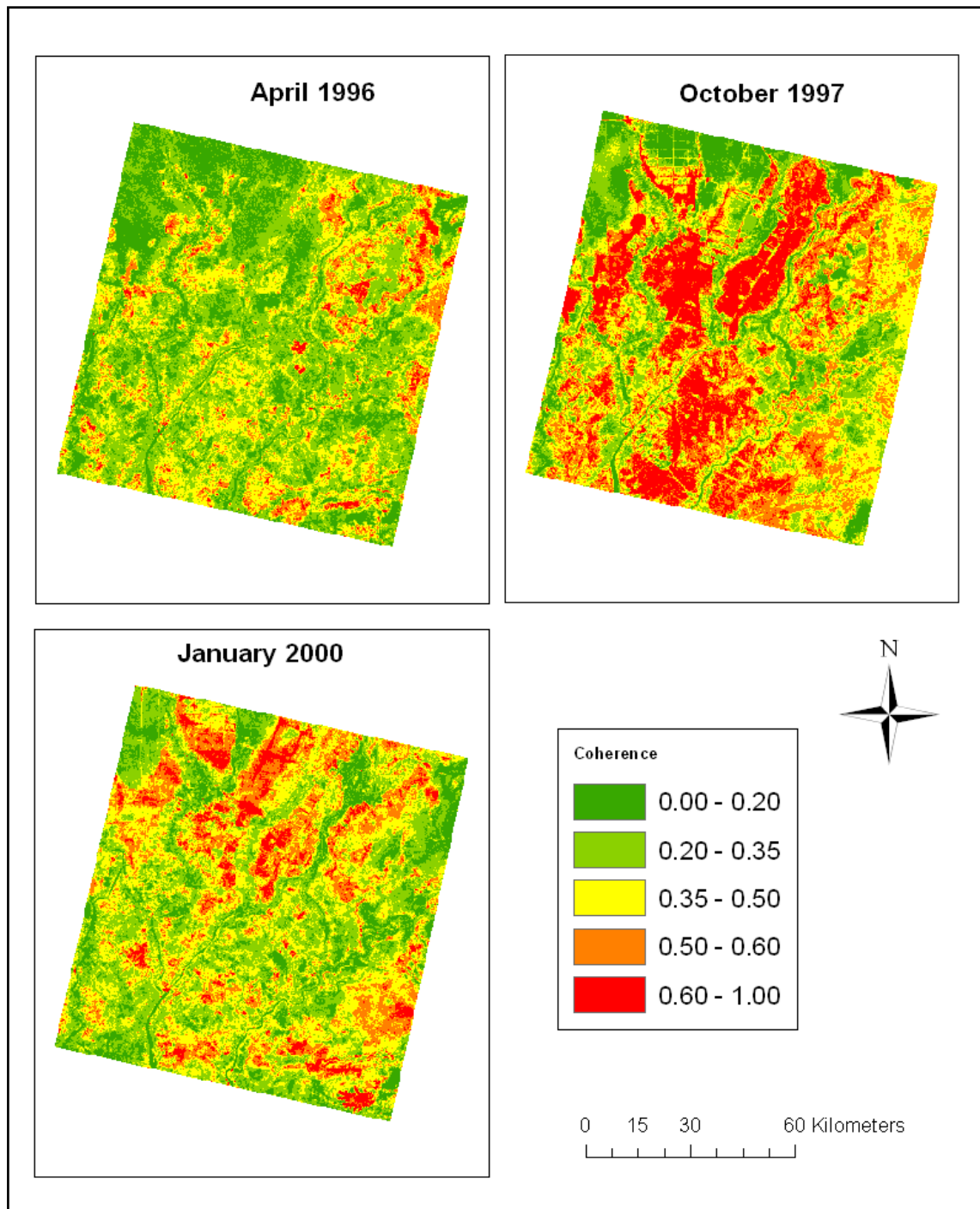


Figure 5.13: Time series of coherence in frame 6.

The coherence histograms of the whole interferometric pairs in Figure 5.14 show slightly normal distribution (Gaussian curve shape). The Gaussian curve shifts left in 1996 while it shifts right in 1997 because of low coherence in the wet season in 1996, whilst the coherence increases in the dry season and after fire in 1997. The bell-shaped curve histograms in 2000 indicate that the variation of coherence within the process is

random and likely future values could be predicted by using standard deviation equals to 0.16. However, an interesting result is found in Table 5.4 when comparing the results of Pair 1 and that of Pair 2 and Pair 3 in the forest area. Pair 1997 achieves a much higher mean coherence value (0.44) than Pair 1996 (0.30) even though it has a larger baseline. The better coherence of Pair 1997 is due to less rainfall and weak wind during the dry season which increases the backscatter and suppresses the volume scattering effect correspondingly. In the deforestation area, the response of coherence dramatically increases in all 3 tandem acquisitions as the volume scattering effect decreases.

As was shown in Figure 5.13, the coherence images cover all of frame 6 (1 million hectares). Therefore, as the areas of interest are located in block A, the coherence of block A was extracted from the whole ERS coherence map and shown in Figure 5.15. Almost half of block A has a coherence of more than 0.6 in the Pairs 1997 with a mean value of 0.44, whilst the coherence decreases in 2000 and 1996 to 0.38 and 0.31 respectively.

Table 5.4: Summary of statistical parameters for coherence change in frame 6.

	Min	Max	Mean	Median	Std.Dev
April 1996	0.00	0.93	0.31	0.30	0.15
October 1997	0.00	0.84	0.44	0.46	0.18
January 2000	0.00	0.92	0.38	0.38	0.16

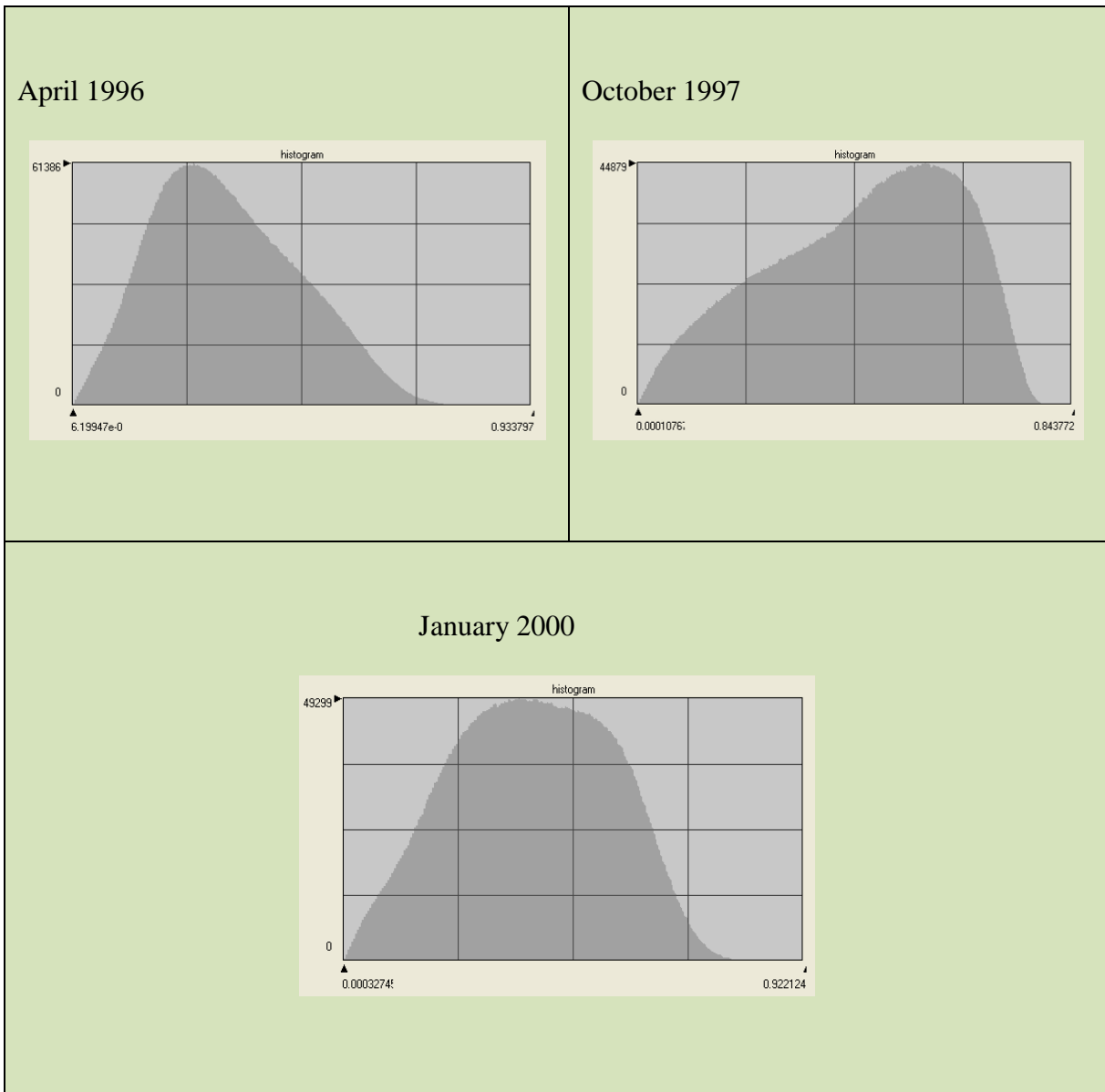


Figure 5.14: Histograms of the coherence images in frame 6.

5.8 Deforestation detection in Block A

The situation in block A is not the same as in block C because the area was under severe drainage and clear cut since 1995. By adding the influence of the fire in 1997, the land cover change has been changed dramatically in this area. However, to identify the deforested area, the 1996 and 2000 pairs were used to minimize the seasonal effects. As mentioned in identifying burn scar in block C, the tandem pairs in 1997 have not been used because there is only one tandem pair in the dry season and the comparison with other tandem pairs acquired in the wet season will not be accurate.

The coherence maps reported in Figure 5.16 show the coherence values of three different time intervals: from April 1996 to October 1997, from April 1996 to January 2000 and from October 1997 to January 2000. However, to minimize the seasonal changes, differencing the coherence of 1996 and 2000 datasets was only considered in deforestation estimation. The same assumptions that have been used to identify burn scar in block C have been used in this case. The results of the coherence change analysis suggested new deforestation and burn scar area for the value over than 0.2 and most of the resulting deforested area has an increase in coherence of over than 0.4. In this difference image, the green patches are newly cleared areas, while the yellow and red patches are areas that remained the same, either vegetated or non-vegetated for both dates.

Figure 6.17 shows the deforested area in block A, which occurred between March 1996 and January 2000. The forest loss in block A was about (50 %) of the whole study area (0.3 million hectares). Forest loss was mostly concentrated near the top of study area, which has the highest rates of deforestation. The rates of forest loss were considerably lower within Block C than block A which has the highest deforestation rates in the Ex-MRP area.

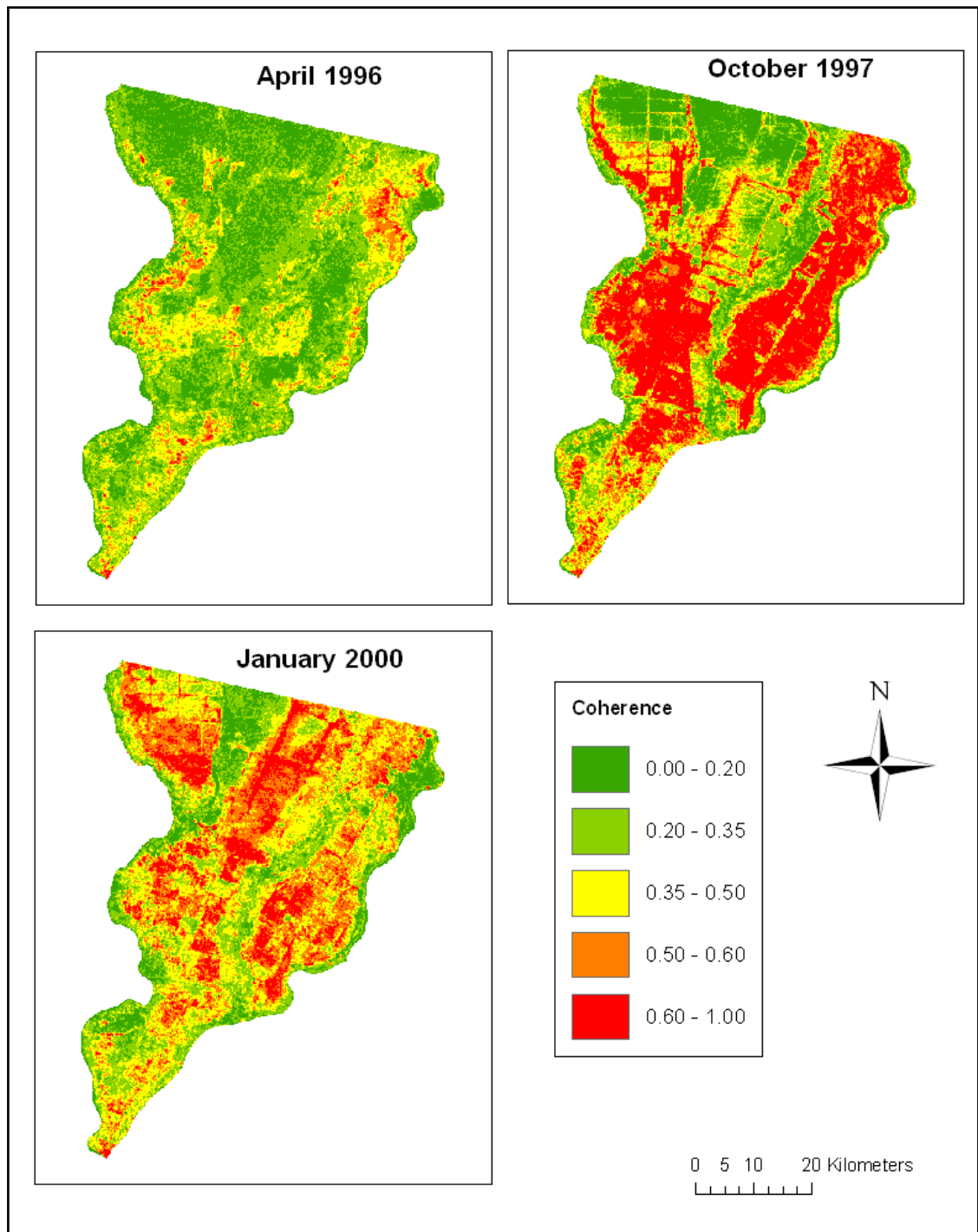


Figure 5.15: Time series of Coherence in Block A within Frame 6.

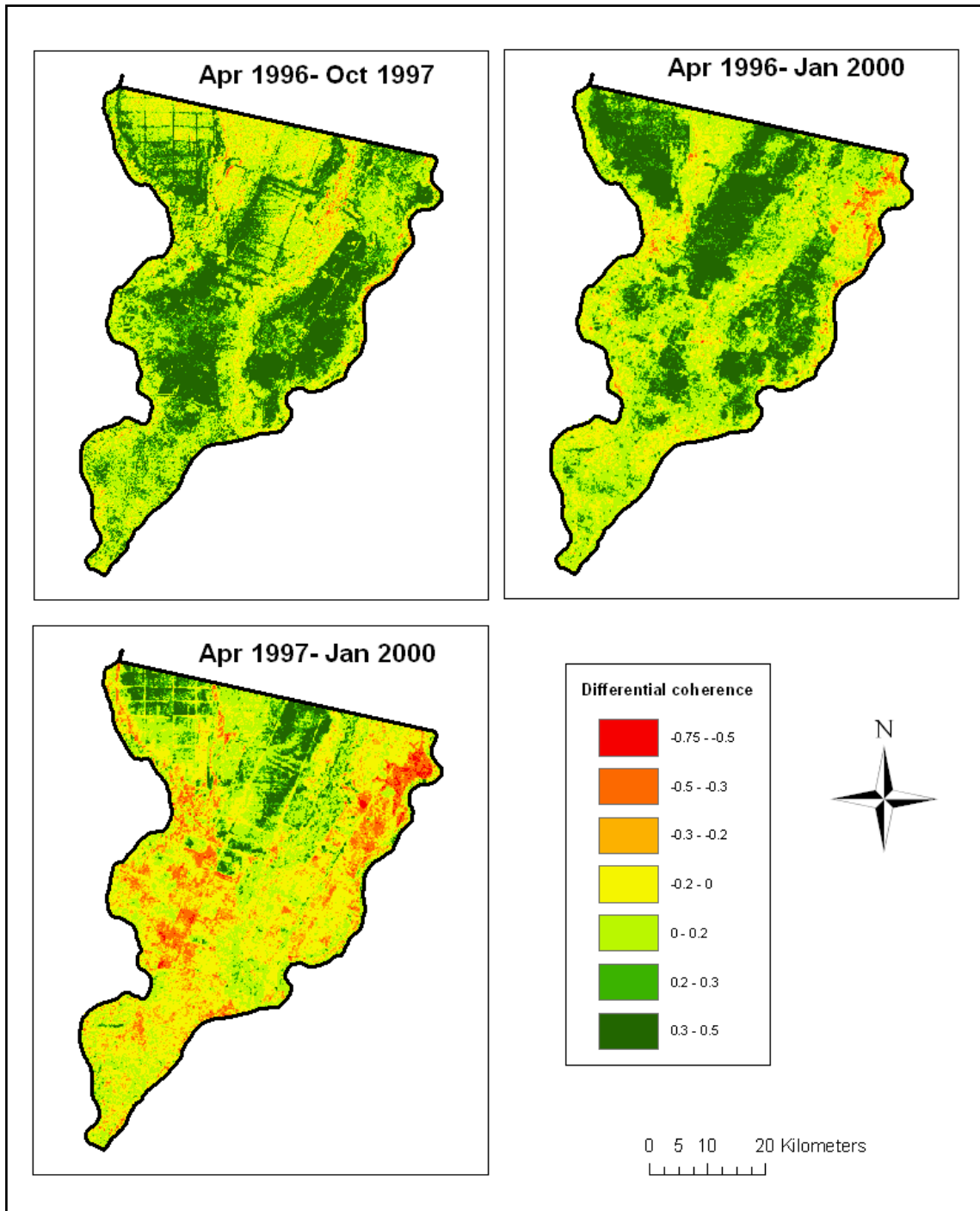


Figure 5.16: The change of coherence in Block A of three different time intervals.

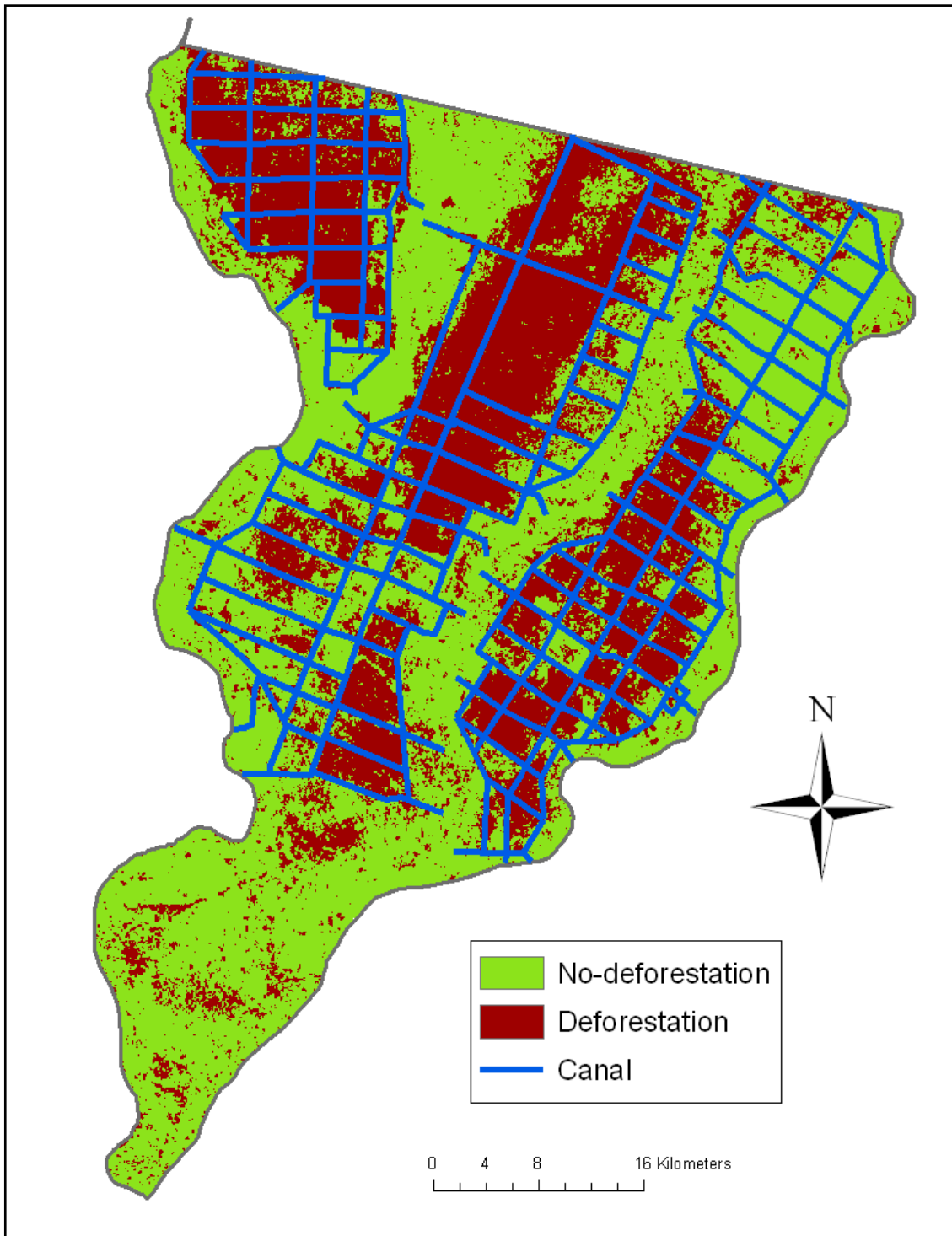


Figure 5.17: The deforestation area in Block A as derived from ERS images based on differential coherence value of more than 0.2.

5.9 Discussion

Many studies have highlighted that the majority of deforestation in tropical peatlands forest are directly associated with human activities (Siegert *et al.*, 2001, Langner and Siegert, 2007). Local people have used fire as the way to clear and maintain their land, keeping it free of woody growth (Rieley and Page, 2005). Land clearing increased dramatically under the transmigration programme that was supported by the Indonesian government to move more than a million poor people from crowded Indonesian islands to less populated provinces such as Central Kalimantan province (Fearnside, 1997). A lack of knowledge of crop cultivation on peat and other natural problems forced the transmigrants to look at alternative sources of income such as illegal logging. Over logging and illegal activities degraded the forest condition making logged forest more vulnerable to future fires (Siegert *et al.*, 2001, Cochrane and Chulze, 1999). However, the most extensive forest loss occurred following the implementation of Ex-MRP. The intensive drainage infrastructure, consisting of numerous canals, had an impact on the peatland hydrological system and increased the risk of fire. The canals allowed easier access for people into previously remote areas of peatland and their activities provided ignition sources. In addition, the widespread fires during 1997 mainly affected previously disturbed (logged) and drained peat swamp forest which was at higher fire risk than undisturbed forest.

Various assessments have been made of the amount of land in Indonesia that was damaged by the 1997 fires. Initial estimates indicated that approximately 4.5 Mha were affected (Liew *et al.*, 1998), but this was subsequently increased to 9 Mha (BAPPENAS, 1998, Page *et al.*, 2002). However, in terms of measuring changes in forest cover, it is important to be able to detect when, where and how much of an area

of forest has been burnt or cleared. Therefore, the first objective of this study is estimating the amount of deforestation and burnt area in central Kalimantan, Indonesia due to fire in 1997 by using interferometric coherence technique.

The 1997/98 fire was the worst ever fire catastrophe encountered in Central Kalimantan, Indonesia. 5.2 million ha or about 25% of the entire province was fire affected. Almost 2.3 million ha was tropical swamp forest. Almost 75% of the plantation areas (forest, oil palm, etc.), that were located within the 1997/98 fire zone have been fire affected, a large number of them severely. Several approaches were undertaken to determine the extent of the 1997 forest fires using optical and microwave sensors. Studies were based on the visual interpretation of multi-temporal SPOT quicklook mosaics, the evaluation of NOAA (National Oceanic and Atmospheric Administration) -AVHRR (Advanced Very high Resolution Radiometer) and the combined use of ERS-2 SAR coherence data and ATSR (Along Tracking Scanning Radiometer) data. Moreover, with the combined use of ERS-SAR and ATSR, Antikidis *et al.* (1998) produced a first estimation of the forest surfaces burnt in Central Kalimantan in 1997. Out of an area of 21.76 million ha analyzed, a total of 588,000 ha of forest were burnt at that time. This number was corrected later to 1.8 million ha.

ERS is working in C-band and this radar signal cannot reach the ground in forested areas with the water content and the structure of the canopies mainly influencing the backscatter (Kuntz *et al.*, 1999). However in burnt forest areas with canopy removed, the radar signal indicates the scattering from this burnt ground layer. The ground soil's radar reflectivity depends on its moisture content, so dry soil appears dark in radar images while moist soil has a bright signature (Ulaby *et al.*, 1986). SAR is capable of

mapping the fire scar in tropical forests for two reasons: the first one is related to the increased moisture in post-fire soil while the second reason is about SAR's sensitivity to soil moisture (Bourgeau-Chavez *et al.*, 2001; Hilland *et al.*, 1998). Fire removes a large portion of the vegetation layer which shades the ground, thus increasing the microwave signals reaching the ground. In addition, fire removes much of the dead organic matter layer that insulates the ground (Huang and Siegert, 2005). Kasischke *et al.* (1992) found that in ERS SAR images of Alaska, fire scars reflected 3-6 dB brighter than adjacent unburned forest while Huang and Siegert (2005) found that fire scars had a backscatter signal 2-4 dB higher than the surrounding unburned forest. However, the backscatter dynamics of fire scars strongly varied with seasonal changes (Huang and Siegert, 2006; Bourgeau-Chavez *et al.*, 1997; Luckman *et al.*, 1998). Bourgeau-Chavez *et al.* (2002) found that seasonal variations of fire scar visibility in SAR images occurs all over the boreal region.

Interferometric coherence, between image pairs, has proven to be a valuable source of information in forestry (Balzter, 2001). Coherence properties have been used by Askne *et al.* (1997) to identify forested/non-forested areas and the interferometric effective height of the forest. Wegmüller and Werner (1997a) used ERS SAR coherence interferometry to map different types of land changes due to farming activity, vegetation development and meteorological influences. They found that during the main growing season, low interferometric correlation resulted from both dense vegetation and farming activities. Harvesting was recognized by the high interferometric correlation of the post-harvest bare or stubble fields.

The size of the estimation window is a crucial factor determining the coherence estimate and has been tested in this study to detect any influence on the burn scar identification. The mean and maximum coherence decreased, whilst the search window size increased, but this change was almost negligible and will not have a big influence in the burn scar coherence change in further analysis. In addition, no evidence of weighting function effects were observed on the coherence image. Only non-weight function overestimates the coherence for more than 0.25 over most of the area. Therefore, using any weight functions over the search window should give more accurate coherence estimation in forested areas. By analyzing the coherence change between 1996 and 2000 in the Ex-MRP area, it was found that the coherence increased dramatically due to fire and deforestation between observations. However, the temporal effects, which follow from physical changes in the surface over the time period between observations and seasonal weather, affected the coherence more than baseline length.

A first visual inspection of the coherence change has been used to identify the burn scar in Block C. by comparing the coherence and the burn scars identified by Hoschilo (2009) using optical remote sensing methods, it was found that coherence value (0.35) allowed maximizing the discrimination of burnt areas from unburned areas and thus this was selected as the input for the burnt-unburned forest classification. This approach shows that the burnt forest area has a coherence value of more than 0.35 after three years from time of fire 1997. It was also shown that the coherence in January 2000 increased by over 0.2 with respect to forest coherence in the March 1996 image. Therefore, an alternative approach was adopted using differencing coherence of the two datasets in block C and block A. The coherence change in block C shows that the coherence of burnt areas increased between 0.2 to 0.4 between March 1996 and January 2000. By

contrast, the coherence change value for more than 90 % of the deforested area exceeded 0.4.

A basic verification of burn scar mapping in both block C and block A was done by overlaying burnt area that have been estimated by Page *et al.* (2002) and derived from analysis of post-fire Landsat TM 5 and multi-temporal ERS SAR images covering before and after the 1997 fires (Figure 5.18) onto the ERS-SAR coherence classification result. The outlined area of the ERS-2 SAR burn scar map corresponded well with the fire affected area represented by Landsat TM 5 and multi-temporal ERS SAR hot spots. Figures 5.10 and 5.12 show that fires were most abundant and persistent in the degraded peat areas and the forest edge while forested areas did not burn. Fires were relatively most numerous in Blocks A and C. Page *et al.* (2002) calculated that 32% (0.79Mha) of the area had burned, of which peatland accounted for 91.5% (0.73 Mha). Roughly half (47.4%) of the fire-damaged area was peat swamp forest, most of which was previously logged or fragmented.

In this study, a quantitative analysis in block C showed that, for 1997, the total area investigated by INSAR coherence was (333,121.03 ha). Out of this, up to January 2000, about 90,000 ha (28 %) had burnt. Table 5.5 shows quantitative results of this analysis. Both coherence methods identified almost the same burn scar area. It can be seen that the SAR burnt area represented, on average, 71% of the areas identified by Hoscilo (2009). The burn scar estimates reported here for Block C are likely to be underestimates and are lower than those reported by Hoscilo (2009) by approximately 40,000 ha. Most of the different areas are located in the south of block C. From the coherence image changes in Figure 5.10 it is clear this area has a low coherence even in

the dry season of 1997 and it is less likely to be burnt. Indeed, many burned areas which have been identified by Page *et al.* (2002) using only ERS SAR images were found undetectable by Landsat TM 5, owing to plant re-growth (Figure 5.18). These areas which are mostly plantation and pervious burnt areas have a high coherence in all tandem images since March 1996 and therefore could not be forest or plantation areas, so burn scar estimation based on coherence assessment seem to be more accurate than the estimation using optical data alone. However, as burn scar area has been identified by different optical and microwave methods; a one to one correspondence between the two burnt area estimates should not be expected.

Table 5.5: Comparison of burn scar area identified by different methods.

	Block C area(hec)	Burn scar (hec)	Precentage (%)
First method	333121.03	94345.14	28.32
Second method		89038.32	26.73
Optical method		133450.35	40.06

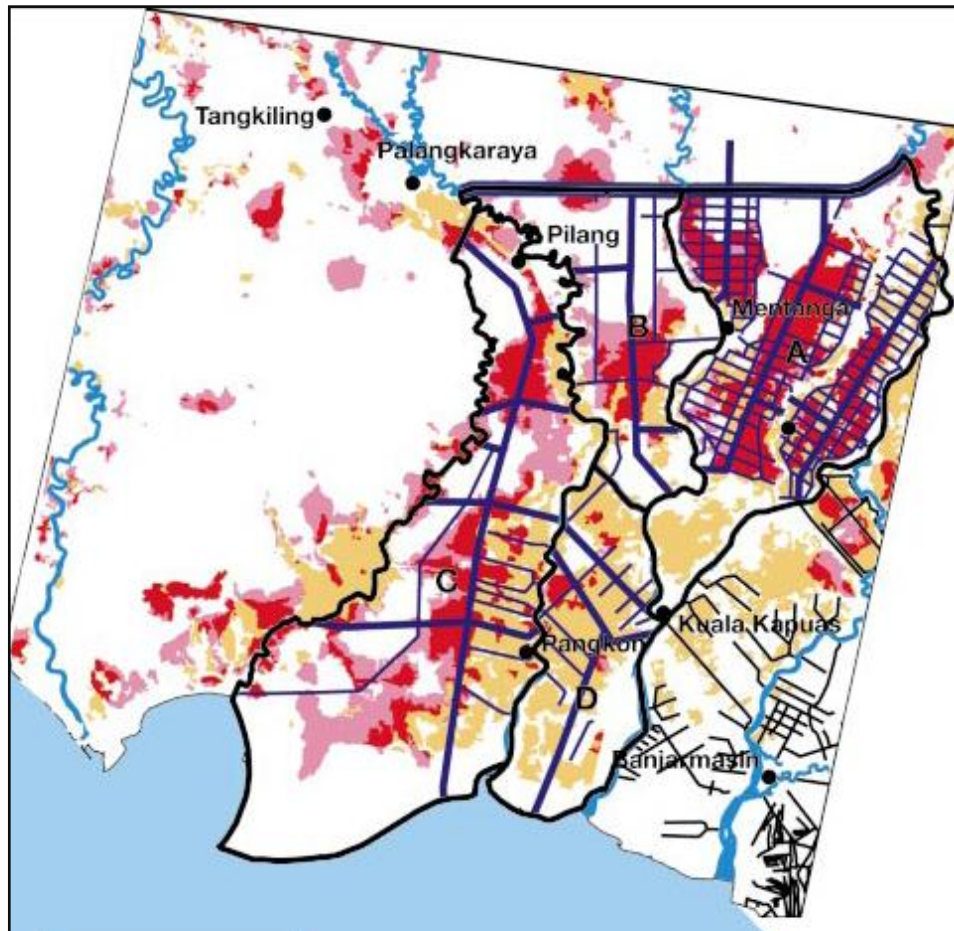


Figure 5.18: Study site in Central Kalimantan, Borneo, Indonesia. Burned area derived from analysis of post-fire Landsat TM 5 and multi-temporal ERS SAR images burnt areas detected by both Landsat and ERS are indicated in red; burnt areas detected only by Landsat are shown in palevioletrered; burnt areas detected only by ERS SAR and undetectable by Landsat TM 5, owing to plant re-growth are shown in moccasin (Source: Page et al., 2002).

The extensive fire damage caused in 1997 in block A has accelerated changes already being caused in tropical peatlands by forest clearance and drainage. This area is extremely fire prone in the dry season and has frequently burnt. Most of the original forest is severely degraded or has disappeared altogether, often subsequently damaged by (repeated) fires. Two linked factors have played key roles in determining the distribution of fire scars in block A: degree of forest disturbance and lack of peatland hydrological integrity. Areas of degraded peatland experienced excessive water-table

drawdown during the 1997 ENSO drought whilst, in contrast, large areas of peat swamp forest, despite experiencing a significant drop in water table, were relatively unaffected by fire. In the study area, Block A was a major location for fire hot spots because the area was criss-crossed by an extensive system of wide and deep channels that facilitated excessive drainage of the peatland landscape. Logging operations raise the fire risk in natural forest. Many people were able to access the previously inaccessible interior of this peatland landscape to exploit the residual timber resources, mostly using fire in the process. Wide opening up of stands, bad logging practice (conventional logging) and large amounts of logging waste result in an increased fire danger. Forests which had been logged shortly before the fire event especially were very seriously damaged.

Figure 5.17 showed that areas subjected to fires and deforestation between 1996 and 2000 in block A were all located within close proximity to canals and the extent of burn scars declined with distance away from these features. The peat is likely to have burnt, at least close to canals, along many transects. However, the exact burning history of the area is unknown. By assessing logging activity in coherence images for 0.3 Mha in the study area in block A between 1996 and 2000, deforestation (logging, fire) had increased by 44% during this period, thus making the remaining forests more susceptible to fire in the future. The official figure for total deforestation area identified in this study stands at 153,000 ha, although the actual figure is likely to be much larger. The statistics on forest deforestation damage are very poor in Block A. In the absence of proper data, it is difficult to arrive at the accurate losses from the forest through deforestation. In recent years, the expansion of oil palm and timber plantations, together with illegal logging have been identified as the driving forces of the destruction and of deforestation overall

This study agrees with the findings of other authors, that SAR interferometry (InSAR) products, especially coherence images, can optimize the use of ERS SAR tandem images for land use and land cover mapping. The results presented here confirm that tropical peat swamp forest and vegetated areas have low coherence, while non-vegetated areas have high coherence. In addition to this, an accuracy assessment of two images when compared with optical data has shown that the coherence images provide a more acceptable land cover map of the study area owing to the all weather capability of SAR.

5.10 Limitations

Among the limitations of the current research are the following;

- A problem with the interpretation of the results in deforestation in block A is that there is no means of differentiating between clearings due to fire or other clearings. In many cases land clearing without fire might be misclassified as burnt area. That is why the term “deforestation” has been used in block A rather than burn scar. Whilst in block C, logging and clearing activities are less frequent and have a lower influence on the burn scar classification. It appears that the coherence method has to rely on SPOT or other high-resolution remote sensing images to assist in such differentiation. SPOT data can distinguish the burnt areas based on colour as well as the fire smoke plumes.
- Lack of available ERS images before and after the 1997 fire that has been taken in the dry season. Some studies suggested that the most suitable image pairs for burn scar identification were the ones with both images acquired under dry weather conditions. Weather conditions have a strong impact on the coherence because rainfall before and in-between ERS-1/2 tandem acquisitions can result

in a significant loss of correlation that can affect the accuracy of identifying burn scar and lead to an underestimation of the burnt areas.

- The tandem pair images should have similar baselines to reduce the effects of baseline on resulting coherence images. It has been shown that coherence decreases approximately linearly with the increase in baseline length. The longer the baseline is, the lower the coherence.

5.11 Further work

Suggestions for further areas of research that build on the results of this study are described below.

- Further burn severity analysis using coherence change to improve understanding of the links between burn severity and coherence change. The methods that have been used in this study are not able to recognize different burn or deforestation severity.
- Future work should focus on integration of interferometric information, including coherence with radar backscatter information to characterize change in biomass and structure and the distribution of burn scar and deforestation in the study area. Moreover, a linkage between coherence change and backscatter intensity should be developed for tropical swamp forest monitoring.

5.12 Summary

To sum up, this study shows that InSAR techniques can detect land cover change including old and new burn scar and deforestation areas using a coherence technique. Based on the verification results, it has shown that the burned areas mapped by InSAR coherence maps have minimum coherence value around 0.35 and the coherence change not less than 0.2 before and after the fire in 1997. However, the burn scar areas that have been detected in this study have a high accuracy and indicates even a slightly underestimate of the size of the 1997 fire affected areas. There was an excellent agreement between the classified burn scar and polygon burnt area obtained by optical remote sensing methods. This information on fire spread and fire distribution is important to tropical swamp forest fire monitoring and assessment because the region is covered by persistent cloud and haze during fire seasons, which makes optical sensors, of limited use.

The burn scar areas that have been estimated by using the InSAR coherence technique provides valuable information about their locations for the prevention of future fires in the same area. In conjunction with the exact location and extent of burn scars, it becomes feasible to determine important data on CO₂ emissions. Peat drainage, fires and deforestation do not just emit carbon into the atmosphere, they also destroy one of the most important terrestrial carbon sinks, which takes carbon out of the atmosphere and helps to regulate the global climate. If logging practices are not changed and fire prevention measures are not implemented, future fires will follow the logging activities even deeper into the central areas of Central Kalimantan. Fire management is a key issue in achieving the goal of sustainable forest management.

Chapter 6: InSAR DEM generation

6.1 Introduction

This chapter presents the results of generating DEMs from ERS tandem pairs using two interferogram calculation methods (intensity, orbit) with two phase unwrapping (PU) techniques (Branch Cut(BC) and Minimum cost flow(MCF)). Adaptive filtering was applied to the previous methods to test the influence of filtering on the resulting DEMs. The processing steps are supported by differential GPS measurements (DGPS), which were used to generate DEM and assist DEM accuracy. Two approaches for evaluating DEM quality have been used in this study; empirical approach and visual approach. The empirical approach mainly depends on validation datasets (check GCPs or reference DEM) to calculate the statistical quality measures such as standard deviation or RMSE. Qualitative assessment can be done through visual appearance of a DEM and DEM derivatives. Visualization provides a powerful mechanism for identifying pattern, spatial distribution and possible causes of DEM errors.

6.2 Phase Unwrapping

Phase unwrapping, which restores the real phase difference from repeated observations of the same terrain point, is one of the main steps in InSAR processing. The accuracy of real phase difference directly influences the precision of DEM generation or deformation detection. The ERS SAR observations areas were covered by high dense vegetation or forest canopy, therefore the phase noise was large (Zebker and Villasenor, 1992). Therefore, before unwrapping the phase, it is important to improve fringe

visibility and reduce phase noise. To deal with this condition, an adaptive interferogram filtering algorithm (Goldstein and Werner, 1998) was applied to the flattened image. The results of phase unwrapping in frame 4 using ERS tandem pairs acquired in October 1997 are illustrated in Figure 6.1. The colour in the image represents the difference in the phase of the radar signal image that has been acquired with one day interval time. Phase images tend to have colour bands called fringes where one complete fringe cycle represents a 2π phase shift. A fringe can be thought of as a collection of contours where each unique colour level within and along the fringe corresponds to a constant phase difference. The constant phase difference within a fringe is directly related to constant path difference. The black parts in this figure represent interferogram pixels that cannot be unwrapped. Such pixels do not contribute to the generation of DEM and result in holes in the DEM.

The implementation of the BC algorithm provides a robust and efficient unwrapping solution that works well for images with high correlation. Branch-cut algorithms tend to “wall-off” areas with high residue density (for example, a lake in a repeat-pass interferogram where the correlation is zero) so that holes exist in the unwrapped solution as it is shown in Figure 6.1. Under these certain conditions applying adaptive filtering many times with a smaller coefficient and decreasing window size (128, 64, 32, and 16) can facilitate the unwrapping especially in low coherence area. Filtering the signal will reduce the residues in any given image to make the selection of appropriate cuts feasible. The cost of this reduction might be a loss of spatial resolution in the final DEM. It is clear that adaptive filtering was filling up all the gaps that were left by the BC method, by interpolation these holes using surrounding phase values.

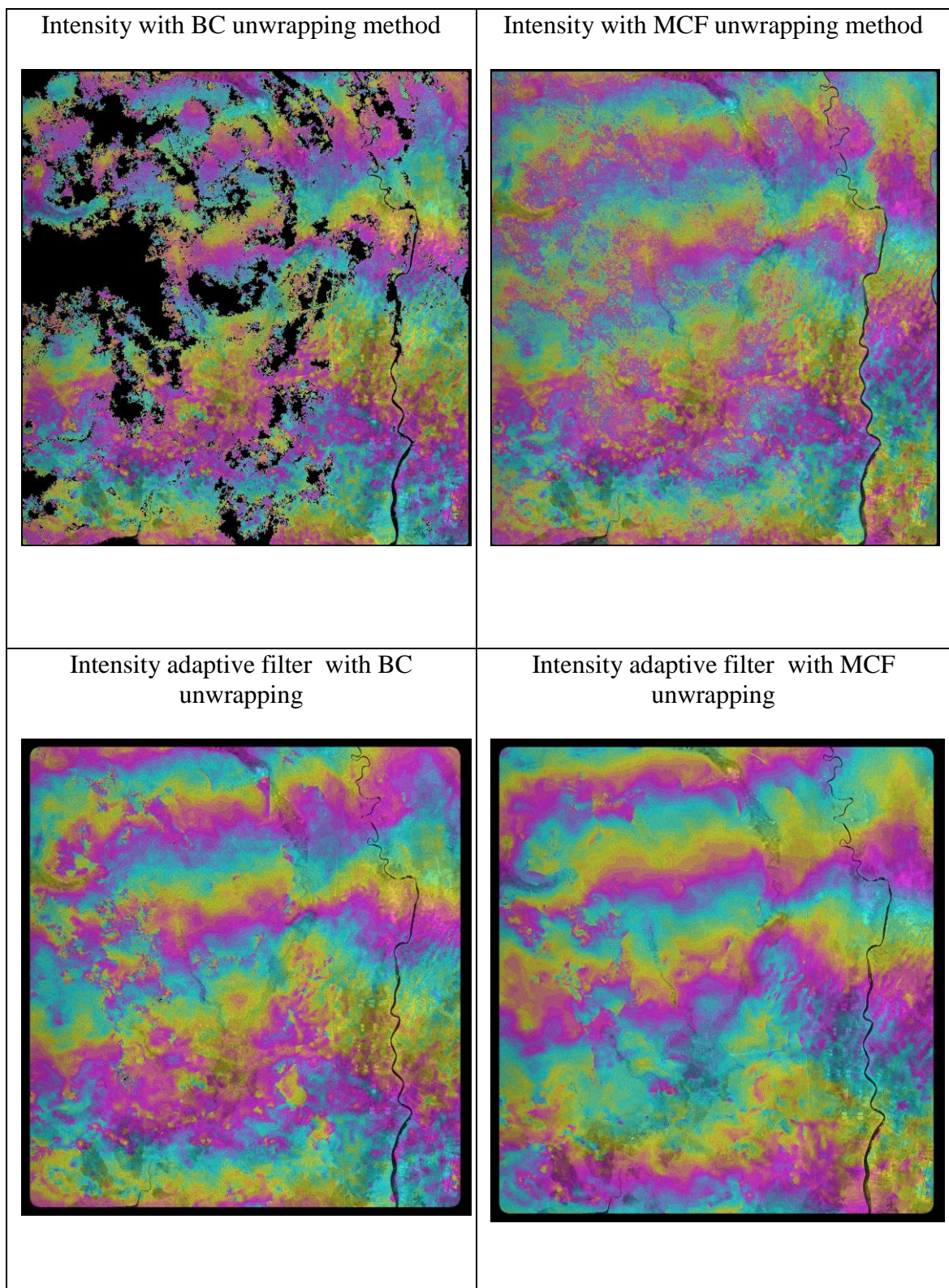


Figure 6.1: The unwrapped phase maps for the interferogram generated by ERS tandem pair acquired in

October 1997 in frame 4.

MCF algorithm (Costantini, 1998) was used to deal with a low coherence area due to dense forest and vegetation. This technique is a global optimization technique to the PU problem that gives the advantages in dealing with the gaps in an area caused by low coherence by considering their density in triangular network. MCF algorithms provide continuous solutions even where the phase noise is high. This can be considered as both a strength and a weakness of the MCF approach since, on one hand MCF leaves no holes, but on the other hand it may provide erroneous data in these areas.

By analyzing the statistical results of the PU methods in Table 6.1, it can be seen that the difference between global and local algorithms consists of regions with different mean levels. The borders between the regions are sharp. The mean increased by applying adaptive filtering in both unwrapping approaches, whilst standard deviation is slightly lower when using adaptive filtering many times.

With the BC method, error spread can be prevented in the unwrapping process, but serious phase inconsistencies exist in the phase distortion region; In comparison with the MCF method, this keeps better consistency over the whole image. It is obvious that the discontinuity region of the unwrapped map for MCF is less than that for the BC method, which means that the proper weight unwrapping method actually plays a role in reducing errors, preventing error spread and improving the accuracy of unwrapping. The PU accuracy assessment by the elevation comparison method will be presented in the following chapters. It is an indirect precision estimation method of unwrapping, that is, using same processing steps to generate DEM after PU of different methods, transmitting the errors of PU to DEM, then assess the accuracy of PU through comparison of DEM accuracy generated.

Table 6.1: Summary of statistical parameters for phase unwrapping.

	PU methods	Mean(radian)	St. Dev(radian)
BC	Intensity	1.81	13.89
	Intensity adaptive filter	2.18	12.55
MCF	Intensity	-11.39	13.32
	Intensity adaptive filter	-16.83	12.60

6.3 DEM generation

Once the interferometric phases are unwrapped, an elevation map in SAR coordinates is obtained. The SAR elevation map has been referred to WGS84 ellipsoid and re-sampled to Universal Transverse Mercator (UTM) projection system. Since this study is mainly focusing on the evaluation of the quality of derived DEMs from ERS scenes, two sub-regions from the two ERS scenes have been extracted for this study: Maliku in block C, and Dadahup in block A (see section 4.1). By using two interferogram calculations, applying two PU and run adaptive filtering once and for many times with a smaller coefficient and decreasing window size, six and eight DEMs for each tandem pairs have been generated for Maliku and Dadahup respectively. That means twenty four DEMs in total have been generated for each test site. The DEM validation is conducted through several techniques such as visual and statistical analysis. The descriptive analysis of the DEMs in each site will be introduced in the following sections.

6.3.1 Maluku: Digital elevation model

Figure 6.2 show six DEMs generated by tandem ERS pairs acquired in October 1997. Visual comparison between DEMs generated using the BC unwrapping method shows many holes in the DEM. These areas cannot be unwrapped due to low correlation between master and slave images. These holes disappear when adaptive filtering is applied or when using the MCF unwrapping method. However, filling the gaps by running adaptive filters many times or by using MCF PU method might produces incorrect elevation values for these areas. The histograms of the six DEMs in Figure 6.3 can illustrate the discrepancy between different DEMs. The intensity DEM with BC unwrapping method has a minimum value of -37.25 m representing the weakness of the technique compared to other techniques that have been used.

Figure 6.4 shows four DEMs generated by four tandem ERS pairs at different times with spatial resolution (40x40 m). As the terrain is flat in the study area, the 40 m DEMs can be suitable for this type of land relief in terms of keeping the topographic information and reducing the noise. These DEMs have been derived by using an intensity method to calculate the interferogram, running adaptive filtering many times and applying the MCF unwrapping algorithm. Visual comparison between DEMs shows that height values from the March 1996 DEM are the smallest values among other DEMs. On the contrary, the left side of the April 1996 DEM image shows high values (more than 60m) compared to other DEM values.

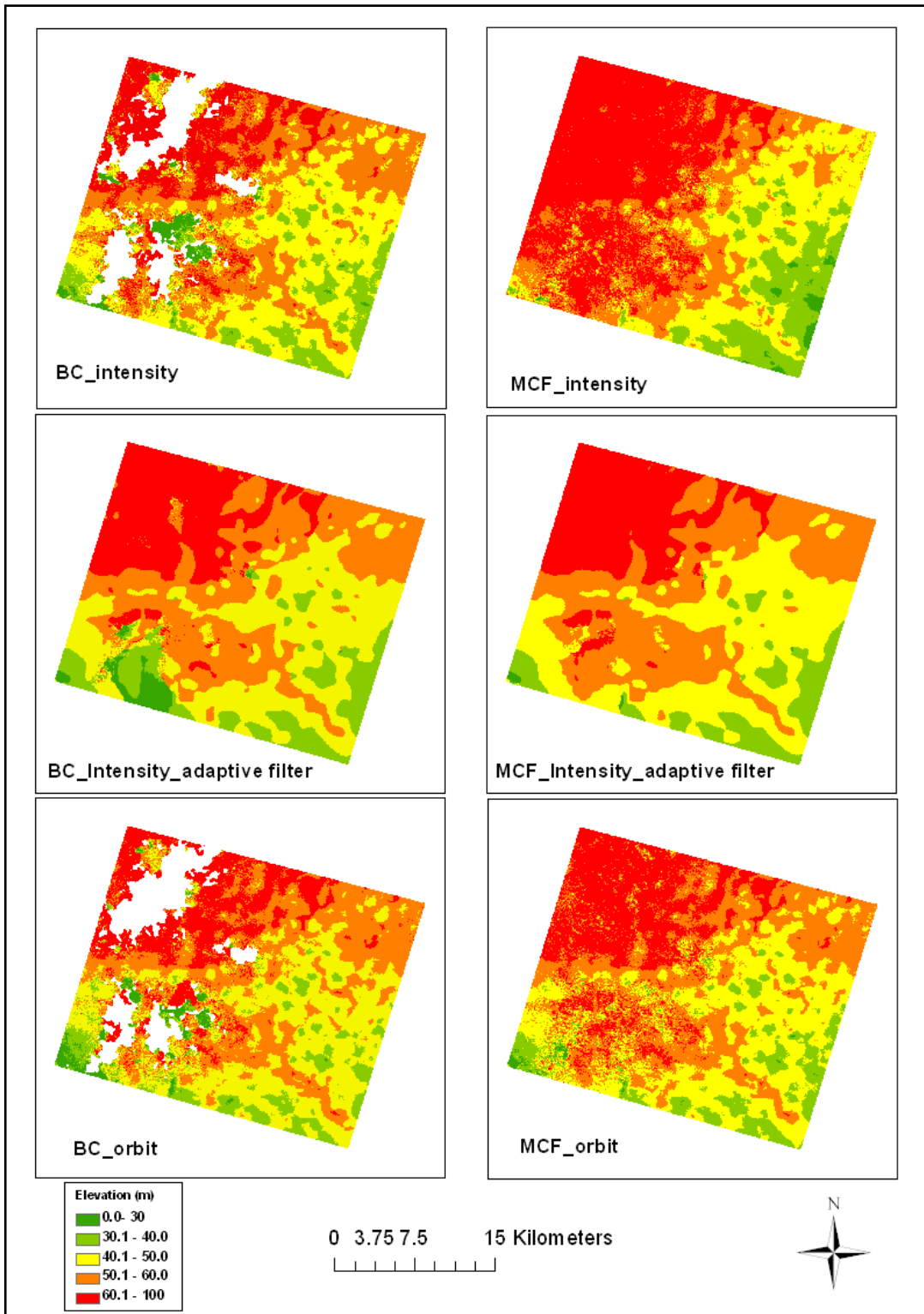


Figure 6.2: DEM for the Maliku test site generated from ERS-1/2 tandem radar images using different processing techniques.

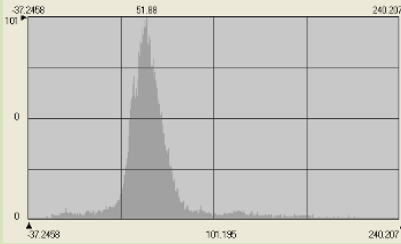
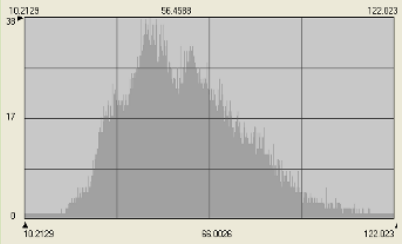
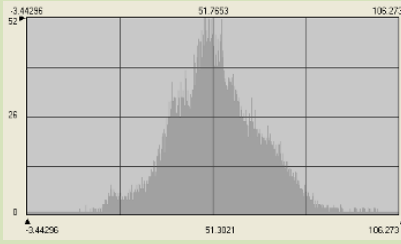
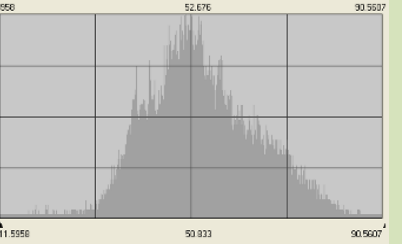
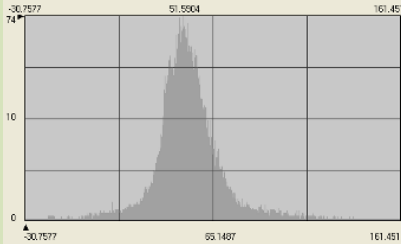
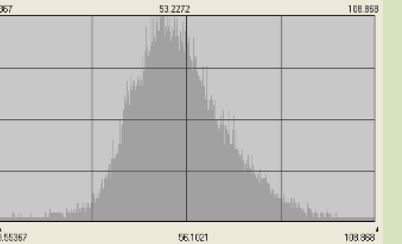
October 1997 DEMs	BC unwrapping method	MCF unwrapping method
Intensity		
Intensity with adaptive filter		
Orbit		

Figure 6.3: Histograms of elevation frequency of 1997-DEMs in Maliku.

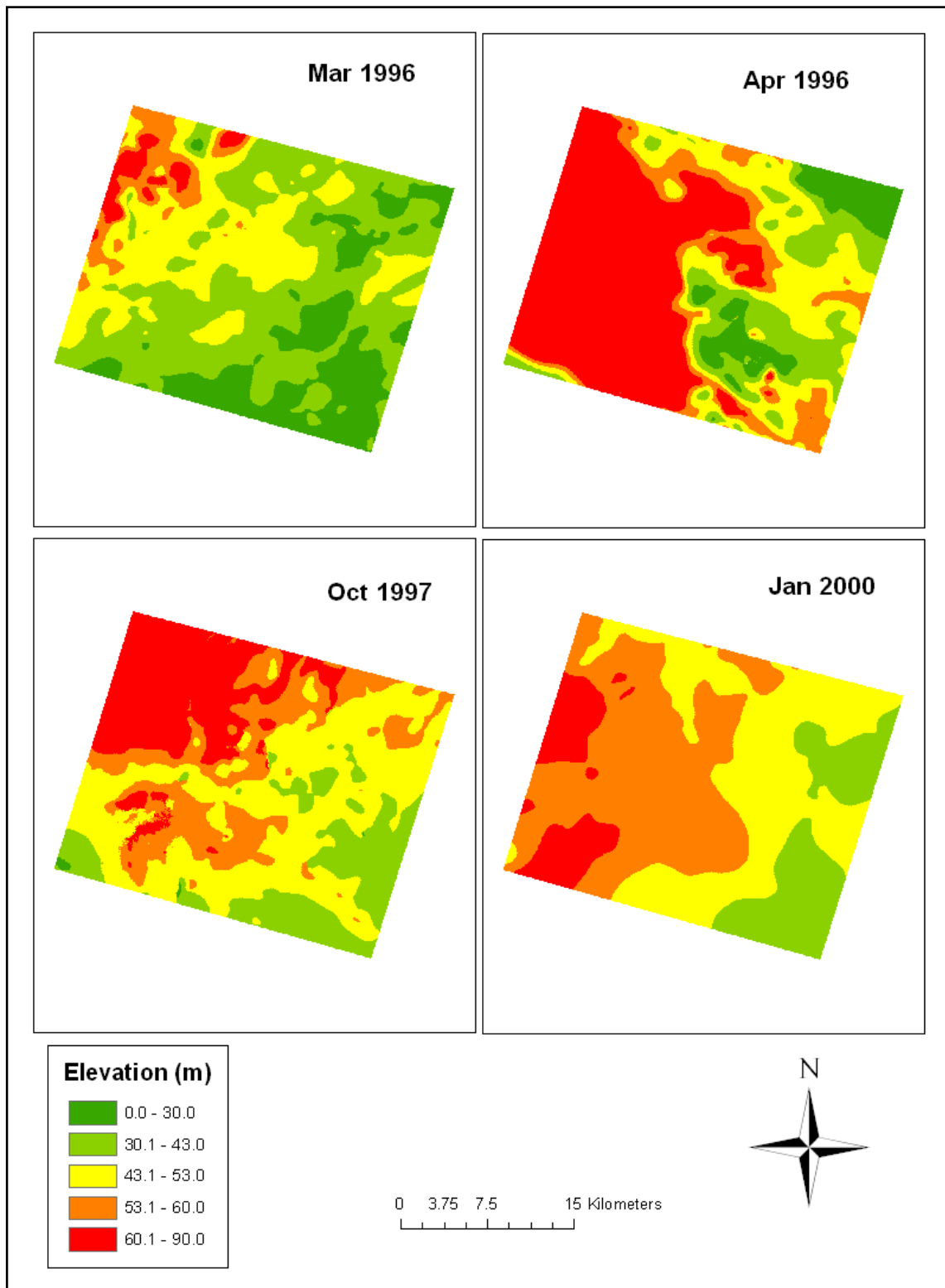


Figure 6.4: DEM of Maliku test site generated from eight ERS-1/2 tandem radar images using intensity adaptive filter processing technique with MCF unwrapping method.

6.3.2 Dadahup: Digital elevation model

The second test site to be examined is the Dadahup area in Block A. Unlike the Maluku area, this area is more open and has less forest and plantation. Therefore, it is interesting to compare InSAR DEM derived from two different tropical forest areas. As mentioned earlier in Section 4. The coherence in this area is higher than in Maluku due to heavy drainage and deforestation. Figure 6.5 and Figure 6.6 show eight DEMs generated by tandem ERS pairs acquired in January 2000. Unlike the Maluku DEMs, the Dadahup DEMs have been generated using BC unwrapping method and does not have any holes due to relatively high coherence (Figure 6.7). However, the intensity and orbit method have the same height value distribution in both BC and MCF unwrapping methods. In addition, applying adaptive filters many times before PU reduces the noise in the DEMs, which is the result of actual reduction of the noise of the interferometric phase.

Figure 6.8 shows the histogram of elevation. As can be seen from the histogram, most of the area had elevation values of between 40m and 50m. Histogram for DEM that applied adaptive filtering many times shows larger variability compared to those that use only one adaptive filtering. Also MCF unwrapping methods slightly increase the variability in all DEMs. Intensity and orbit method have a higher numbers of frequencies concentrated at the central peak and a small number at the tail, whilst the adaptive filter method in both unwrapping methods shows a lower and a wide spread of frequency indicating a large variation in elevation than the rest of the DEMs.

Figure 6.8 shows three DEMs generated by three tandem ERS pairs at different times. These DEMs have been derived by using the orbit method to calculate interferogram, running adaptive filtering many times and applying an MCF unwrapping algorithm. Visual comparison between DEMs shows that height values in DEM 1996 show sharp

variations within the DEM. In contrast, the other two DEMs show smooth changes in elevation change and a similar elevation distribution in the entire DEMs.

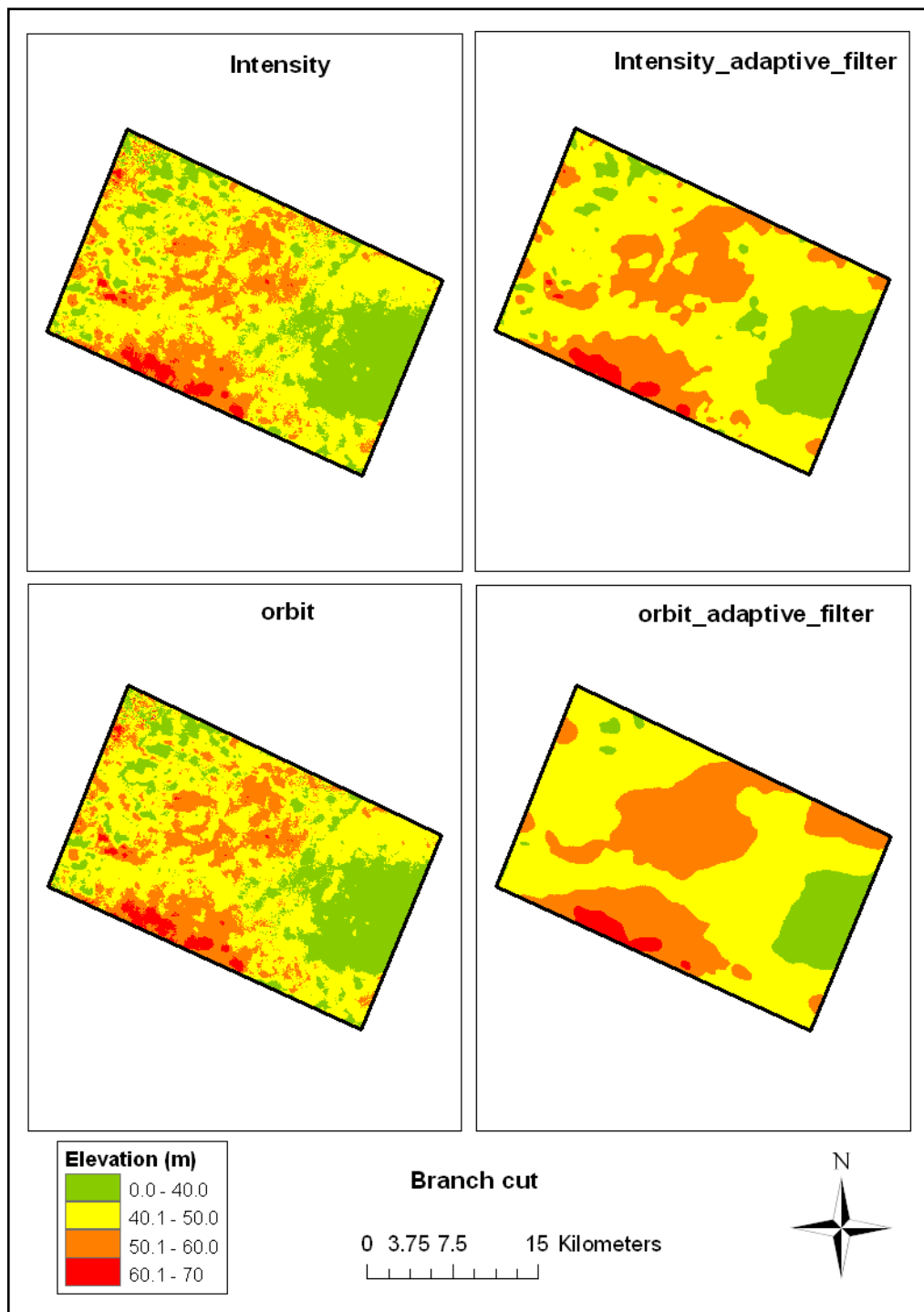


Figure 6.5 DEM for the Dadahup test site generated from ERS-1/2 tandem radar images using different processing techniques with BC unwrapping method.

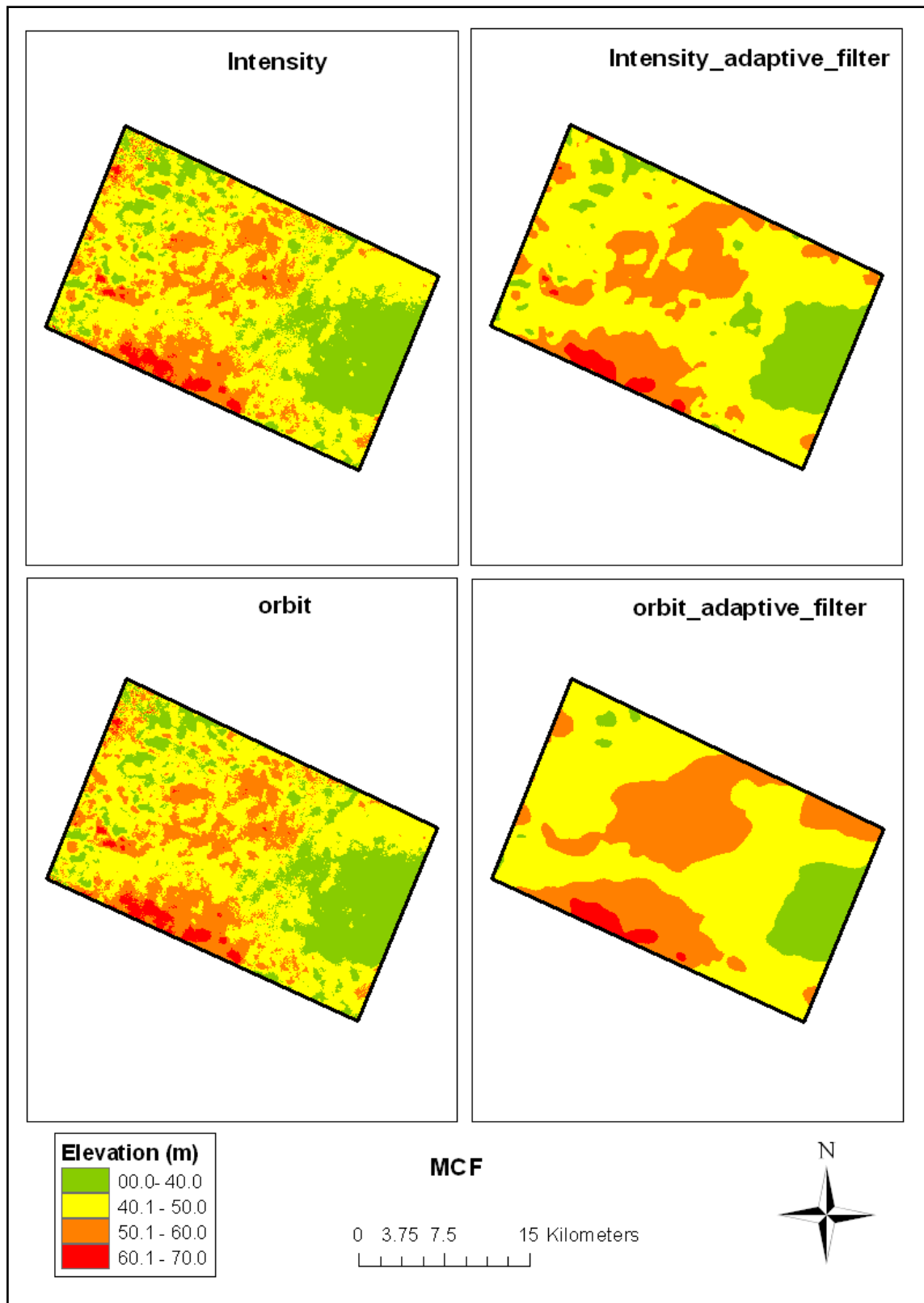


Figure 6.6: DEM for the Dadahup test site generated from ERS-1/2 tandem radar images using different processing techniques with MCF unwrapping method.

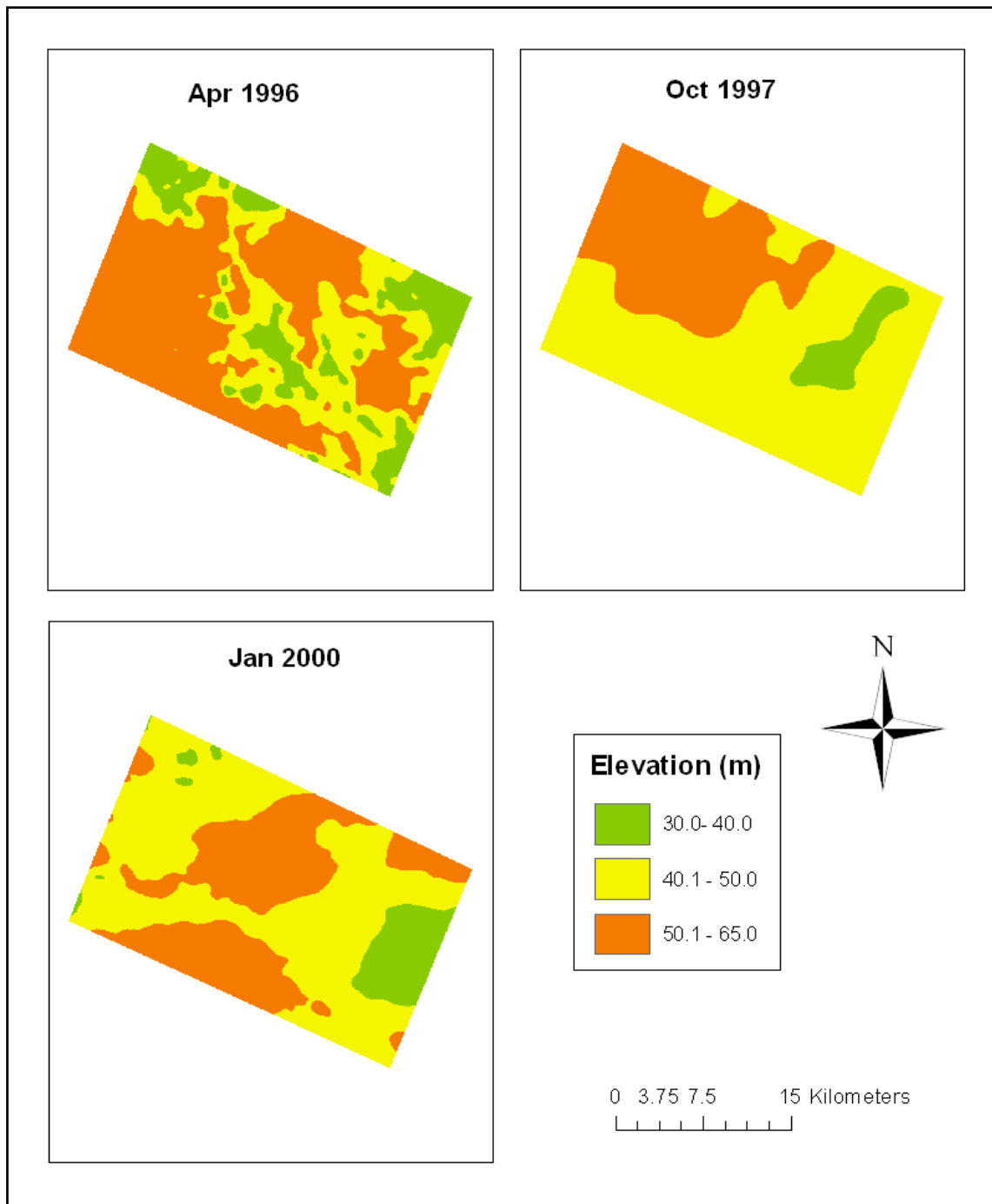


Figure 6.7: DEM for the Dadahup test site generated from three ERS-1/2 tandem radar images using intensity adaptive filter processing technique with MCF unwrapping method.

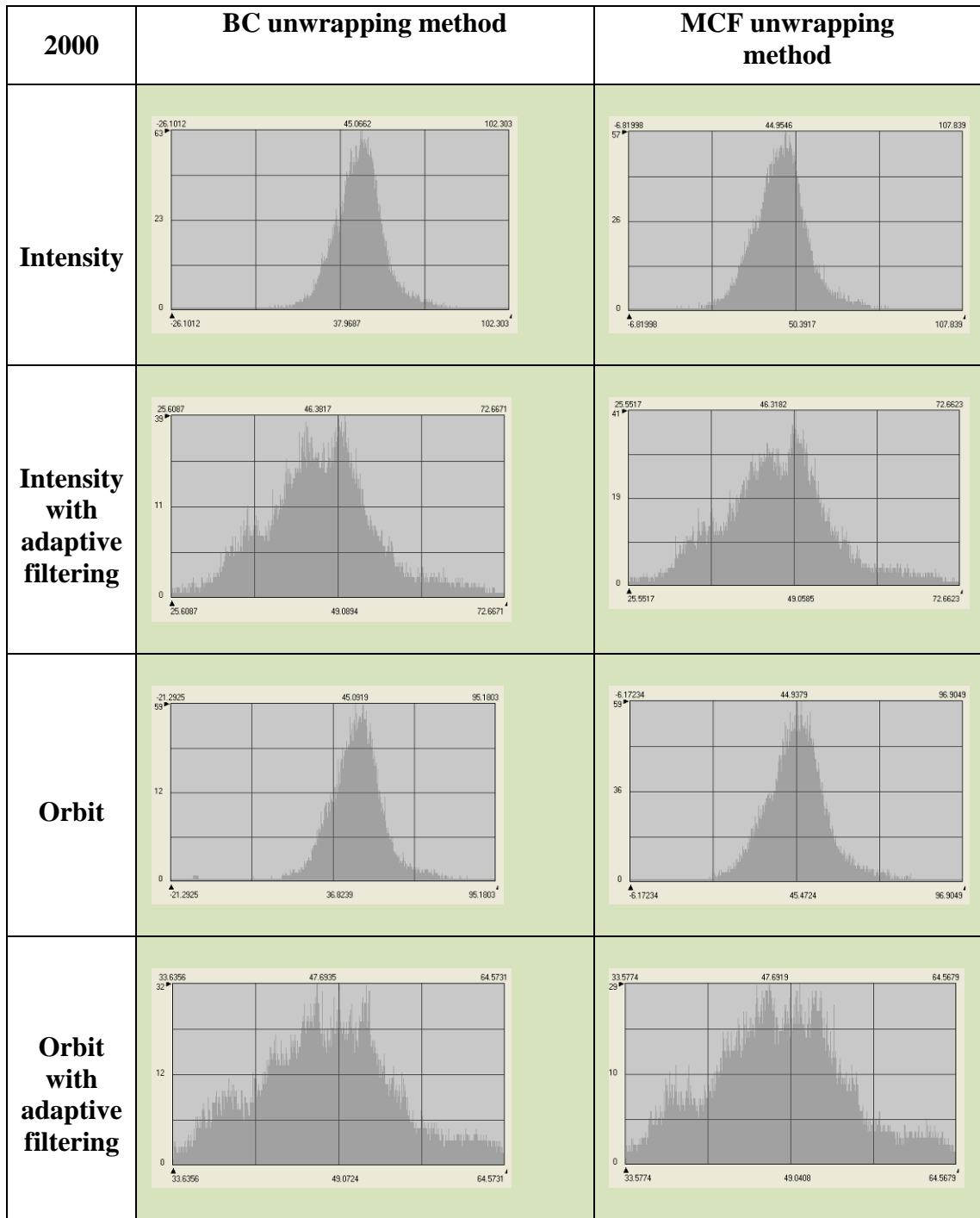


Figure 6.8: Histograms of elevation frequency of 2000- DEMs in Dadahup.

6.4 Statistical analysis for DEMs

6.4.1 Maluku: Statistical analysis

The descriptive statistics of Maluku DEMs generated from the different processing methods over four time periods were calculated and shown in Table 6.2. These statistics show the maximum difference between mean elevation values of different processing methods in each pair of ERS images of 6.2, 3.3, 4.7 and 1.2 m whilst the maximum standard deviations difference are 6.3, 3.7, 5.4 and 2.5 m for DEMs March 1996, April 1996, October 1997 and January 2000 respectively (Table 6.3). However, the mean difference of using different InSAR processing technique is about 4 ± 6.4 m in all image pairs that have been used in this study.

Compared to the mean elevation and standard deviation that were obtained from one-adaptive filter results, running adaptive filters many times increased the mean elevation and standard deviation in March 1996 and decreased them in April 1996 to be close to the elevation mean and standard deviation in 1997 and 2000. The lowest standard deviation has been found using an intensity adaptive filtering method with MCF PU in 1997 and 2000. Furthermore, the differences between maximum and minimum elevation values decreased when applying adaptive filtering many times. Also, this difference decreased rapidly in DEMs 1997 and DEMs 2000 due to increasing the coherence and baseline. In general, there was also a slight decrease in standard deviation by using MCF, compared to the BC unwrapping method.

These statistics indicate that the mean and the standard deviation of elevation of DEM 1997 and DEM 2000 have values close to each other, whilst elevation values of DEMs that have been produced in 1996 are more variable from other DEMs. The lowest mean elevation is recorded in DEMs of March 1996 while the highest ones can be seen in

DEMs of April 1996 (Figure 6.9). One explanation of the higher elevation values of April 1996 DEMs is that C-band wavelength does not penetrate through the volume of tree canopies. Therefore, the interferometric DEMs generated with C-band would represent the height of the terrain including the height of vegetation. The reason for overall less elevation values in the March 1996 DEMs compared to 1997 and 2000 DEMs cannot be explained. However, it may be concluded that DEMs in 1997 and 2000 represent a more realistic topography in this case.

Table 6.2: Descriptive statistics of InSAR DEM in Maliku site
Table 6.3: Statistic information for different DEM processing in Maliku.

Date	Unwrapping methods	Interferogram methods	DEM No	Min (m)	Max (m)	Mean (m)	Median (m)	St.dev (m)
199603	BC	Intensity	DEM1	-156.15	216.93	38.56	38.61	17.58
		Intensity adaptive	DEM2	-37.67	93.33	38.24	38.86	12.49
		Orbit	DEM3	-188.92	230.41	37.99	38.18	18.74
	MCF	Intensity	DEM4	-76.43	156.50	33.21	33.41	16.56
		Intensity adaptive	DEM5	-54.81	76.78	39.14	39.79	10.69
		Orbit	DEM6	-72.15	140.15	32.92	33.19	16.41
199604	BC	Intensity	DEM7	-101.78	159.01	63.17	60.91	26.96
		Intensity adaptive	DEM8	-72.83	131.12	61.12	57.21	24.51
		Orbit	DEM9	-102.27	161.97	63.18	60.94	26.95
	MCF	Intensity	DEM10	-100.41	154.35	63.14	61.25	26.26
		Intensity adaptive	DEM11	-63.63	126.97	59.92	55.93	23.30
		Orbit	DEM12	-101.61	154.44	63.17	61.26	26.23
199710	BC	Intensity	DEM13	-37.25	240.21	51.88	50.66	15.22
		Intensity adaptive	DEM14	-3.44	106.27	51.77	51.08	11.02
		Orbit	DEM15	-30.76	161.45	51.59	50.76	12.10
	MCF	Intensity	DEM16	10.21	122.02	56.46	54.70	14.97
		Intensity adaptive	DEM17	11.60	90.56	52.68	51.59	9.79
		Orbit	DEM18	3.55	108.87	53.23	52.18	10.81
200001	BC	Intensity	DEM19	-8.84	144.61	52.53	52.99	9.48
		Intensity adaptive	DEM20	30.56	92.83	51.92	53.00	8.23
		Orbit	DEM21	-25.08	138.58	52.75	53.25	9.65
	MCF	Intensity	DEM22	8.63	112.95	52.18	52.15	10.46
		Intensity adaptive	DEM23	32.25	91.24	51.53	52.86	7.99
		Orbit	DEM24	6.05	113.20	52.06	52.08	10.29

Table 6.3: Statistic information for different DEM processing in Maluku

	Max mean Difference	Max St.dev difference
March 1996	6.2	6.3
April 1996	3.3	3.7
October 1997	4.7	5.43
January 2000	1.2	2.5

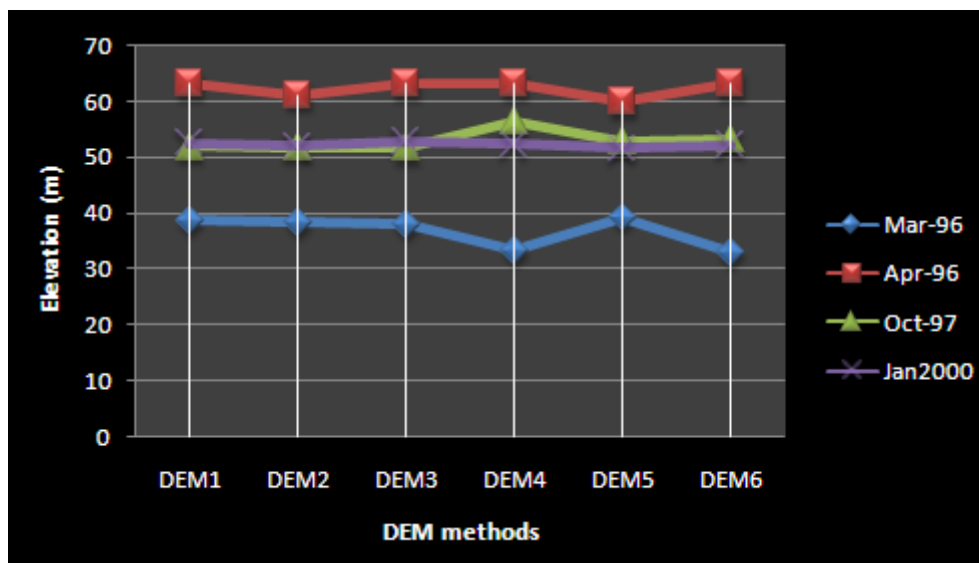


Figure 6.9: The mean elevation of Maluku DEMs.

6.4.2 Dadahup: Statistical analysis

From the descriptive statistics of InSAR DEMs of the Dadahup test site illustrated in Table 6.4, it can be noted that the difference between maximum and minimum elevation values, mean and standard deviations are the lowest in the DEMs 1997 and slightly close to DEMs 2000 while DEMs of 1996 have the biggest value difference. This fact may be explained by systematic differences due to vegetation and forest cover.

Similar to Maluku DEMs, standard deviation was moderately decreased by using adaptive filtering or by using the MCF unwrapping method. This decrease has a higher

value in 1996 DEMs, which have the smallest baseline (see Table 4.1) and lowest coherence values compared with 1997 and 2000 DEMs.

Table 6.4: Descriptive statistics of InSAR DEM in Dadahup site.

Date	Unwrapping methods	Interferogram methods	DEM No	Min (m)	Max (m)	Mean (m)	Median (m)	St.dev (m)
April 1996	BC	Intensity	DEM1	-124.57	245.75	48.08	47.44	20.13
		Intensity adaptive	DEM2	-38.61	111.54	49.76	49.40	13.53
		Orbit	DEM3	-134.31	205.64	48.17	47.55	20.13
		Orbit adaptive	DEM4	-17.05	91.05	51.80	51.18	11.04
	MCF	Intensity	DEM5	-100.39	203.35	50.94	50.26	20.34
		Intensity adaptive	DEM6	-70.73	118.24	49.37	48.90	14.71
		Orbit	DEM7	-101.44	178.8	51.03	50.40	20.26
		Orbit adaptive	DEM8	17.35	91.05	51.52	51.11	11.07
October 1997	BC	Intensity	DEM9	14.51	83.74	46.98	46.56	5.30
		Intensity adaptive	DEM10	37.62	64.20	46.94	46.24	4.95
		Orbit	DEM11	3.28	108.56	47.01	46.57	5.31
		Orbit adaptive	DEM12	38.34	62.16	46.79	45.97	4.82
	MCF	Intensity	DEM13	17.96	83.99	46.91	46.54	5.32
		Intensity adaptive	DEM14	37.63	64.51	46.96	46.29	4.95
		Orbit	DEM15	8.36	86.06	46.95	46.57	5.30
		Orbit adaptive	DEM16	38.35	62.18	46.80	45.98	4.82
January 2000	BC	Intensity	DEM17	-26.10	102.30	45.07	45.38	7.58
		Intensity adaptive	DEM18	25.61	72.67	46.38	46.63	6.25
		Orbit	DEM19	-21.29	95.18	45.09	45.39	7.55
		Orbit adaptive	DEM20	33.64	64.57	47.69	47.76	5.39
	MCF	Intensity	DEM21	-6.82	107.84	44.96	45.24	7.51
		Intensity adaptive	DEM22	25.55	72.66	46.32	46.58	6.25
		Orbit	DEM23	-6.17	96.91	44.94	45.22	7.56
		Orbit adaptive	DEM24	33.58	64.57	47.69	47.75	5.39

6.5 Accuracy assessment and comparison of DEMs

There are several ways which are used to assess DEM quality. Relative assessment is used when accuracy is only referring to random errors in a data set, also when referring point to point accuracy. Then a statistical computation determines the amount of error between the two datasets. In this method, no new image is created, validation points can be overlaid on the DEM image. The average error is expressed as the root mean square error (RMSE) which is often used to report both horizontal and vertical error. If the error distribution is Gaussian and has a mean of zero, the RMSE is equivalent to the statistical standard deviation of the measured errors (USGS, 1998). Absolute assessment is used as a measure which counts for all systematic and random errors in the data set and is commonly used. During an absolute assessment, one DEM is compared against a reference DEM covering the same area, pixel-wise. In a relative way, the result is a new raster indicating the difference in elevation at each pixel. This could be analyzed further statistically. The accuracy assessment in this chapter have been done to detect the DEM error by two factors; the DEM processing technique that have been used and the land cover change and baseline-length effects.

However, error distribution is an important aspect to validate the DEM accuracy that has been applied in many applications. The quality measures, by absolute and relative assessment means, gave global statistical measures without showing error distribution that can help to identify error prone areas. The error magnitude and spatial distribution within the DEMS is examined using error mapping techniques for absolute and relative comparisons.

6.5.1 Maliku: Accuracy Assessment of DEMs against GPS profiles

This is one of the methods to assess the DEMs quality based on common ground control points (GCPs) which might provide accurate point data. 100 check GCPs were extracted from all DEMs to be validated. Figure 6.10 shows the mean elevation height GCPs extracted from all DEMs against check GCPs mean elevation values. The mean height of March 1996 DEMs show the lowest height compared to other DEMs and heights differences with other DEMs exceed 15 m. However, the mean elevation of GCPs (47.2 m) did not match the mean elevation of the whole DEMS and the differences are represented in Figure 6.10. The mean value of March 1996 is still lower than other DEMS but the mean value of April 1996 is higher for GCPs compared to the mean of the entire image. The mean elevation of DEMs 1997 and DEMs 2000 are close to each other and fit with the mean of the whole Maliku site. However, statistical methods through root mean square values, together with histograms of the distribution of the height differences might give more reliable results. The statistical value for absolute elevation differences between the common points; mean, median, standard deviation and RMSE were obtained. Figure 6.11 show the histogram of the frequency distribution of the absolute elevation values of DEMs generated by ERS tandem images acquired in 1997.

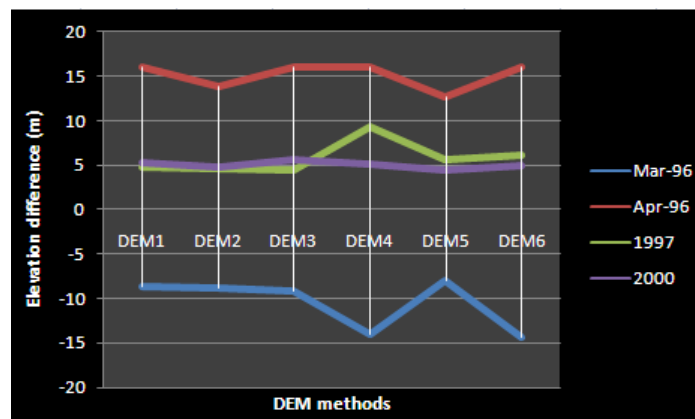


Figure 6.10: The elevation difference between the mean values of DEMs and the mean value of DGPS check points.

Absolute elevation difference histograms were drawn to show the relationship of elevation difference distributions. Histograms are a useful tool in graphical data analysis by showing frequency and distribution, which characterises data behaviour and estimates data variability ranges. The mean absolute elevation difference is about 4.25 m. The histogram of intensity and orbit DEM elevations resembles an exponential distribution while the histogram of adaptive filter DEMs follows the skewed fitting curve. However, the histogram indicates that there is a significant decrease in the frequency of occurrence of larger error (more than 5 m) by applying an adaptive filter many times and using the MCF unwrapping algorithm.

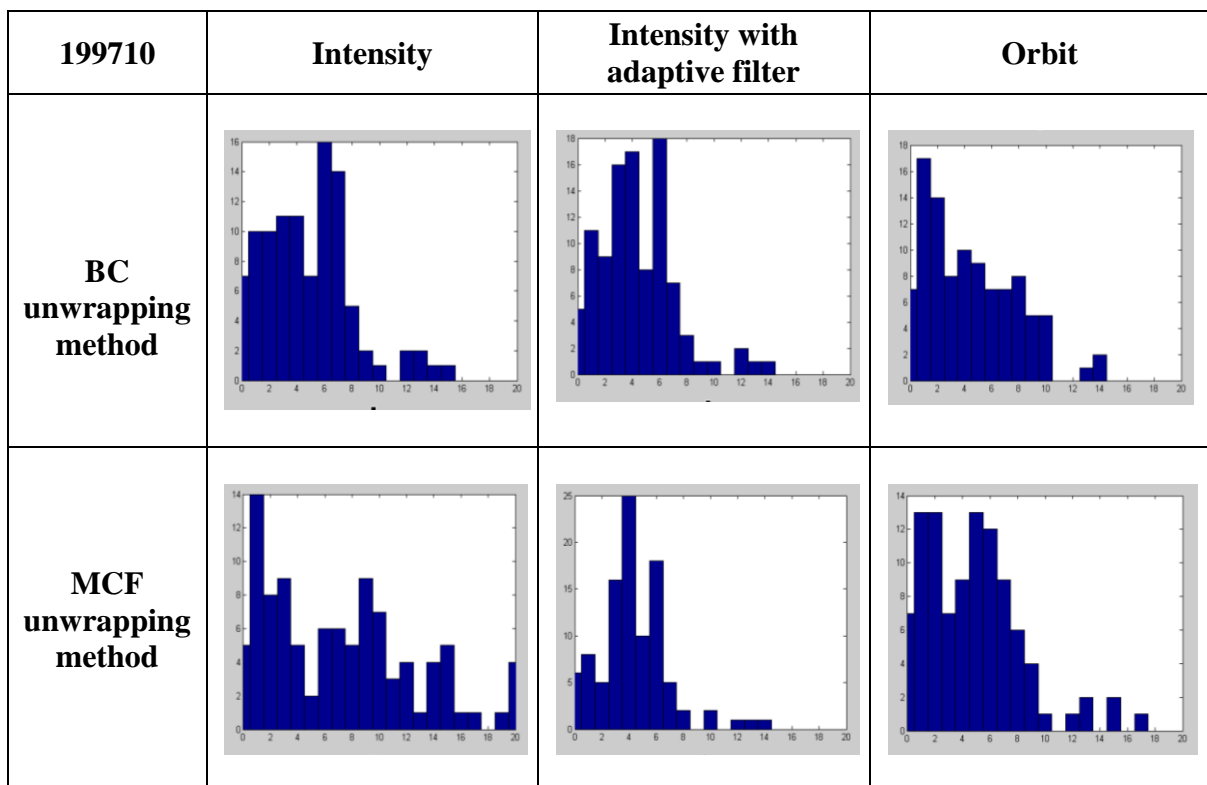


Figure 6.11: Histogram of the absolute elevation differences (m) between InSAR DEMs and GCPs in Maliku using 100 points.

From the descriptive statistics for absolute elevation differences illustrated in Table 6.5, it can be seen that the difference between maximum and minimum elevation values, mean, RMSE and standard deviation are the highest in April 1996 DEMs with a mean RMSE of 26 . The second highest error is found in March 1996 DEMs with a mean

RMSE of about 18m. The lowest error found in DEMs 1997 and DEMs 2000 with a mean RMSE of 5m and 6m respectively. These results of the statistical properties can be explained by the coherence change between 1996 and 2000. It is clear that the error decreased between 1996 and 2000 due to an increase in coherence. The baseline of tandem images might be another explanation of the results, DEMs 1997 and DEMs 2000 have a larger baseline compared to 1996 DEMs (see Table 4.1). Compared with DEMs 2000, the baseline of DEMs 1997 is larger and therefore results in a smaller error. Besides that, the mean, standard deviation and RMSE decline significantly by applying an adaptive filter many times. In addition, no clear difference was found between orbit and intensity method as well as between BC and MCF unwrapping methods. In addition, applying adaptive filter together with MCF unwrapping gave the best accuracy over all DEMs.

Further analysis was carried out to correlate the RMSE with coherence; the coherence values are separated into two classes (less than 0.42 and more than 0.42) to explore its relationship with their contributing RMSE. The RMSE was calculated for these two classes and the results are shown in Table 6.6. From Figure 6.12 it is quite evident that areas with coherence less than 0.42 are significantly larger in RMSE as compared to RMSE from a high coherence area. From this observation it can be concluded that RMSE increased when the coherence decreased. These results also shows that the smallest difference between RMSE was found when applying adaptive filter many times before unwrapping, which reduces PU errors due to phase noise.

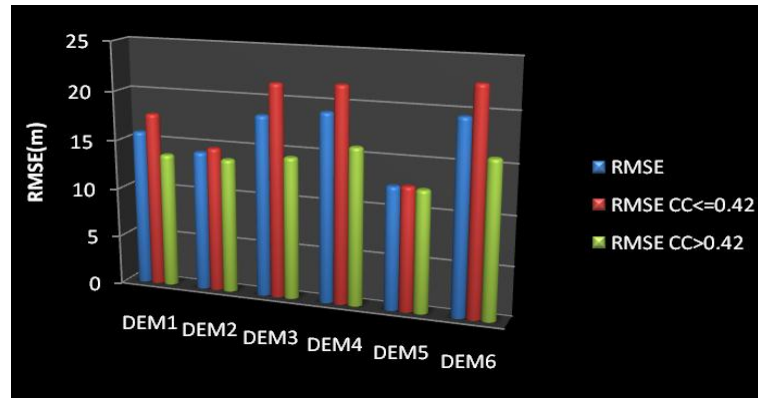


Figure 6.12: RMSE change due to coherence change.

Table 6.5: Accuracy of Maliku DEMs from DGPS check points.

Date	Unwrapping methods	Interferogram methods	DEM No	Min (m)	Max (m)	Mean (m)	St.dev (m)	RMSE (m)
199603	BC	Intensity	DEM1	0.95	35.74	13.16	8.78	15.82
		Intensity Adaptive	DEM2	0.05	28.89	12.12	7.38	14.19
		Orbit	DEM3	0.23	64.34	14.69	10.98	18.34
	MCF	Intensity	DEM4	1.28	47.45	16.21	10.06	19.08
		Intensity Adaptive	DEM5	0.04	26.24	10.64	6.41	12.42
		Orbit	DEM6	1.26	53.01	16.53	10.40	19.53
April 1996	BC	Intensity	DEM7	0.03	72.29	21.13	15.60	26.27
		Intensity Adaptive	DEM8	0.57	63.70	20.08	15.55	25.40
		Orbit	DEM9	0.05	74.06	21.45	15.88	26.68
	MCF	Intensity	DEM10	0.06	71.58	20.89	15.72	26.14
		Intensity Adaptive	DEM11	0.03	61.54	19.34	15.46	24.76
		Orbit	DEM12	0.01	72.32	20.88	15.77	26.16
October 1997	BC	Intensity	DEM13	0.04	14.96	4.84	3.26	5.84
		Intensity Adaptive	DEM14	0.05	13.50	4.32	2.73	5.10
		Orbit	DEM15	0.04	13.68	4.42	3.31	5.52
	MCF	Intensity	DEM16	0.10	21.27	7.18	5.51	9.05
		Intensity Adaptive	DEM17	0.02	13.98	4.33	2.56	5.03
		Orbit	DEM18	0.02	17.02	4.77	3.51	5.92
January 2000	BC	Intensity	DEM19	0.07	16.99	5.67	3.89	6.88
		Intensity Adaptive	DEM20	0.08	14.11	4.96	3.47	6.05
		Orbit	DEM21	0.14	17.53	5.82	4.23	7.19
	MCF	Intensity	DEM22	0.08	16.98	5.75	4.09	7.05
		Intensity Adaptive	DEM23	0.03	12.80	4.75	3.23	5.74
		Orbit	DEM24	0.07	16.39	5.65	4.06	7.00

Table 6.6: RMSE values of Maliku DEMs against coherence.

199603	DEM1	DEM2	DEM3	DEM4	DEM5	DEM6
Overall RMSE(m)	15.82	14.19	18.34	19.08	12.42	19.52
RMSE(m) CC≤0.42	17.72	14.70	21.56	21.79	12.53	22.63
RMSE(m) CC>0.42	13.65	13.67	14.40	15.90	12.31	15.83
Difference(m)	4.07	1.03	7.16	5.89	0.22	6.8

6.5.2 Maliku: Spatial distribution of relative assessment

The resulting absolute elevation difference of the check GCPs are mapped using graduated symbols with different colours. The purpose is to find the relationship between the specified elevation differences with different DEM processing and with baseline and land cover changes for the time spanning between ERS tandem pair images. The absolute elevation differences error magnitudes are categorized by colour intensity and spatial pattern. This allows the study of the distribution of error, point by point, and helps in identifying the part of the test site with the greatest magnitude of error. From this, the factors causing the error can also be identified.

To analyze the spatial distribution of errors resulting from DEM processing, the overall results of error mapping of DEM 2000 are represented in Figure 6.13. Two patterns of the distribution of errors can be recognized, errors due to processing technique and errors due to other factors such as coherence and DGPS accuracy. Figure 6.13 shows that error of intensity and orbit methods decreased by about 3 m by applying adaptive filter and the MCF unwrapping method. Furthermore, it may be observed that most of the points with a large error magnitude (more than 7 m) are located in the western part and north east part of the DEM. This error, which was found in all DEMS, indicates that

the distribution of the error is not related to processing errors. The error distribution in the western part of DEM might be due to poor interpolation to fill voids.

However, to isolate the errors due to processing methods, only one processing method (intensity adaptive filter: DEM5, DEM11, DEM17, and DEM23) has been used to determine the error distribution (Figure 6.14). According to the coherence maps in Figure 6.15, the large error points which are located in the western part of the GCPs profile have low coherence in all DEMs and that can explain the high errors in this area. Furthermore, the large error points in the north east are located in high coherence in 3 DEMs and the magnitude error, decreased from about 10m in 1996 to just under 4m in 1997 and 2000. The most likely reason for the decrease of these errors is the baseline length change which explains the high accuracy of DEM 17 and DEM23.

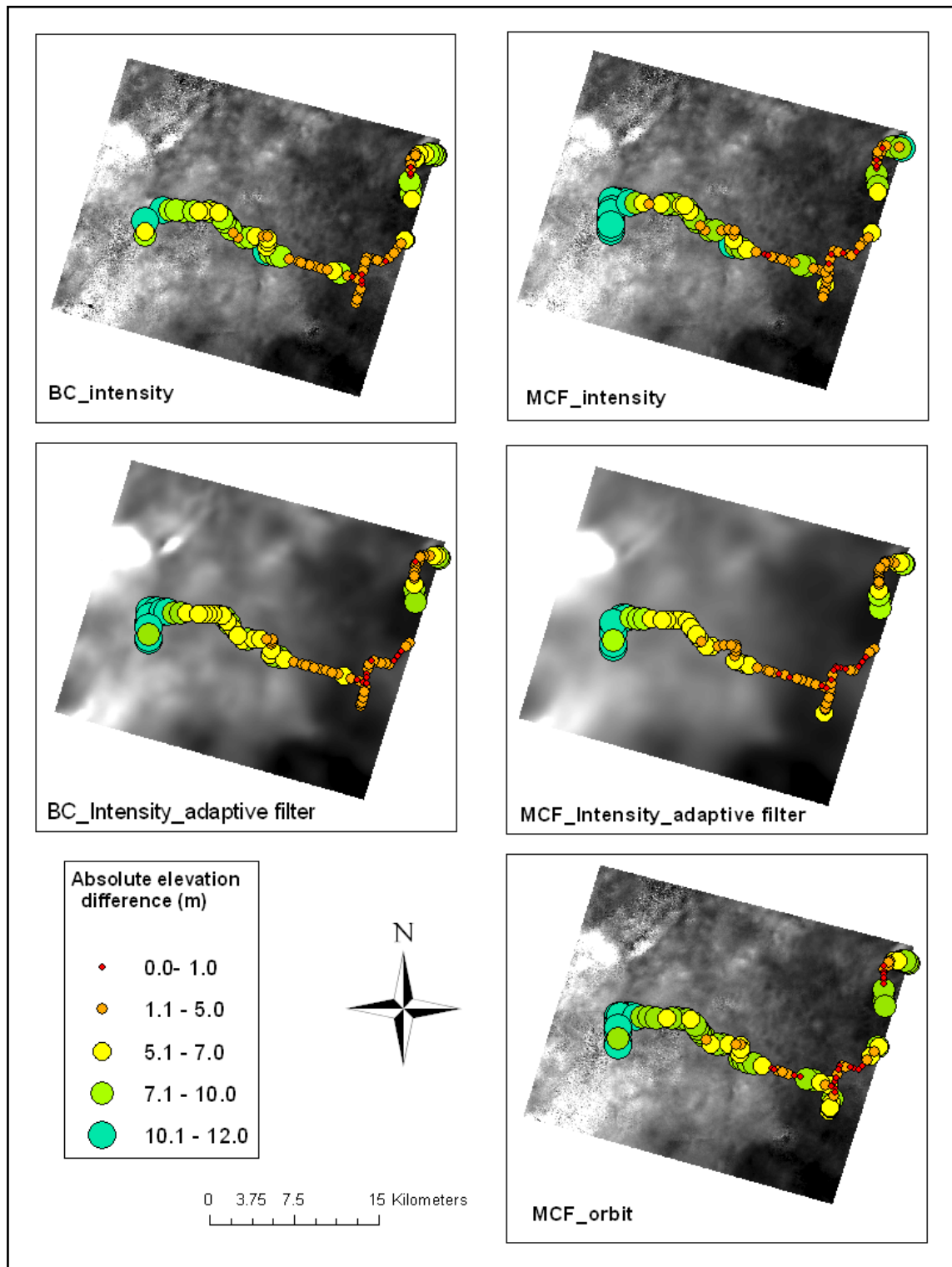


Figure 6.13: Error distribution of check GCPs in DEM2000 in Maliku.

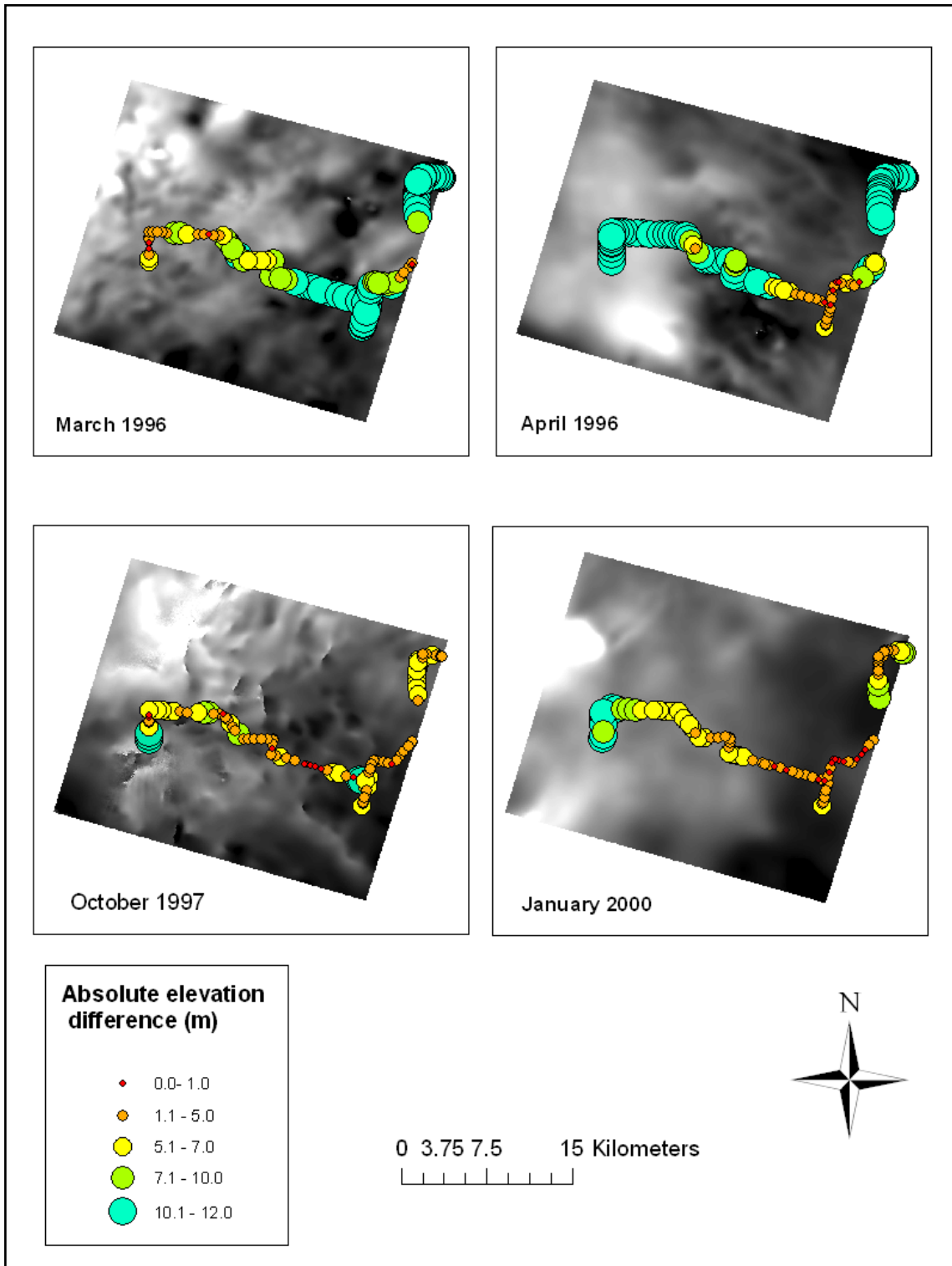


Figure 6.14: Error distribution of check GCPs for four DEMs generated from eight ERS-1/2 tandem radar images over Maliku site using intensity adaptive filter processing technique with MCF unwrapping method.

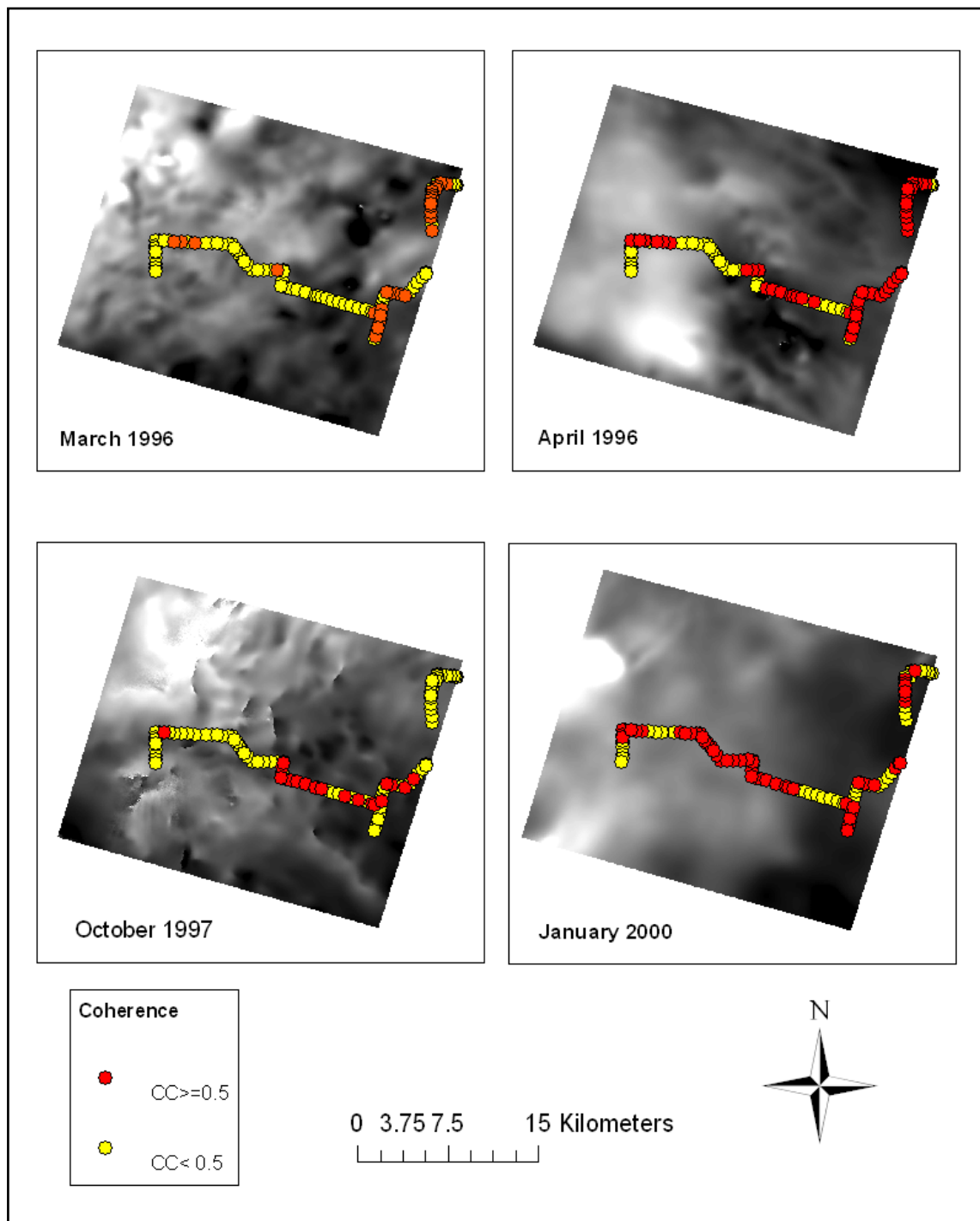


Figure 6.15: Coherence changes of GCPs in Maliku between 1996 and 2000.

6.5.3 Dadahup: Accuracy assessment of DEMs against GPS profiles

Accuracy assessment using relative assessment was achieved by comparing the DGPS elevations profiles with the elevation data extracted from the Dadahup DEMs. The elevation of each DGPS check point was compared with the elevation of the respective DEMs pixel. 100 DGPS points spread over Dadahup region with different elevations were used in this comparison. The errors between each elevation profile drawn from the DEMs against the DGPS surveys are summarised in Table 6.7. Also, the histograms of the errors of the DEMs are shown in Figure 6.16 to indicate the distribution of errors.

Table 6.7 shows the RMSE of 24 DEMs. InSAR derived DEMs based on intensity and orbit methods had a poor accuracy, whilst the intensity adaptive filter and orbit adaptive filter derived DEMs had a good accuracy as expected. For example, for the orbit method in DEM 1996, the mean error equals 18.49 m and it is reduced to 10.21 m in the orbit adaptive filter method. Similar to Maluku DEMs, the difference between BC and MCF unwrapping methods are almost the same and sometimes the BC gives slightly better accuracy. In addition, an orbit method looks better than intensity, especially in high coherence areas. By applying the adaptive filter many times, the accuracy of orbit method improves the marginal compared to the intensity method. The lowest RMSE and standard deviation of the absolute elevation difference was found in the orbit adaptive method with a value of 2.87 RMSE, 1.51 Std.Dev and 2.93 RMSE, 1.54 for BC and MCF unwrapping methods respectively.

It was shown that the reason DEMs in April 1996 had a large RMSE was that it was difficult to unwrap the phase of SAR signal because of the area of low coherence such as forest covered area. Generally, it was clear that height accuracy increased with baseline and the coherence. The effects of baseline is clearer than coherence. Although

the average coherence in 1997 was more than the average coherence in 2000, the RMSE in 2000 is lower than 1997. This is because of the longer baseline in tandem ERS images in 1997. From the comparison between InSAR DEMs elevation and DGPS profile check points, it can be noted that about 95% of the elevation difference values in DEMs 2000 and DEMs 1997 were less than 15 m while this number increased to more than 25 m in DEMs 1996. In addition, the maximum elevation difference for adaptive filtering is less than 9 m in all DEMs of 1997 and 2000.

Table 6.7: Accuracy of Dadahup DEMs from DGPS check points.

Date	Unwrapping methods	Interferogram methods	DEM No	Min (m)	Max (m)	Mean (m)	St.dev (m)	RMSE (m)
April 1996	BC	Intensity	DEM1	0.33	54.05	16.11	11.28	19.67
		Intensity adaptive	DEM2	0.22	28.45	10.11	6.90	12.24
		Orbit	DEM3	0.04	48.47	15.17	10.58	18.49
		Orbit adaptive	DEM4	0.07	24.39	8.66	5.42	10.21
	MCF	Intensity	DEM5	1.50	58.59	16.75	12.59	20.95
		Intensity adaptive	DEM6	0.19	30.05	11.08	7.67	13.48
		Orbit	DEM7	0.18	53.82	15.96	12.00	19.97
		Orbit adaptive	DEM8	0.26	24.66	8.68	5.44	10.24
October 1997	BC	Intensity	DEM9	0.14	8.93	3.81	2.26	4.43
		Intensity adaptive	DEM10	0.05	8.38	3.57	2.21	4.15
		Orbit	DEM11	0.29	8.76	3.72	2.20	4.33
		Orbit adaptive	DEM12	0.03	7.75	3.48	2.03	4.03
	MCF	Intensity	DEM13	0.14	8.86	3.79	2.25	4.41
		Intensity adaptive	DEM14	0.04	8.42	3.57	2.15	4.16
		Orbit	DEM15	0.26	8.71	3.72	2.18	4.31
		Orbit adaptive	DEM16	0.02	7.79	3.48	2.05	4.04
January 2000	BC	Intensity	DEM17	0.08	16.08	3.49	3.01	4.61
		Intensity adaptive	DEM18	0.03	6.87	2.51	1.81	3.10
		Orbit	DEM19	0.03	16.56	3.49	3.08	4.66
		Orbit adaptive	DEM20	0.03	6.10	2.44	1.51	2.87
	MCF	Intensity	DEM21	0.00	16.12	3.52	3.05	4.66
		Intensity adaptive	DEM22	0.02	6.96	2.53	1.83	3.12
		Orbit	DEM23	0.00	16.15	3.55	3.10	4.71
		Orbit adaptive	DEM24	0.04	6.28	2.49	1.54	2.93

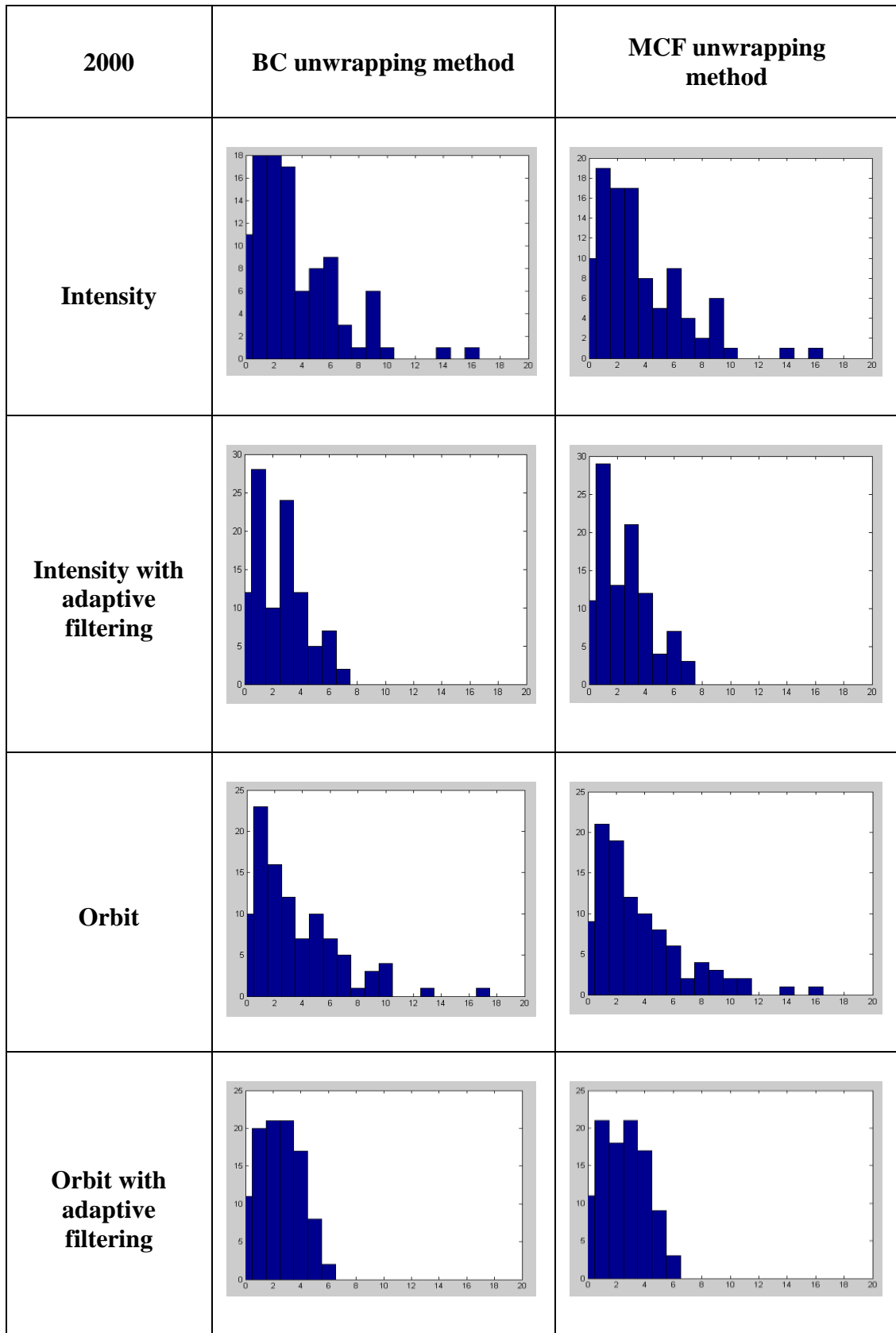


Figure 6.16: Histogram of the absolute elevation differences (m) between InSAR DEMs and GCPs in Dadahup using 100 points.

6.5.4 Dadahup: Spatial distribution of relative assessment error

It was shown in a previous chapter that statistical values do not give information of how errors are distributed in the DEM. The difference between the processing methods has been assessed by comparing DGPS profile with DEM elevation. Figure 6.17 and Figure 6.18 show the distribution error of GCPs in Dadahup DEMs in 2000. It can be seen that the absolute elevation difference is less than 5 m for approximately 95% of the check points of 2000 DEMs. The large error points appear in MCF and BC unwrapping DEMs, whilst it disappears when applying adaptive filters many times before PU. On the other hand, the orbit method seems to have fewer large error points compared with the intensity method. However, the distribution of error is random and no specific location of the prone error can be identified.

Similar to Maluku case, in order to examine the error distribution due to land cover and time span, only the most accurate DEM from each tandem pair image have been chosen and analyzed (DEM 8, DEM 16 and DEM 24). Figure 6.19 shows the absolute elevation differences, which have been classified depending on the value of the difference. The error decreased rapidly from 1996 to 2000. Most of the large error points are located in low coherence areas in 1996 and 1997 (Figure 6.20). These areas appear as yellow points in 1997 DEM with errors between 5 and 7 m, while the error was more than 10 m in 1996. However, the low error points of this area in 2000 can lead to a conclusion that this error distribution is due to land cover change more than processing error.

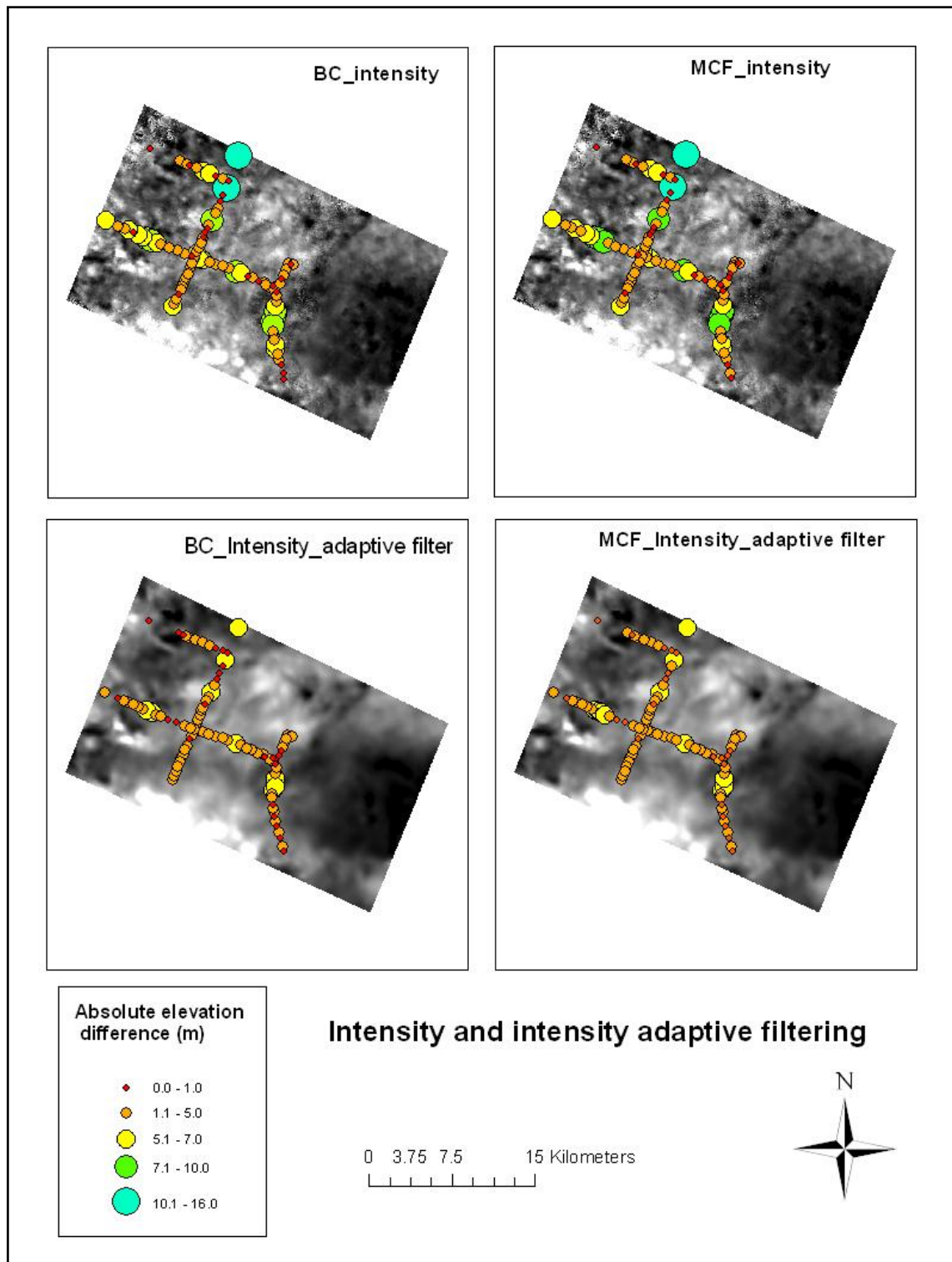


Figure 6.17: Error distribution of check GCPs in DEM2000 in Dadahup using intensity and intensity adaptive filter processing technique.

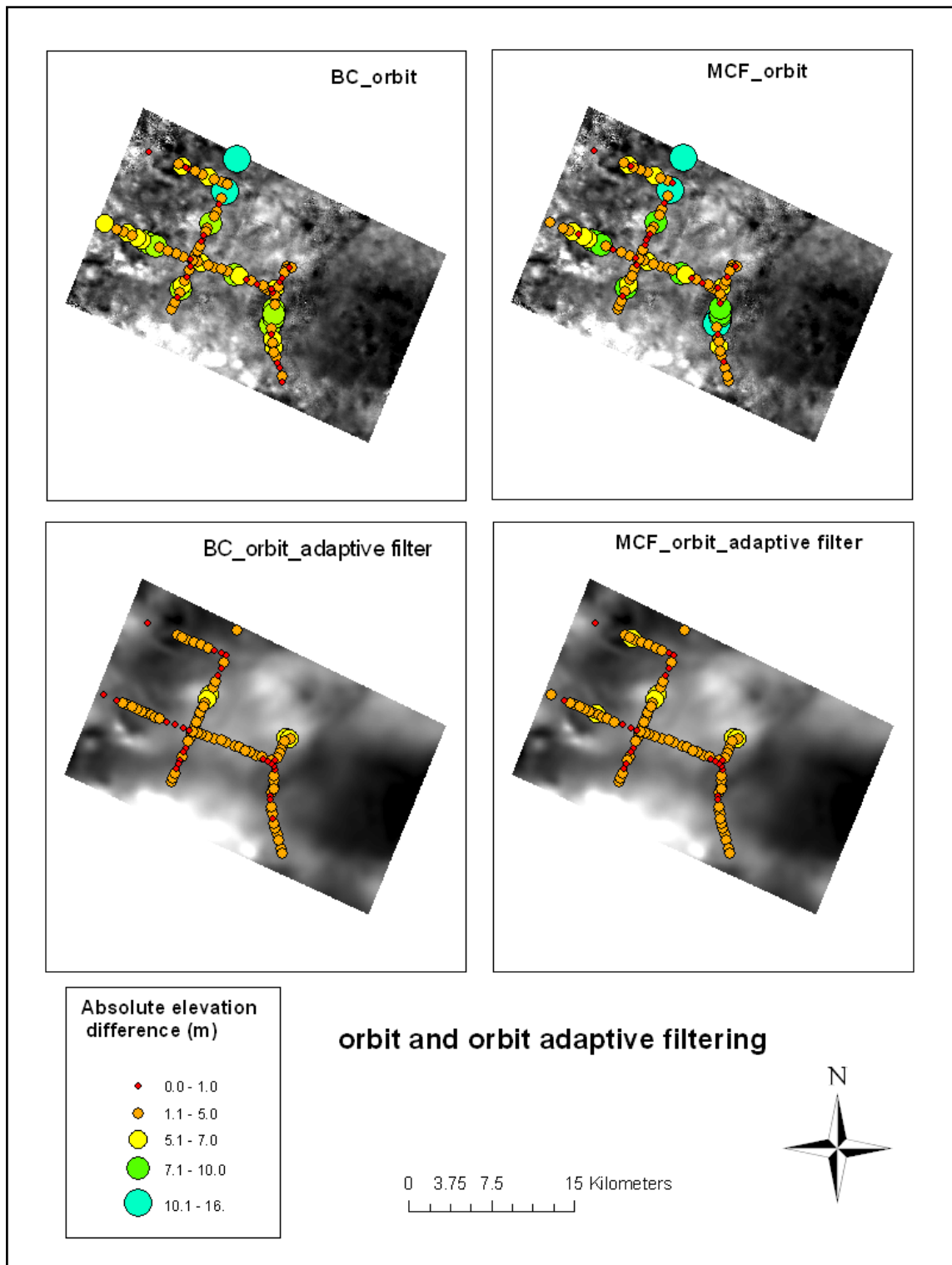


Figure 6.18: Error distribution of check GCPs in DEM2000 in Dadahup using orbit and orbit adaptive filter processing technique.

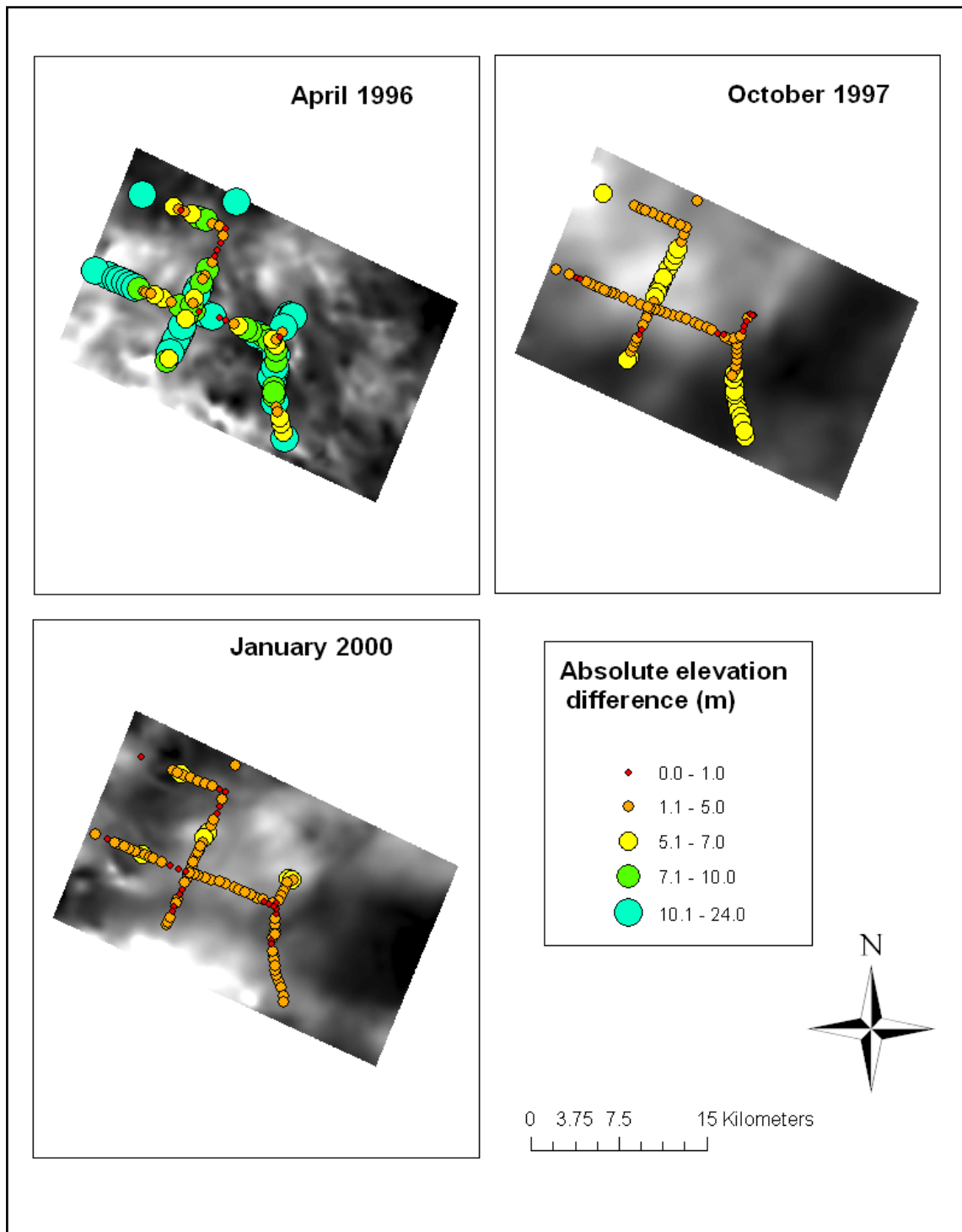


Figure 6.19: Error distribution of check GCPs for three DEMs generated from six ERS-1/2 tandem radar images over Dadahup site using intensity adaptive filter processing technique with MCF unwrapping method.

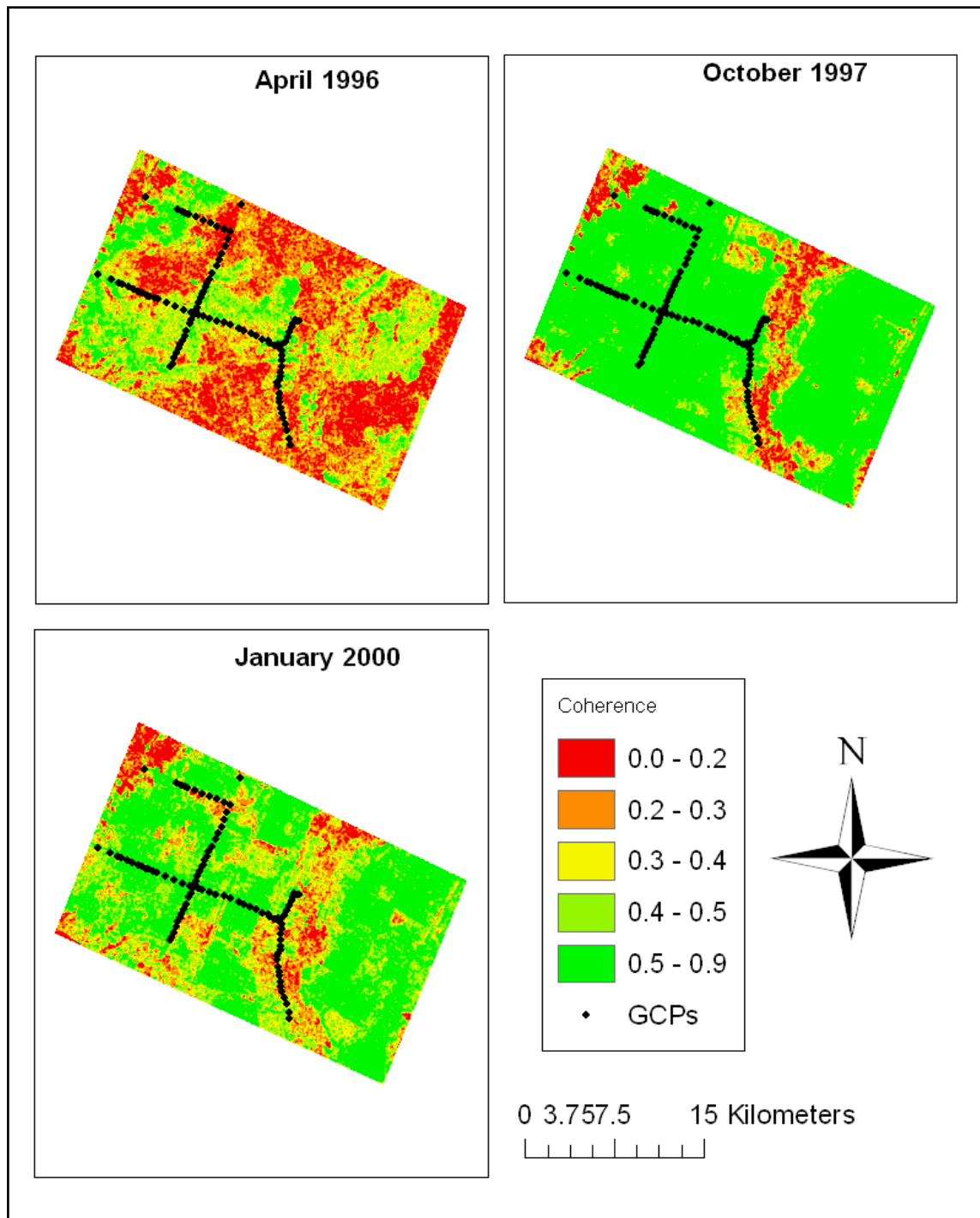


Figure 6.20: Coherence change in Dadahup between 1996 and 2000.

6.5.5 Maluku: Absolute assessment comparison

Absolute comparison is required for accurate validation of the DEM. The reference DEM was not available and instead, the most accurate DEM from InSAR results was chosen as a reference DEM. As it was noted that the DEM 1997 in Maluku using the intensity adaptive filter with MCF unwrapping method (DEM17) was the most accurate DEM compare to other DEMs (Figure 6.21). Therefore, this DEM will be considered as a reference DEM to analysis the elevation difference distribution in other DEMs. The elevation differences (difference map) are computed using simple map algebra:

$$\text{Elevation Difference} = \text{Reference DEM} - \text{Other DEMs} \quad (6.1)$$

This method gives two results; statistical results and error image (error map) showing error magnitude within the DEM. The error map will be analyzed in later chapters.

To analyze the difference between the different DEM processing, different maps between DEM 17 and other DEMs of the same tandem pairs were calculated (Figure 6.22). The difference image is analyzed to obtain positive numbers for cases in which the DEM overestimates the elevation (green colour) and negative numbers for those cases in which it underestimates the elevation (red colour). It is clear that elevation differences fluctuate at around zero in many of DEMs. Table 6.8 show the statistic information about the elevation difference for all DEMs.

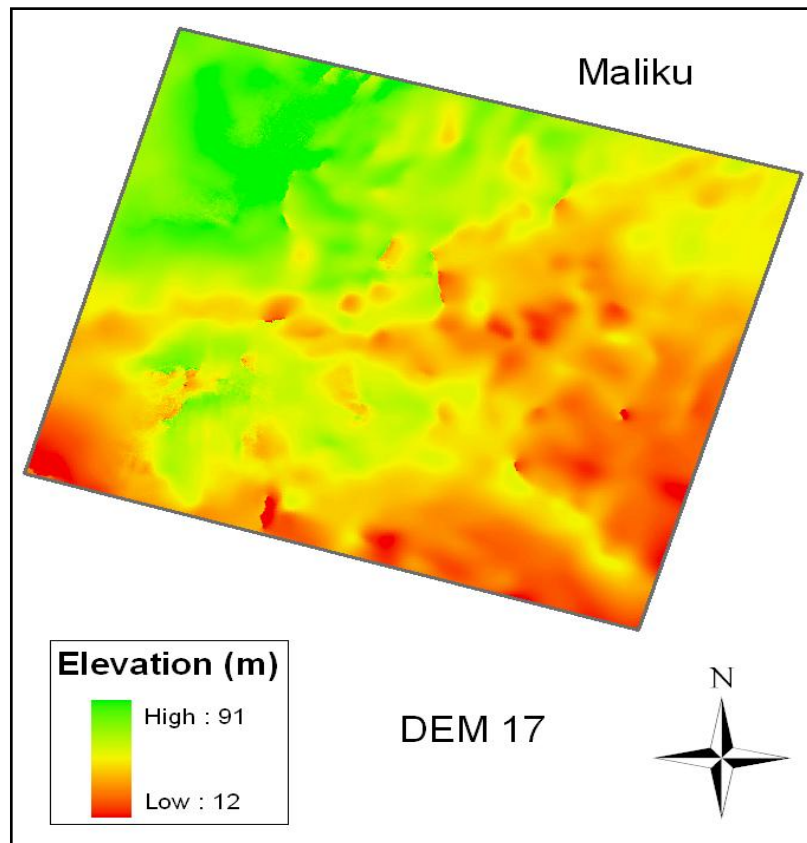


Figure 6.21: Final DEM for Maliku using intensity processing technique with MCF unwrapping method.

Table 6.8: Descriptive statistics of DEMs 1997 in Maliku relative to DEM17.

Unwrapping methods	Interferogram methods	DEM No	Min (m)	Max (m)	Mean (m)	St.dev (m)	RMSE (m)
BC	Intensity	DEM13	-172.2	93.8	-0.4	11.6	11.6
	Intensity adaptive	DEM14	-41.4	61.8	0.9	5.5	5.6
	Orbit	DEM15	-111.4	79.7	-0.3	8.5	8.5
MCF	Intensity	DEM16	-57.2	40.1	-3.8	7.9	8.8
	Orbit	DEM18	-38.3	46.5	-0.6	4.8	4.8

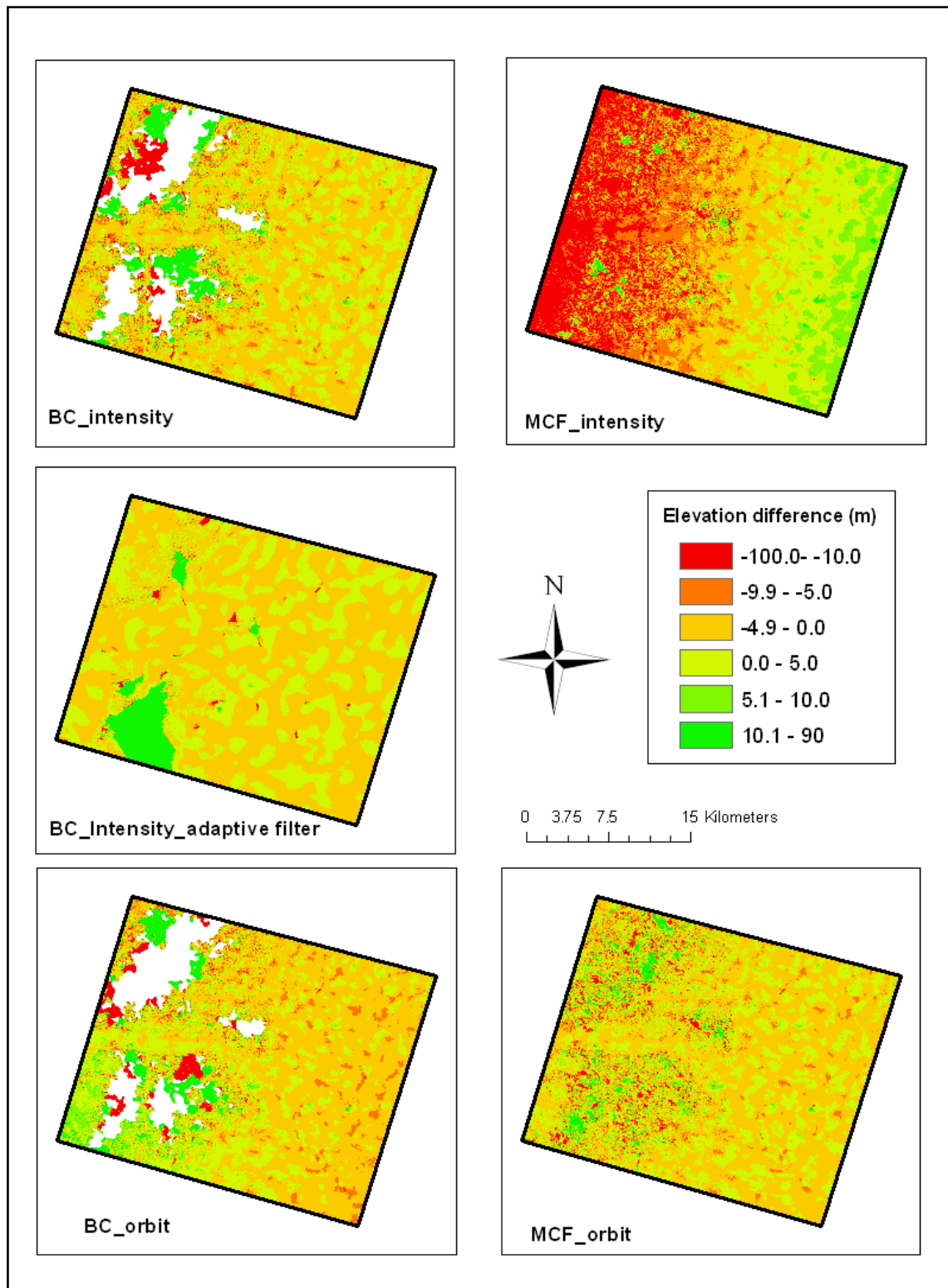


Figure 6.22: Spatial distribution of elevation difference between DEMs-1997 and DEM17 (reference).

The Min and Max values decreased gradually when applying the MCF unwrapping method as well as after applying adaptive filtering many times. Similar to relative assessment, Orbit with the MCF unwrapping method have the lowest RMSE and standard deviation while intensity have the bigger error. However, the elevation of most of the DEMs is higher than the reference DEM with the mean error about 1.2 m and RMSE around 7.9 m. the absolute elevation distribution will be discussed in a later chapter.

Figure 6.23 shows the elevation difference between the reference DEM and the other DEMs generated using intensity adaptive filtering with the MCF unwrapping algorithm over the three different time periods. The new difference maps describe the error resulting from temporal change effects such as land cover, wind/water condition, local surface level, baseline and atmospheric effects.

Similar to the statistical results in Table 6.2, the difference images show that the DEMs of March 1996 have the lowest elevation, whilst the DEMS that have been generated in April 1996 shows the height elevation compare to the reference DEM. The DEMs of 2000 have the smallest differences, with RMSE of 8.86, whilst the RMSE is 16.06 and 23.33 for March and April 1996 respectively (Table 6.9). In case of one standard deviation, the error was expected to lie within 8.86 ± 8.8 , which determines 68.27 % of the reliability. By using two standard deviations, 95.45 % of the errors are located between -8.8 and 26.4 m. Figure 6.24 shows the distribution of the error, which follows a Gaussian curve. It is clear that the mean error is located at the centre of histogram and it is close to zero when the accuracy increases as is shown in DEM 2000. The whole of the histogram for the resultant DEM in April 1996 seems to have been shifted towards lower value. From the elevation difference images, it seems that the majority of the

overestimation area is located in the south west of DEMs while the underestimation area is located in the north and north east. More than 90% of the test area is underestimated in the March 1996 DEM.

Table 6.9: Summary of statistical parameters for absolute elevation difference in Maliku between three-ERS tandem image DEMs (DEM5, DEM11 and DEM23) and DEM17 (reference).

	DEM17-DEM5(m)	DEM17-DEM11 (m)	DEM17-DEM23 (m)
Min	-22.8	-78.1	-48.0
Max	100.1	117.4	37.8
Mean	13.5	-7.2	1.1
RMSE	16.05	23.33	8.86
Std. Dev	8.6	22.2	8.8

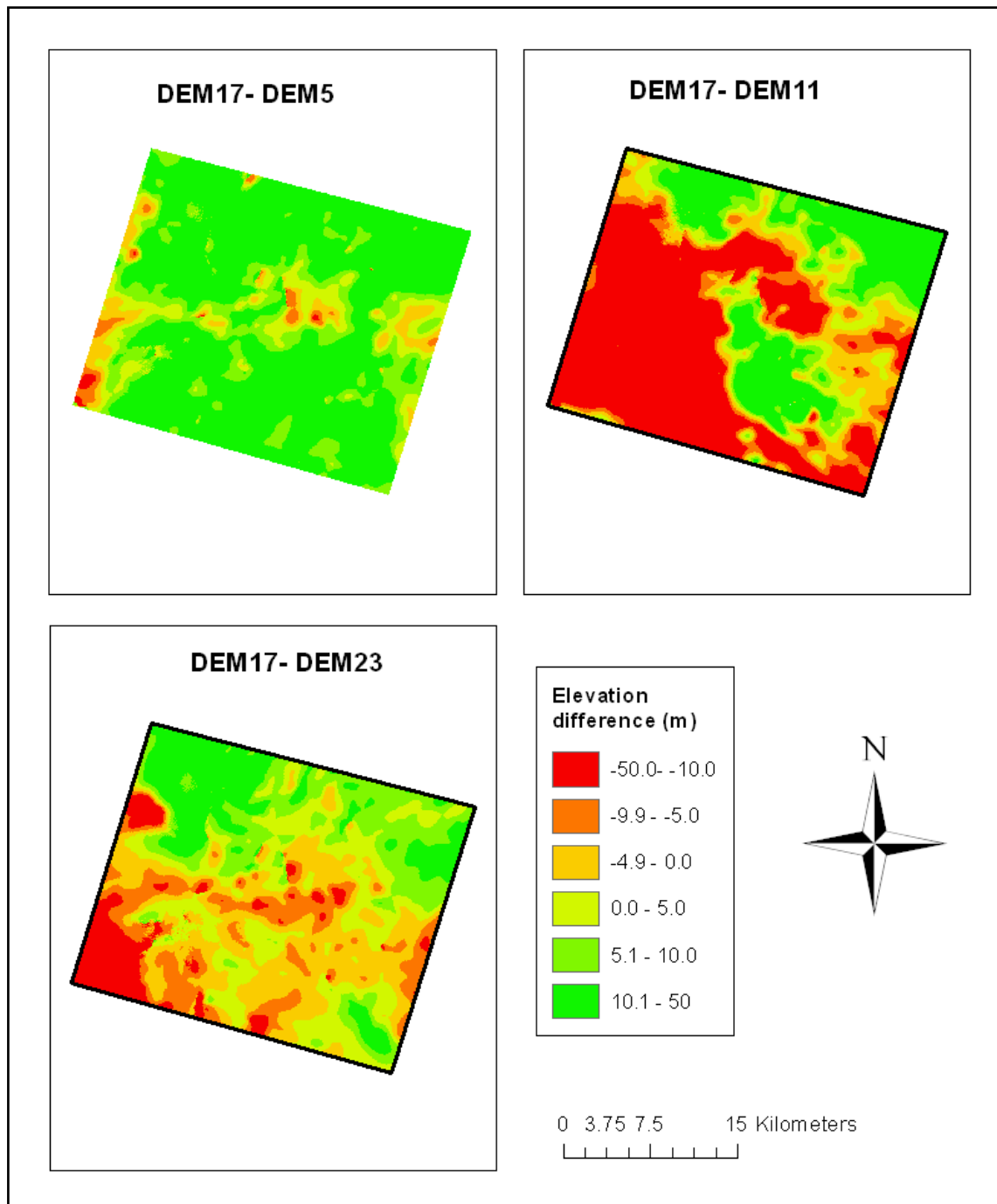


Figure 6.23: Spatial distribution of elevation difference in Maliku between three tandem ERS image DEMs (DEM5, DEM11 and DEM23) and DEM17 (reference).

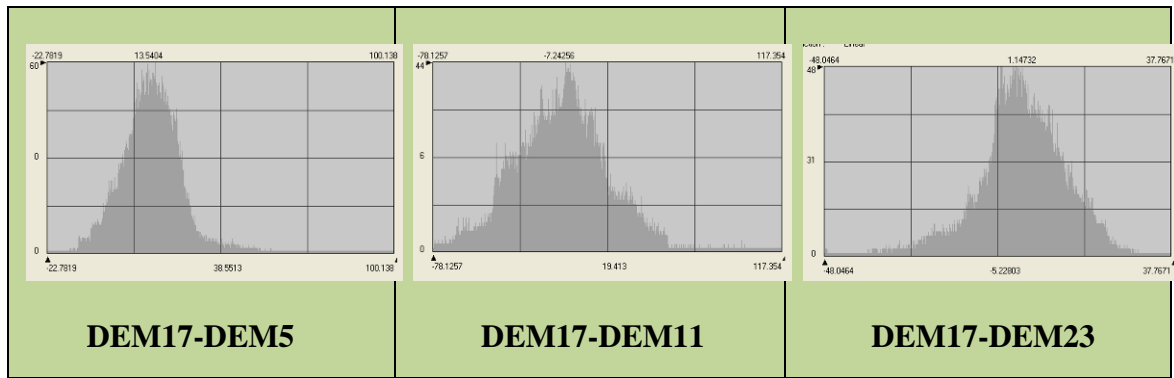


Figure 6.24: Histograms of variation between Maliku reference DEM and generated DEMs

6.5.6 Maliku: Spatial distribution of absolute assessment error

To analyse error distributions in different areas of the DEMs and relate it to the processing methods, land cover, moisture condition and atmospheric effects, a colour coding is used to quantify the error magnitude and spatial distribution in various parts of the study area. The absolute elevation difference maps were classified into absolute elevation difference classes such as 0-5m, 5-10m, 10-15, 15-20m, 20-25, and more than 25 m. The difference maps in Figure 6.25 indicate that in 90% of the DEM area, the height estimation from differently processed DEMs deviate by less than 4 m with respect to DEM 17. The higher errors were found only in and closest to the holes. As discussed earlier, adaptive filter and MCF unwrapping methods fill these gaps with different interpolation methods. The error observation shows high error close to these interpolations, with more than 20 m in some cases. However, only the MCF intensity DEM show increased errors towards the west, while other DEMs show random distribution of error except for the gaps area. Table 6.10 shows the basic statistics of the absolute elevation difference with minimum mean difference of 2 m and standard deviation of 5.2.

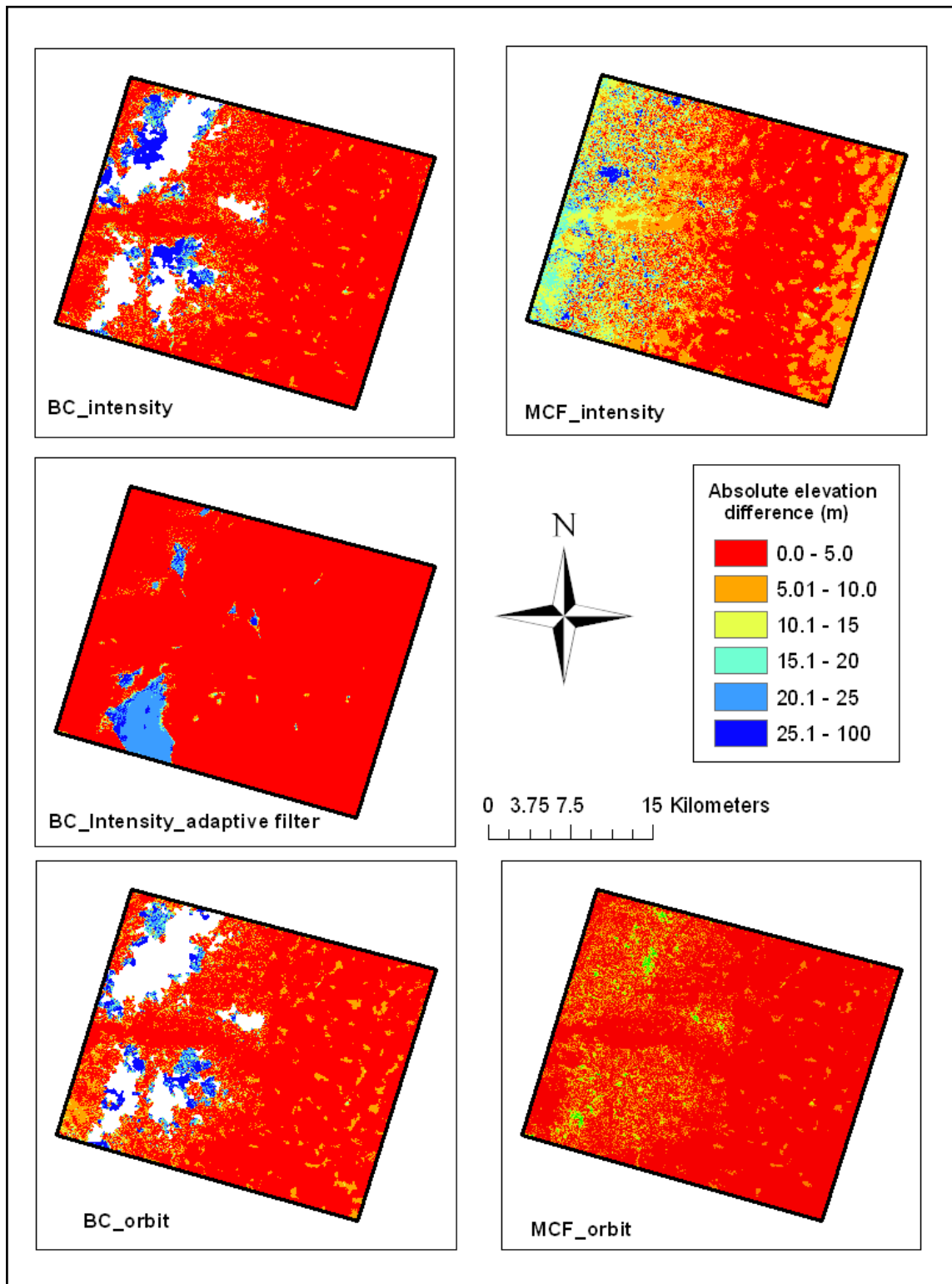


Figure 6.25: Spatial distribution of absolute elevation difference between DEMs-1997 and DEM17 (reference.)

However, looking at absolute difference maps between the four tandem pairs using only intensity adaptive MCF method, it is clear that there is an increase of error in the western half of the DEMs. The coherence in this part is low, which indicates forest and dense vegetation. There is a high error even in relatively high coherence areas such as the northwest corner of the DEMs and this cannot be explained by land cover or forest distribution. By analyzing the difference elevation in Figure 6.26, it was clear that this area has a higher value in all the DEMs compare to the 1997 DEM, which means the high values decreased in the dry season, but increased in the wet season. This can be explained by the fact that the area is a plantation near Kahayan River and has high coherence. Table 6.11 shows the basic statistics of the difference image with a mean absolute elevation difference of 14.02 m, 18.3 and 6.9 m and RMSE of 16.1 m, 23.3 m and 8.9 m for the March 1996, April 1996 and October 1997 DEMs respectively.

From the error images, it is clear that the blue colour value (more than 20 m) is dominating many parts of the areas in 2000-199604 images, whereas the red colour (less than 5m) is dominating the 2000-97 images. This shows the accuracy of DEM 2000 is much better than other DEMS. The 2000-199603 error image show few areas with error between 5 and 20 m, which means that DEM has a very high error and acceptable error at the same time. However, the error image 2000-199604 shows more variation in the error over most of the image.

The absolute height difference between different DEMs and the reference DEM indicates an acceptable fit in the centre and east part of the DEMs but some problems in the left parts where coherence decreased between 1996 and 1997. However, the difference between the two elevation models was found to range from 0 to more than 20

m. The mean difference is at 13.1 m resulting in a standard deviation for the difference of 9.3.

Table 6.10: Summary of statistical parameters for elevation difference between DEMs 1997 and reference DEM (DEM17).

Unwrapping methods	Interferogram methods	DEM No	Min (m)	Max (m)	Mean (m)	St.dev (m)	RMSE (m)
BC	Intensity	DEM13	7.6	172.2	4.9	10.5	11.6
	Intensity adaptive	DEM14	3.8	62.0	2.0	5.2	5.6
	Orbit	DEM15	1.1	111.4	4.5	7.2	8.5
MCF	Intensity	DEM16	1.9	57.2	6.6	5.8	8.8
	Orbit	DEM18	3.8	46.5	3.1	3.7	4.8

Table 6.11: Summary of statistical parameters for absolute elevation difference in Maliku between three-ERS tandem image DEMs (DEM5, DEM11 and DEM23) and DEM17 (reference).

	DEM17-DEM5	DEM17-DEM11	DEM17-DEM23
Min (m)	6.48	4.58	2.29
Max (m)	100.13	117.35	48.04
Mean (m)	14.02	18.33	6.86
RMSE (m)	16.05	23.33	8.86
Std. Dev (m)	7.82	14.44	5.61

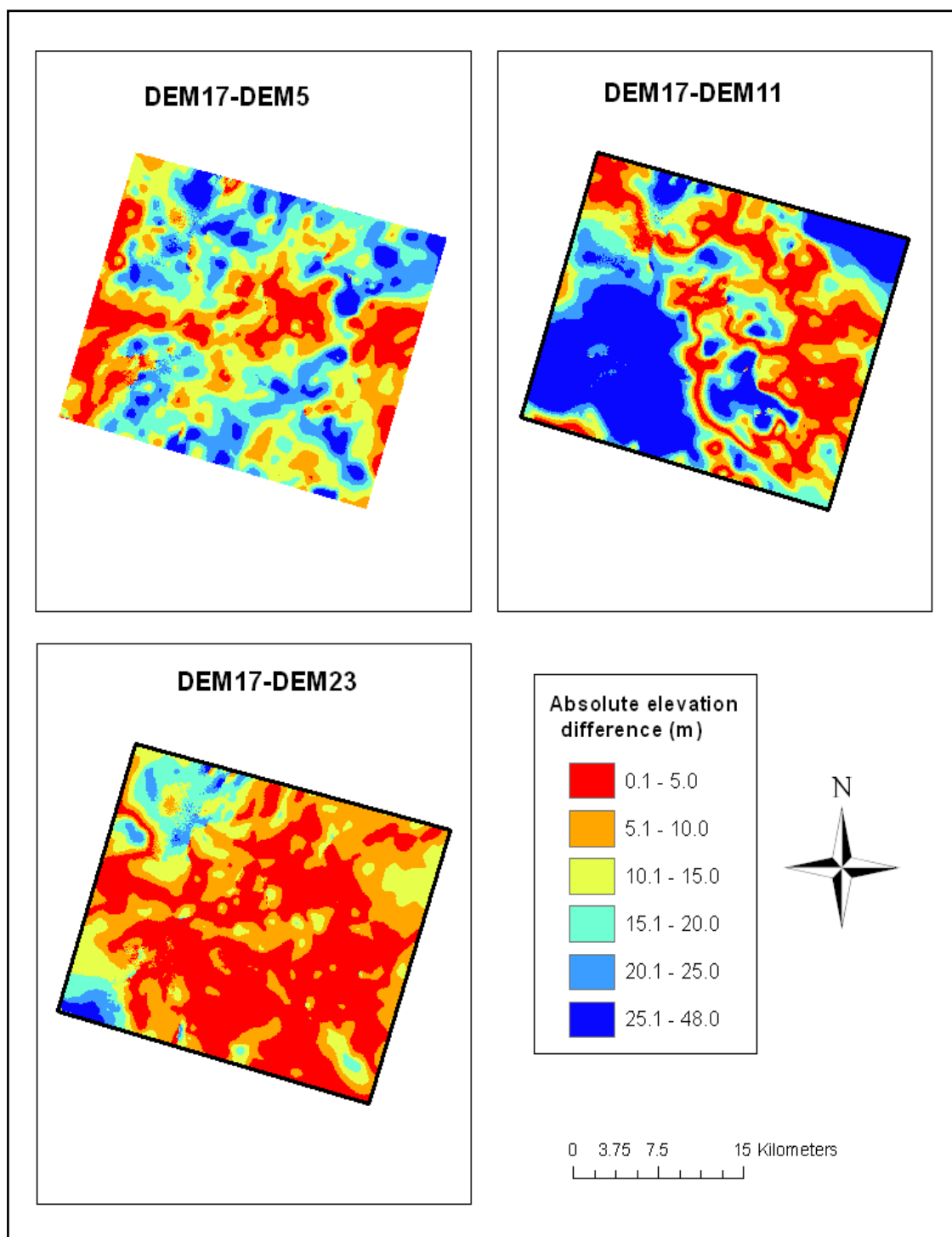


Figure 6.26: Spatial distribution of absolute elevation difference in Maliku between three tandem ERS image DEMs (DEM5, DEM11 and DEM23) and DEM17 (reference).

6.5.7 Dadahup: Absolute assessment comparison

Absolute assessment of Dadahup DEMs is done by comparing elevation differences between the reference DEM (24) (Figure 6.27) and DEMs delivered by the other InSAR methods. According to statistical information in Table 6.4 and the accuracy assessment of Dadahup DEMs against GPS profiles in Table 6.7, it is clear that DEM 20 and DEM 24 are more accurate compared to other DEMs. Therefore, DEM 24 was chosen as a reference DEM to evaluate the other DEM accuracies using a difference map technique. In a similar way to the Maluku DEMs, the difference maps were used to examine the accuracy of processing methods that have been used in this study. Figure 6.28 and Figure 6.29 show the difference maps of DEMs of 2000 tandem pair images generated using different processing methods. Unlike Maluku DEMs, the minimum, maximum, mean, standard deviation and RMSE is almost similar between BC and MCF unwrapping methods as well as between intensity and orbit methods (Table 6.12). However, applying an adaptive filter reduces the RMSE and standard deviation dramatically.

To analyze the temporal change effects, only the more accurate DEMs from the different time pairs have been studied (DEM 8 and DEM16) and the difference maps have been calculated (Figure 6.30). From the descriptive statistics of elevation differences illustrated in Table 6.13, The RMSE for elevation differences of DEM 8 and DEM 16 is 16.99 m with a maximum and minimum of 61.67 m and 0.21 m respectively. In the case of using 2 Std.Dev, 95.45 % of the errors are expected to be between -12.3 and 14.1 m. DEMs histogram was drawn to show the relationship of elevation difference distribution (Figure 6.31). The histograms of both DEMs errors follow a Gaussian curve distribution.

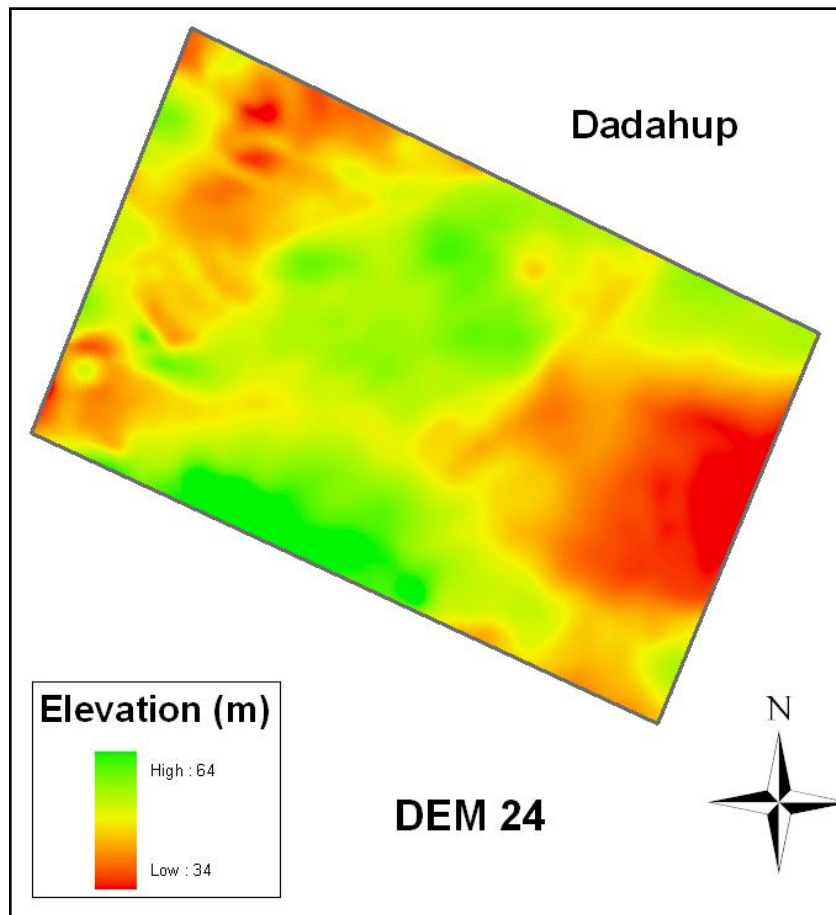


Figure 6.27: Final DEM for Dadahup using orbit processing technique with MCF unwrapping method.

Table 6.12: Summary of statistical parameters for elevation difference between 2000-DEMs and reference DEM (DEM24).

Reference	Unwrapping methods	Interferogram methods	Min (m)	Max (m)	Mean (m)	St.dev (m)	RMSE (m)
DEM 24	BC	Intensity	-59.6	74.7	2.6	3.9	4.8
		Intensity adaptive	-12.4	14.6	1.3	1.8	2.2
		Orbit	-52.0	64.8	2.6	3.9	4.7
		Orbit adaptive	-2.0	1.8	0.0	0.2	0.2
	MCF	Intensity	-64.1	51.5	2.7	3.9	4.8
		Intensity adaptive	-12.1	14.3	1.4	1.7	2.2
		Orbit	-50.4	52.6	2.8	3.9	4.8

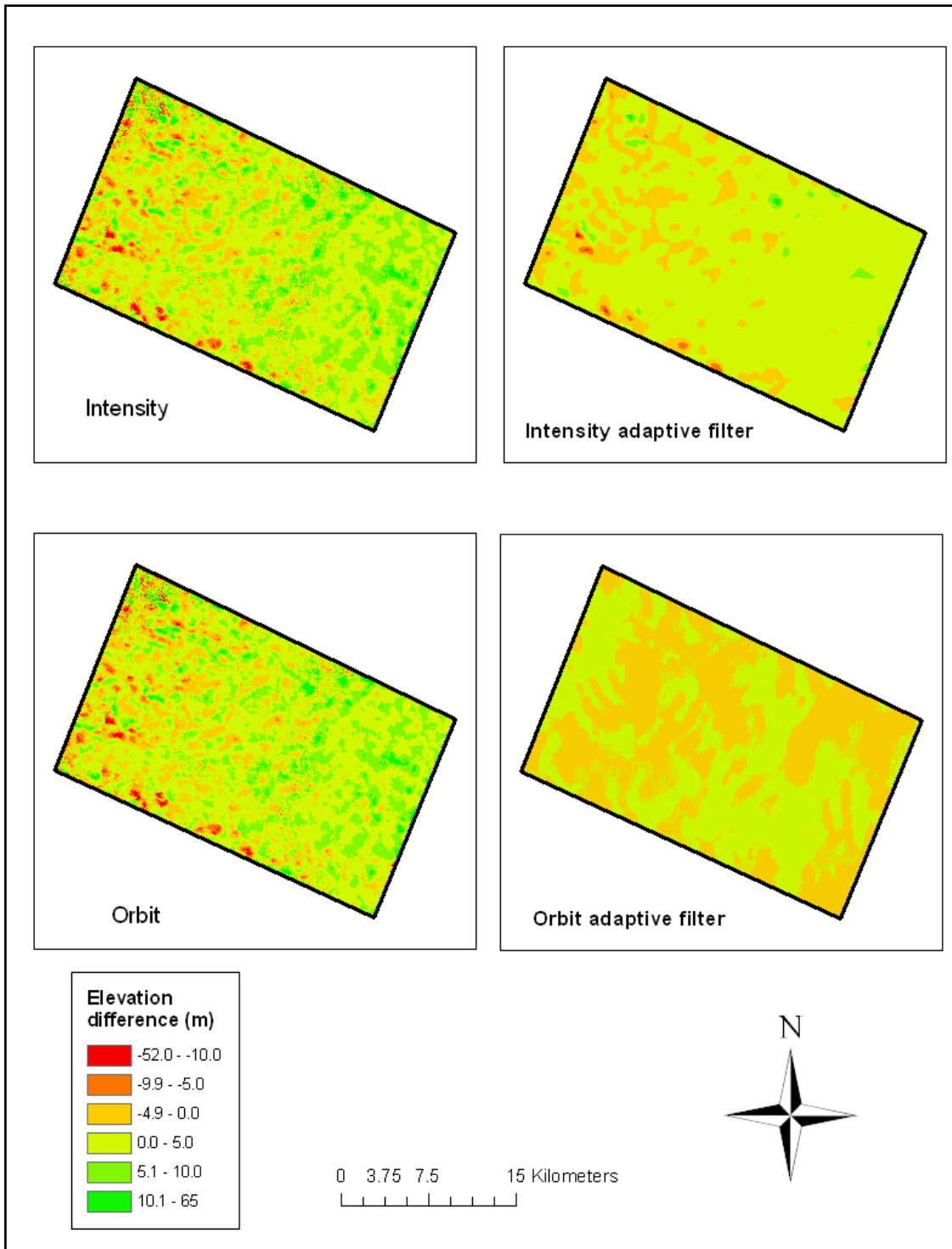


Figure 6.28: Spatial distribution of elevation difference between DEMs-2000 and DEM24 (reference) using BC unwrapping method.

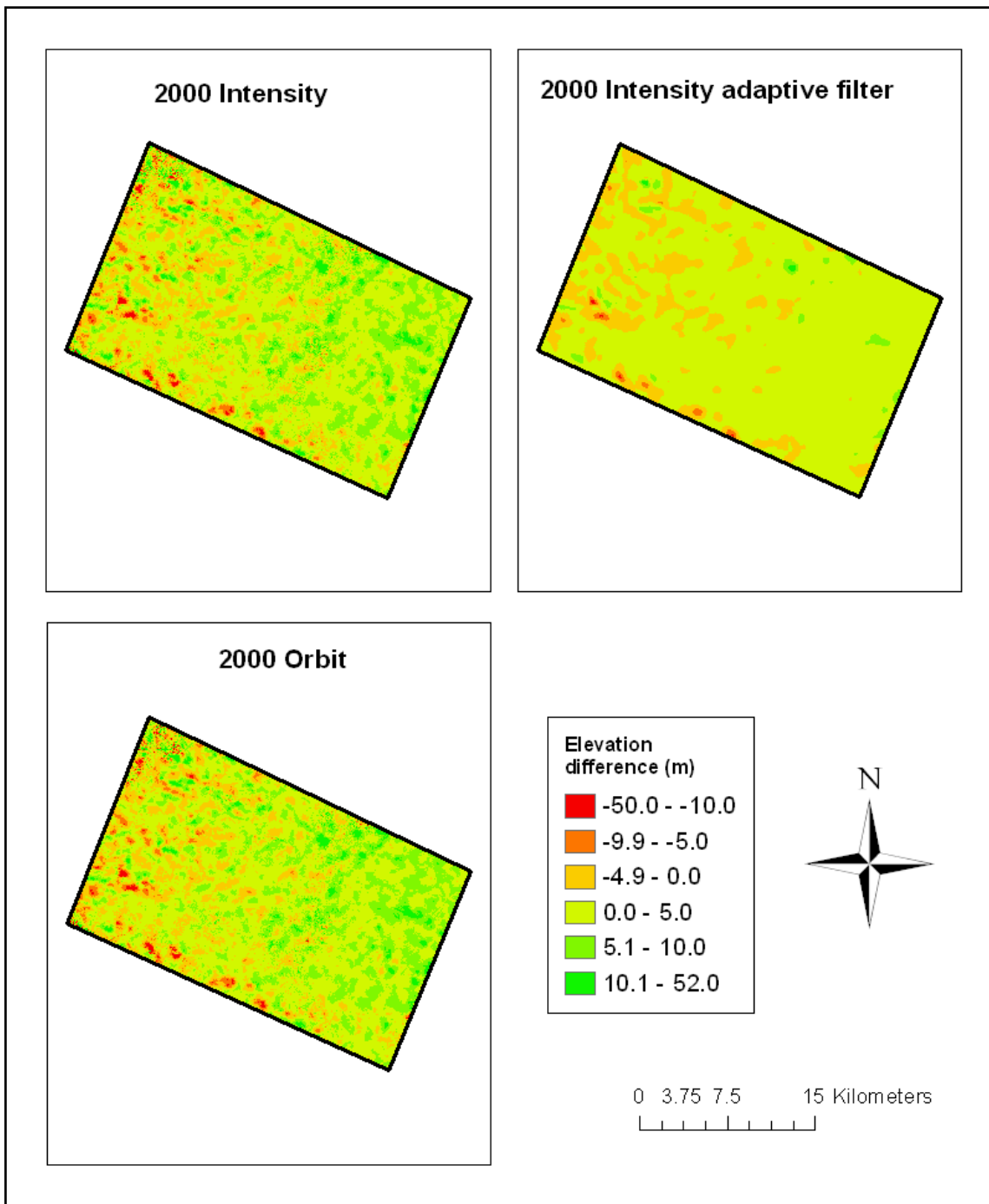


Figure 6.29: Spatial distribution of elevation difference between DEMs-2000 and DEM24 (reference) using MCF unwrapping method.

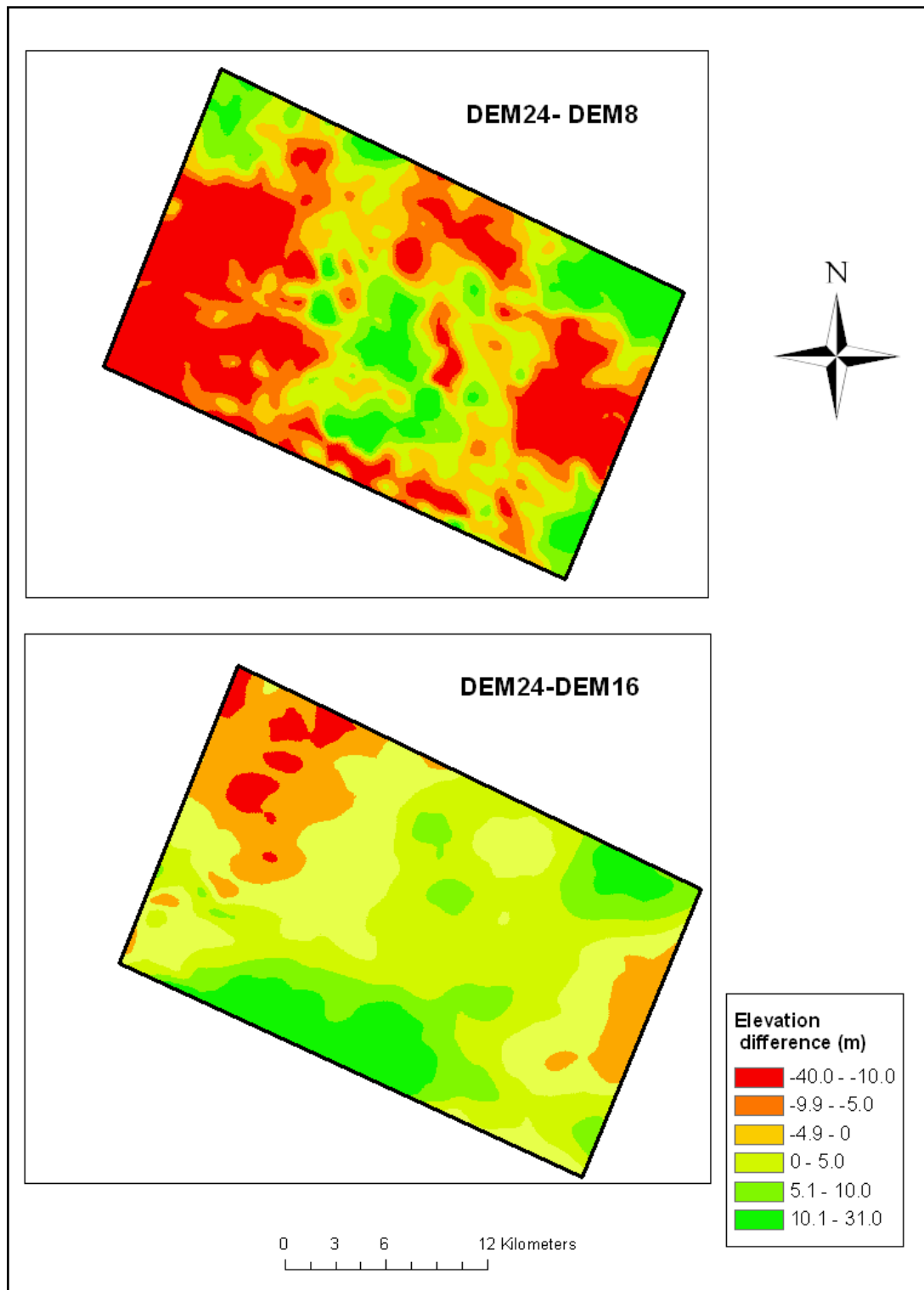


Figure 6.30: Spatial distribution of absolute elevation difference in Dadahup between two tandem ERS image DEMs (DEM8 and DEM16) and DEM24 (reference).

Table 6.13: Summary of statistical parameters for elevation difference in Dadahup between two-ERS tandem image DEMs (DEM8, DEM16) and DEM24 (reference).

	DEM24-DEM8	DEM24-DEM16
Min (m)	-40.04	-16.3
Max (m)	31.8	22.1
Mean (m)	-3.9	0.9
RMSE (m)	11.58	6.63
Std.Dev (m)	10.9	6.6

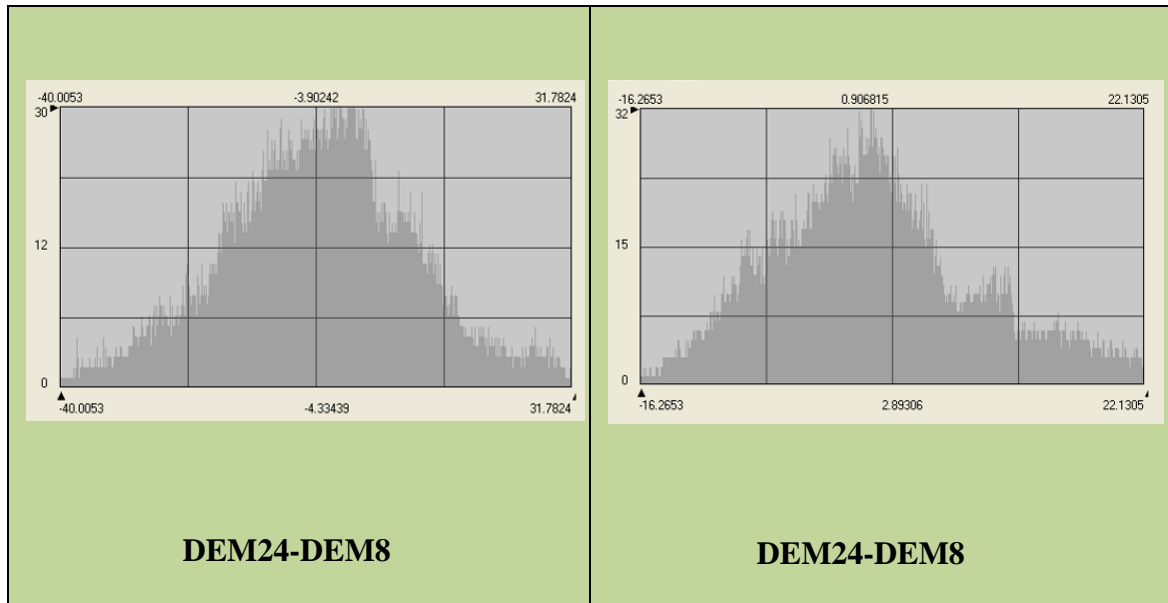


Figure 6.31: Histograms of variation between Dadahup reference DEM and generated DEMs.

6.5.8 Dadahup: Spatial distribution of absolute assessment error

Difference maps of Dadahup DEMs have been generated in order to see where the elevation differences from different processing methods and from different tandem pair images have occurred. DEM 24 has been used to analyze the spatial distribution of errors resulting from DEM processing shown in Figure 6.32 and Figure 6.33. Absolute elevation difference was divided into six classes and each class were assigned to a different colour. It is clear that the red colour dominates most of the DEM, which indicates that most of the areas have an absolute elevation difference of less than 5 m (Table 6.14). Also unwrapped phase image of this area shows continuous smooth

elevation indicating no significant error in phase unwrapping. Few anomalies with a difference value of more than 5 m appear in both intensity and adaptive filter and few of them appear in adaptive filter DEMs. The distribution of these anomalies is random which indicates that the error is distributed uniformly throughout the area.

The absolute differences show high variation when different tandem images from different times have been used (Figure 6.34). Visual interpretation of error distribution shows that the absolute difference increases dramatically from about 3 m in the same pair to more than 9 m and 5m in 1996 DEM and 2000 DEM respectively. Most of the pixels in class 2 and upper classes, which have high elevation differences, are located near deforested areas where the coherence has been changed by more than 0.4. However, the pixels in class 1 covered about 50% of the test site in both images and they are located in the centre and north part of the test site. Table 6.15 shows the basic statistics of the difference image with a mean absolute elevation difference of 9.1 m and 5.1 m and RMSE of 11.6 m and 6.6 m for 1996 and 1997 DEM respectively.

Table 6.14: Summary of statistical parameters for absolute elevation difference in Dadahup between 2000-DEMs and reference DEM (DEM24).

Reference	Unwrapping methods	Interferogram methods	Min (m)	Max (m)	Mean (m)	St.dev (m)	RMSE (m)
DEM 24	BC	Intensity	7.6	74.6	3.8	2.9	4.8
		Intensity adaptive	3.8	14.6	1.8	1.3	2.2
		Orbit	3.4	64.7	3.7	2.9	4.7
		Orbit adaptive	0	2.0	0.1	0.1	0.2
	MCF	Intensity	1.5	64.1	3.8	2.9	4.8
		Intensity adaptive	3.8	14.3	1.8	1.3	2.2
		Orbit	3.8	52.6	3.8	2.9	4.8

Table 6.15: Summary of statistical parameters for absolute elevation difference in Dadahup between two-ERS tandem image DEMs (DEM8, DEM16) and DEM24 (reference).

	DEM24-DEM8	DEM24-DEM16
Min (m)	5.72	1.91
Max (m)	40.00	22.13
Mean (m)	9.12	5.09
RMSE (m)	11.58	6.63
Std.Dev (m)	7.13	4.23

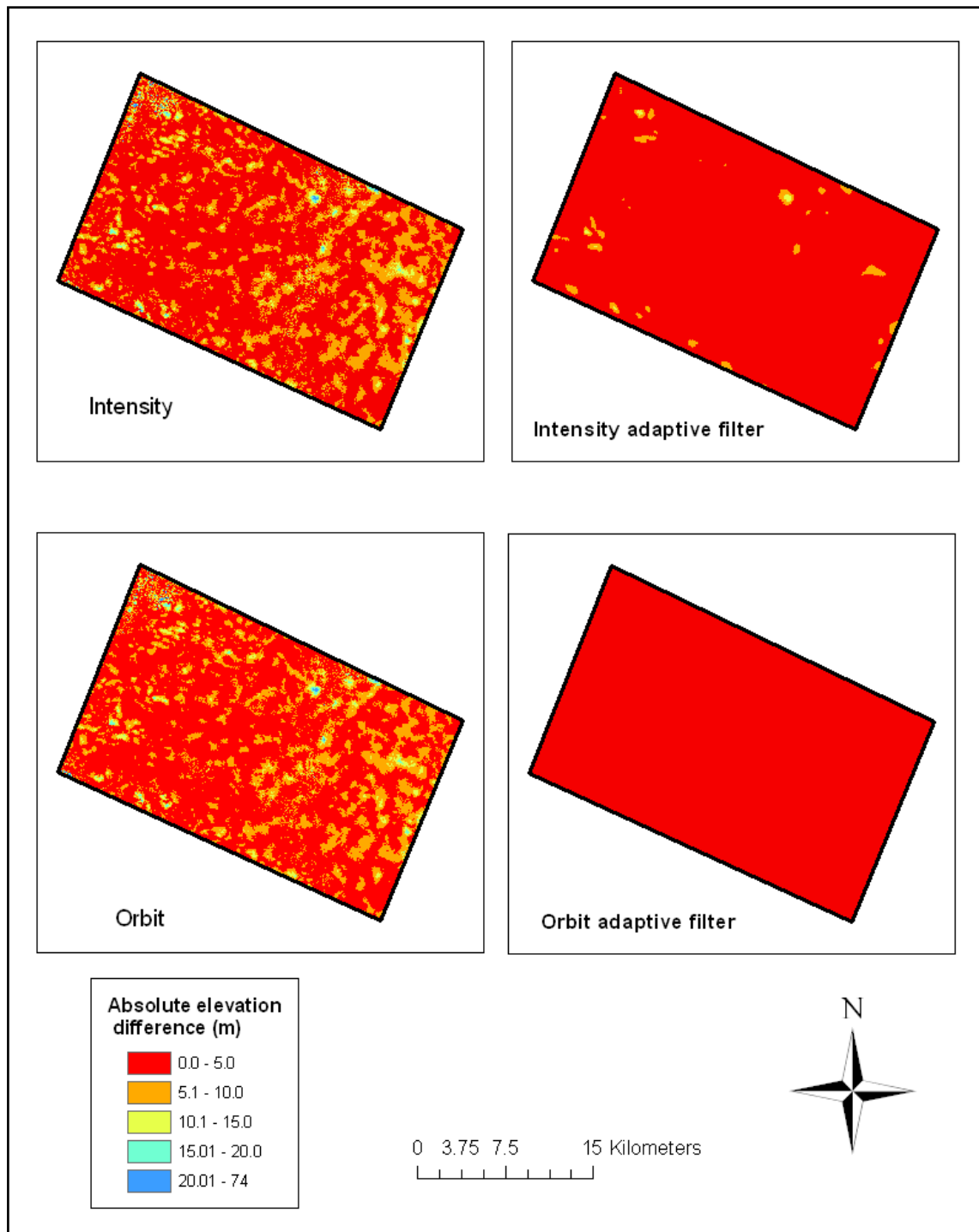


Figure 6.32: Spatial error distribution of absolute elevation difference of 2000-DEMs using BC unwrapping method relative to DEM24.

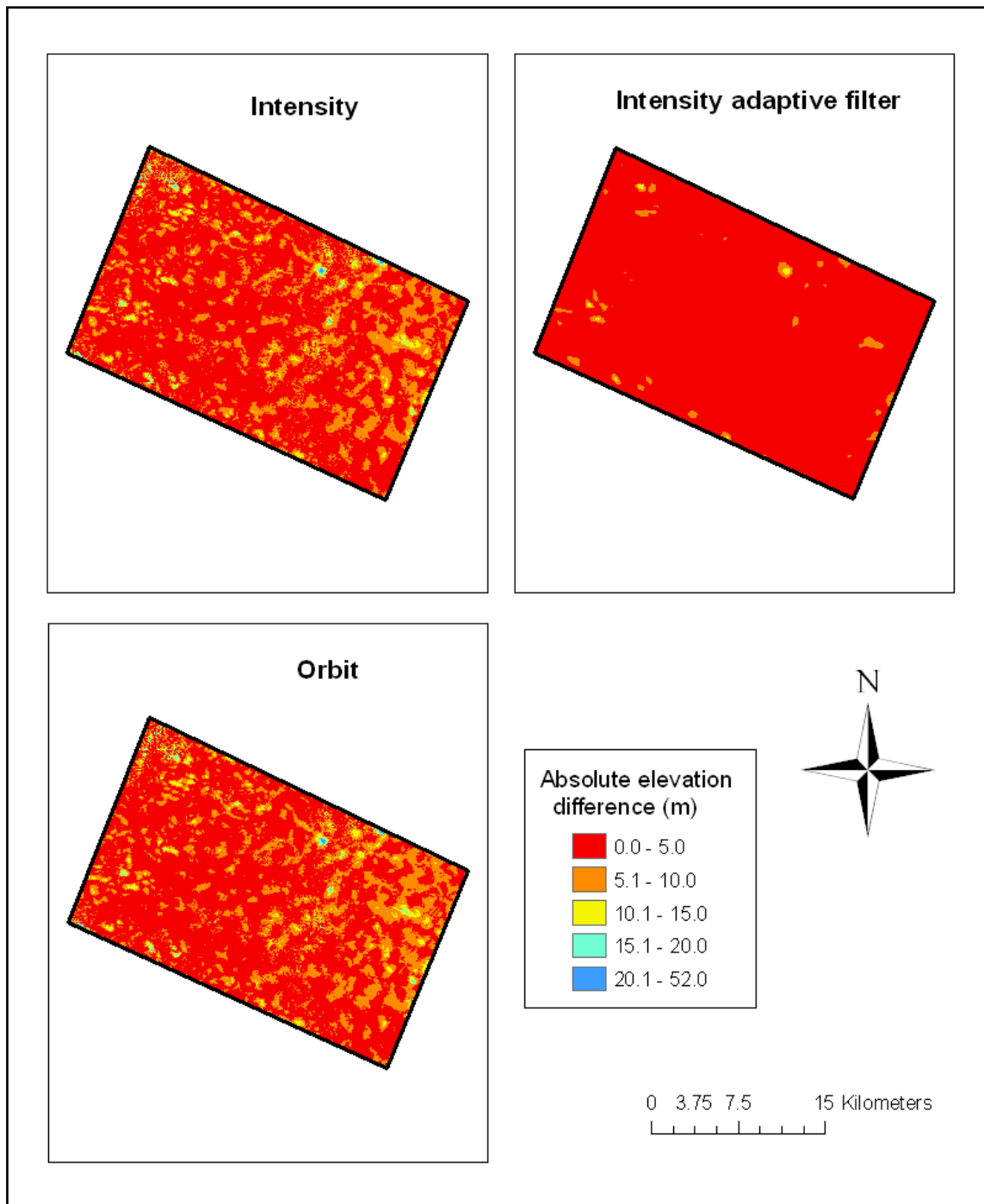


Figure 6.33: Spatial error distribution of absolute elevation difference of 2000-DEMs using MCF unwrapping method relative to DEM24.

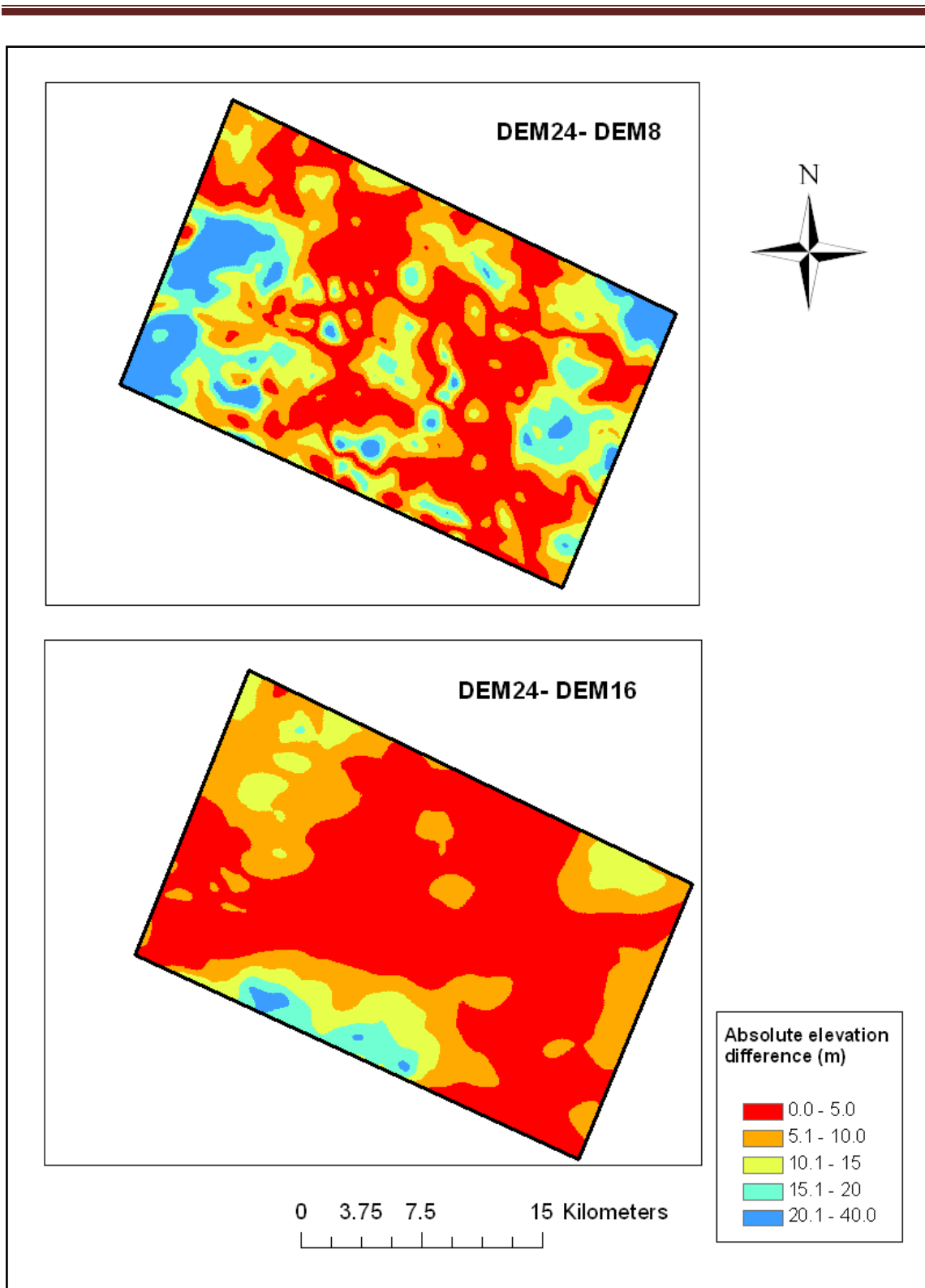


Figure 6.34: Spatial distribution of absolute elevation difference in Dadahup between two ERS tandem image DEMs (DEM8, DEM16) and DEM24 (reference).

6.6 Discussion

There are a number of studies on the use of ERS interferometry data for DEM generation and retrieval of terrain parameters (Zebker *et al.*, 1994a; Rufino *et al.*, 1998; Bourgeau-Chavez *et al.*, 2001; Kamaruddin *et al.*, 2003). Due to the lack of suitable reference DEMs, the quantitative evaluation of the result is often difficult. The main problem of this approach is the identification of ground features in both sources. In most of the cases, validation of the DEM has been done either by comparing with a DEM generated from other sources or from available topographic maps. The DEM validations were also carried out by ground surveyed data using GPS and total station (Dongchen *et al.*, 2004). Contour maps were often used for the comparison with the interferometric data sets (Zebker and Goldstein, 1986; Prati and Rocca, 1990). SRTM InSAR data has also been used for DEM generation and its validation (Rabus *et al.*, 2003; Koch *et al.*, 2002).

Accuracy is the most important factor to be considered when a DEM is used. DEMs are used in a wide range of applications. Despite this fact, there is still a lack of quality control. A standard procedure for this kind of assessment as well as generally accepted specifications about the accuracy of DEMs does not exist (Ackermann, 1996). In 1997, the United States Geological Survey (USGS) proposed standards for the collection, processing and quality control of DEM data for the entry into the National Digital Cartographic Data Base (USGS, 1997). The International Cartographic Association (ICA) established a commission on spatial data quality which defined seven elements to describe the quality of data used in a GIS (Guptill and Morrison, 1995). Despite these efforts, quite a number of unsolved problems on how to treat the quality of spatial data still remain.

The quality of DEMs produced from ERS tandem pairs seems to be strongly affected by four issues; the offset estimation, interferogram computation, filtering and PU methods. All these issues have been addressed and assessed in this chapter. The most common practice to assess the accuracy of a DEM is to generate statistical measures, such as RMSE, mean error and standard deviation. This assessment is carried out by verification of the DEM against a number of independent check points (ICPs) collected using differential GPS or by comparison DEMs with a reference DEM, which is more accurate (Lin *et al.*, 1994). According to previous studies on the evaluation of DEM generated by ERS, the RMSE of approximately 16.9 m (Jayaprasad *et al.*, 2008), 20 m (Rufino *et al.*, 1998), 5 m (Zebker *et al.*, 1994a), 11.3 m (Baek *et al.*, 2005) and 7 m (Al-harbi, 2009) can be achieved while RMSE predicted in forest land cover was around 18.7 m by Rufino *et al.* (1998) and 18.1 m and 5.1 m by Guritz *et al.* (1999).

Quality assessment in this section was done using absolute and relative comparison methods. The error were classified into two groups; error due to different processing methods and error due change of land cover, seasonal condition, baseline and atmospheric effects. The relative assessment has been carried out using 100 DGPS survey points as ground truth. The points have not been distributed very well due to access limitations in the tropical swamp forest areas. The average RMSE range between 26 m to 5 m and the minimum RMS errors in Maluku and Dadahup test site are 5.0 m and 2.9 m respectively and agree with results found by other authors (Figure 6.35 and Figure 6.36). That means that the accuracy was quite good for the whole area at least in terms of the requirements of small to medium scale topographic mapping. The InSAR DEM accuracy decreased only in very low coherence areas. Generally, the DEM of dense forest was successfully generated. Therefore, under favourable conditions, DEM

with acceptable accuracy could be easily generated. However, this method was ideal in terms of comparing the DEM values by direct measurement using DGPS points. The DEMs derived in this study, generally have slightly high RMS errors. However, they are still better than those predicted in Hagberg and Ulander (1993) and Al-harbi (2009), which were 5 and 7 m respectively. Of course, the RMS errors in this study include very low coherence values which could affect RMS errors in a negative way. The interferometric coherence is an important parameter determining how accurate the interferometric measurements are. Over forested terrain to the west of Maluku and north of Dadahup, the coherence is usually very low but it is still possible to make measurements.

Quantitative analysis of different DEMs generated using different processing techniques indicates that intensity method is slightly better in low coherence areas, whilst orbit method is slightly better in high coherence. In addition, both PU methods show almost similar accuracy, especially in open areas while there is a slight difference over forest areas. This might be due to filling the gaps, which have low coherence and are isolated by the BC method. The average RMSE between two unwrapping methods was found to be less than 1 m in all DEMs. However, applying adaptive filtering many times with a smaller coefficient and decreasing window size (128, 64, 32, and 16) can facilitate the unwrapping, especially in low coherence areas. The average RMSE change resulting from applying adaptive filtering many times to the intensity method is around 0.7 m to 6.6 m. For example, in March 1996 tandem pairs, the RMSE increased from 15.8 m to 19.08 m after applying the MCF unwrapping method and decreased to 12.4 m after applying adaptive filtering. Actually the differences in height errors among individual data pairs are the largest for Maluku site compared to Dadahup site. However, DEMs

that have been produced by different tandem pairs acquired with different baseline lengths have a large variation of error. From the descriptive statistics for absolute elevation differences, it is clear that the error decreased between 1996 and 2000 due to an increase in coherence. The lowest error in Maluku DEMs found in DEM 1997 and DEMs 2000 with lowest RMSE of 5.10 m and 5.74 m respectively, whilst it was found in Dadahup DEMs around 4.03 m in DEMs 1997 and 2.87 m in DEMs 2000.

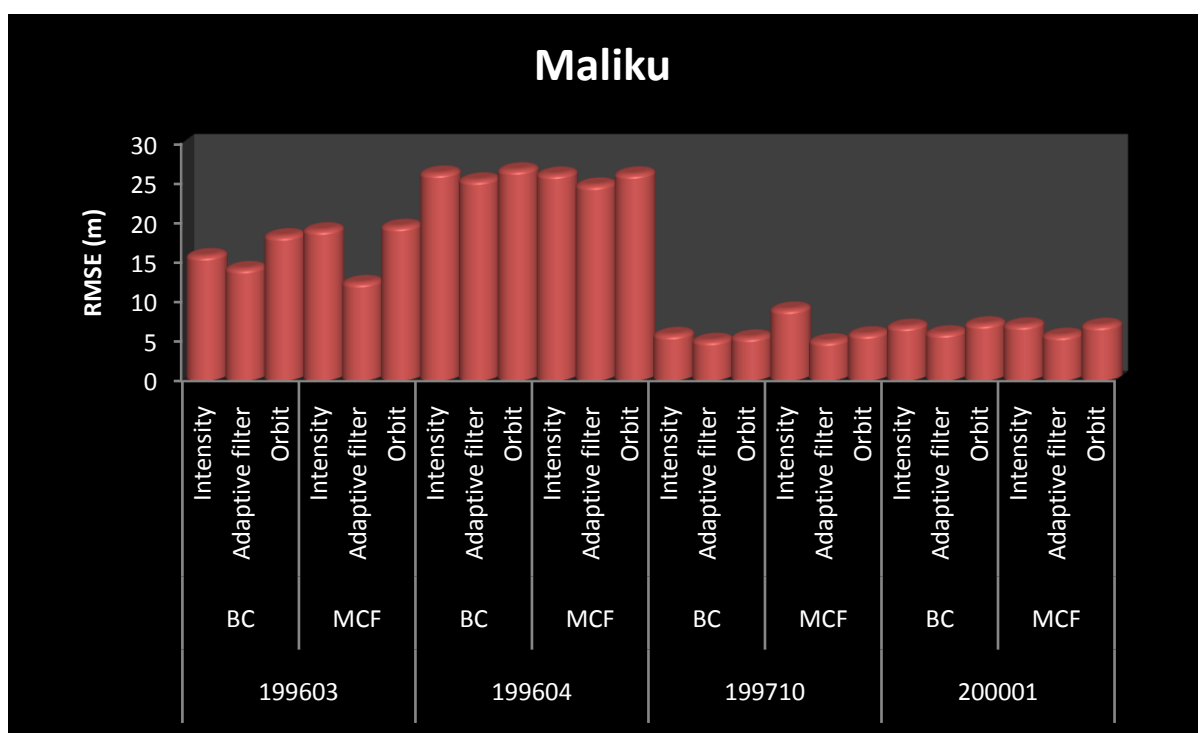


Figure 6.35: RMSE comparison of twenty four DEM profiles against GPS height profiles in Maluku.

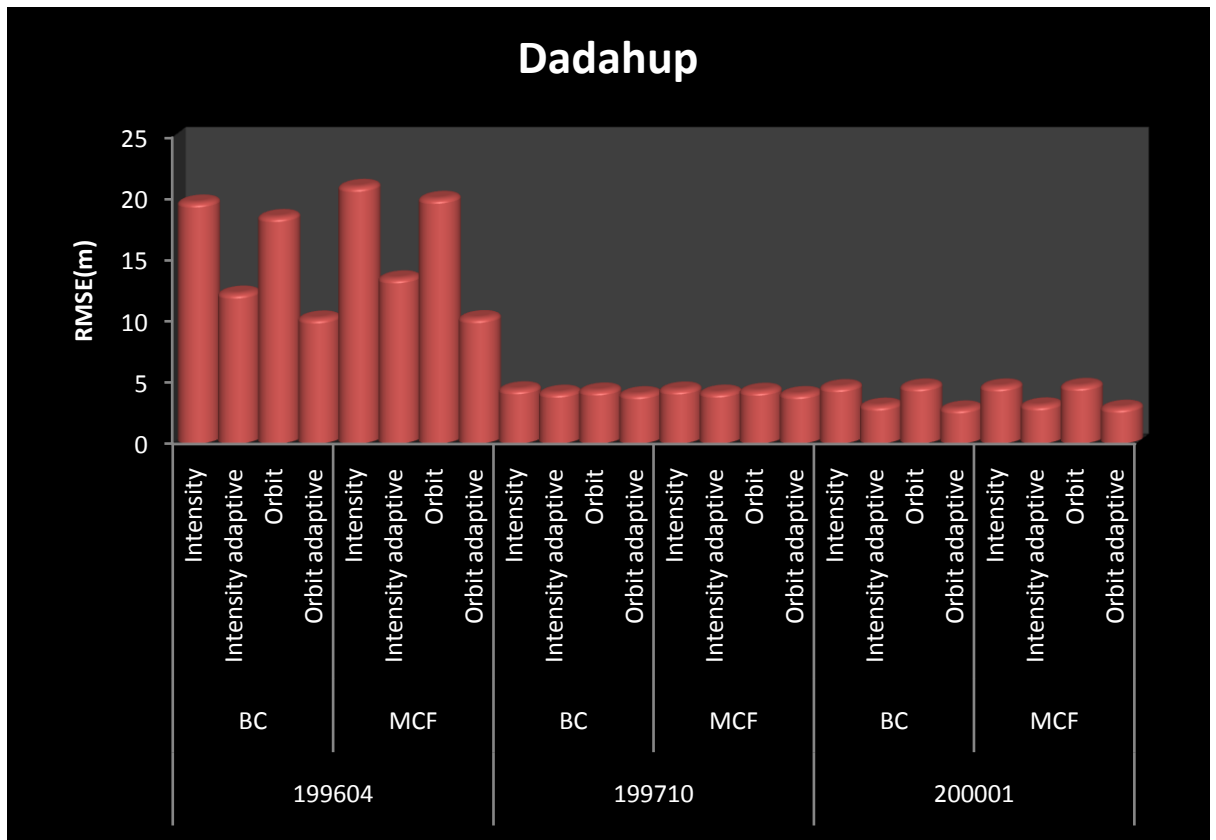


Figure 6.36: RMSE comparisons of twenty four DEM profiles against GPS height profiles in Dadahup test site.

Furthermore, understanding the spatial distribution of the elevation error is important in assessing the accuracy of InSAR DEMs in order to avoid any misrepresentation of the potential and limitations of the technique. The results show that most of the points with large error magnitude (more than 7 m) are located in the same area in all DEMs in each tandem pair image which indicates that the distribution of the error is not related to the processing errors. The error distribution of different tandem pair images shows the DEM accuracy is strongly related to the coherence values in many parts of the DEM. It was found that RMSE values were quite small in high coherence sites, but bigger in forest and vegetated areas.

Absolute comparison is another common procedure for the quality assessment of a DEM by comparing DEMs with a reference DEM (Lin *et al.*, 1994). From the statistical point of view, the reference DEM should be more accurate than the DEM to be evaluated, therefore, the reference DEM chosen is the most accurate DEM from a previous relative assessment. The elevation differences calculated between all DEMs and the reference DEM.

The results showed that 90% of the difference in the DEMs generated by different processing methods has an absolute elevation difference of less than 5 m and RMSE of about 6.6 m to 16 m. All Maluku DEMs have overestimated elevation compared to the adaptive filtered reference DEM, whilst all DEMs in Dadahup have lower values compared to the reference DEM. Orbit method and the MCF unwrapping method at the Maluku site seems to be more accurate than intensity and BC unwrapping methods respectively. In contrast, these methods have similar accuracy in the Dadahup area due to a decrease of signal noise and improved PU. However, the RMSE at the Dadahup site range between 0.2 m and 4.8 m for adaptive filter and other methods respectively, whilst the standard deviation ranges between 0.2 m to 3.9 m. The relatively low standard deviations of both relative and absolute difference surfaces indicate that large differences are small in number and contribute very little to the mean differences between the two DEMs. Comparing the results of two assessment methods, an absolute comparison had bigger standard deviation values than a relative assessment. This is due to the fact that statistically absolute comparison is done for all elevation points, whereas with relative comparison, only few points are used.

On the other hand, the error distribution of absolute assessment shows random distributions of small errors in the same tandem pair images, whilst the high error was found only close to the holes with more than 20 m especially in Maliku DEMs. In contrast, the variation of error found is much bigger when using different tandem pairs compared to the same tandem pair. Most of the high elevation differences are located in or near burn or deforested areas where the coherence has been changed by more than 0.2. However, as the height error is actually much affected by various factors such as baseline, season and weather condition, the quality of the DEMs derived by many tandem pairs are considered unstable.

These results of the statistical properties and error distribution can be explained by two factors: coherence and baseline length change. Coherence provides a useful measure of the interferogram quality and the capability of applying efficiently PU procedures. The complex correlation coefficient is affected by environmental conditions. These conditions depend on temporal observations including the season and time separation between observations. Longer time separation will degrade the coherence between images, especially in a tropical region that is characterized by high humidity and dense vegetation. It is clear that the error decreased between 1996 and 2000 in both test sites due to increased coherence. For dense forest where coherence is around zero, the phase can take on any value. The low coherence over forests gives rise to large height standard deviations as well as RMSE. Many adaptive filtering passes will decrease the phase noise and the height standard deviation. A large part of this area is covered by forests, so an additional error caused by the trees is expected in the interferometric DEM. Part of the RMS error in the above interferometric DEM can thus be explained by forests at the scene.

The baseline length of tandem images might be another explanation of the DEM errors. The baseline is a proprietary parameter to the interferometric synthetic aperture radar system. Successful implementation of an interferometric topographic mapping instrument requires that both the uncertainty in the baseline components and the phase noise be minimized. For optimal system performance, the baseline must be large enough to give sufficient phase sensitivity to height, yet be small enough as to not introduce too much decorrelation noise; therefore, this defines a trade-off in interferometer design (Zebker *et al.*, 1994a). In this study, DEMs 1997 and DEMs 2000 have a larger baseline compared to 1996 DEMs. Compared with Maluku DEMs 2000, the baseline of DEMs 1997 is larger and therefore has a smaller error, whilst 2000 DEMs in Dadahup have slightly smaller errors compared the 1997 DEMs which have a larger baseline. The results obtained from this study on the relationship between baseline and relative height error and between average coherence and relative height error are shown that when the coherence is high and the baseline is longer; the accuracy is the best, as in the 1997 DEMs at the Maluku site. On the other hand, height accuracy is better correlated to coherence than to baseline length at the Dadahup test site and therefore the more accurate DEM were those which have high coherence with moderate baseline length. These results conclude that the accuracy is increased for the data pair acquired in dry seasons (October) compared to those in wet seasons (January to April). To get the best results of DEM generation in tropical forest area, the tandem image should be taken in the dry season for baseline ranges from 200 to 400 m.

The PU is a very important step in the processing chain of interferometric data. The errors of PU mainly come from the following two sources; phase distortion caused by

poor SNR and the type of PU algorithm. Poor SNR is caused by the noise in image formation and original scattered signal reception due to many source errors such as temporal and baseline decorrelation and atmosphere effects. The PU algorithm is another factor that affects the PU results. The difficulty of PU lies in the strategy of error control to the low quality region of the interferogram and how to restore the true phase to the maximum extent as well. However, improper algorithms will cause residual errors which may promulgate to non-residual regions. The evident disadvantage of up to date advances in PU is that any PU algorithm cannot be used to unwrap any kind of wrapped phase. Many PU algorithms were developed during the last twenty years to overcome the pixels affected by noise. One of the aims of this study is to ascertain optimal unwrapping strategy for tropical forest DEM generation by studying error sources of PU and analysing the accuracy of two PU algorithms. Gan and Pan (2008) analyzed the accuracy of PU using ERS1/2 interferogram of Bonn, Germany. They used two assessment methods, rewrapping after unwrapping and an elevation comparison method. The height accuracy is evaluated through calculating the RMSE of corresponding ground control points. The RMSE of BC and MCF unwrapping methods was almost the same at about 10 m. This is supported by results in this research, which found that the BC and MCF unwrapping methods gave almost the same errors in both test sites. The maximum RMSE difference between these two unwrapping methods was found less than 3.2 m. However, the difference decreased significantly in high coherence areas in both sites.

Using an adaptive filter many times has a strong impact to reduce the number of residues, which can reduce the complexity of the PU problem and which can increase the PU efficiency. Besides that, another important reason for filtering is the actual reduction of the noise of the interferometric phase by the filtering of the complex data

set values rather than filtering of the real unwrapped phase values. However, there is some limitations of filtering, including unwanted effects in the case of phase discontinuities such as layover and high phase gradients such as loss of fringes which may lead to PU errors and the increasing spatial dimension of the granular phase variation in the case of dominant noise. In this study, it was proved that the benefit of applying adaptive filtering many times before PU was obvious and gives significant improvement of qualities of the DEMs generated by space-borne InSAR. The results of this work show that adaptive filter DEMS seem to offer elevation values of higher accuracy than other method DEMs. This is shown by lower RMSE and standard deviation of adaptive filter DEMs. The RMSE for all methods, which have been used in this study, decreased dramatically up to 9 m after applying adaptive filter many times. These results agree with the results found by Goldstein and Werner (1998) who suggested that an adaptive interferogram filter derived from the power spectrum of the fringes effectively improves the performance of the branch cut algorithm as it reduces the number of residues, leading to a higher fringe visibility and a reduced phase noise.

Intensity and orbit methods that have been used in this study were characterized by two processing steps; tandem image registration and interferogram calculation. Few studies have been carried out about the accuracy of these processing methods (Wegmüller *et al.*, 2005). Madsen *et al.* (1995) evaluated topographic data acquired by the TOPSAR system and found a significant impact of registration error in the order of 2-5 m of the DEM errors. Ferretti *et al.* (2007) recommended using the orbit processing method especially in the case of large registration offsets or any kind of problems with the registration.

However, this study highlights the accuracy of these methods and found that the difference in RMSE between these two methods was less than 3 m. The difference in RMSE decreased significantly when the coherence increased or when the baseline length decreased as well. Furthermore, the data processing method proposed in this study is to be one of the practical approaches for realizing acceptable DEM generation in tropical swamp forest areas based on space-borne InSAR technology.

There is a large variety of products that can be derived from DEMs and be used for various purposes (Burrough, 1986). Producing a digital elevation model with certain specifications in terms of accuracy already implies the decision about the usability for a specific application. It also shows that there is still a lack of specific requirements for DEMs from the user's side about the accuracy level needed for their application, since digital elevation models are often created for general use and not for a specific application. A large number of parameters can be derived from DEMs for various purposes, at different scales and with different accuracy levels. Therefore, it is difficult to find a general quality measure which suits most of the potential applications. As stated by Ackermann (1996), there is no standard procedure for this kind of assessment. Gens (1998) also stated that generally accepted specifications about the accuracy of DEMs do not exist.

6.7 Limitation

DEM error has only been measured at a limited number of survey points. Although these points represent a variety of terrain characteristics, only accessible locations can be surveyed and the most inaccessible areas could not be included. So the low coherence areas are not represented. Consequently, the largest errors are found in the low coherence areas. Voids remain in DEMs created with the BC method, but they were

filled by interpolation using the MCF unwrapping method and adaptive filtering method, but this could not be validated properly here due to the poor distribution of GCPs.

The quality of these DEMS could satisfy the public and private sector intended applications such as cartographic mapping or installation of communication towers and global representation of terrain. Other applications that need more detailed representation such as civil engineering designs might need more accuracy and another source of data. LIDAR data might be another source and could give more accurate DEMS, but it is not widely available and it is expensive.

The successful generation of DEM using InSAR in tropical region is not guaranteed by just having many ERS tandem pair images from different times. The correlation between the data pair is the most important factor. It was observed that volume decorrelation between the dataset was the main limiting factor that degraded the degree of correlation. The effects from other limiting factors such as the perpendicular baseline length could not be observed without many good pairs of data. However, SAR tandem pair images in dry season with moderate baseline length are still needed for further studies.

6.8 Further work

Future work should include the effects of the number and the distribution of GCPs to estimate precise baseline and convert phase to heights. Co-registration and interferogram computation techniques have to be developed to get a standard method for InSAR applications. Continuous research could be carried out to improve the results

by using other tandem pairs and combination of descending and ascending orbit data pair.

A good and stable PU technique for low coherence areas also has to be developed. PU has faced great challenges, especially when the data contains discontinuous and contiguous features at the same time. There exists no algorithm that can solve this problem even though less complex featured data rely extensively on weights to produce acceptable results. PU is still an active research field, firstly because of the conviction that there is still room for new algorithms and improvements and secondly because PU is fascinating and has interesting links with many other image-processing problems. Probably statistical analysis of the signal of interest, together with a proper combination of all the available information will reduce the number of algorithms effectively used to a few and there will finally be a 'standard PU procedure' for InSAR DEM reconstruction.

In Central Kalimantan, 1998 was an exceptionally wet year in which there was widespread flooding, particularly in and around the Ex-MRP area. These floods were worse than in previous prolonged wet seasons because removal of the forest and peatland drainage, combined with the consequences of the fires, impaired the hydrological functions of degraded peatland areas. Future work should include flood modelling and analysing possible scenarios for the future using the DEMs that have been generated in this study. This can potentially have a significant impact on the application of DEMs in sustainable management and conservation of the Ex-MRP area.

6.9 Summary

This study presents many processing methods for DEM generation using ERS tandem images. These methods were applied to two different locations in Central Kalimantan, Indonesia. The first location was severely burnt during the big fire in 1997, whilst the second location was under extreme drainage and logging activities since 1996. Early ERS-1 SAR results indicated that the scene coherence over forested areas was not sufficient for repeat-pass interferometry at C-band. However, this study shows that this technique can be used to estimate the topography over forest during dry- wet seasons, where the coherence varies between 0.2 and 0.5. Several statistics of SAR errors were calculated and compared to assess which DEM offers more accurate point elevation data. The average RMSE of ERS DEMs against the GPS height profiles was around 5 m for Maluku site and 3.5 m for Dadahup site. In some areas covered with dense forest the RMS error increases to around 6 m .The most accurate DEMs evaluated were those produced from adaptive filter methods, at least in terms of vertical accuracy. However, the resulting implementation will meet many, but not all, objectives of a global mapping mission.

Chapter 7: Subsidence rates and carbon loss in peat soils

7.1 Introduction

Repeat-pass radar interferometry has a high potential for the measurement of land subsidence and other surface changes. This study utilises the four-pass and complex interferogram combination (CIC) DInSAR approach to measure the displacement of the peat surface in two different locations in Blocks C and A of the Ex-MRP. It also estimates the carbon loss and CO₂ emissions from the study area between 1997 and 2000 based on deformation results. The results described in this chapter aim to demonstrate the principles involved in subsidence caused by drainage and fire, study the rate of subsidence under different differential technique scenarios and explore the uncertainties and further data required to reduce these uncertainties and errors.

For detecting peat subsidence in the Ex-MRP occurring primarily due to fire in 1997 and deforestation, the InSAR data pairs acquired in 1997 and 2000 have been chosen according to the accuracy of DEM generation (see previous chapter). The other SAR tandem images show low coherence and high DEM error in DEM analysis and therefore have not been chosen to generate differential interferograms. On the other hand, the three-pass and four-pass methods, using three radar images have not been successfully generated. The long temporal baseline data pairs, temporal decorrelation and atmospheric artefacts have been found to create serious difficulties in generating differential interferograms, especially in terms of losing coherence. Therefore, only the four-pass method and complex interferogram combination, using four ERS-1/2 images, have been successfully generated for the study areas.

7.2 Subsidence in Block C

The SAR-derived subsidence map of Block C for the time period 1997-2000 at a spatial resolution of 40 m is shown in Figure 7.1. The temporal baselines span from 246 to 1750 days (see Table 4.1), whilst the spatial baselines are distributed in the range of 204 m to 383 m. Subsidence rates range between less than 1 cm/y in the north of Block C and 5 cm/y in the south using the complex interferogram combination method, whilst the subsidence rate decreases to less than 1 cm/y using the 4-pass method. The mean subsidence in block C ranges between 0.12 cm/y and 2.4 cm/y in the 4-pass method and CIC method respectively. The 3D visualisation of the subsidence rate is shown in Figure 7.2. The 4 pass method indicates only one zone of subsidence, which is in the west part of Block C. The subsidence zone resulting from the 4-pass method also shows a high rate of subsidence in the CIC method.

In order to investigate these subsidence phenomena, the DInSAR mean deformation velocity map of Figure 7.1 is compared with the coherence map (see Chapter 5; Figure 5.3). From the comparison it is apparent that all the subsiding areas occur in correspondence with the decrease of forest cover from north to south. From previous studies it was found that subsidence rates under forest cover are less than half of what they are in degraded land (Hooijer *et al.*, 2009). The presence of natural forest covers the land surface and shelters the top peat from drying out; this might be a factor that controls the peat subsidence using the second scenario. The land cover is dense forest in the north of Block C with more open areas in the middle and south. That might explain why the subsidence increased towards the south. No relation is found between subsidence rate from the 4-pass scenario and the coherence map. However, as much of the Ex-MRP was burnt and cleared after 1997, it is expected that the subsidence rates

following the 1997 fires would have been higher than the subsidence rate given by the 4-pass method. Furthermore, the subsidence maps from the two differential approaches cannot be validated by other methods or by field measurement.

Some subsidence features, visible in the subsidence map, can be easily assessed by delineation using profiles drawn on the two subsidence scenario images in two directions at the Maliku site and all other relevant features can be extracted (Figure 7.3). The first line was drawn in West-East direction across low and high subsidence areas and crossed many burnt areas with a total length of 30 km (Figure 7.4). The ESE-WNW transect crossed two canals spaced approximately 10 km apart and two burn scar areas. The graphs were plotted (subsidence against distance) to show subsidence discrepancies at various places. On visual inspection, it is clear that the subsidence variation shows almost similar subsidence trends in both scenarios but with different subsidence rate values. About 80% of the ESE-WNW transect has a subsidence rate greater than 2.5 cm/y using the CIC method, whilst 50% of the transect area has a subsidence rate of more than 0.5 cm/y using the 4-pass method.

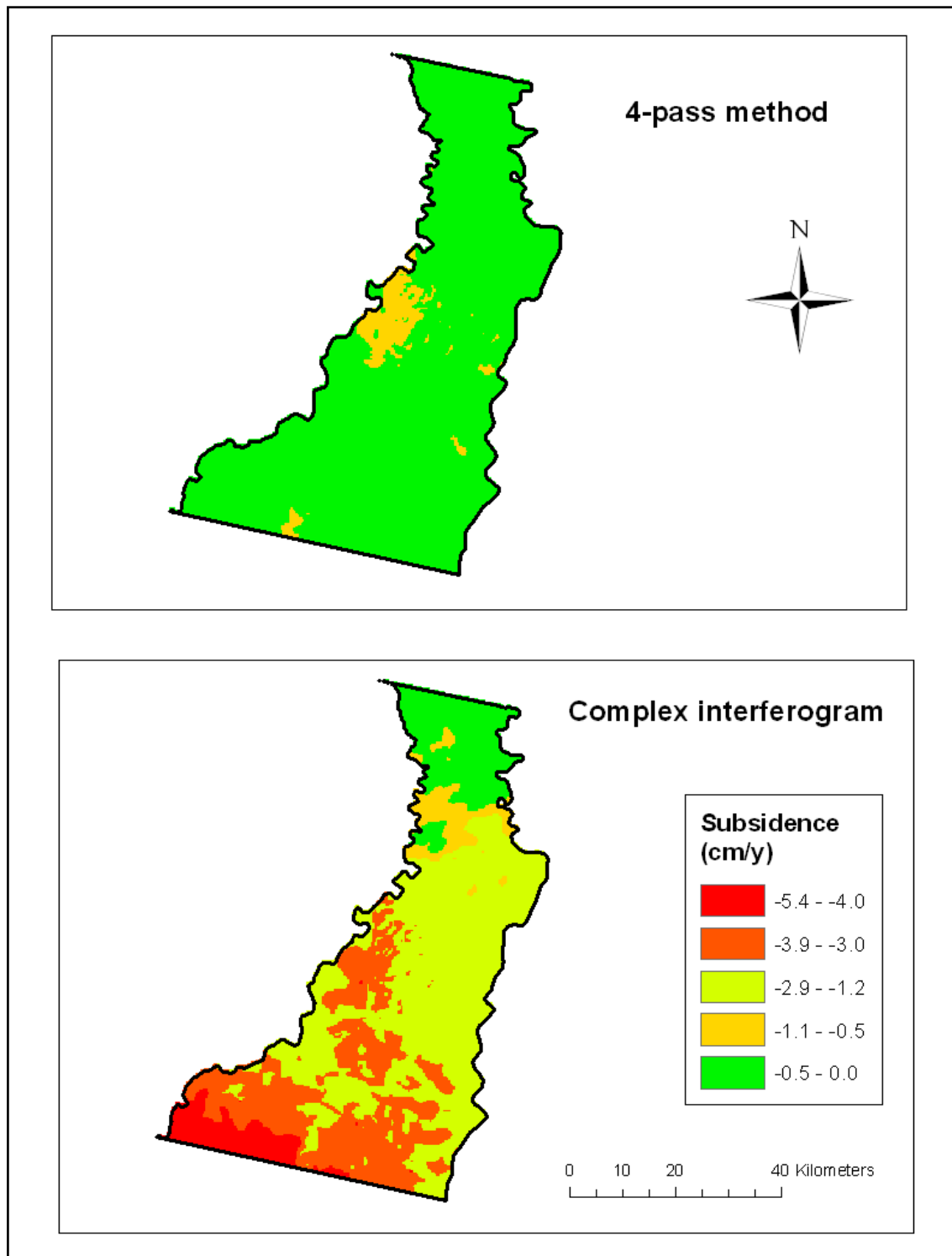


Figure 7.1: Peat subsidence rate (cm/y) for Block C during the time period 1997-2000 using two DInSAR techniques.

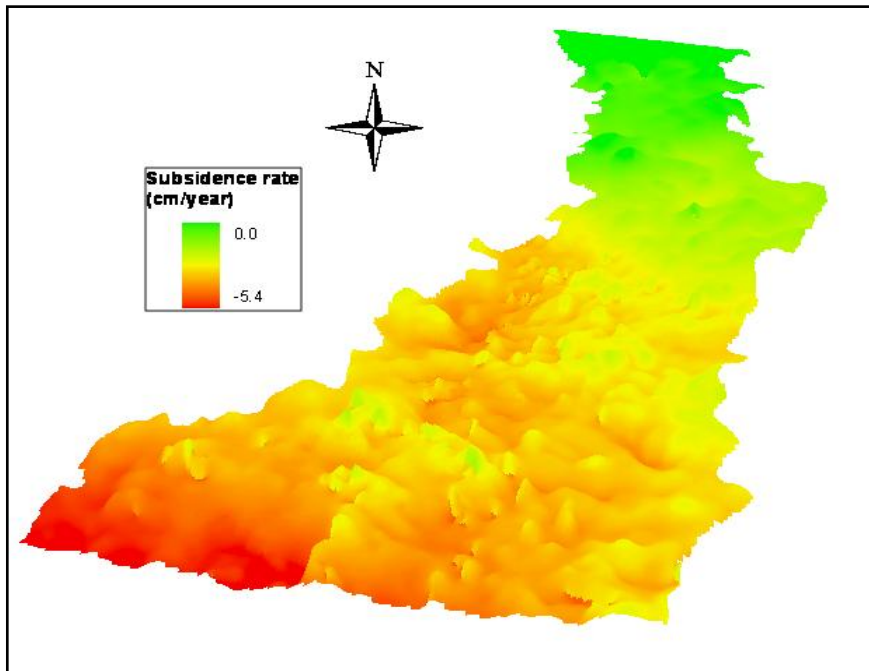


Figure 7.2: DInSAR derived subsidence in Block C using complex interferogram method represented in 3D view with 1000 vertical exaggeration.

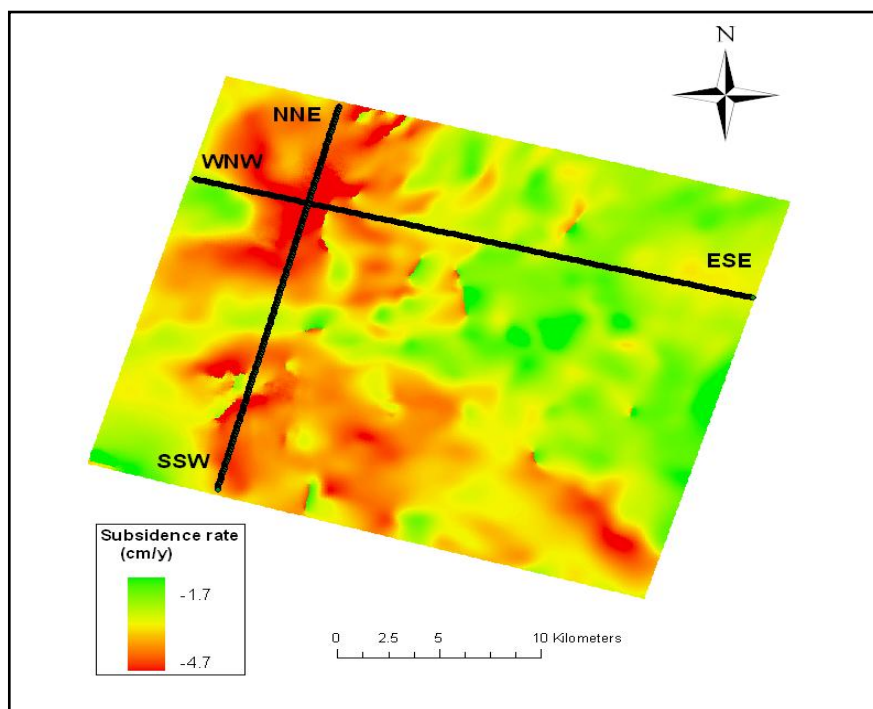


Figure 7.3: Profile lines along and across Maliku.

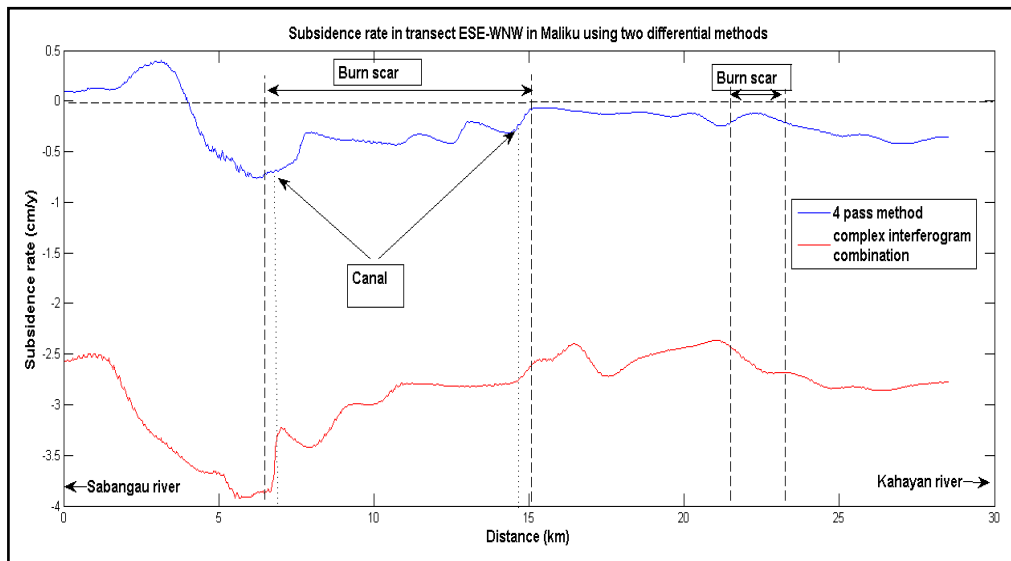


Figure 7.4: Profiles comparison graph along the ESE-WNW transect line in Maliku.

Further analysis was carried out to correlate the subsidence with coherence; by looking at the coherence change along the ESE-WNW transect in Figure 7.5, it is clear that the high subsidence rate correlates with high coherence change between 1997 and 2000. High coherence change indicates either a burn area or deforestation between the two acquisitions. The slope of the subsidence rate profile to the west of the burn scar is more than the average for the rest of the area. However, the subsidence reaches its peak at the main canal and then decreases again. The fact that water tables in the wet season are lower near canals but higher further away has created a gradient in subsidence rates. This explains the surface slopes towards canals that are found in all Ex-MRP peatlands (Hooijer *et al.*, 2008).

Figure 7.6 shows a profile representing the deforming in the NNE-SSW transect from the DInSAR results. The vertical axis is subsidence rate (cm/y), while the horizontal axis is the length of the profile. The NNE-SSW transect, which is randomly placed,

crossed six canals spaced approximately less than 5 km apart and one burn scar area. The average subsidence along the 25 km transect is 2.5 cm/y for the CIC deformation and less than 0.5 cm/y using the 4-pass approach. In addition, subsidence was not as well predicted for the burn scar section of the NNE-SSW transect and this might be due to the difficulty of predicting subsidence where complex drainage systems are operating together with fire occurrence. In addition, no clear correlation was found between subsidence rate and coherence in these transects (Figure 7.7). However, in both transects, the amount of peat subsidence is slightly correlated with the burn scar and canal locations.

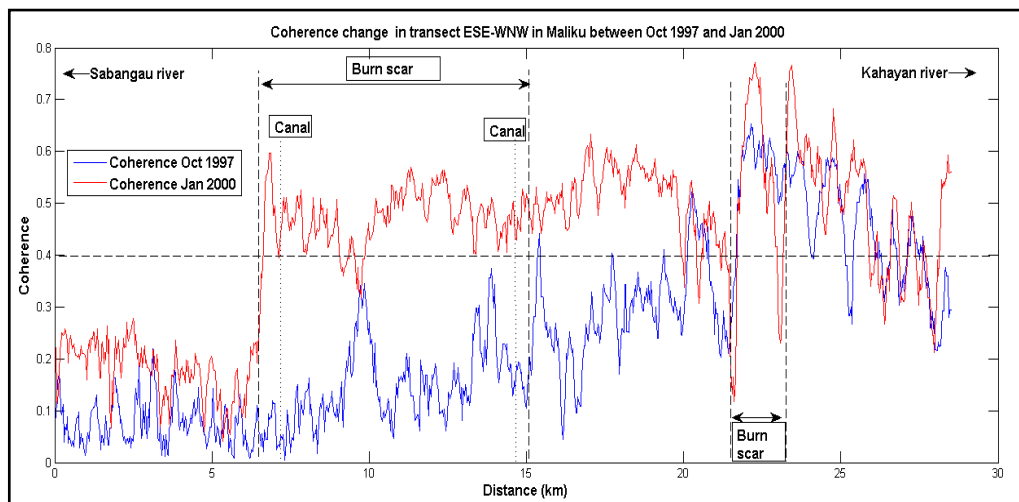


Figure 7.5: Coherence change between 1997 and 2000 in the ESE-WNW transect line in Maluku.

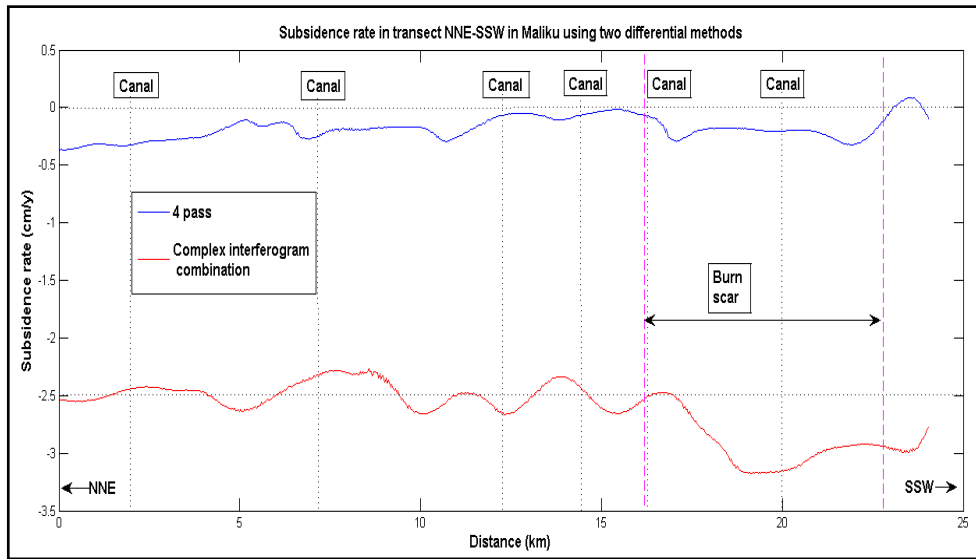


Figure 7.6: Profiles comparison graph along the NNE-SSW transect line in Maliku.

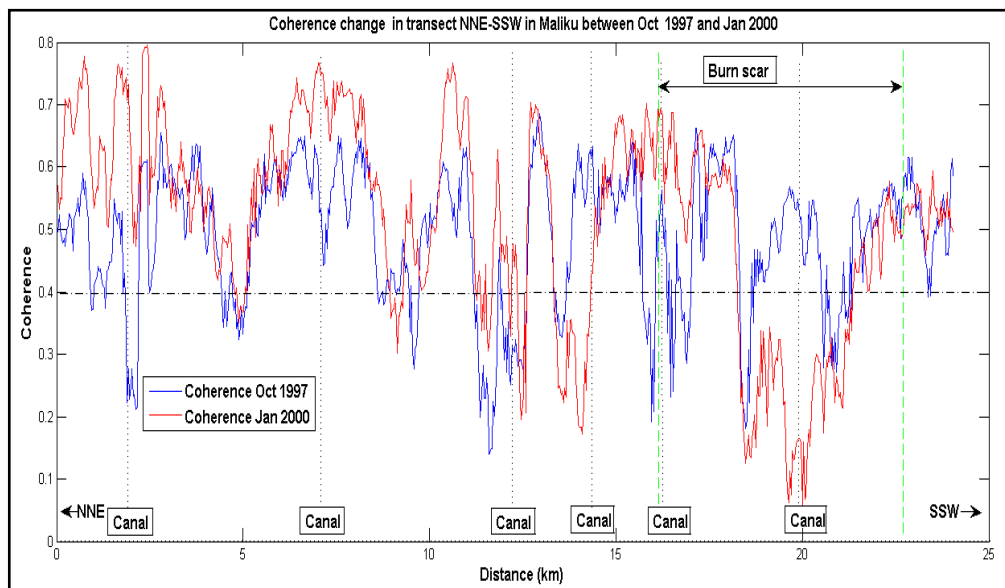


Figure 7.7: Coherence change between 1997 and 2000 in the NNE-SSW transect line in Maliku.

7.3 Subsidence in Block A

The extreme drought which led to the widespread peat and forest fires in 1997/98 was not solely the effect of El Niño, as commonly claimed, but it was intensified by the over-draining of Kalimantan's peatlands. Land subsidence is a major result of drainage (see Chapter 2). Uncontrolled drainage may result in unpredictable changes in surface levels as a result of variations in peat characteristics (e.g. bulk density, water holding capacity, subsidence potential) (Rieley and Page, 2005). In Block A, some dense forest parts remain, but overall severe deforestation and fire damage has occurred since 1996, which is linked to the drainage infrastructure. The peat area is crossed by the main canal, with a dense network of lower order canals.

The results obtained with DInSAR in Block A are presented in Figure 7.8. The subsidence in the complex interferogram combination increased from north to south and the subsidence rates range from 0 - 3.5 cm/y. The mean subsidence in Block A ranged between 0.07cm/year and 0.6 cm/y in the 4-pass method and the CIC methods respectively (Table 7.1). These results did not correlate with the location of the deforestation areas and burn scars that were identified in this study (see Figure 5.17 in Chapter 5). On the other hand, the subsidence result from the 4-pass method shows only a few subsiding zones in the north of Block A with subsidence rates around 1 cm/y. There is a good agreement between the 4-pass method subsidence and deforestation location for the same period. Moreover, subsidence results suggest that the subsidence rate is relatively uniform over most of Block A, especially in areas that are located away from canals.

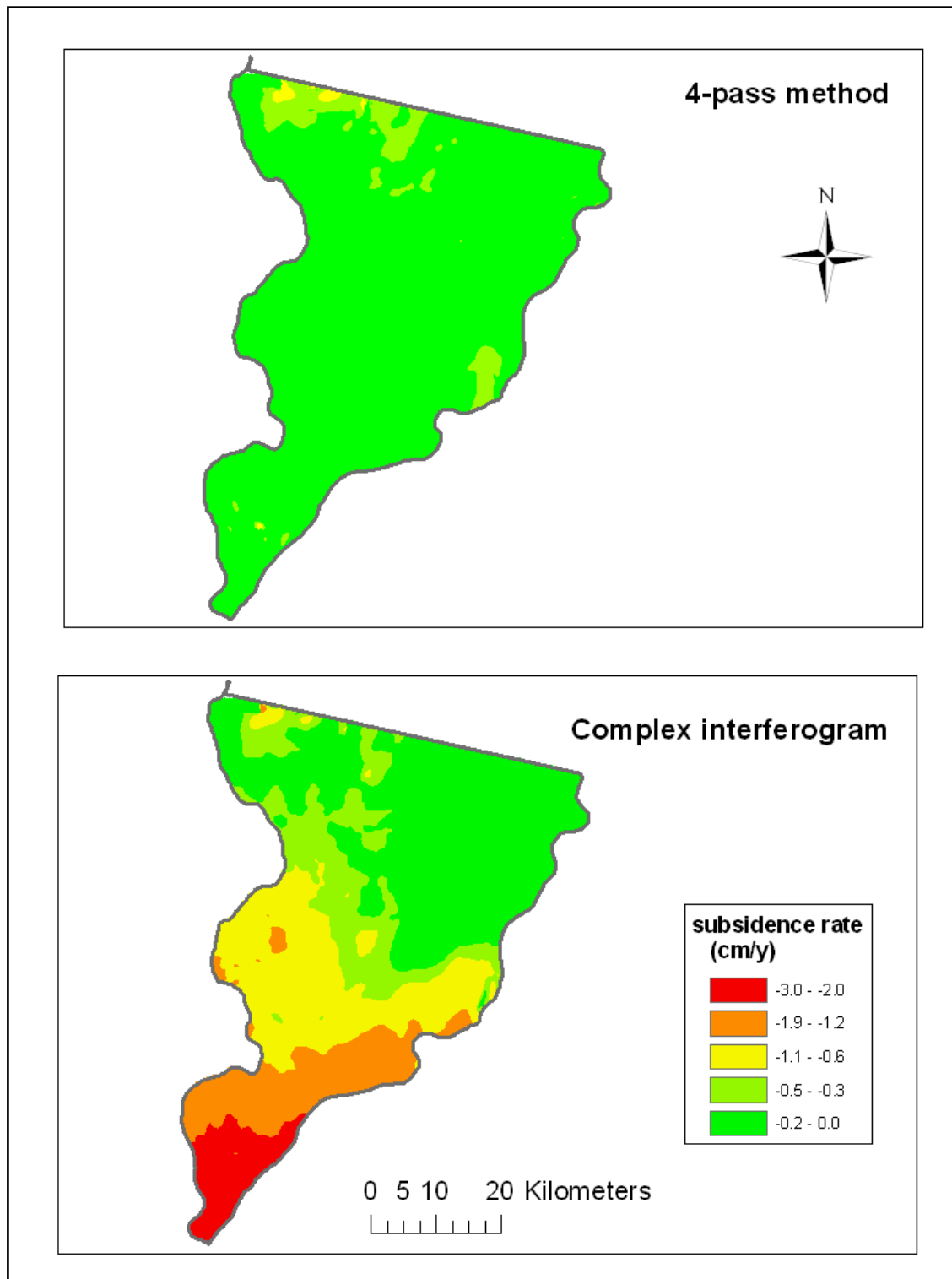


Figure 7.8: Peat subsidence rate (cm/y) for Block A during the period 1997-2000 using two DInSAR techniques.

Table 7.1: Statistical information about peat subsidence rate (cm/y).

Site	Method	Min(cm/y)	Max(cm/y)	Mean(cm/y)	St.Dev(cm/y)
Block C	4-pass	0	1.2	0.12	0.18
	CIC	0	5.4	2.4	1.2
Block A	4-pass	0	1.2	0.07	0.12
	CIC	0	3.5	0.6	0.7

Sites for surface profile transects, with a total length of around 30 km, were identified on the main areas of the Dadahup site where the peat has been drained and converted to mineral soils for several years (Figure 7.9). By comparing the subsidence in these profiles (Figures 7.10 and 7.11), it is noted that the subsidence rates along the NNE-SSW profile show similar average values. Along the ESE-WNW transect, it is clear that the subsidence variation shows an almost similar subsidence trend in both differential methods with different values, whilst there are different trends in the NNE-SSW transect. The average subsidence rate along the ESE-WNW transect using the CIC approach is about 1.25 cm/year, whilst there is an uplift trend when using the 4-pass method, with an average accumulation of less than 0.25 cm/y. However, both differential methods show an increase in the displacement rate in the right burn scar area, whilst they show almost no change in the left burnt area. In addition, subsidence rates are generally higher near canals, as water tables are lower there. However, there is no correlation between the subsidence along the NNE-SSW transect and the canal locations and this might be due to the large scale of the subsidence map and the complex drainage systems located in this area.

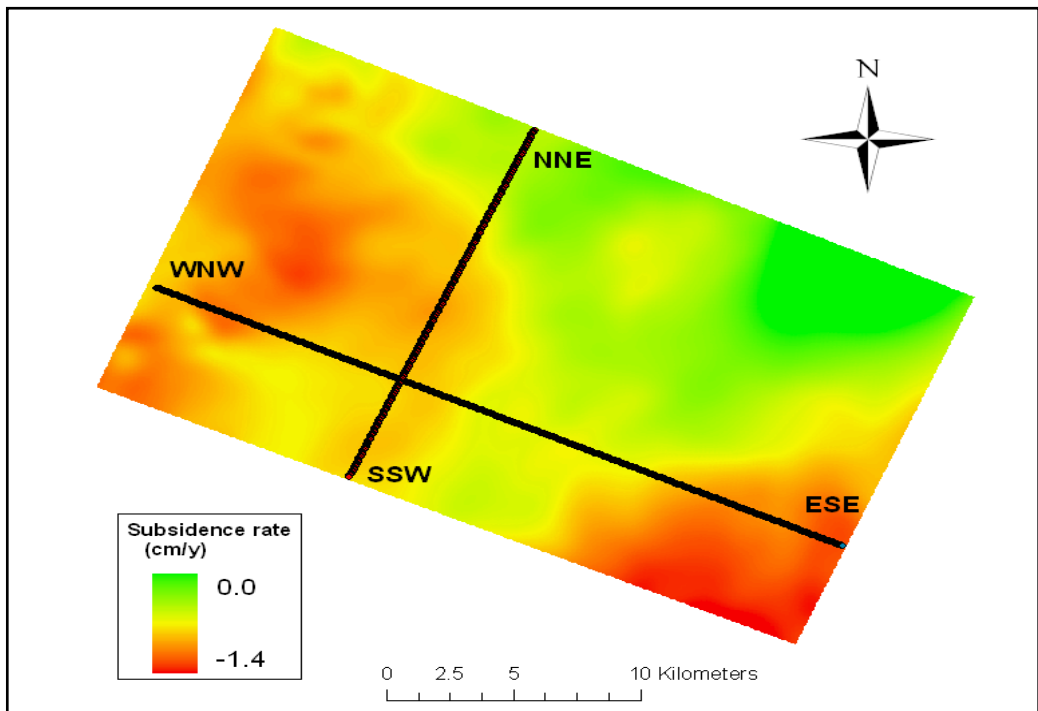


Figure 7.9: Profile lines along and across the Dadahup site.

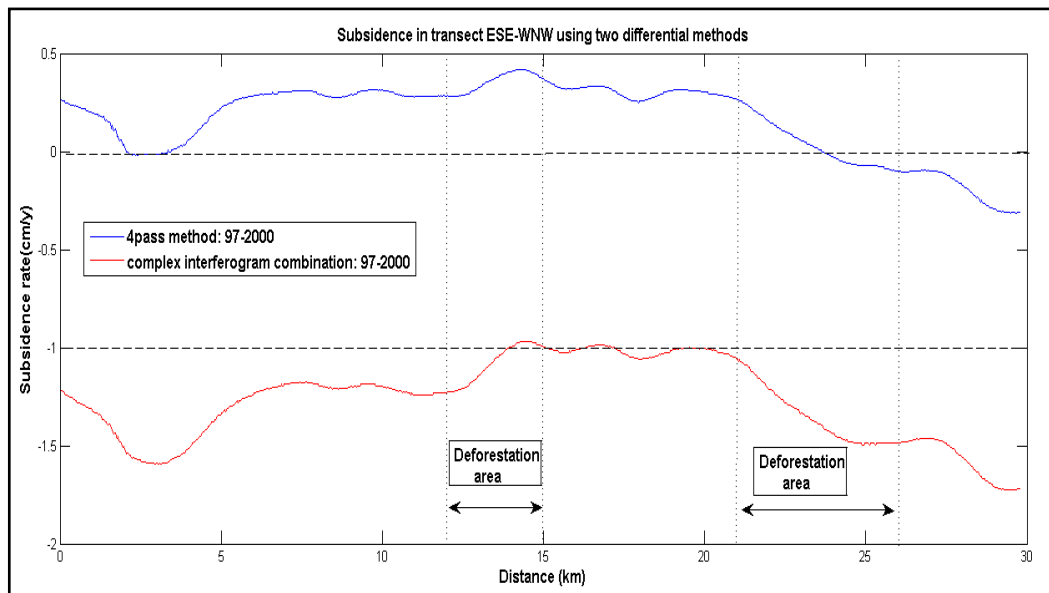


Figure 7.10: Displacement profiles along an ESE-WNW transect in Dadahup.

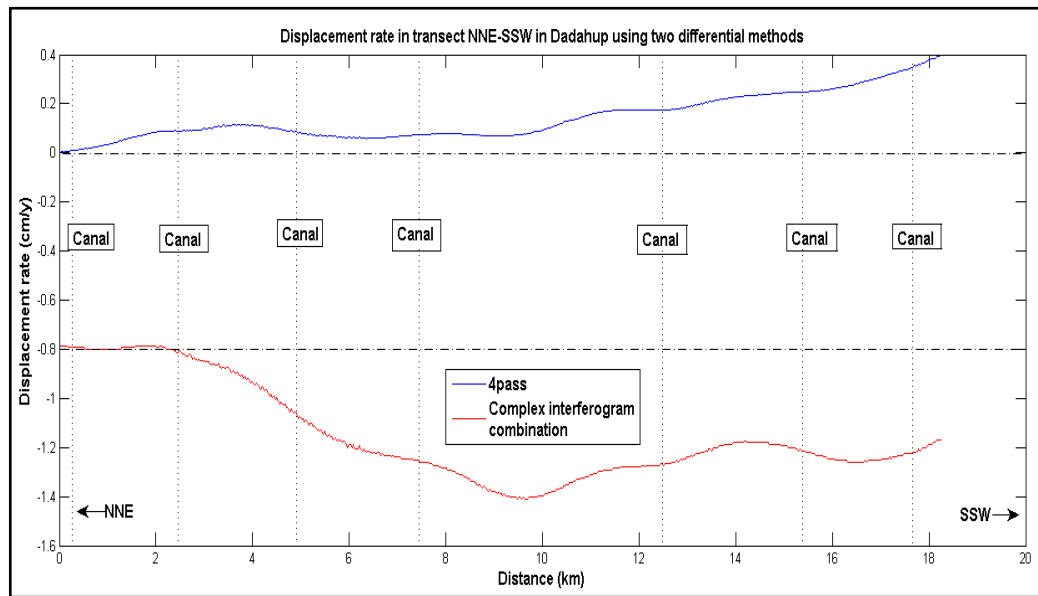


Figure 7.11: Profiles comparison graph along a NNE-SSW transect line near Dadahup.

7.4 Estimation of peat and carbon loss due to peat soil subsidence

This study focuses exclusively on the peat volume loss and the subsequent peat carbon loss as a result of peat subsidence. These estimations are achieved by calculating the peat loss in each pixel in the subsidence map by multiplying the subsidence rates by the cell size. Figures 7.12 and 7.13 show the spatial pattern of average peat loss in Block C and Block A using only the complex interferogram combination differential method. The results show that the maximum peat loss ranges between 85 m³/y in Block C and 55 m³/y in Block A.

According to a peat thickness map presented by Page *et al.* (2002), the average peat thickness in the Ex-MRP is about 3 m. With an average subsidence rate of 2 cm/y in Block C it will take 75 years for the peat soils to disappear. In this study, the peat loss can be understood by realizing that within approximately 75 years, 280,628 ha of peat soils will have been transformed into mineral soils with average losses of 88 m³/y.

To estimate the carbon loss, the peat volume loss was calculated by multiplying peat volume by appropriate values for peat bulk density and carbon content.

$$\text{Carbon loss rate (t/y)} = \text{subsidence rate} \cdot \text{Area} \cdot \text{carbon content} \cdot \text{peat bulk density} \quad (7.1)$$

It should be noted that peat type descriptions are subjective; bulk density and carbon content data are needed for accurate analysis. Although there are no scientific rules for relating bulk density to peat type in tropical peat, peat bulk density between 0.1 and 0.2 g/cm³ is often considered to be ‘hemic’. Higher bulk density indicates ‘sapric’ peat, and lower bulk density indicates ‘fibric’ peat. Almost all reported bulk density measurements for the Ex-MRP confirm that the peat in Blocks A, B and C can be classified as hemic or sapric (Hooijer *et al.*, 2008), and thus the bulk density values are in the range 0.1-0.2 g/cm³.

A map of total carbon loss (Figure 7.14 and Figure 7.15) in Block C and Block A respectively, was produced by combining spatial subsidence values, bulk density and carbon content. Values of 0.1 g/cm³ and 57% were applied respectively, because it is most conservative values. Based on the estimated subsidence rate obtained by the CIC differential method, it is found that the carbon loss rates ranged between 0.94 Mt/y to 4.0 Mt/y in Block A and Block C respectively (Table 7.2).

Table 7.2: Total carbon loss from Block C and Block A during the period between 1997 and 2000.

Method	Area (ha)	Volume of peat lost each year (m ³ /y)	Loss of peat per year (Mt/y)	Rate of C loss (Mt/y)	loss of C (t/ha/y)
Block C	280628	70551817	7.06	4.02	14.33
Block A	190663	16469657	1.65	0.94	4.93

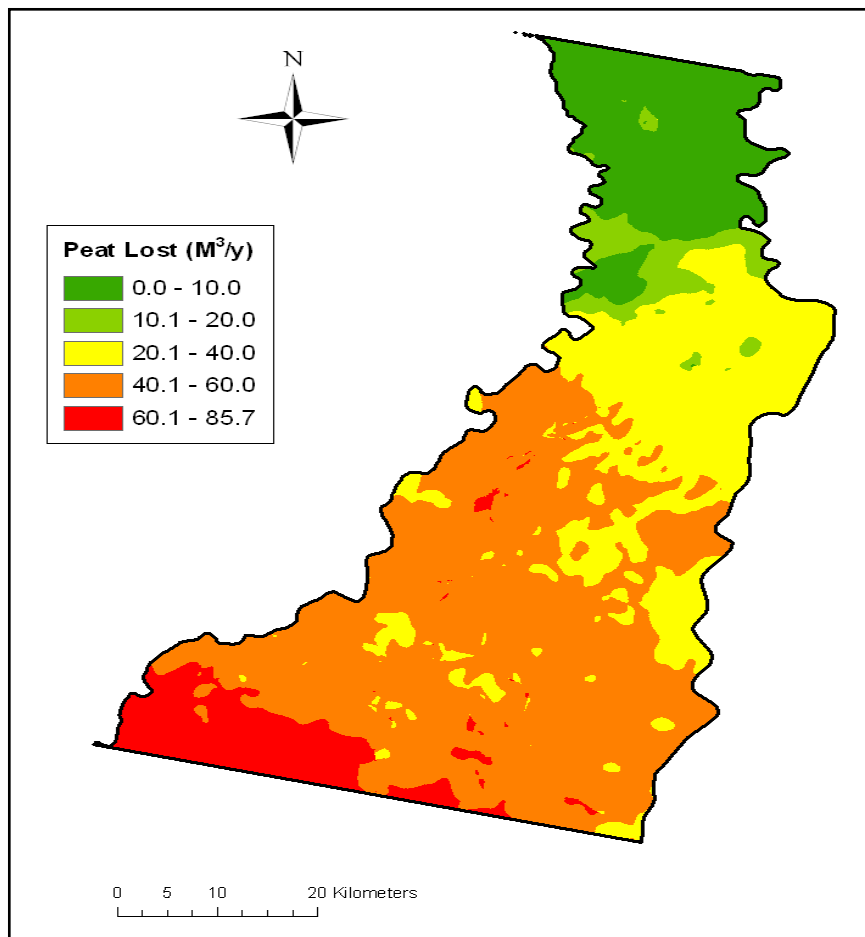


Figure 7.12: Peat loss rate in Block C based on CIC differential method between Oct 1997 and Jan 2000.

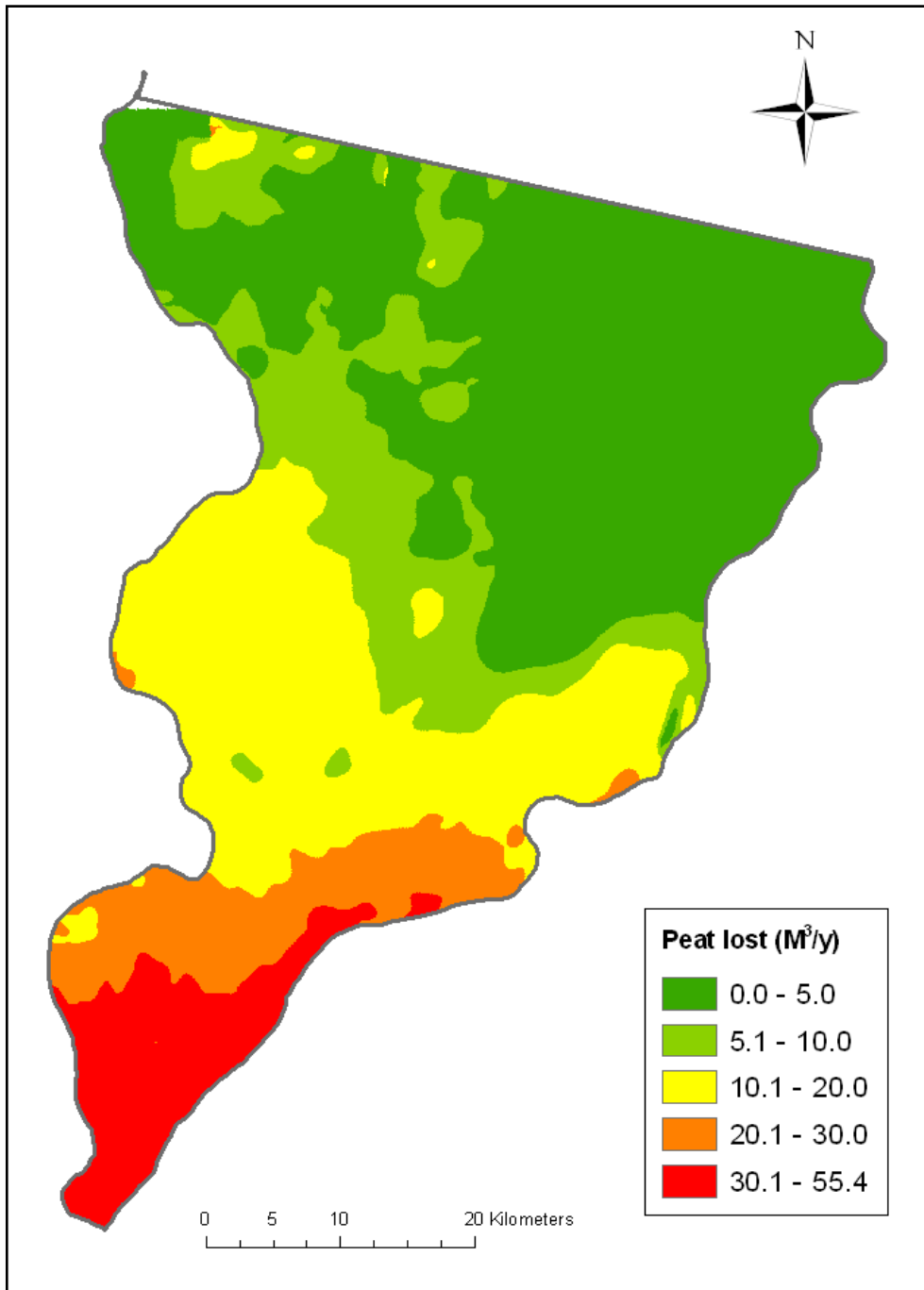


Figure 7.13: Peat loss rate in Block A based on CIC differential method.

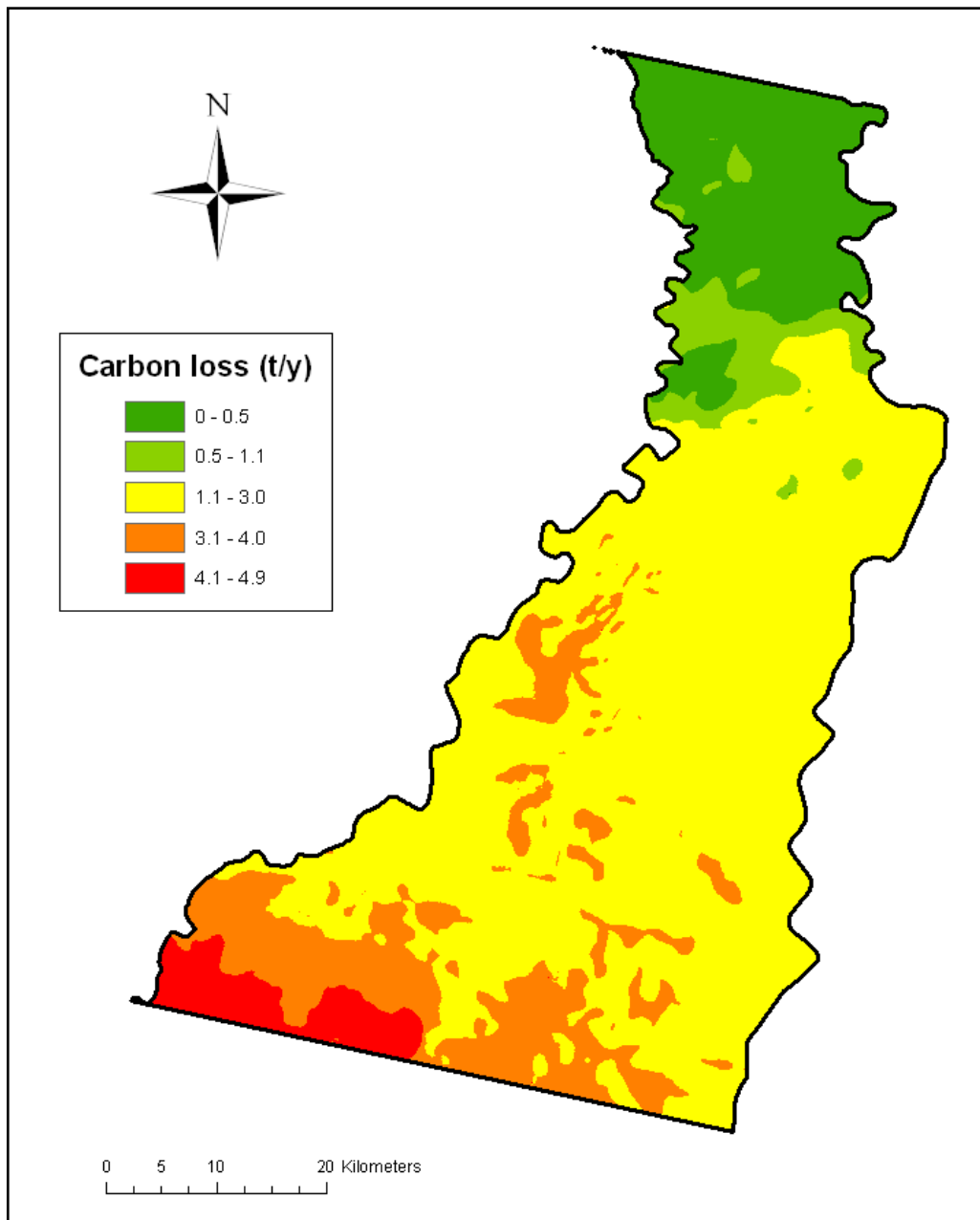


Figure 7.14: The rate of carbon loss in Block C based on CIC differential method.

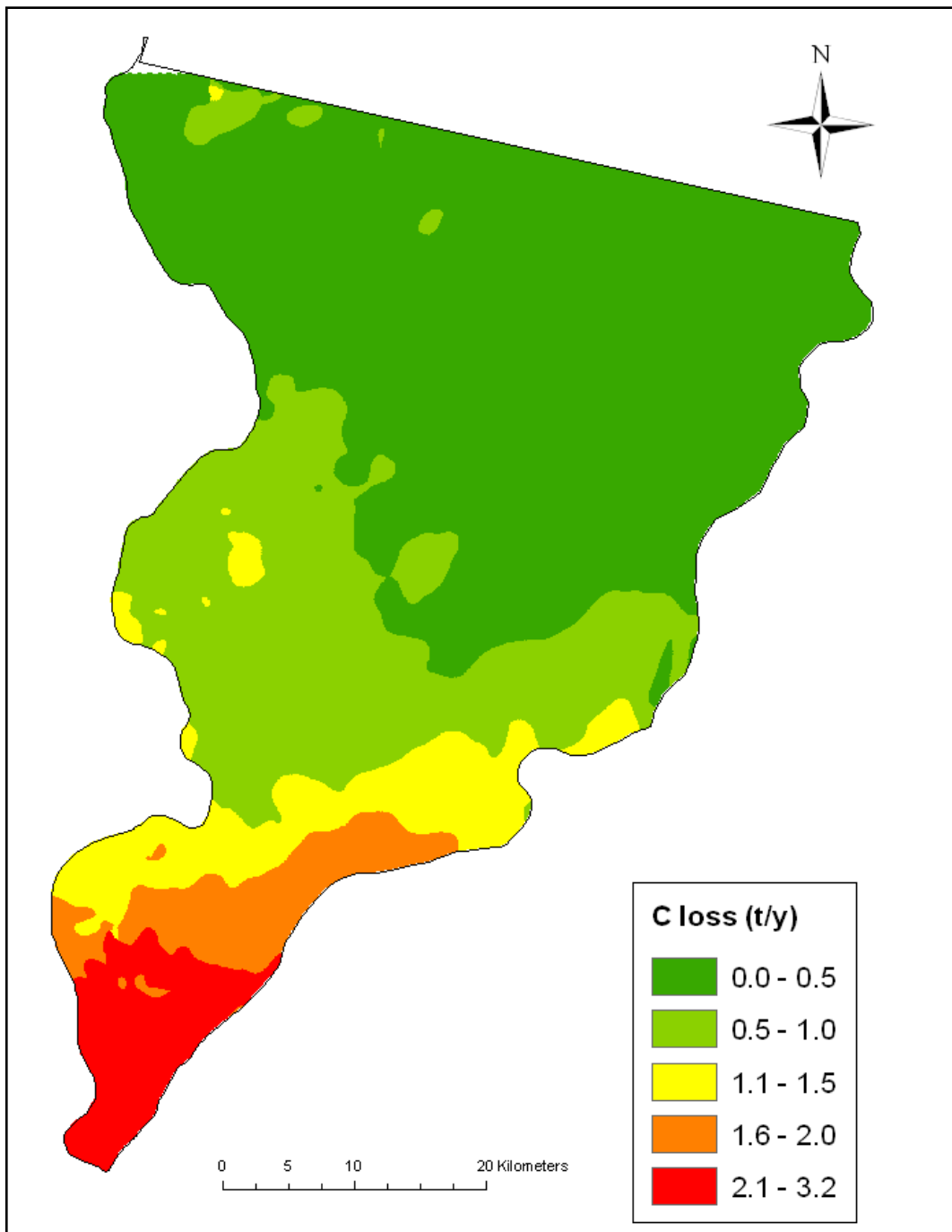


Figure 7.15: The rate of carbon loss in Block A based on CIC differential method.

7.5 Water table change between 1997 and 2000

Wösten *et al.* (1997) interpreted the subsidence record of Johor, Malaysia, in terms of a relationship between subsidence and water depth. They found that the increase in subsidence rate was 0.9 cm/y for each 10 cm lowering of the groundwater level, whereas this increase has been reduced later to 0.4 cm/y. Their linear relationship between water table change (WT) and subsidence rate has been used in this study to map the water table change over Block C and Block A.

$$\text{Peat subsidence rate (cm/y)} = \text{XO} \cdot \text{WT (cm/y)} \quad (7.2)$$

Therefore, the water table modelling can be obtained as an inverse of the subsidence rate modelling:

$$\text{WT (cm/y)} = \text{Peat subsidence rate (cm/y)} / \text{XO} \quad (7.3)$$

The actual co-efficient value (XO) depends on the peat characteristics and it has been found to vary between 0.1 – 0.04. The co-efficient 0.04 has been found to be the best value to express the peat subsidence in Western Johor, Malaysia (DID and LAWOO, 1996) while a co-efficient value of 0.1 is the suitable value for Sarawak, Malaysia (DID, 2001). No co-efficient value is available for peat in the Ex-MRP area.

Wösten *et al.* (2008) conclude that the increase in the subsidence rate of 0.4 cm/y for each 10 cm lowering of the groundwater level is considered to be the best possible prediction for peat subsidence rate in Johor, Malaysia. Figures 7.16 and 7.17 show the water table changes between 1997 and 2000 in Blocks C and A. The maximum and minimum co-efficient values have been used to calculate the highest and lowest water table levels. By applying 0.04 as a coefficient value in the previous equation, the highest level change in Block C was below 134 cm/y reflecting the highest subsidence rate in the CIC differential approach, whilst the highest water table depth change of around 67

cm/year was found in Block A. Using a coefficient value (0.1), the maximum water table change ranges between 53 cm/y and 35 cm/y in Block C and Block A respectively.

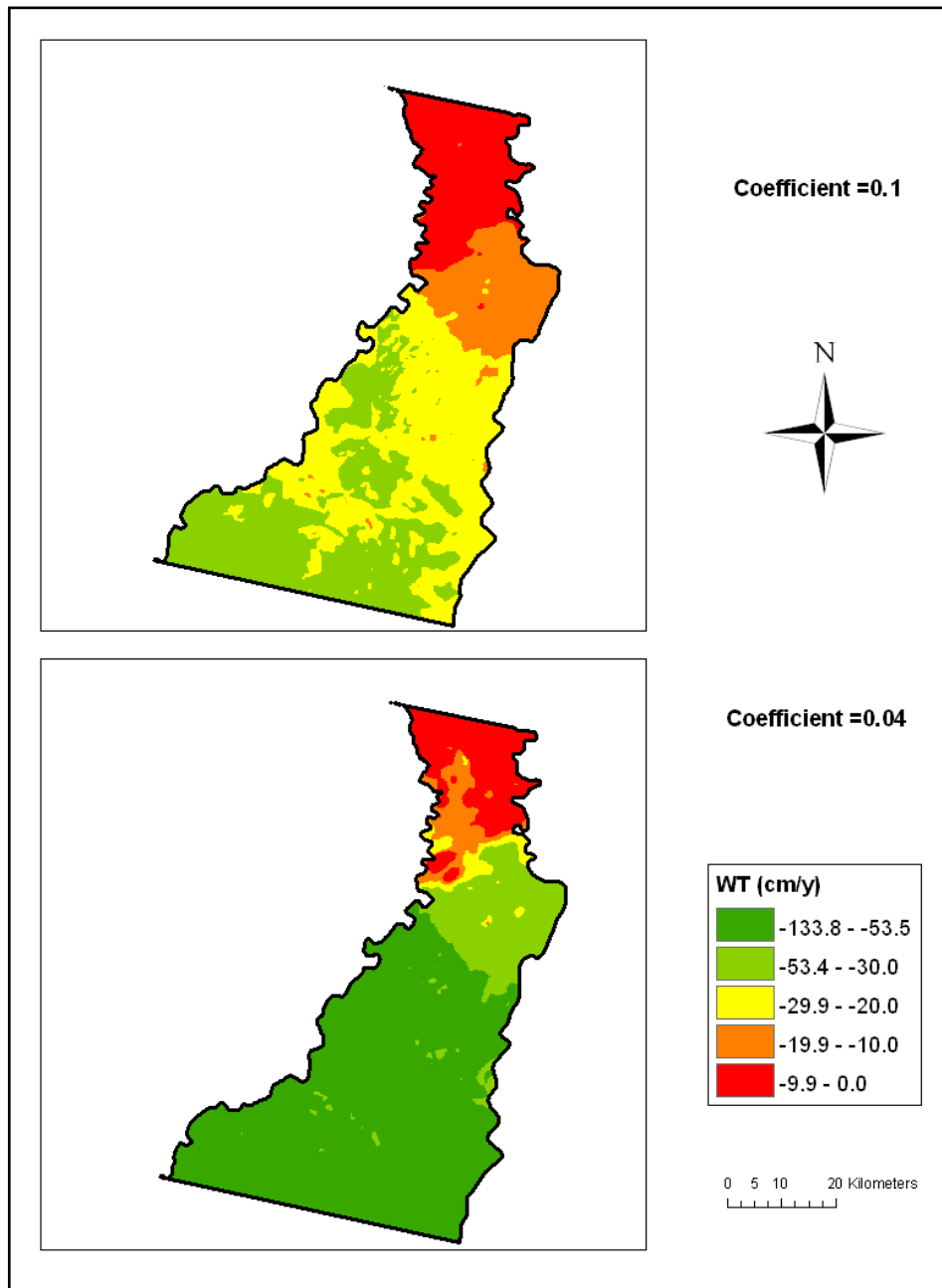


Figure 7.16: Water table changes in Block C based on CIC differential method using the coefficient values of the linear relationship between subsidence and water table depth change.

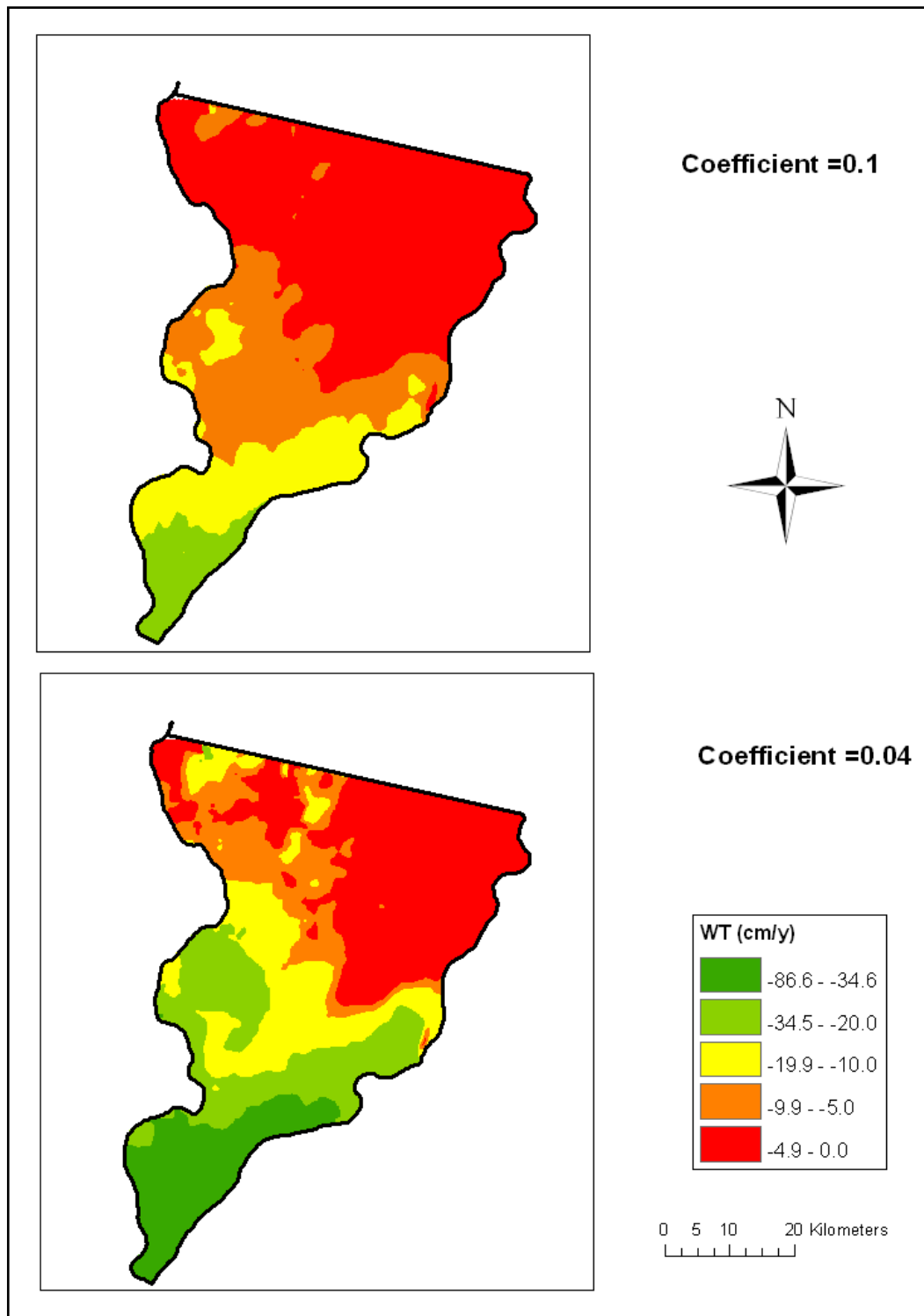


Figure 7.17: Water table changes in Block A based on CIC differential method using the coefficient values of the linear relationship between subsidence and water table depth change.

7.6 CO₂ emissions between 1997 and 2000

Carbon emissions caused by peatland drainage, fires and subsidence, are a major driver for the international interest in the importance of tropical peat carbon stores and their role in environmental change processes, especially in Indonesia's peatlands. There are two main sources of CO₂ emission from drained peatlands: decomposition and fires. Both emission types occur in drained and/or degraded peatlands and both can, broadly speaking, be quantified in two ways. On the one hand, the depth of the water table below the surface has been cited as the most important factor determining oxidation-reduction conditions and therefore CO₂ emission from peatland. Many researchers have studied the relationships between groundwater depth, subsidence and CO₂ emissions and referred to linear and non-linear relationships between them (Hooijer *et al.*, 2006). The basic relationship between peat subsidence and CO₂ emission is that every centimetre of peat subsidence results in a CO₂ emission of approximately 13 tCO₂/ha/y (Wösten *et al.*, 2010). This value can be combined with information on long-term average relationships between peat subsidence and water table depths for different regions of the world in order to obtain estimates of CO₂ emissions under different environmental conditions.

The relationship between CO₂ gas emission monitoring and water depth has been discussed by Hooijer *et al.* (2010) and is used in this study to calculate CO₂ gas emissions from water depth change which can be expressed by the following equation;

$$\text{CO}_2 \text{ emission} = \text{Area} \cdot \text{WT} \cdot \text{CO}_2 \text{ 1m [t/y]} \quad (7.4)$$

Where:

Area = drained or burnt area within peatland area [ha]

WT = average groundwater depth change in study area [m/y]

CO₂ 1m = CO₂ emission at an average groundwater depth of 1m = 91 [t CO₂/ha/y]

Where CO₂ emission is expressed in t/ha/y and groundwater depth is the average depth of the water table below the peat surface, expressed in metres. By using the water table change in equation (7.2), the CO₂ emission in equation (7.3) can be expressed as:

$$\text{CO}_2 \text{ emission} = 0.91 \cdot \text{Area} \cdot \text{Peat subsidence rate (cm/y)} / \text{XO} \quad (7.5)$$

By considering the peat subsidence obtained by CIC differential technique, the CO₂ emissions in Block C and Block A can be calculated as shown in Figures 7.18 and 7.19 respectively.

The results shows that between 23 and 57 t CO₂/ha/y have been released from Block C, and between 8 and 20 t CO₂/ha/y have been released from Block A (Table 7.3). The CO₂ emissions vary due to the coefficients that represent the linear relationship between subsidence rate and water table change. The results of these analyses show that whilst Block A was subjected to much lower rates of subsidence than Block C, they still lost appreciable amounts of peat and carbon and contributed as much as 1.5-3.7 Mt of CO₂ equivalent to 35% of total emissions from Block C. It should be noted that these results provide a possible indication of emission levels. No accurate assumption and assessment is possible with the data and knowledge currently available.

Table 7.3: Emission estimates of carbon dioxide (CO₂)

Method	Co-efficient (X0)	Area (ha)	Mean CO ₂ (t/y)	CO ₂ (t/y)	CO ₂ (Mt/y)	CO ₂ (t/ha/y)
Block C	0.1	280628	3.49	6428873	6.43	22.91
	0.04		8.71	16044551	16.04	57.17
Block A	0.1	190663	0.92	1502293	1.5	7.88
	0.04		2.29	3739403	3.74	19.6

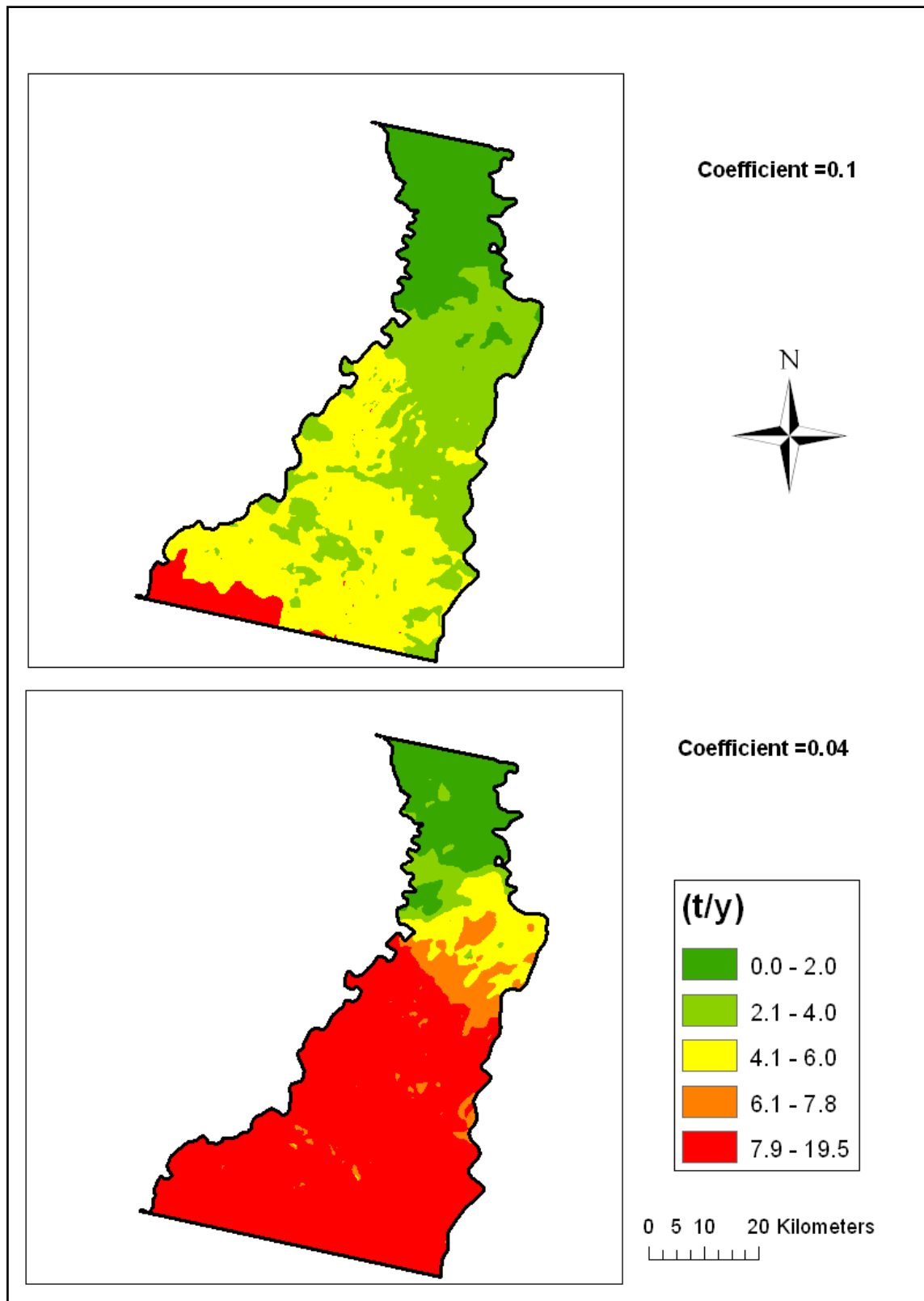


Figure 7.18: CO₂ emissions for the maximum and minimum drainage scenario in Block C based on CIC differential method using the coefficient values of the linear relationship between subsidence and water table depth change.

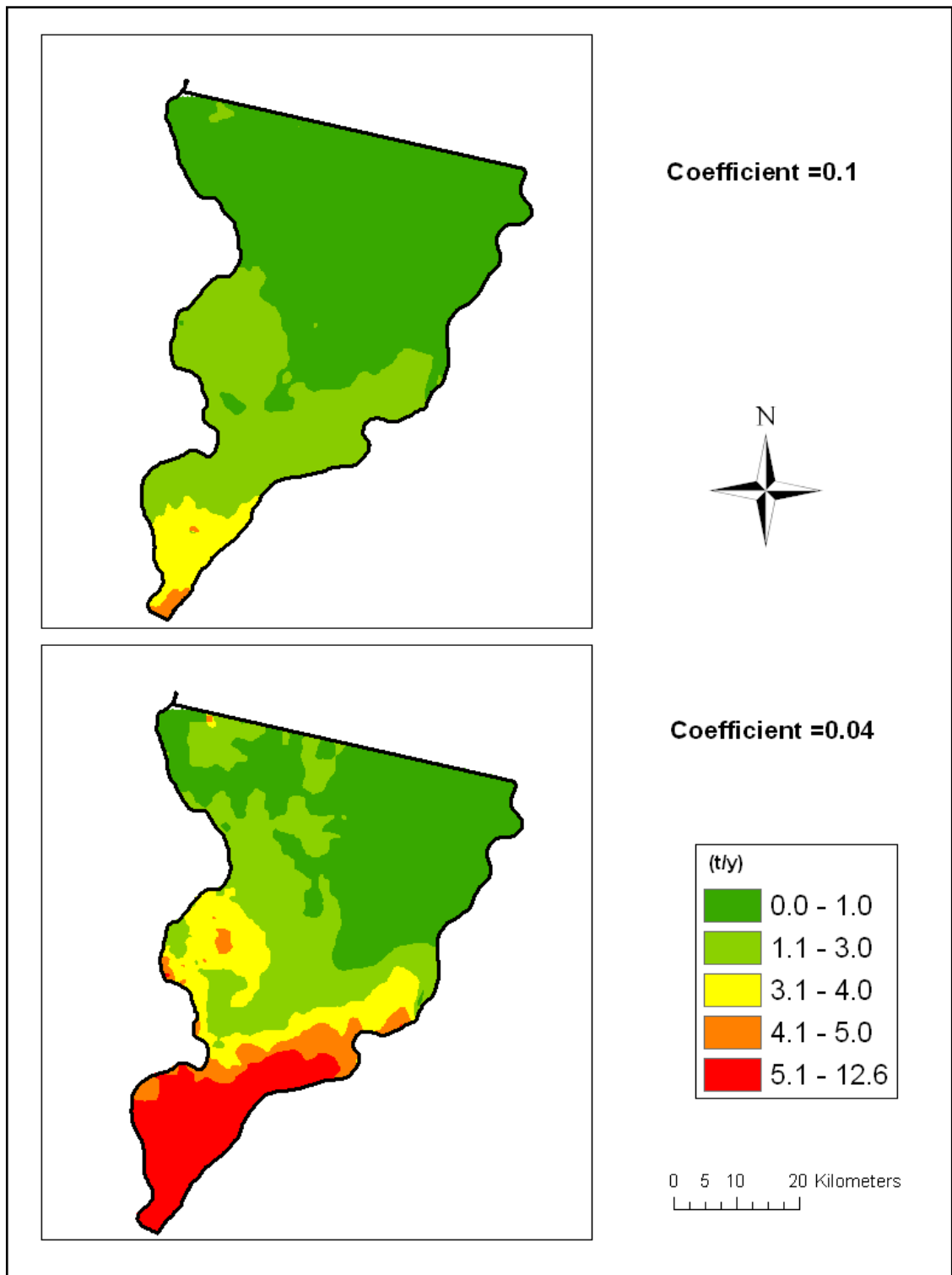


Figure 7.19: CO₂ emissions for the maximum and minimum drainage scenario in Block A based on CIC differential method using the coefficient values of the linear relationship between subsidence and water table depth change.

7.7 Modelling the relationship between carbon loss, subsidence rate and water table change

The results in Tables 7.2 and 7.3 show that carbon loss that have been calculated by multiple peat lost by carbon content and bulk density, increases in a linear relationship with CO₂ emissions that have been estimated using equation 7.4. From these results, it is clear that using subsidence rate-water table change coefficient value (XO=0.1), the CO₂ emissions calculated in equation 7.5 are 1.6 times larger than the carbon loss calculated in equation 7.1. While using coefficient value (XO=0.04), the CO₂ emissions are 4 times larger than the carbon loss. The CO₂ is comprised of one atom of organic carbon (C) units with two atoms of oxygen (O) from the air. The atomic weight of carbon is 12 while the atomic weight of oxygen is 16; hence, the atomic weight of carbon dioxide is 44. Therefore, the amount of CO₂ should not be more than (3.67) times the amount of C. By using the coefficient value (XO=0.048), the amount of CO₂ calculated in equation 7.5 will be equal to the amount of carbon loss calculated in equation 7.1 which means that all carbon loss is released as CO₂. This coefficient value is more likely to represent the linear relationship between peat subsidence and water table change that gives acceptable carbon loss and CO₂ emission estimation.

However, by merging equation 7.1 and equation 7.3, the carbon loss could be calculated in a similar way to calculate CO₂ emissions in equation 7.4 by assuming the suitable value for the carbon loss due to one meter of water table change:

$$C \text{ loss} = \text{Area} \cdot \text{WT} \cdot \text{carbon content} \cdot \text{peat bulk density} \cdot X0 \quad (7.6)$$

$$C \text{ m} = \text{carbon content} \cdot \text{peat bulk density} \cdot X0 \quad (7.7)$$

C m: C loss at an average groundwater depth of 1m [t C ha/y]

X0: the coefficient of water table change and subsidence rate (0.04-0.1).

In this study, the $C_m = 570 \cdot X_0$: $X_0=0.1, 0.04$.

Finally, the carbon loss can be identified using the following equations derived from the CO₂ emission equation:

$$C \text{ loss rate} = \text{Area} \cdot \text{WT} \cdot C_m \text{ [t/y]} \quad (7.8)$$

Where:

Area: drained or burned area within peatland area [ha]

WT: average groundwater depth change in study area [m/y]

C_m : C loss at an average groundwater depth of 1m [t C/ha/y]

Compared with equation 7.1, equation 7.8 can link the co-efficient of a linear relationship between subsidence and water table change and also the peat carbon content and peat bulk density as well to calculate the carbon loss. So if the subsidence rate and water table change can be measured in the field, the co-efficient values can be identified and the carbon loss and CO₂ emission can be estimated.

To convert the estimates of carbon loss obtained by equation 7.8 to CO₂ emission, the carbon loss should be multiplied by the conversion factor of 3.66 and equation 7.4 can be modified as follows:

$$\text{CO}_2 \text{ emission} = 3.67 \cdot \text{Area} \cdot \text{WT} \cdot C_m \text{ [t/y]} \cdot P \quad (7.9)$$

Where: Area: drained or burned area within peatland area [ha]

WT: average groundwater depth change in study area [m/y]

$$\text{CO}_2 \text{ 1m} = 3.67 \cdot C_m = 3.67 \cdot \text{carbon content} \cdot \text{peat bulk density} \cdot X_0 \text{ [t CO}_2\text{/y]} \quad (7.10)$$

P: is the percentage of C released as CO₂ (P=100% when assuming that all carbon loss is converted into CO₂ and methane emissions are negligible).

The equation 7.9 is different from equation 7.4 because it takes into account the carbon content, peat bulk density, oxidation percentage and the coefficient of the linear

relationship between subsidence and water table change. The adapted CO₂ emissions are presented in Table 7.4. The results show that the CO₂ emission rate based on CIC differential method is 53 t/ha/y and 8 t/ha/y in Block C and Block A respectively (Figure 7.20). Although this assumes that all leaching C losses are considered to ultimately result in CO₂ oxidative loss, which may be an oversimplification as some C could be released as methane (CH₄).

Table 7.4: adjusted Emission estimates of carbon dioxide (CO₂).

Study area	Area(ha)	Loss of C (Mt)	Annual C loss(t/ha/y)	CO₂(Mt)	Annual CO₂ (t/ha/y)
Block C	280628	4.02	14.33	14.75	52.6
Block A	190663	0.94	4.93	3.45	18.09

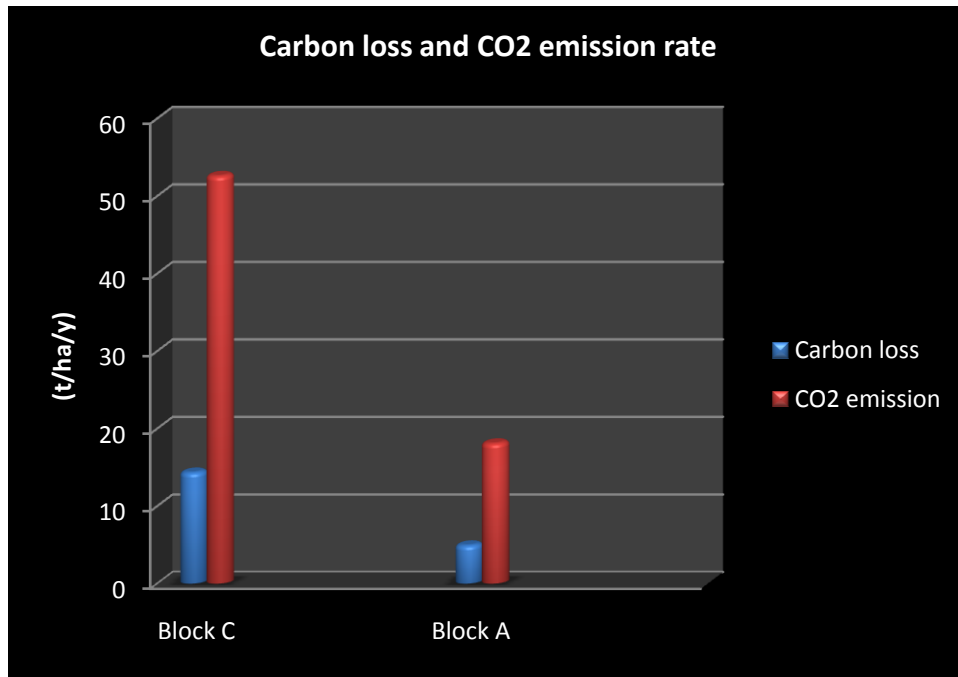


Figure 7.20: Carbon loss and CO2 emission rate in Block C and Block A.

7.8 Discussion

Based on DEM accuracy discussed in a previous chapter, only four interferograms with temporal baselines over 27 months were developed for deformation detection using eight ERS1-2 scenes acquired between 1996 and 2000 over the Ex-MRP area.. In order to derive the ground displacement from an interferogram, the effects due to baseline accuracy, atmosphere effects, system noise, coherence, and phase wrapping (UP), which can affect the deformation accuracy, need to be taken into account. Furthermore, the main problem associated with DInSAR in this study is the temporal decorrelation due to changes in the electromagnetic properties or relative positions of scatterers within a resolution cell. Due to the 27-month time difference, coherence is seriously lost except in the urban and deforested areas. InSAR cannot be used to make high-precision measurements over fairly long time periods for landscapes that lack substantial stable radar reflectors; such landscapes include forest areas where the phase image of such landscapes will show an incoherent speckled pattern. Since the test site is a densely vegetated area, with

little urbanization and open regions, the loss of coherence is significantly high even after a few days. However, in this study, the possibility of obtaining DInSAR maps on some burnt or deforested areas has been examined at two field sites.

Beside the temporal decorrelation, the baseline estimation and baseline length might be another source of error. The ground deformation error basically depends on the interferometric phase error and the perpendicular baseline error of the differential pair. Initial estimates of the baseline obtained might be inaccurate so that the differential interferogram might contain residual fringes. The error in a displacement measurement resulting from inaccurate baseline increases with the size of the area investigated. The length of the baseline also has an influence on the amount of noise in differential interferograms. A small baseline leads to a higher accuracy of the detected height differences. With an increasing length of the baseline, the noise level rises, and that leads to a decorrelation of the radar signals. The baseline decorrelation is always in the system and cannot be avoided (Zebker *et al.*, 1996). It can be reduced to a certain extent at the expense of image resolution since the “geometrical decorrelation” can be removed (Gatelli *et al.*, 1994).

In general, the operational use of DInSAR is limited to a) short temporal baselines b) areas with limited vegetation, and c) advantageous weather conditions during master and slave acquisitions. Subject to these limitations, no studies have been performed on the measurement of peat subsidence. The success of the technique of repeat pass interferometry depends largely on high correlation and coherence of the two sets of signals recorded during the two repeat passes if the scattering properties of the ground surface remain undisturbed between the repeats. A low coherence corresponds with a

high noise in the interferograms and prevents successful generation of differential interferograms using 3-pass, 4-pass and complex interferogram combination approach using 3 ERS images.

For the 4-pass differential interferometric approach, two independent SAR image pairs are used. One of the pairs is used to estimate the topographic phase while the other pair (differential pair) has the topographic and deformation phase. This approach depends on the successful unwrapping of the interferometric phase in both topographic and differential interferograms. However, the UP required in the multi-pass approach is found difficult to resolve in this study and far from operational for low coherence areas in both interferograms pairs which might affect the resulting subsidence results. With the unwrapped phase images of the differential pair and the topographic pair, the scaling factors determined by the different baselines of the two image pairs have to be determined using two methods. The first method is the least squares fit approach which determines the scaling factor for the phase. The second approach is scaling the unwrapped phase topographic interferogram by calculating the scale factor from the baselines of the interferogram used as topographic reference and the differential interferogram

While the 4-pass approach is dependent on the successful unwrapping of the interferometric phase, the complex combination of interferograms can be performed without meeting this requirement. The sensitivity of this differential interferogram to topography is therefore much smaller compared to the original interferograms, whilst the combined interferogram is more suited for detecting the displacements than any of the original interferograms. However, the scaling of the wrapped phase also leads to

scaling the phase noise. Therefore the approach is limited to small integer numbers of scaling factors for combination.

4-pass results show small deformation pattern in both Block C and Block A with few subsidence zones with maximum subsidence rate around 1 cm/year. In contrast, the complex interferogram combination method shows one direction deformation pattern from north to south with maximum subsidence rate around 5 cm/y in Block C and 3.4 cm/y in Block A. Based on DInSAR calculation, the subsidence rate in Block C is higher than the subsidence rate in Block A where illegal logging and forest clearing occurred earlier compared to Block C. The subsidence rate values remain lower than expected when compared to the results of other researchers. However, the two subsidence scenarios presented in this study, which are based on different DInSAR techniques within each region in the Ex-MRP, are less likely to represent actual subsidence, especially within burn scar and deforested areas. Despite this, they define a range of two possible subsidence scenarios. The complex interferogram combination scenario is the 'worst case' scenario in terms of a high subsidence rate of around 5 cm/y.

The accuracy of DInSAR measurements reported in this study could not be assessed due to lack of field measurements between 1996 and 2000. Analysis of the subsidence rates obtained in this study reveal that the maximum subsidence rates for the period 1997 to 2000 are 4.6 cm/y in Block C and 3.2 cm/y in Block A. A very few measurements of subsidence have been made in the Ex-MRP area in the north of Block C by a team from Center for International Cooperation in Sustainable Management of Tropical Peatland (CIMTROP), University of Palangkaraya, Indonesia. These measurements have been taken place between 2000 and 2004 and have been used to give an indication of the

accuracy of this work (Table 7.5). Their subsidence measurements suggest an average subsidence rate of around 1 cm/y. The results show accumulation of peat material as well as subsidence, which might agree with the uplift of the peat surface in the 4-pass and CIC methods. Many tropical deposits are actively accumulating peat or are in a steady state (Brady, 2002), although evidence suggests that climatic and land use conditions are no longer conducive to continued accumulation at all sites particularly in locations subject to drainage (Page *et al.*, 1999; Sieffermann *et al.*, 1988; Page *et al.*, 2004). The apparent accumulation recorded by CIMTROP was most likely due to a recording error or swelling of the peat surface following heavy rain.

Another subsidence monitoring survey was done in the northern part of Block C by CIMTROP team for two years (2006 to 2008) along a 10 km transect between the Kahayan and Sebangau Rivers (Table 7.6). The recorded subsidence rates on this transect are between 0 and 2.5 cm/y. This low rate may be explained by the fact that the peat in this location has already undergone much decomposition in the past and is now less prone to further decomposition owing to low inputs of labile carbon from the regenerating vegetation. This may be especially true for peat that has been exposed to fires, where the forest vegetation has been replaced by a low biomass fern-dominated community. However the lack of peat characteristic data does not allow quantification of such a relationship. The results also indicate that subsidence rates are lowest in forest, between 0 and 1 cm/y. In degraded areas, they are between 1 and 2.5 cm/y. As these differences do not correspond to measured differences in water depths, the different subsidence rates could be explained by the fact that the presence of natural forest cover shelters the top peat from drying out, thus reducing decomposition and hence subsidence. These results support the subsidence rate from the CIC methods

which shows an increase in the subsidence with decreasing forest cover from north to south in Block C.

Table 7.5: Peat subsidence in the north of Block C measured by CIMTROP team.

Code	S	E	Setting date (5 Apr 2004) (cm)	Readout date (24 Feb 2006) (cm)	Different (2004-2006) (cm)	Readout date (24 Feb 2007) (cm)	Different (2004-2007) (cm)	Readout date (24 Feb 2008) (cm)	Different (2004-2008) (cm)
WIB1-50	-2.33023	114.02245	55	55	0	55	0	55	0
WIB1-200	-2.33158	114.02177	152.5	148	4.5	148	4.5	148	4.5
WIB1-400	-2.33335	114.0211	203	200	3	199	4	199	4
WIB2.5-50	-2.33757	114.03013	60	58	2	58	2	57.5	2.5
WIB2.5-200	-2.33845	114.02918	84	88	-4	89	-5	87.5	-3.5
WIB2.5-400	-2.33978	114.02782	89	92	-3	91.5	-2.5	89.5	-0.5
WIB3.5-50	-2.34518	114.03875	104	104	0	107	-3	104	0
WIB3.5-200	-2.34622	114.03795	82.5	83	-0.5	83	-0.5	89	-6.5
WIB3.5-400	-2.34747	114.03667	138	140	-2	140	-2	139	-1
EIB1-50	-2.32902	114.02325	80	80	0.3	79.7	0.3	79	1
EIB1-400	-2.32677	114.02550	121	123	-2	123	-2	114	7
EIB2.5-50	-2.33588	114.03118	77	78	-2.7	79.7	-2.7	78.5	-1.5
EIB2.5-400	-2.33363	114.03333	79	80	18	61	18	80	-1
EIB3.5-50	-2.34392	114.04003	228	236	-6	234	-6	233	-5
EIB3.5-400	-2.34143	114.04215	268	270	-4	272	-4	268	0

Notes: + : is accumulation of peat material
 - : is subsidence of peat material

WTR= West transect , ETR= East transect

Table 7.6: Peat subsidence rate along a 10 km transect between the Kahayan and Sebangau Rivers
measured by CIMTROP team.

Distance (KM)	Land cover	Peat Depth(m)	Water depth 06-07 (m)			Depth below mark (m)		Difference (cm)	Subsidence (cm/y)
			mean	25%	min	26 Feb 2006	09 Mar 2008		
Kahayan River									
0	Degr.	4.0	-0.06	-0.12	-0.91	80	83	3	1.5
500	Degr.	3.2	-0.13	-0.21	-0.88	274	276	2	1
1000	Degr.	2.7	-0.11	-0.15	-0.82	213	215	2	1
1500	Degr.	3.3	-0.14	-0.26	-0.89	224	226	2	1
2000	Degr.	3.2	-0.22	-0.25	-1.32	170	174	4	2
2500	Degr.	3.5	-0.18	-0.29	-1.01	137	140	3	1.5
3000	Degr.	3.8	-0.31	-0.45	-1.20	190	195	5	2.5
Canal: Tarunal									
3500	Degr.	4.0	-0.07	-0.07	-0.88	216	218	2	1
4000	Degr.	3.3	-0.13	-0.11	-0.97	108	110	2	1
4500	Degr.	3.9	-0.01	-0.02	-0.78	144	147	3	1.5
5000	Degr.	4.8	-0.08	-0.05	-0.84	159	161	2	1
5500	Degr.	4.7	-0.01	-0.01	-0.76	148	150	2	1
6000	Degr.	4.3	-0.01	-0.01	-0.62	249	251	2	1
6500	Degr.	4.2	-0.13	-0.16	-1.04	111	114	3	1.5
Canal: Sebangau									
7000	Forest	4.2	-0.52	-0.74	-1.51	104	104	0	0
8000	Forest	3.0	-0.22	-0.35	-0.66	138	139	1	0.5
8500	Forest	3.5	-0.17	-0.26	-0.47	219	220	1	0.5
9000	Forest	5.3	-0.25	-0.33	-0.72	85	84	-1	-0.5?
9500	Forest	3.7	-0.26	-0.37	-0.77	219	214	-5	-2.5?
10000	Forest	0.6	-0.23	-0.39	-0.75	141	142	1	0.5
Sebangau River									

The subsidence results from this study are lower than expected as subsidence rates in the order of 5 to 10 cm/y are reported by Jaya (2005) who collected subsidence data in the northern part of Block C over an 18-month period in 2001-2002. Average subsidence measured at 5 transects of 110 m length, perpendicular to canals over the period, was found to be 8 cm/y (Hooijer *et al.*, 2008). A set of monitoring records over 28 years, for a drained peatland in Johor (Malaysia Peninsular), was published by Wösten *et al.* (1997). This is probably the longest subsidence record for SE Asian peatland available in the public domain and it provides valuable information on the development of subsidence rates in time. Averaged over the 17 records for separate subsidence markers, subsidence over 14 to 28 years after drainage implementation was

found to be 4.6 cm/y, and subsidence over 28 to 36 years about 2 cm/y. The reduction in subsidence is extrapolated to the future, suggesting that subsidence rates are expected to be below 2 cm/y over the long term (Hooijer *et al.*, 2008). Dradjad *et al.* (2003) examined the peat subsidence in a transmigration settlement in Barambai, South Kalimantan. He estimated the rate of subsidence due to shrinkage by calculation to be 0.5 – 2.2 cm/y while actual field measurements showed even higher values of 1.6 – 4.8 cm/y. The combined effects of shrinkage and consolidation resulted in a subsidence varying from 1.0 – 4.7 cm/y by calculation, or 2.4 – 5.3 cm/y from field data.

Although subsidence is a key and frequently discussed topic with regard to tropical peatland management, there is limited data on actual subsidence rates. There has been no long-term subsidence monitoring that would help with the reconstruction of subsidence history and extrapolation of point data to larger areas. The present study describes the subsidence scenario for part of the Central Kalimantan peatland during 1997–2000 from the available InSAR data pairs. Unexpectedly, the subsidence results do not yet allow a determination of a relationship between subsidence and burn scar or drainage network. However, due to the lack of sufficient temporal correlation in InSAR data pairs over the entire area especially before 1997 and due to a lack of field measurements at the time of observation, it is difficult to conclude definitively if any of the deformation results are accurate. SAR image pairs should cover representative conditions including dry seasons before and after the fire or deforestation with short temporal baselines to yield accurate results.

The major causes of peat subsidence are water loss and biological oxidation. If the water loss is great enough to reduce the surface water level, then there may have been an initial subsidence of the peat layer. Water loss leads to a decrease in the soil volume

through shrinkage and, eventually, to the subsidence of the peat layer. The greatly reduced rainfall during 1997 led to a very marked drop in the level of the peat water table. A study by Page *et al.* (2002) found that the water table fell to 98 cm below the surface in mid-November, 1997 in the northern part of Block C in an area that was unaffected by forest fires, whilst there was a drawdown of only 20 cm in the same location in 1995 and 1996 during the dry season. They also found that after the drought ended in December 1997 the peat water table responded very rapidly to rainfall events and returned to its normal wet season level within one month.

Fluctuations in the ground water table obtained from an automatic water table measuring device and data logger by Ludang *et al.* (2007) in Ex-MRP, Central Kalimantan, showed that the ground water table only came above the peat surface between March and June. They found that the pattern of fluctuation in the water table in the forest and re-growing forest areas were quite similar and significantly different compared with an agricultural area. They concluded that the water table fluctuations might be influenced by temperature profiles, which were significantly different between agricultural and forested areas (Ludang *et al.*, 2007). In the Central Kalimantan area, the groundwater levels have been affected by the main channel that was excavated as part of the drainage and irrigation system created for the Ex-MRP. The drainage channels in the Ex-MRP area affect the drawdown of the water table. Ludang *et al.*, (2007) found that, during the rainy season, there was no significant difference between the water table drawn down in re-growing forest and forested areas (around 50 cm). However, the water table dropped considerably in the dry season to below 89.9 cm and 138 cm in re-growing forest and forested areas respectively.

Many studies have shown that peat subsidence increases with decreasing water table conditions (Wösten *et al.*, 1997; Chimner and Cooper, 2003; Mäkiranta *et al.*, 2007; Mäkiranta *et al.*, 2009), whilst other studies of peatlands have shown only a weak correlation or even no correlation between peat subsidence and water table position (Lafleur *et al.*, 2005; Mäkiranta *et al.*, 2009). Wösten *et al.* (1997) presented a relationship between peat subsidence and water table depth and this rule has been applied in several subsidence assessments (for example; Hooijer *et al.*, 2006) and it still may be the best approach for rapid assessments in areas where no local subsidence data are available. As the data on the peat water table in the Ex-MRP are not available, this relationship has been used in this study to predict water table change from subsidence maps. It should be noted that some significant uncertainties are involved in this linear relationship as other parameters that are not accounted for by this relationship, also affect subsidence, including peat type, vegetation cover, fertilizer regime, mechanical compaction and soil management (Hooijer *et al.*, 2008). Another limitation of the equation is that subsidence tends to increase with increasing water depth without any limitations, whilst other studies have suggested that the subsidence rates will not increase beyond a certain threshold water depth.

With these considerations, the water table changes were calculated from the subsidence map and it was found that the maximum water table change ranged between 54 to 133 cm/y in Block C and between 35-86 cm/y in Block A. The water table results have been further used to estimate CO₂ emissions based on the linear relationship presented by Hooijer *et al.* (2010). A large number of studies have shown that CO₂ emissions increase with decreasing water table conditions, owing to increased oxygen availability in the unsaturated surface peat. In tropical peatlands, a non-linear modelling approach has been generally applied to describe the peat surface CO₂ respiration–water table

depth relationship (Jauhiainen *et al.*, 2008; Hirano *et al.*, 2009). However, Hooijer *et al.* (2006, 2010) and Uryu *et al.* (2008) applied only linear relationships between peat respiration and water table depth and they concluded that the linear relationship is the best estimate currently available for determining CO₂ emissions (Hooijer *et al.*, unpublished).

Peat soils globally, store about 20% of all terrestrial organic soil carbon, totalling 1,220 Gt (Immirzi and Maltby, 1992). Diemont *et al.* (1997) estimated that peatlands contain up to 5000 t/ha of carbon with a total amount of at least 20 Gt while Page *et al.* (2004) suggest it could be as much as 70 Gt (Rieley and Page, 2005). Peatlands can contribute to global climate conditions through their capacity to store carbon in natural conditions for thousands of years, or emit it to the atmosphere when drained and/or burnt, mainly as carbon dioxide (CO₂). The balance between the ecosystem carbon uptake and continuous losses to the atmosphere may change as a result of natural climate change or human activities (development), leading to lower carbon accumulation rates or increased carbon losses (Maltby and Immirzi, 1993). Carbon storage in South East Asia's peatlands, some 85% of which is in Indonesia, is upward of 42 Gt. Most of this peat carbon can be released to the atmosphere in the coming decades if drainage and fires continue. Note that even without fires; peat carbon will be lost from drained areas through oxidation of dry soil. Current CO₂ emissions from South East Asia are estimated by Hooijer *et al.* (2006) at 2000 Mt/y, about a third of which (630 Mt/y) is caused by peat soil oxidation and the rest by fires. In their natural condition most tropical peat swamp forests function as carbon sinks and stores, but forest clearance, drainage and fire can convert them rapidly to carbon sources.

One of the methods for measuring carbon gas flux on peatland is by estimation from peat subsidence rates, which depends on both physical processes (compaction and shrinkage) and biological processes (oxidative peat decomposition). By knowing the peat bulk density and C content of the peat before and after subsidence, it is possible to estimate the C loss and CO₂ emissions. Hooijer *et al.* (unpublished) conclude that the difficulty with monitoring subsidence is that it is a very slow process and it is not easy to define the ‘ground level’ that is monitored on a soft peatland. In addition, peat bulk density and C content measures also need to be acquired, preferably at the start of drainage as well as subsequently. If the subsidence rates are low, it can therefore take a number of years before they can be quantified sufficiently.

The results of this study show that between 2 and 9 Mt of peat carbon was lost over the period 1997-2000. The estimate of 280,000 ha of peat subsidence in Block C during the period 1997-2000 provides a carbon loss value of 14 t/ha/y whilst in Block A, losses were much smaller, at around 5 t/ha/y, with a total subsidence area of 190,000 ha. According to calculations by Hoscilo (2009) over an area of 320,000 ha in Block C between 1997 and 2005, the rate of carbon loss from peat soil was around 25.4 t/ha/y. This result may have been considerably overestimated, mainly because of the assumption about the peat depth that has been burnt in the 1997 fire, which was assumed to be around 0.51 ± 0.05 m. In this study, the peat losses were calculated for two subsidence scenarios; in the worst case scenarios the peat loss was less than 60 m³/y resulting from a maximum peat subsidence of 5 cm/y.

There are uncertainties associated with the estimation of carbon loss due to large variations of the value of bulk density and, to a lesser extent, for carbon content. This study cautiously assumed an average bulk density of 0.1 g/cm³ and a carbon content of

57% (a commonly used value for Indonesian peat). There are some indications that more mature peat with higher bulk density yields higher emissions when drained. However this finding is still highly uncertain. Bulk density values of peat soils in Kalimantan vary between 0.15 and 0.25 g/cm³ under natural conditions (Lambert and Staelens, 1993; Kurnain *et al.*, 2001; Sajarwan *et al.*, 2002). All peat descriptions and bulk density measurements available suggest that all or most peat in Blocks A, B and C in the Ex-MRP area is moderately to highly humified (hemic to sapric). In Kalampangan, in the north of Block C, the bulk density values of the upper 30 cm layer vary between 0.12 and 0.17 g/cm³ under pristine peat swamp forest, whilst in cultivated and fire damaged peatlands, they vary between 0.17 and 0.31 g/cm³ (Kurnain *et al.*, 2001; Rieley and Page, 2005). On the other hand, organic C contents of peat soils in the upper 100 cm profile at Kalampangan range from 49% to 57% (Kurnain *et al.*, 2001). A bulk density of 0.1 g/cm³ which gave maximum carbon loss 14.3 t/ha/y has a large uncertainty in this study. When instead this value is set at 0.05 or 0.15 g/cm³ the C loss will be 7.2 and 21.5 t/ha/y respectively. This large variation in C loss indicates the uncertainty associated with its estimation.

The most important carbon containing gases emitted from peatlands are carbon dioxide (CO₂) and methane (CH₄) with the former far exceeding the latter in both amount and effect. The CO₂ emission rate has been estimated by two different methods in this study. The first method was based on multiplying the carbon loss values derived from the peat subsidence calculations, whilst the second method used the linear relationship presented by Hooijer *et al.* (2010) using water table depth change. The results from the latter method shows that between 23 and 57 t CO₂/ha/y have been released from Block C over the period 1997-2000, whilst CO₂ emissions from Block A in the same period were between 8 and 20 t/ha/y. The results showed a wide range and depended on the linear

relationship accuracy between subsidence rate and water table change. These results represent between 44% and 109 % of the total CO₂ emissions calculated by the first method, which assumed that all carbon lost as measured by subsidence was emitted as CO₂. The first method suggests CO₂ emissions of 53 t/ha/y in Block C and 18 t/ha/y in Block A over 1997-2000. These results are in agreement with Wösten *et al.* (1997) who estimated that subsidence of every centimetre of a tropical peatland results in the emission of 13 t CO₂/ha/y, whilst Ballhorn *et al.* (2009) estimated that between 9.6-17.6 t/ha of carbon were released from burnt peatlands during the 2006 El Niño episode.

This study highlights a linear relationship between carbon loss and CO₂ emission estimations calculated using water table change measurement (method-two of CO₂ estimation). Two equations (7.8 and 7.9) have been developed to estimate carbon loss taking into account the relationship between peat subsidence rates and water table change. By measuring the subsidence rate and water table change in different points in the study area, a coefficient value map could be interpolated and the carbon loss and CO₂ could be estimated for a large scale map. This method was applied on Block C and Block A and gave similar results to those obtained by calculating carbon losses using bulk density and carbon content. The advantage of this model is that there is no need to use a linear relationship between CO₂ emission and water table depth, but alternatively, coefficient value map can be used with water table change to estimate CO₂. The scenarios used in this analysis are indicative only and do not reflect different types of peat and different subsidence behaviours, therefore the emissions estimates are also indications of the potential levels of emissions that could have resulted from subsidence over the period.

7.9 Limitation

Among the limitations of current research are the following

- The absence of field observation measurements during the period of the study was one of the most important limitations of this research. Without these field data, the original DInSAR measurements cannot be quantitatively used due to different sources of errors. Besides that, the use of the DInSAR technique is affected by some important limitations, like the unwrapping-related errors, temporal decorrelation, and the effects caused by different atmospheric conditions (atmospheric effects). The unwrapping related errors usually occur in low coherence areas where the interferometric phase noise is high. However, if the coherence is too low, the density of the good pixels may not be sufficient to guarantee a correct sampling of the deformation signal. The peat subsidence phenomena are only detectable over large time intervals where the ERS images had very low coherence. Furthermore, the atmospheric artefacts represent a very important error source, which can strongly degrade the quality of the DInSAR observations and make it difficult to distinguish atmospheric fringes from true ground deformation. The resulting fringes of true displacement in this study could not be separated from atmospheric fringes. All these error sources represent a strong limitation of the DInSAR technique to measure peat subsidence in tropical swamp forest areas, especially to generate differential interferogram using 3 ERS images. Such successful differential interferograms might be used to make comparisons with current deformations and identify confidently the subsidence values that represent the actual deformation.
- There are limitations in available ERS data to select suitable ERS images for DInSAR technique. The ERS images should be acquired under dry weather

conditions to get a high coherence and to exclude irregularity due to different soil moisture conditions or due to atmospheric artefacts. Unfortunately, only one set of pair images were available in the dry season in each test site area. Furthermore, the deformation of this study may show seasonal changes as the ERS images acquired under dry (1997) and wet (2000) weather conditions. Another limitation of the available data is the spatial decorrelation which comes from long perpendicular baselines. To maintain an acceptable noise level with the spatial decorrelation introduced by the baseline length, a baseline less than 100 m is recommended while the baseline length in this study is in the range of between 204m and 383m.

- DInSAR results do not take into account the different peat subsidence phases namely consolidation, oxidation and shrinkage. The subsidence maps in this study represent the total subsidence from a combination of oxidation and shrinkage. It is important to break down total subsidence into these three phases, because each represents a characteristic behaviour of peat and has different practical consequences for environmental issues of CO₂ emissions. Also, the results were not able to discriminate different subsidence behaviours due to different peat types, and this is an area that requires further work.

7.10 Further work

Suggestions for further areas of research that build on the results of this study are described below.

- Subsequent work should focus on improving the results using different DInSAR techniques such as the 2 pass method by using an external DEM. This approach has several advantages such as; 1) no noise from the simulated interferogram while when differencing interferograms there are two noise contributions, from both the reference and second interferogram. Also, there are no possible PU errors in the simulated interferogram that can introduce errors in the final results. 2) The DEM information can be used to improve the baseline estimate. Using the unwrapped phase with the baseline will improve the baseline and remove linear phase trends in the image.
- A likely cause of the different subsidence results from the 4-pass and complex interferogram combination methods is the poor initial estimates of the baseline, so the differential interferogram might contain residual fringes. The error in a displacement measurement resulting from inaccurate baseline increases with the size of the area investigated. Another reason for unmatched results might be the scaling factors determined by the different baselines of the two image pairs. Further work should focus on these factors in order to improve the DInSAR technique.
- Further work is still needed to identify what percentage peat oxidation contributes to the total peat subsidence in the Ex-MRP area. Many studies in Indonesia have assumed that a fixed percentage of total subsidence (around 60%) is due to oxidation (DID and LAWOO, 1997), whilst studies in other parts

of the world suggest that this range can be much wider, between 35% and 100% (Couwenberg *et al.*, 2010).

- To address the issue of the poor coherence where the land cover is characterised by heavy forest or plantations, it is recommended to use the ALOS PALSAR L-band SAR because it is more robust against temporal decorrelation. The L-band signal penetrates deeper into the vegetation cover than the C-band and provides the possibility of obtaining useable interferometric pairs over longer timeframes than provided by C-band SAR. The L-band signal is, therefore, much less sensitive to the temporal decorrelation due to changes in the vegetation cover. On the other hand, because the subsidence observations are expected to be in decimetres after the 1997 fire, L-band interferograms acquired immediately after the fire are, therefore, well suited for the detection of peat subsidence in the order of decimetres, while C-band serves best for vertical deformations of a few centimetres. The phase of L-band with wavelength of about 23 cm is less sensitive to the deformation (one fringe corresponds to about 11.5 cm instead of the 2.8 cm of ERS).
- In the present study several assumptions had to be made on the relationship between subsidence rate, water table and CO₂ emissions. There is uncertainty associated with the values used for peat bulk density, carbon content and the C-CO₂ conversion factor, since not all carbon lost from the peat profile will be emitted to the atmosphere (e.g. there could also be fluvial losses). The assumptions taken on the values for these variables used in this study have strongly influenced the carbon flux estimation. Research in all of these areas will contribute to reduced uncertainties and ensure the validity or acceptability of the assumptions made in estimation of both tropical and global carbon budgets.

-
- The innovative approach to estimate carbon losses from peat subsidence, proposed in this study, could be implemented on a larger scale to improve current quantification of carbon losses in the whole Southeast Asian region. This methodology can be additionally enhanced by developing more reliable and precise DInSAR techniques to measure peat subsidence over a larger area.

7.11 Summary

The DInSAR technique can provide deformation measurements with a quality that is comparable with that of the traditional geodetic techniques. This capability, which can only be achieved by implementing advanced DInSAR processing and analysis procedures, is associated with three other important features of this remote sensing technique: the wide area coverage, the high spatial resolution and the availability of large historical SAR datasets, which for the ERS satellites, cover the last 12 years. In this study, the most relevant aspects of a flexible DInSAR procedure for peat subsidence measurement have been discussed. Information on peat subsidence in all tropical countries is very inadequate, making it virtually impossible to calculate accurate estimates of peat loss and therefore carbon pools. DInSAR methods could offer a good tool to provide reasonably accurate values for the total peat loss and carbon store within the peatlands of Kalimantan from which to derive approximations for the whole of Indonesia and all tropical peatlands.

However, these results highlight the potential use of spatially detailed InSAR measurements to provide better constraints for computer simulations of land subsidence and CO₂ emissions. The volume of peat subsidence was 921 m³ over the study area and this volume can further be used to estimate the total CO₂ emissions by taking into account peat bulk density and carbon content. If, however, the relationship between

subsidence and water table and water table and CO₂ emissions is known, i.e. the relative contribution of oxidation (which leads to emissions) can be quantified separately from consolidation and contraction/shrinkage, then subsidence measures may provide a good basis for large scale assessment of C loss which may be interpreted as CO₂ emissions from peatland degradation. Because Block C and Block A have a large carbon stock and suffer high deforestation rates, improving the effectiveness of protected areas in reducing emissions in this region might reasonably be given high priority. There is evidence that improved forest management strategies can greatly reduce carbon emissions and might be more beneficial in carbon terms than imposing stringent restrictions on forest use, which might cause 'leakage' of deforestation into surrounding areas. Obtaining information on subsidence rates and the extent of subsidence from fire and drainage is important for future tropical forest management and the development of mitigation strategies to reduce subsidence rates and CO₂ emission from peat soil and to protect peatland for nature conservation.

Chapter 8: Conclusion

8.1 Introduction

The aim of this project was to examine the potential application of InSAR technique in tropical peatland forest by considering three main applications; mapping out clear cuts and burn scar areas, measuring the terrain elevation and detecting land subsidence.

Specific objectives were to:

4. Examine if InSAR coherence technique alone can be used to identify burn scar and deforestation areas in tropical swamp forest in Central Kalimantan, Indonesia.
5. Using ERS-1 and ERS-2 SAR images to derive a digital elevation model by means of InSAR techniques and examine different processing stage errors that could affect the DEM accuracy.
6. Examine if DInSAR can detect peatland subsidence accurately and test the validity of this method to provide quantitative spatial information on the amount of peat soil that has subsided and determine carbon loss and CO₂ emissions.

8.2 Findings: Objective 1

In answer to objective 1, the following conclusions have been made.

- The study indicates that interferometric coherence can be used as an additional channel, with the backscatter channel to enhance the capabilities of SAR data for various applications in tropical forest. The fact that interferometric coherence does not rely on actual backscatter from the target but random dislocation of the scatterers between the two passes, makes it an independent physical parameter that is different from the SAR backscatter. Results obtained using ERS repeat-pass data shows that the interferometric coherence is significantly lower over forest than burnt areas; therefore the one-day repeat pass coherence is a useful tool to define the position of burned surfaces.
- The coherence threshold value of 0.35 has been shown as distinguishing value to maximize the discrimination of forest-non forest area and thus was selected as the indicator for the burnt-unburnt forest classification. The coherence of burnt area in 2000 has increased between 0.2-0.4 with respect to forest area in 1996 images.
- A quantitative analysis in Block C showed that, out of 0.33 million hectares of the total area investigated by InSAR coherence, about 90,000 ha (28 %) had burnt in the 1997 fire. The calculated burnt areas represent, on average, 71% of the areas identified by optical data for the same area in the same period of time. Despite the underestimation, SAR is a useful tool to detect burn scar areas, especially in tropical regions where they are normally covered by clouds.
- The deforestation was found in this study directly or indirectly associated with human activities through logging, land clearing, intensive drainage and fires.

The intensive drainage infrastructure in Block A of the EMRP greatly damaged the peatland hydrological system, increasing the risk of fire. By investigation 0.3 million hectares in the study area in Block A between 1996 and 2000, deforestation (logging, fire) had increased by 44% during this period, thus making the remaining forests more susceptible to fire in the future. The network of canals allowed easy access for people whose activities provided ignition sources. Hence most of the areas subjected to fires and deforestation were all located within close proximity to canals.

- The radar methodology applied in this study proved to be fast and accurate enough to estimate the extent of the burnt and deforested areas on a provincial scale. The effects of future droughts and fires will be cumulative. Long-term prospects for this area are not promising, even though the MRP has now been abandoned (July 1998). This area will experience a greatly heightened risk of fire damage during future dry seasons and flooding during rainy seasons.

The contributions of this objective to knowledge are:

- a) Acknowledges the ability of InSAR coherence to discriminate between forest and non-forest, identify burn scar areas and determine areas that have been clear-cut.
- b) Provides sufficient knowledge of the change of the coherence before and after the fire in tropical peat swamp forests.
- c) Estimates burn scar area by identifying the minimum coherence value of burn area and the coherence change value that represents the land cover change.

8.3 Findings: Objective 2

In answer to objective 2, the following conclusions have been made.

- The InSAR technique is mainly influenced by baseline length, coherence and temporal decorrelation. In this study, different methods of generating interferograms and phase unwrapping were evaluated.
- This study shows the results evaluated through the comparison with highly accurate independent check points collected using DGPS. The average absolute elevation difference range between 26 m to 5 m and the minimum RMS errors from the Maluku and Dadahup test sites are 5.0 m and 2.9 m respectively. RMS errors of the InSAR DEMs being generated was less than 3 m for lightly vegetated regions and between 5 to 26 m for heavily vegetated regions. These results suggest that high resolution InSAR can meet the requirements of many applications in low relief areas, since it can capture small variations
- Quantitative analysis of DEMs against DGPS check points show the intensity method is slightly better in densely forested areas, whilst the orbit method is slightly better in open areas. The average RMSE between two unwrapping methods was found to be less than 1 m. Both phase unwrapping methods show almost similar accuracy, especially in open areas, whilst there is a slight difference over forested areas where MCF trend tends to be more reliable. The average RMSE between the two interferogram generation methods or between the two unwrapping methods was found to be less than 1 m in all DEMs. However, applying adaptive filtering many times with a smaller coefficient and decreasing window size (128, 64, 32, and 16) can reduce the complexity of the phase unwrapping problem and facilitate the unwrapping. The average RMSE

change resulting from applying adaptive filtering many times ranges between 0.7 m and 6.6 m.

- It was indicated that the phase noise increases according to the decrease of coherence. It was also indicated experimentally that the height error increases with the decrease of coherence. However, this study suggests that the height error can be specified by average coherence value better than by the baseline length in the test site.
- The difference map accuracy assessment shows that that 90% of the difference in the DEMs generated by different methods have an absolute elevation difference of less than 5 m and an RMSE of about 6.6 m to 16 m. The absolute assessment of error distribution shows random distributions of small errors in the same tandem pair images, whilst the highest error, of more than 20m, were found only close to the holes, especially for the Maluku DEMs. The results highlight that DEM accuracy is strongly related to the coherence values in many parts of the DEM. Larger absolute elevation errors appear in areas with low coherence areas (forest and vegetated areas) with extreme errors of a few tens of metres, whilst the errors are smaller in high coherence areas (open and urban area).

The contributions of this objective to knowledge are:

- a) Provides DEM in two test sites in central Kalimantan, Indonesia with acceptable accuracy.
- b) Demonstrates that adaptive filter applied many times increased DEM accuracy due to improved phase unwrapping in this regional context.

-
- c) Shows that different phase unwrapping techniques and different interferogram computations have lower effects on the DEM accuracy compared to temporal and baseline decorrelation, and atmospheric effects.
 - d) Shows that average coherence value has more effects on DEM accuracy, compared to the baseline lengths.

8.4 Findings: Objective 3

In answer to objective 3, the following conclusions have been made.

- This study proposed a conservative approach to estimate the peat subsidence using 4-pass and complex interferogram combination DInSAR techniques. The main problems associated with DInSAR in this study were temporal decorrelation, long baseline length and poor baseline estimations. Due to the 27-month time difference, coherence is greatly reduced, except in the urban and deforested areas. The baseline ranged between 200 m and 375 m and was longer than the ideal baseline length of 100 m of differential interferograms, whilst it was suitable for topographical interferograms. Furthermore, these limitations prevent the successful generation of differential interferograms using 3-pass, 4-pass and by using a complex interferogram combination approach employing 3 ERS images, whilst differential interferograms applying 2 ERS pairs have been successfully generated. Surface change detection is found to be a difficult task on tropical swamp forest zones where temporal decorrelation effects are undistinguishable from displacement-related effects.
- The subsidence maps obtained by two differential methods show almost similar subsidence trends but different subsidence rate values. That was more likely due to poor initial baseline estimation in both of the two methods. 4-pass results

show small deformation pattern in both Block C and Block A with few subsidence zones with maximum subsidence rate around 1 cm/y. By contrast, the complex interferogram combination method shows one direction deformation pattern from north to south with maximum subsidence rate around 5 cm/y in Block C and 3.4 cm/y in Block A. Obviously, the subsidence rate in Block C is more rapid than that occurring in Block A and that agrees with the deforestation history of the Ex-MRP area, which shows earlier illegal logging and forest clearing occurred in Block A compared to Block C. The subsidence rate was not significantly correlated with deforestation or burn scar locations, where peat subsidence should be more likely to occur, than in other tropical swamp forest areas. However, the values remain lower than expected.

- The total amount of carbon lost from peat subsidence in Ex-MRP was estimated to be in the range of 0.4-7.1 Mt/y in Block C and 0.2-1.7Mt/y in Block A. By using bulk density (0.1 g/cm^3) and carbon content (57%), it was found that the rate of carbon loss ranged between 1.3-14.3 t/ha/y in Block C, whilst in Block A, losses were much smaller at between 0.7-4.9 t/ha/y. These estimations indicate that for every centimetre of subsidence in a tropical peatland results in carbon losses of 3t/ha/y, which is still underestimated compared to the other researchers findings. CO_2 emissions could be estimated from the carbon loss by assuming that all carbon lost was emitted as CO_2 . By multiplying the carbon loss by the conversion factor 3.66, the CO_2 emissions calculated was estimated at 4.8-52.6 t/ha/y in Block C and 2.5-18.1 t/ha/y in Block A from 1997 to 2000.
- The CO_2 emission rate has been estimated by another method using the linear relationship between subsidence rate, water table change and CO_2 emissions. The results from this method showed that between 23 and 57 t/ha/y have been

released from Block C over the period 1997-2000, whilst CO₂ emissions from Block A in the same period was between 8 and 20 t/ha/y. It was found from the results that there is a linear relationship between carbon losses and CO₂ emissions. This relationship has been developed through a new formula to estimate carbon losses, taking into account the relation between peat subsidence rate and water table changes. The implementation of the new equation is based on measuring the subsidence rate and water table changes at different points in the study area, a coefficient value map could then be interpolated and the carbon losses and CO₂ emissions could be estimated on a large scale map. The advantage of this new equation can be shown through identifying separate locations where a linear relationship between subsidence rate and water table change exists and then applying it to estimate the carbon loss from peat subsidence.

The contributions of this objective to knowledge are:

- a) Provide a conservative and unique methodology to estimate peat subsidence using two DInSAR techniques. While such uncertainties in subsidence rates and location mean that these scenarios are a poor substitute for reliable deformation in the study areas, but they provided a basis for calculating the range of possible peat loss over the period 1997-2000. The results can, therefore, not be used for detailed planning purposes, but they do provide a basis for further work of general management strategies for peatlands and for identifying knowledge gaps that need to be filled in further projects.
- b) Provide a geographical estimation of carbon loss and CO₂ emissions by examining different relationships between peat subsidence, water table changes,

carbon loss and CO₂ emissions, which can improve carbon flux estimation on a global scale.

- c) The new carbon loss calculation equation can be combined with information on long-term average relationships between peat subsidence and water table depths for different regions of the world in order to obtain estimates of CO₂ emissions under different environmental conditions. These estimates can be used to make an initial identification of regions where improved investment to protect these areas with a mechanism aiming to reduce emissions from tropical peatlands. Also, this study illustrates the potential role of tropical swamp forest in climate change mitigation and will be a useful input to current discussions on a mechanism for reducing emissions from peat losses.

To summarise, InSAR coherence techniques can be used in rapid assessment to identify fire scars and deforestation areas in tropical peatland forest. The minimum coherence value of burned forest has been found around 0.35. This coherence value has been changed by more than 0.2 after the fire occurrence. This study shows that DEM can be successfully generated over burned areas. The average RMSE of ERS DEMs against the GPS height profiles range between 3.5 to 5 m depends on the land cover and the baseline length of tandem images. Applying adaptive filter many times has reduced the complexity of the phase unwrapping problem and increase DEM accuracy. Subsidence rates obtained by two DInSAR techniques are less likely to represent actual subsidence in tropical peatland. Both the 4-pass and the complex interferogram combination methods give unrealistic subsidence values and should therefore not be used. However, these results highlight the potential use of spatially detailed InSAR measurements to provide better carbon loss estimation and CO₂ emissions. Based on the highest

subsidence rate scenario, a relationship between peat subsidence rate and water table change has been developed to estimate carbon loss and CO₂ emissions. Finally, this research presents some potential applications of spaceborne SAR for monitoring the tropical peatland environments and could be used in further works to improve mapping and monitoring peatland forest with high resolution SAR systems such as TerraSAR-X and RADARSAT-2.

Bibliography

- Ackermann, F. (1996) Techniques and strategies for DEM generation. *Digital Photogrammetry: An Addendum to the Manual of Photogrammetry*, pp. 135-141.
- Ahuja, R. K., Magnanti, T. L. and Orlin, J. B.(1993) *Network Flows: Theory, Algorithms, and Applications*. Prentice-Hall, Englewood Cliffs, New Jersey, USA .
- Al-Harbi, S. (2009) *Suitability of DEMs derived from SAR interferometry and ASTER stereoscopy for hydrological applications using GIS; a case study of Al-Jafer Basin, Jordan*. Thesis submitted for the degree of Doctor of Philosophy at the University of Leicester.
- Ali, M., Taylor, D. and Inubushi, K. (2006) Effects of environmental variations on CO₂ efflux from a tropical peatland in eastern Sumatra. *Wetlands*, 26, pp. 612-618.
- Amelung, F., Galloway, D. L., Bell, J.W., Zebker, H. A. and Laczniaak, R.J. (1999) Sensing the ups and downs of Las Vegas: InSAR reveals structural control of land subsidence and aquifer-system deformation. *Geology*, 27(6), pp. 483-486.
- Anderson, J .A. R. (1983) *The tropical peat swamps of western Malaysia*, Elsevier, Amsterdam.
- Andriessse, J. P. (1988) *Nature and Management of Tropical Peat Soils*. FAO Soils Bulletin 59, Food and Agricultural Organisation of the United Nations, Rome, Italy.
- Anonymous, (1996) *Report of the national forest inventory for Indonesia*. DG of Forest Inventory and Land-use Planning Ministry of Forestry, Government of Indonesia and Food and Agriculture Organisation of the United Nations, Jakarta.
- Antikidis, E., Arino, O., Janodet, E. and Achard, F. (1998) Development of a new method for burned forest area assessment in Borneo during the 1997 exceptional fire

event. Data Management and Modelling Using Remote Sensing and GIS for Tropical Forest Land Inventory. *Proceedings of the FIMP-INTAG International Conference*. October 6-29, Jakarta, Indonesia.

Applegate, G., Chokkalingam, U. and Suyanto, S. (2001) The underlying causes and impacts of fires in south-east Asia. *Final Report Bogor Indonesia*, CIFOR, ICRAF, USAID, and USFS.

Askne, J. and Hagberg, J. O. (1993) Potential of interferometric SAR for classification of land surfaces. *IGARRS*, 3, pp. 985-987, Tokyo, Japan.

Askne, J. and Smith, G. (1996) Forest INSAR decorrelation and classification properties *FRINGE 96 ESA Workshop on Applications of ERS SAR Interferometry*, Zurich.

Askne, J. I., Dammert, P.B., Ulander, L. M. and Smith, G. (1997) C-band repeat-pass interferometric SAR observations of the forest. *IEEE Transactions on Geoscience and Remote Sensing*, 35, pp. 25–35.

Atlantis Scientific Inc. (2002) *EV-InSAR User Guide*, Atlantis Scientific Inc., Canada.

Baek, S., Lee, S. H. and C. K. Shum, C. K. (2005) Multi-temporal, multi-resolution data fusion for Antarctica DEM determination using InSAR and altimetry. *Proceedings of the IEEE International Geoscience and Remote Sensing Symposium*, 4, pp. 2827–2829.

Ballhorn, U., Siegert, F., Mason, M. and Limin, S. (2009) Derivation of burn scar depths and estimation of carbon emissions with LIDAR in Indonesian peatlands. *Proceedings of the National Academy of Science of the United States of America (PNAS)*, 106(50), pp. 21213-21218.

Balzter, H. (2001) Forest mapping and monitoring with interferometric synthetic aperture radar (InSAR). *Progress in Physical Geography*, 25(2), pp. 159-177.

Balzter, H., Talmon, E., Wagner, W., Gaveau, D., Plummer, S., Yu, J. J., Quegan, S., Gluck, M., Shvidenko, A., Tansey, K., Luckman, A. and Schmullius, C. (2002) Accuracy assessment of a large-scale forest map of central Siberia from synthetic aperture radar. *Canadian Journal of Remote Sensing*, 28, pp. 719–737.

BAPPENAS. (1998) *Planning for fire prevention and drought management project - interim report*. BAPPENAS (Bureau of Marine, Aerospace, Environment, Science and Technology), Jakarta, Indonesia.

Berardino, P., Fornaro, G., Lanari, R., and Sansosti, E. (2002) A new algorithm for surface deformation monitoring based on small baseline on small baseline differential SAR interferograms. *IEEE Transactions on Geoscience and Remote Sensing*, 40, pp. 2375-2383.

Bingyuan, H., Chao, M., Guifang, Z., and Lixun, K. (2008) Analyzing decorrelation of multi-temporal SAR data on InSAR. *Congress on Image and Signal Processing*, 1, pp. 452-461.

Boehm, H-D.V. and Siegert, F. (2001) Ecological impact of the one million hectare rice project in Central Kalimantan, Indonesia, using remote sensing and GIS, *22nd Asian Conference in Remote Sensing*, November 5-9, Singapore.

Bone, D. J. (1991) Fourier fringe analysis-the 2- dimensional phase unwrapping problem, *Applied Optics*, 30, pp. 3627-3632.

Borgeaud, M. and Wegmüller, U. (1996) On the use of ERS SAR interferometry for the retrieval of geo and bio-physical information. *FRINGE 96 Workshop on Applications of ERS SAR Interferometry*, Zurich.

Bourgeau-Chavez, L. L., Harrell, P. A., Kasischke, E. S. and French, N. H. F. (1997) The detection and mapping of Alaskan wildfires using a spaceborne imaging radar system. *International Journal of Remote Sensing*, 18, pp. 355-373.

Bourgeau-Chavez, L. L., Kasischke, E. S., Brunzell, S. M., Mudd, J. P., Smith, K. B., and Frick, A. L. (2001) Analysis of spaceborne SAR data for wetland mapping and flood monitoring in Virginia riparian ecosystems. *International Journal of Remote Sensing*, 22, pp. 3665– 3687.

Bourgeau-Chavez, L. L., Kasischke, E. S., Brunzell, S. and Mudd, J. P., (2002) Mapping fire scars in global boreal forests using imaging radar data. *International Journal of Remote Sensing*, 23(20), pp. 4211-4234.

Brady, M.A. (2002) Peat accumulation in Sumatra: Does Clymo's model apply? In: J.O. Rieley, J.O., Page, S.E. and Setiadi, B. (eds). (2002) Peatlands for people, natural resources function and sustainable management. *Proceedings of the International Symposium on Tropical Peatland*, Jakarta, Indonesia. BPPT and Indonesian Peat Association, Jakarta, pp. 50-51.

Burgmann, R., Rosen, P. A. and Fielding, E. J. (2000) Synthetic aperture radar interferometry to measure earth's surface topography and its deformation, *Annual Review of Earth and Planetary Sciences*, 28, pp. 169–209.

Burrough, P. A. (1986) Principles of geographical information systems for land resources assessment. Clarendon Press, Oxford, USA.

Canada centre for remote sensing, (2007) SAR research interferometry: InSAR. Available from http://www.ccrs.nrcan.gc.ca/resource/tutor/gsarcd/pdf/gsarcd_e.pdf [Cited 05 August 2007].

Chimner, R. A. and Cooper, D. J. (2003) Influence of water table levels on CO₂ emissions in a Colorado sub alpine fen: an in situ microcosm study. *Soil Biology and Biochemistry*, 35, pp. 345-351.

Chuvieco, E. and Martin, M. P. (1994) Global fire mapping and fire danger estimation using AVHRR images. *Photogrammetric Engineering and Remote Sensing*, 60, pp. 563–570.

Cochrane, M. A. and Chulze, M. D. (1999) Fire as a recurrent event in tropical forests of the eastern Amazon: effects on forest structure, biomass, and species composition. *Biotropica* 31(1), pp. 2-16.

Cochrane, M. A. (2003) Fire science for rainforests. *Nature*, 421, pp. 931-919.

Coppin, P. R. and Bauer, M. E. (1995) The potential contribution of pixel-based canopy change information to stand-based forest management in the northern U.S., *Journal of Environmental Management*, 44, pp. 69–82.

-
- Costantini, M. (1997) Validation of a novel phase unwrap algorithm using true and simulated ERS tandem SAR interferometric data, *Proceedings of the 3rd ERS symposium*, Florence, Italy.
- Costantini, M. A. (1998) Novel phase unwrapping method based on network programming. *IEEE Transactions on Geosciences and Remote Sensing*, 36 (3), pp. 813 – 821.
- Costantini, M., Farina, A., and Zirilli, F. (1999) A fast phase unwrapping algorithm for SAR interferometry. *IEEE transactions on geosciences and remote sensing*, 37(1), pp. 452 – 460.
- Couwenberg, J., Dommain, R. and Joosten, H. (2010) Greenhouse gas fluxes from tropical peatswamps in Southeast Asia. *Global Change Biology*, 16(6), 1715-1732.
- Crosetto, M. (2002) Calibration and validation of SAR interferometry for DEM generation. *ISPRS Journal of Photogrammetry and Remote Sensing*, 57, pp. 213–227.
- Crosetto, M., Tscherning, C. C., Crippa, B. and Castillo, M. (2002) Subsidence monitoring using SAR interferometry: reduction of the atmospheric effects using stochastic filtering. *Geophysical Research Letters*, 29(9), pp. 26-29.
- Crosetto, M., Castillo, M. and Arbiol, R. (2003a) Urban subsidence monitoring using radar interferometry: Algorithms and validation. *Photogrammetric Engineering and Remote Sensing*, 69(7), pp. 775-783.
- Crosetto, M., Arnaud, A., Duro, J., Biescas, E. and Agudo, M. (2003b) Deformation monitoring using remotely sensed radar interferometry data. *Proceedings, 11th FIG Symposium on Deformation Measurements*, Santorini, Greece.
- Crosetto, M., Biescas, E., Duro, J., Closa, J. and Arnaud, A. (2008) Quality assessment of advanced interferometric products based on time series of ERS and Envisat SAR data, *Photogrammetric Engineering and Remote Sensing*, 74(4), pp. 443-450.

Crosetto, M., Monserrat, O., Iglesias, R. and Crippa, B. (2010) Persistent scatterer interferometry: potential, limits and initial C and X-band comparison. *Photogrammetric Engineering and Remote Sensing*, 76 (9), pp. 1061-1069.

Dammert, P.B.G. (1996) Accuracy of INSAR measurements in forested areas. *Fringe 96 Workshop: ERS SAR Interferometry*, 30 September-3 October. Zurich.

Dammert, P.B.G. and Wegmüller, U. (1999) JERS INSAR DEM quality assessment for a boreal test site, *Geoscience and Remote Sensing Symposium (IGARSS)*, 4, pp. 1930-1932.

Dammert, P. B. G., Askne, J. I. H. and Kuhlmann, S. (1999) Unsupervised segmentation of multitemporal interferometric SAR images, *IGARSS*, 37(5), pp. 2259 - 2271.

Davies, K. (1965) *Ionospheric radio propagation*, U. S. Department of Commerce, 210-2145.

Dennis, R. (1999) *A review of fire projects in Indonesia (1982-1998)*. Center of International Forestry Research (CIFOR), Jakarta, Indonesia.

Dennis, R. A., Mayer, J., Applegate, G., Chokkalingam, U., Pierce Colfer, C. J., Kurniawan, I., Lachowski, H., Maus, P., Pandu Permana, R., Ruchiat, Y., Stolle, F., Suyanto and Tomich, T. P. (2005) Fire, People and Pixels: Linking Social Science and Remote Sensing to Understand Underlying Causes and Impacts of Fires in Indonesia. *Human Ecology*, 33, pp. 465-504.

Derauw, D., and Moxhet, J. (1996) Multiple images SAR interferometry. *Fringe 96 ERS SAR Interferometry Workshop*, ESA/ESRIN Remote Sensing Exploitation Frascati, Italy. Available from http://earth.esa.int/workshops/fringe_1996/derauw/ [Cited 21 June 2008].

Department of Irrigation and Drainage (DID) and Land and Water Research Group, Wageningen (LAWOO). (1996) *Western Jahore integrated agricultural development project*. Consultancy services on peat soil management.

Department of Irrigation and Drainage (DID). (2001) *Water management guidelines for agricultural development in lowland peat swamps of Sarawak*. Department of Irrigation and Drainage, Kuching. Malaysia.

Diemont, W. H., Nabuurs, G. J., Rieley, J. O. and Rijkssen, H. D. (1997) Climate change and management of tropical peatlands as a carbon reservoir. In: Rieley, J. O. and Page, S. E. (eds.) *Biodiversity and Sustainability of Tropical Peatlands*. Samara Publishing, Cardigan, UK. pp. 363-368.

Dongchen, E., Chunxia, Z. and Mingsheng, L. (2004) Applications of SAR interferometry on DEM Generation of the Grove Mountains. *Photogrammetric Engineering and Remote Sensing*, 70(10), pp. 1145–1149.

Dow, J. M., Rosengren, M., Marc, X., Zandbergen, R., Piriz, R. and Romay Merino, M. (1996) *Achieving, assessing and exploiting the ERS-1/2 tandem orbit configuration*. *ESA Bulletin*, 85.

Drajad, M., Soekodarmodjo, S., Hidayat, M.S. and Nitisapto, M. (1986) Subsidence of peat soils in the tidal swamplands of Barambai, South Kalimantan. *Proceedings of the Symposium on Lowland Development in Indonesia. Research Papers*, pp. 168-181. ILRI, Wageningen, The Netherlands.

Dradjad, M., Soekodarmodjo, S., Shodiq Hidayat, M. S. and Nitisapto, M. (2003) Subsidence of peat soils the tidal swamplands of Barambai, south Kalimantan. *Jurnal Ilmu Tanah dan Lingkungan*, 4 (1), pp. 32-40.

Driessen, P. M. and Soepraptohardjo, M. (1974) Soils for agricultural expansion in Indonesia. *bulletin 1*, Soil Research Institute, Bogor, Indonesia.

Duchossois, G. and Martin, P. (1995) ERS-1 and ERS-2 tandem operations. *ESA Bulletin*, 83, pp. 54-60.

El-Rabbany, A. (2002) *Introduction to GPS: The global positioning system*. pp.176, Artech House Publishers, Boston , USA.

Endreny, T., Wood, E. and Lettenmaier, D. (2000) Satellite derived digital elevation model accuracy: hydrological modeling requirements. *Hydrological Processes*, 14(2), pp. 177–194.

Engdahl, M., Borgeaud, M. and Rast, M. (2001) Use of ERS 1 / 2 tandem interferometric coherence in the estimation of agricultural crop heights. *IEEE transactions on geosciences and remote sensing*, 39(8), pp. 1799 –1806.

Escuin, S., Navarro, R. and Fernandez, P. (2008) Fire severity assessment by using NBR (Normalized Burn Ratio) and NDVI (Normalized Difference Vegetation Index) derived from LANDSAT TM/ETM images. *International journal of Remote Sensing*, 29, pp. 1053-1073.

Fearnside, P.M. (1997) Transmigration in Indonesia: Lessons from its environmental and social impacts. *Environmental Management*, 21(4), pp. 553-570.

Ferretti, A., Prati, C., Rocca, F. and Monti Guarnieri, A. (1997) Multibaseline SAR interferometry for automatic DEM reconstruction, *3rd ERS Symposium*, 17-21 March, Florence, Italy, *ESA SP-414*, pp. 1809-1820.

Ferretti, A., Prati, C. and Rocca, F. (1999) Multibaseline INSAR DEM reconstruction, the wavelet approach. *IEEE Transactions on Geoscience and Remote Sensing*, 37, pp. 705- 715.

Ferretti, A., Prati, C. and Rocca, F. (2000) Nonlinear subsidence rate estimation using the permanent scatterers in differential SAR interferometry. *IEEE Transactions on Geoscience and Remote Sensing*, 38(5), pp. 2202-2012.

Ferretti, A., Prati, C. and Rocca, F. (2001) Permanent scatterers in SAR interferometry. *IEEE Transactions on Geoscience and Remote Sensing*, 39(1), pp. 8-20.

Ferretti, A., Massonnet, D., Monti-Guarnieri, A., Prati, C. and Rocca, F. (2007) *InSAR principles: guidelines for SAR interferometry processing and interpretation*, European Space Agency (ESA) (TM-19). ESA Publications, Noordwijk , The Netherlands.

-
- Fielding, E. J., Blom, R. G. and Goldstein, R. M. (1998) Rapid subsidence over oil fields measured by SAR interferometry. *Geophysical Research Letters*, 27, pp. 3,215–3,218.
- Fitzgerald, N., Basheer, S. and McLeod, M. (2005) Peat subsidence near drains in the Waikato region. *Environment Waikato technical report*, New Zealand.
- Fornaro, G. and Franceschetti, G. (1995) Image registration in interferometric SAR processing. *IEE Proceedings-Radar Sonar and Navigation*, 142(6), pp. 313-320.
- Fornaro, G., Franceschetti, G. and Lanari, R. (1996) Interferometric SAR phase unwrapping using Green's formulation. *IEEE Transactions on Geoscience and Remote Sensing*, 34(3), pp. 720-727.
- Fornaro, G., Franceschetti, G., Lanari, R., Rossi, D. and Tesauro, M. (1997a) Interferometric SAR phase unwrapping using the finite element method. *IEE Proceedings-Radar Sonar and Navigation*, 144(5), pp. 266-274.
- Fornaro, G., Franceschetti, G., Lanari, R., Sansosti, E. and Tesauro, M. (1997b) Global and local phase-unwrapping techniques: a comparison. *Journal of the Optical Society of America A - Optics Image Science and Vision*, 14, pp. 2702-2708.
- Fornaro, G. and Monti Guarnieri, A. (2002) Minimum mean square error space-varying filtering of interferometric SAR data, *IEEE Transactions on Geoscience and Remote Sensing*, 40(1), pp. 11-21.
- Franceschetti, G. and Lanari, R. (1999) *Synthetic aperture radar processing*. CRS Press, New York, USA, pp.1-284.
- Francesco, S. and Benedicte, F. (2000) Detection of ground subsidence in the city of Paris using radar interferometry: isolation of deformation from atmospheric artefacts using correlation. *Geophysical Research Letters*, 27(24), pp. 3981-3984.
- Freeman, T. (1994) What is imaging radar. California institute of technology, Available from http://www.ccrs.nrcan.gc.ca/resource/tutor/fundam/pdf/fundamentals_e.pdf, [Cited 10 August 2007].

French, N. H., Kasischke, E. S., Bourgeau-Chavez, L. L. and Harrel, P. A. (1996) Sensitivity of ERS-1 SAR to variation in soil water in fire disturbed boreal forest ecosystems. *International Journal of Remote Sensing*, 17(15), 3037–3053.

Fuller, D. O. and Murphy, K. (2006) The ENSO-Fire dynamic in insular Southeast Asia. *Climatic Change*, 74, pp. 435-455.

Gabriel, A. K. and Goldstein, R. M. (1988) Crossed orbit interferometry: theory and experimental results from SIR-B. *International Journal on Remote sensing*, 9(5), pp. 857-872.

Gabriel, A. K., Goldstein, R. M. and Zebker, H. A. (1989) Mapping small elevation changes over large areas: differential radar interferometry. *Journal of Geophysical Research*, 94 (B7), pp. 9183-9191.

Gabriel, A. K., Goldstein, R. M. and Blom, R. G. (2001) ERS radar interferometry: Absence of recent surface deformation near the Aswan Dam. *Environmental and Engineering Geoscience*, 7(2), pp. 205-210.

Galloway, D. L., Hudnut, K. W., Ingebritsen, S. E., Phillips, S. P., Peltzer, G., Rogez, F. and Rosen, P. A. (1998) Detection of aquifer system compaction and land subsidence using interferometric synthetic aperture radar, Antelope valley, Mojave Desert, California. *Water Resources Research*, 34(10) , pp. 2573-2585.

Galloway, D. L., Jones, D. R. and Ingebritsen, S. E. (2000) Measuring land subsidence from space. *U.S. Geological Survey Fact Sheet 051–00*, pp. 4.

GAMMA Remote Sensing and Consulting AG. (2007) *GAMMA Software*. Available at: <http://www.gamma-rs.ch/nc/software/> [Cited 22 Nov 2007].

GAMMA Remote Sensing and Consulting AG. (2008a) *Interferometric SAR processor-ISP. documentation-user's guide*. Gumligen, Switzerland

GAMMA Remote Sensing and Consulting AG. (2008b) *Differential interferometry and geocoding software -DIFF and GEO. documentation-user's guide*. Gumligen, Switzerland.

-
- Gan, J. and Pan, B. (2008) Error analysis and accuracy assessment of InSAR phase unwrapping. *Proceedings of the 8th international symposium on spatial accuracy assessment in natural resources and environmental sciences*, Shanghai, China, pp. 107-113.
- Garbrecht, J. and Martz, L.W. (1999) Digital elevation model issues in water resources modelling. *Proceedings the 19th ESRI International User Conference*, Environmental Systems Research Institute, San Diego, California.
- Gatelli, F., Monti, Guarnieri, A., Parizzi, F., Pasquali, P., Prati, C. and Rocca, F. (1994) The wavenumber shift in SAR interferometry. *IEEE Transactions on Geoscience and Remote Sensing*, 32(4), pp. 855-865.
- Ge, L., Rizos, C. and Tsujii, T. (2000) Interpolation of GPS results incorporating geophysical and InSAR information. *Earth Planets Space*, 52(11), pp. 999-1002.
- Ge, L., Chang, H. C., Chen, M. H., Qin, L. and Rizos, C. (2003) Ground subsidence monitored by L-band satellite radar interferometry. *Geomatics Research Australasia*, 79, pp. 75-90.
- Gens, R. and Van Genderen, J. L. (1996) Review article SAR interferometry-issues, techniques, applications. *International Journal of Remote Sensing*, 17(10), pp. 1803-1835.
- Gens, R. (1998) *Quality assessment of SAR interferometric data*. Ph.D. Dissertation, Hanover University: Hanover, Germany.
- Gens, R. (2003) Two-dimensional phase unwrapping for radar interferometry: developments and new challenges. *International Journal of Remote Sensing*, 24(4), pp.703-710.
- Ghiglia, D. C. and Pritt, M. D. (1998) *Two-dimensional phase unwrapping: theory, algorithms and software*. pp. 493, John Wiley and Sons, New York.

Global Peatland Initiative. (2002) World Peatland Map. In Page, S., Hooijer, A., Silvius, M., and Wosten, H. (2006) Peat-CO₂: Assessment of CO₂ emissions from drained peatlands in SE Asia. *Delft Hydraulics report Q3943*.

Goldstein, R. M., Zebker, H. and Werner, C. L. (1988) Satellite radar interferometry- Two dimensional phase unwrapping, *Radio Science*, 23, pp. 713-720.

Goldstein, R. M. (1995) Atmospheric Limitations to repeat-pass interferometry. *Geophysical Research Letters*, 22(18), pp. 2517-2520.

Goldstein, R. M. and Werner, C. L. (1998) Radar interferogram filtering for geophysical applications. *Geophysical Research Letters*, 25(21), pp. 4035-4038.

Gorham, E. (1991) Northern peatlands: role in the carbon cycle and probable responses to global warming. *Ecological Applications*, 1(2), pp. 182-195.

Graham, L. C. (1974) Synthetic interferometric radar for topographic mapping. *Proceedings of the IEEE*, 62(6), pp. 763-768.

Guptill, S. C. and Morrison, J. L. (1995) *Elements of spatial data quality*. Oxford:Elsevier Science, pp. 202 .

Guritz, R., Ayers, M., Logan, T., Li, S. and Lawlor, O. (1999) Automated DEM production using ESA tandem mission data for the Caribou-Poker Creek LTER watershed, Alaska. *Fringe 99 Meeting*.

Gutmann, B. (1999) Phase unwrapping with the branch-cut method: clustering of discontinuity sources and reverse simulated annealing, *Applied Optics*, 38, pp. 5577-5793.

Hagberg, J. O. and Ulander, L. M. H. (1993) On the optimization of interferometric SAR for topographic mapping. *IEEE Transactions on Geoscience and Remote Sensing*, 31(1), pp. 303-306.

Hagberg, J. O., Ulander, M. L., and Askne, J. (1995) Repeat-pass SAR interferometry over forested terrain. *IEEE Transactions on Geoscience and Remote Sensing*, 33(2), pp. 331-340.

-
- Hanssen, R. and Feijt, A. (1996) A first quantitative evaluation of atmospheric effects on SAR interferometry. *Fringe 96 Workshop on ERS SAR Interferometry*, 30 September.-2 October, Zurich, Switzerland, pp. 277-282.
- Hanssen, R. (1998) Atmospheric heterogeneities in ERS tandem SAR interferometry. *DEOS Report No.98.1*, Delft University press: Delft, the Netherlands.
- Hanssen, R. and Klees, R. (1998a) Applications of SAR interferometry in terrestrial and atmospheric mapping. *European Microwave week*, 5-9 October, Amsterdam, The Netherlands.
- Hanssen, R. and Klees, R. (1998b) Error analysis for repeat-pass SAR interferometry: applications for deformation analysis. *Proceedings of the Symposium on Progress in Electromagnetics Research*, 13-17 July, Nantes, France.
- Hanssen, R.F. (2000) *Radar interferometry data interpretation and error analysis*. pp. 308, Kluwer Academic Publishers Press: Dordrecht, Netherlands.
- Hanssen, R. F. (2007) Radar interferometric monitoring of ground subsidence due to underground coal mining near Gardanne, France, *the work of TU-DELFT in the PSIC4 project*.
- Haris, A., Herudjito, D., Sabiham, S. and Adimidjaja, S.H. (1998) Physico-chemical properties of peat in relation with irreversible drying processes. *Kalimantan Agriculture*, 5(2), pp. 91-99.
- Haynes, M. (2007) *New Developments in Wide-Area Precision Surveying from Space*. NPA Satellite mapping Group. Available at <http://www.npagroup.co.uk/insar/whatisinsar/insar.htm> [Cited 22 Nov 2007].
- Hilland, J. E., Stuhr, F. V., Anthony, F., Imel, D., Shen, Y., Jordan, R. and Caro, E. R. (1998) Future NASA spaceborne SAR missions. *IEEE AES Systems Magazine*, 11, pp. 9-16.
- Herland, E. A. (1995) SAR interferometry with ERS-I in forested areas. *IGARSS, 10-14 July*, pp. 202-204. Firenze, Italy.

Hirano, T., Jauhiainen, J., Inoue, T. and Takahashi, H. (2009) Controls on the carbon balance of tropical peatlands. *Ecosystems*, 12, pp. 873–887.

Hoekman, D. H. (2007) Satellite radar observation of tropical peat swamp forest as a tool for hydrological modelling and environmental protection. *Aquatic Conservation: Marine and Freshwater Ecosystems*, 17, pp. 265–275.

Hofmann-Wellenhof, B., Lichtenegger, H. and Collins, J. (1999) *GPS Theory and Practice*. Springer Verlag. New York, USA.

Hooijer, A., Silvius, M., Wösten, H. and Page, S. (2006) PEAT-CO₂, assessment of CO₂ emissions from drained peatlands in SE Asia. *Delft Hydraulics report Q3943/2006*, pp. 36.

Hooijer, A., Haasnoot, M., Van Der Vat, M. and Vernimmen, R. (2008) Master plan for the conservation and development of the ex-mega rice project area in Central Kalimantan. *Technical report: peatland subsidence scenarios for the EMRP area*, Euroconsult MottMacDonald/Deltares, Jakarta/Delft.

Hooijer, A., Page, S., Jauhiainen, J., Canadell, J. G., Silvius, M., Kwadijk, J. And Wosten, H. (2010) Current and future CO₂ emissions from drained peatlands in Southeast Asia. *Biogeosciences*, 7, pp. 1505–1514.

Hooijer, A., Page, S., Jauhiainen, J. and Joosten, H. (Unpublished) The Relationship between peatland management and CO₂ exchange in tropical peatlands. Draft document for inclusion in KFCP Technical Panel methodology document.

Hoscilo, A. (2009) *Fire regime, vegetation dynamics and land cover change in tropical peatland, Indonesia*. Thesis submitted for the degree of Doctor of Philosophy at the University of Leicester.

Huang, S. and Siegert, F. (2005) ENVISAR ASAR wide swath backscatter dynamics of the Siberian boreal forest fire scar. *ESA SP-572*.

Huang, S. and Siegert, F. (2006) Backscatter change on fire scars in Siberian boreal forest in ENVISAT ASAR wide swath images. *IEEE Geoscience and remote sensing letters*, 3(2), pp. 154-158.

Hyypä, J., Hyypä, H., Inkinen, M., Engdahl, M., Linko, S. and Zhu, H. (2000) Accuracy comparison of various remote sensing data sources in the retrieval of forest stand attributes. *Forest Ecology and Management*, 128, pp. 109–120.

Ikehara, M. E., Galloway, D.L., Fielding, E., Bürgmann, R., Lewis, A. S. and Ahmadi, B. (1998) InSAR imagery reveals seasonal and longer-term land-surface elevation changes influenced by ground-water levels and fault alignment in Santa Clara Valley, California. *Transactions, American Geophysical Union*, 45, pp. F37.

Immirzi, C. P., Maltby, E. and Clymo, R. S. (1992) The global status of peatlands and their role in carbon cycling. *Report No. 11*, the Wetland Ecosystems Research Group, University of Exeter, Friends of the Earth, London.

Intergovernmental Panel on Climate Change. (2007) Agriculture in climate change 2007: mitigation. *Contribution of Working Group III to the Fourth Assessment Report of the Intergovernmental Panel on Climate Change*, Cambridge University Press.

Jarosz, A. and Shepherd, L. (2002) Is ISAR Interferometry able to detect slope deformations of open pit mines. *fringe 2003*, Curtin University, Western Australian School of Mines, Mine Surveying Program.

Jauhainen, J., Limin, S., Silvennoinen, H. and Vasander, H. (2008) Carbon dioxide and methane fluxes in drained tropical peat before and after hydrological restoration. *Ecology*, 89, pp. 3503-3514.

Jaya, A. (2005) *Study of carbon and water on tropical peatland for ecological planning*. Thesis submitted for the degree of Doctor of Philosophy at the University of Nottingham.

Jayaprasad, P., Narender, B., Pathan, S. and Ajai. (2008) Generation and validation of DEM using SAR interferometry and differential GPS supported by multispectral optical data. *Journal of the Indian Society of Remote Sensing*, 36, pp. 313-322.

Jensen, S. K. and Domingue, J. O. (1998) Extracting topographic structure from digital elevation data for geographic information system analysis. *Photogrammetric Engineering and Remote Sensing*, 54, pp. 1593–1600.

Joughin, I., Winebrenner, D., Fahnestock, M., Kwok, R., and Krabill, W. (1996) Measurement of icesheet topography using satellite-radar interferometry. *Journal of Glaciology*, 42(140), pp.10-22.

Kamaruddin, M. H., Mather, P. M. and Balzter, H. (2003) Digital Elevation Model (DEM) generation using airborne SAR interferometry (InSAR). *Proceedings 23rd EARSeL Symposium, 2-5 June*, Ghent, Belgium.

Kampes, B. (1999) *Delft object-oriented radar interferometric software user's manual*. Delft University of Technology, The Netherlands.

Kang, B. H. (2007) A review on image and video processing. *International Journal of Multimedia and Ubiquitous Engineering*, 2(2), pp. 49-63.

Kaplan, E. D. and Hegarty, C. (2006) *Understanding GPS: Principles and applications (2nd Eds.)*. pp. 379-391, Artech House, INC, Norwood, MA.

Karout, S. (2007) *Two-dimensional phase unwrapping*. Thesis submitted for the degree of Doctor of Philosophy at Liverpool John Moores University.

Kasischke, E. S., Bourgeau-Chavez, L. L., French, N. H. F., Harrel, P. A. and Christensen, N.L.Jr. (1992) Initial observations on using SAR to monitor wild fire scars in the boreal forest. *International Journal of Remote Sensing*, 13(18), pp. 3495–3501.

Kasischke, E. S., French, N. H. F., Harrel, P. A., Christensen, N. L. Jr., Ustin, S. L. and Barry, D. (1993) Monitoring wild fires in boreal forests using large area AVHRR NDVI composite image data. *Remote Sensing of Environment*, 45(1), pp. 61–71.

Kasischke, E. S., Bourgeau-Chavez, L. L. and French, N. H. F. (1994) Observations of variations in ERS-1 SAR image intensity associated with forest fires in Alaska. *IEEE Transactions on Geoscience and Remote Sensing*, 32(1), pp. 206-210

Kasischke, E., Melack, J. and Dobson, M. C. (1997) The use of imaging radars for ecological applications: a review. *Remote Sensing of Environment*, 59(2), pp. 141–156.

Klees, R. and Massonnet, D. (1999) Deformation measurements using SAR interferometry: Potential and limitations. *Geologie en Mijnbouw*, 77, pp. 161-176.

Koch, A. and Lohmann, P. (2000) Quality assessment and validation of digital surface models derived from the shuttle radar topography mission (SRTM). *IAPRS*, 33, Amsterdam.

Koch, A., Heipke, C. and Lohmann, P. (2002) Analysis of SRTM DTM methodology and practical results. *Symposium on Geospatial Theory, Processing and Applications*, Ottawa.

Koskinen, J., Pulliainen, J., Hyypaa, M., Engdahl, M. and Hallikainen, M. (2001) The seasonal behaviour of interferometric coherence in boreal forest. *IEEE Transactions on Geoscience and Remote Sensing*, 39(4), pp. 820 – 829.

Kuntz, S., Siegert, F. and Ruecker, G. (1999) ERS SAR Images for tropical rainforest and land use monitoring: change detection over five years and comparison with Radarsat and JERS SAR images. *IGARRS, IEEE Geoscience and Remote Sensing Society*, pp. 910-912, Piscataway, New Jersey, USA.

Kuntz, S. (2010) Potential of spaceborne SAR for monitoring the tropical environments. *Tropical Ecology*, 51(1), pp. 3-10.

Kwok, R. and Fahnestock, M. A. (1996) Ice sheet motion and topography from radar interferometry. *IEEE Transactions on Geoscience and Remote Sensing*, 34(1), pp. 189-200.

Urnain, A., Notohadikusumo, T., Radjagukguk, B. and Sri Hastuti. (2001) Peat soil properties related to degree of decomposition under different land use systems. *International Peat Journal*, 11, pp. 67-77

-
- Lafleur, P. M., Moore, T. R., Roulet, N. T. and Frolking, S. (2005) Ecosystem respiration in a cool temperate bog depends on peat temperature but not water table. *Ecosystems*, 8(6), pp. 619-629.
- Lambert, K. and Staelens, N. (1993) The agricultural and horticultural value of tropical peatland, a case study. *International Peat Journal*, 5, pp. 41-57.
- Langner, A. and Siegert, F. (2007) The role of fire on land cover change 2002-2005 in Borneo and the role of fire derived from MODIS imagery. *Global Change Biology*, 13, pp. 2329-2340.
- Langner, A., Miettinen, J. and Siegert, F. (2007) Land cover change 2002-2005 in Borneo and the role of fire derived from MODIS imagery. *Global Change Biology*, 13, pp. 2329-2340.
- Lee, I., Chang, H-C. and Linlin, G. L. (2005) GPS Campaigns for validation of InSAR derived DEMs. *Journal of Global Positioning Systems*, 4(1-2), pp. 82-87.
- Lee, J. S., Papathanassiou, K. P., Ainsworth, T. L., Grunes, M. R. and Reigber, A. (1998) A new technique for noise filtering of SAR interferometric phase images. *IEEE Transactions on Geoscience and Remote Sensing*, 36(5), pp. 1456-1465.
- Leica Geosystems AG. (1999) *Introduction to GPS, version 1.0*, Heerbrugg, Switzerland.
- Li, Z. (2006) A study on the applicability of repeat-pass SAR interferometry for generating DEMs over several Indian test sites. *International Journal of Remote Sensing*, 27(3), 595-616.
- Liew, S. C., Lim, O. K., Kwoh, L. K. and Lim, H. (1998) A study of the 1997 forest fires in South East Asia using SPOT quicklook mosaics. *IEEE international Geoscience and Remote Sensing Symposium*, 6-10 July, Seattle.
- Lin, Q., Vesecky, J. F. and Zebker, H. A. (1994) Phase unwrapping through fringe-line detection in synthetic aperture radar interferometry. *Applied Optics*, 33(2), pp. 201-208.

Lu, Z., Kwoun, O. and Rykhus, R. (2007) Interferometric synthetic aperture radar (InSAR): its past, present and future. *Photogrammetric Engineering and Remote Sensing*, 73, pp. 217-221.

Lu, Z., Mann, D., and Freymueller, J., 1998. Satellite radar interferometry measures deformation at Okmok volcano. *Eos, Transactions of the American Geophysical Union*, 79, 461–468.

Luckman, A., Baker, J., Honsak, M. and Lucas, R. (1998) Tropical forest biomass estimation using JERS-1 SAR: seasonal variation, confidence limits, and application to image mosaics. *Remote Sensing of Environment*, 63(2), 126– 139.

Ludang, Y., Jaya, A. and Inoue, T. (2007) Geohydrological conditions of the developed peatland in Central Kalimantan. *World Applied Sciences Journal*, 2(3), pp. 198-203.

Ludwig, R. and Schneider, P. (2006) Validation of digital elevation models from SRTM XSAR for applications in hydrologic modelling. *ISPRS Journal of Photogrammetry and Remote Sensing*, 60(5), pp. 339–358.

Madsen, S. N., Zebker, H. A. and Martin, J. M. (1993) Topographic mapping using radar interferometry: Processing techniques. *IEEE Transactions on Geoscience and Remote Sensing*, 31(1), pp. 246-255.

Madsen, S. N. and Rosen, P. A. (1993) Processing Techniques for Topographic Mapping Using Interferometric SAR. *Proceedings of the Interferometric SAR Technology and Applications Symposium*, Fort Belvoir, Fairfax, Virginia, USA, pp. 159-178.

Madsen, S. N., Martin, J. M. and Zebker, H. A. (1995) Analysis and evaluation of the NASA/JPL TOPSAR across-track interferometric SAR system. *IEEE Transactions on Geoscience and Remote Sensing*, 33(2), 383-391.

Mäkiranta, P., Hytönen, J., Aro, L., Maljanen, M., Pihlatie, M., Potila, H., Shurpali, N. J., Laine, J., Lohila, A., Martikainen, P. J. and Minkkinen, K. (2007) Soil greenhouse gas emissions from afforested organic soil croplands and cutaway peatlands. *Boreal Environment Research*, 12, pp.159–175.

Mäkiranta, P., Laiho, R., Fritze, H., Hytönen, J., Laine, J. and Minkkinen, K. (2009) Indirect regulation of heterotrophic peat soil respiration by water level via microbial community structure and temperature sensitivity. *Soil Biology and Biochemistry*, **41**, pp. 695–703.

Martz, L. and Garbrecht, J. (1992) Numerical definition of drainage network and subcatchment areas from Digital Elevation Models. *Computers and Geosciences*, 18(6), 747–761.

Massonnet, D., Rossi, M., Carmona, C., Adragna, F., Peltzer, G., Feigl, K. and Rabaute, T. (1993) The displacement field of the Landers earthquake mapped by radar interferometry. *Nature*, 364, pp. 138–142.

Massonnet, D., Feigl, K., Rossi, M. and Adragna, F. (1994) Radar interferometry mapping of deformation in the year after the Landers earthquake. *Nature*, 369, pp. 227–230.

Massonnet, D., Briole, P. and Arnaud, A. (1995) Deflation of Mount Etna monitored by spaceborne radar interferometry. *Nature*, 375, pp. 567–570.

Massonnet, D., Vadon, H. and Rossi, M. (1996) Reduction of the need for phase unwrapping in radar interferometry. *IEEE Transactions on Geoscience and Remote Sensing*, 34(2), pp. 489–497.

Massonnet, D., Holzer, T. and Vadon, H. (1997) Land subsidence caused by the East Mesa geothermal field, California, observed using SAR interferometry, *Geophysical Research Letters*, 24(8), pp. 901–904.

Massonnet, D. and Feigl, K. (1998) Radar interferometry and its application to changes in the earth's surface. *Reviews of Geophysics*, 36(4), 441–500.

Maltby, E. and Immirzi, C. P. (1993) Carbon dynamics in peatlands and other wetland soils, regional and global perspective. *Chemosphere*, 27(6), pp. 999-1023.

Melling, L., Hatano, R. and Goh, K. J. (2005) Soil CO₂ flux from three ecosystems in tropical peatland of Sarawak, Malaysia. *Tellus B*, 57, pp. 1–11.

Mendes, V. B., Collins, J. P. and Langley, R. B. (1995) The effect of tropospheric propagation delay errors in airborne GPS precision positioning. *ION GPS-95*, 8th International Technical Meeting of the Satellite Division of the Institute of Navigation, Palm Springs, USA.

Michalek, J. L., French, N. H. F., Kasischke, E. S., Johnson, R. D. and Colwell, J. E. (2000) Using Landsat TM data to estimate carbon release from burned biomass in an Alaskan spruce forest complex. *International Journal of Remote Sensing*, 21(2), pp. 323–338.

Milton, J. S and Arnold, J. C. (1995) *Introduction to Probability and Statistics*, 3rd ed. McGraw-Hill, New York, USA.

MIMAS. (2007) *Introduction to the ERS programme*. The University of Manchester. Available at <http://www.mimas.ac.uk/spatial/satellite/ers/introduction.html> [Cited 22 November 2007].

Moeremans, B. and Dautrebande, S. (1999) The use of ERS SAR interferometric coherence and PRI images to evaluate crop height and soil moisture. *Fringe 99*, ESA SP-478.

NASA. (1994) SAR Interferometry and surface change detection. *Report of a Workshop Held in Boulder, Colorado : February 3-4*, Jet Propulsion Laboratory, California institute of technology.

Page, S. E., Rieley, J. O., Shotyk, W. and Weiss, D. (1999) Interdependence of peat and vegetation in a tropical peat swamp forest. *Philosophical Transactions of the Royal Society*, 354, pp. 1885-1897, The Royal Society, London.

-
- Page, S. E., Rieley, J. O., Böhm, H-D. V., Siegert, F. and Muhamad, N. (2000) Impact of the 1997 fires on the peatlands of Central Kalimantan, Indonesia. *Proceedings of the 11th International Peat Congress*, Quebec, Canada, pp. 962-970.
- Page, S. E., Siegert, F., Rieley, J. O., Boehm, H-D.V., Jaya, A. and Limin, S. (2002) The amount of carbon released from peat and forest fires in Indonesia during 1997. *Nature*, 420, pp. 61-65.
- Page, S. E., Wüst, R. A., Weiss, D., Rieley, J. O., Shotyk, W. and Limin, S. (2004) A record of Late Pleistocene and Holocene carbon accumulation and climate change from an equatorial peat bog (Kalimantan, Indonesia): implications for past, present and future carbon dynamics. *Journal of Quaternary Science*, 19(7), pp. 625–635.
- Page, S. E., Rieley, J. O. and Wüst, R. (2006) Lowland tropical peatlands of Southeast Asia. *Developments in Earth Surface Processes*, 9, pp. 145-172.
- Page, S. E., Hoscilo, A., Langner, A., Tansey, K. J., Siegert, F., Limin, S. and Rieley, J. O. (2009) Chapter 9: Tropical peatland fires in Southeast Asia. In: Cochrane, M. A. (ed) *Tropical fire ecology: climate change, land use and ecosystem dynamics*. Springer-Praxis, Heidelberg, Germany.
- Pedersen, R. and Sigmundsson, F. (2006) Temporal development of the 1999 intrusive episode in the Eyjafjallajökull volcano, Iceland, derived from InSAR images. *Bull. Volcanol*, 68, pp. 377-393.
- Pepe, A., Sansosti, E., Berardino, P. and Lanari, R. (2005) On the Generation of ERS/ENVISAT DInSAR time-series via the SBAS technique. *IEEE Transactions on Geoscience and Remote Sensing Letters*, 2(3), pp. 265–269.
- Prati, C. and Rocca, F. (1990) Limits to the resolution of elevation maps from stereo SAR images. *International Journal of Remote Sensing*, 11(12), pp. 2215-223.
- Prati C. and Rocca, F. (1994) *Process for generating synthetic aperture radar interferograms*. United States Patent, Number 5,332,999.

Prats, P., Reigber, A., Mallorquoi, J. J., Scheiber, R. and Moreira, A. (2008) Estimation of the temporal evolution of the deformation using airborne differential SAR interferometry. *IEEE Transactions on Geoscience and Remote Sensing*, 46(4), pp. 1065–1078.

Price, J. S. and Schlotzhauer, S. M. (1999) Importance of shrinkage and compression in determining water storage changes in peat: the case of a mined peatland. *Hydrological Processes*, 13(16), pp. 2591 – 2601.

Rabus, B., Eineder, M., Roth, A. and Bamler, R. (2003) The shuttle radar topography mission; A new class of digital elevation models acquired by spaceborne radar. *ISPRS Journal of Photogrammetry and Remote Sensing*, 57, pp. 241–262.

Radjagukguk, B. (2000) Changes in the physical and chemical characteristics of peat soil with peatland reclamation for agriculture. *Journal of Soil Science and Environment*, 2(1), pp. 1-15.

Ranson, K. J., Sun, G. Q., Lang, R. H., Chauhan, N. S., Cacciola, R. J. and Kilic, O. (1997) Mapping of boreal forest biomass from spaceborne Synthetic Aperture Radar. *Journal of Geophysical Research-Atmospheres*, 102(D24), pp. 29599-29610.

Ranson, K. J., Kovacs, K., Sun, G. and Kharuk, V. I. (2003) Disturbance recognition in the boreal forest using radar and Landsat-7. *Canadian Journal of Remote Sensing*, 29(2), pp. 271–285.

Rieley, J. O. and Ahmad-Shah, A. (1996) The vegetation of tropical peat swamp forests. In: Maltby, E., Immerzi, C.P., Safford, R.J. (eds.) *The integrated planning and management of tropical lowland peatlands*, pp. 55-74, IUCN, Gland.

Rieley, J. O., Page, S. E., Setiadi, B. (1996) Distribution of peatlands in Indonesia. In: Lappalainen, E. (ed.): *Global peat resources*, International Peat Society, Jyväskylä, pp. 169-178.

Rieley, J. O. and Page, S. E. (2005) *Wise use of tropical peatlands: focus on Southeast Asia*. ALTEERRA, Wageningen, The Netherlands.

-
- Rieley, J., Wust, R. A. J., Jauhiainen, J., Page, S. E., Wosten, H., Hooijer, A., Siegert, F., Limin, S., Vasander, H. and Stahlhut, M. (2008) Tropical peatlands: carbon stores, carbon gas emissions and contribution to climate change processes. *Peatlands and Climate Change; 13th International Peat Congress*, Tullamore, Ireland 8-13 June, pp. 1-30.
- Rignot, E. J., Jezek, K. C., and Sohn, H. G. (1995) Ice flow dynamics of the Greenland ice sheet from SAR interferometry. *Geophysical research letters*, 22(5), 575-578.
- Richardson, J. L. and Vepraskas, M. J. (2000) *Wetland Soils: genesis, hydrology, landscapes, and classification*. Lewis Scientific Publ, Boca Raton, Florida, USA.
- Rocca, F., Prati, C. and Ferretti, A. (1997) Overview of SAR interferometry. *3rd ERS Symposium*, 14–21 March, Florence, Italy.
- Rodriguez, E. and Martin, J. M. (1992) Theory and design of interferometric synthetic-aperture radars. *IEEE Proceedings-F*, 139(2), pp. 147–59.
- Rosen, P. A., Werner, C. L. and Hiramatsu, A. (1994) Two-dimensional phase unwrapping of SAR interferograms by charge connection through neutral trees. *1994 IEEE International Geoscience and Remote Sensing Symposium*, California Institute of Technology, Pasadena, California, USA.
- Rosen, P. A., Hensley, S., Zebker, H. A., Webb, F. H. and Fielding, E. (1996) Surface deformation and coherence measurements of Kilauea volcano, Hawaii, from SIR-C radar interferometry. *Journal of Geophysical Research*, 101(10), pp. 23109–23125.
- Rosen, P., Hensley, S., Joughin, I., Li, F., Madsen, S., Rodriguez, E. and Goldstein, R. (2000) Synthetic aperture radar interferometry. *Proceedings of the IEEE*, 88(3), pp. 333–379.
- Rufino, G., Moccia, A. and Esposito, S. (1998) DEM generation by means of ERS tandem data. *IEEE Transactions on Geoscience and Remote Sensing*, 36(6), pp. 1905-1912.
- Sajarwan, A., Notohadiprawiro, T., Radjagukguk, B., Hastuti, S. (2002) Diversity of tropical peat characteristics in intact peatland forest, under the influence of forest type,

peat thickness, and the position of the peat deposit. In: Rieley, J.O., Page, S.E., Setiadi, B. (eds.): Peatlands for people - natural resource function and sustainable development, *Proceedings of the International Symposium on Tropical Peatlands, 22–23 August, 2002*, Jakarta, Indonesia. BPPT and Indonesian Peat Association, pp. 119-124.

Santoro, M., Wegmüller, U. and Askne, I. H. (2010) Signatures of ERS-Envista interferometric SAR coherence and phase of short vegetation: An analysis in the case of Maize fields. *IEEE Transactions on Geoscience and Remote Sensing*, 48(4), pp. 1702-1713.

Sarabandi, K. and Wilsen, C. B. (2000) Temporal decorrelation of vegetation by environmental and seasonal effects. *IGARSS*, 4, pp. 1399- 1401. Honolulu, Hawaii, USA.

Schmullius, C., Holz, A. and Zimmermann, R. (1998) SIBERIA-first ERS tandem results from the IGBP boreal forest transect. *IGARSS*, 4, pp. 1815- 1817. Seattle, USA.

Schothorst, C. J. (1977) Subsidence of low moor peat in the western Netherlands. *Geoderma*, 17, pp. 265–291.

Seeber, G. (2003) *Satellite Geodesy: Foundations, Methods and Applications*. Walter De Gruyter, Berlin and New York.

Sieffermann, R. G., Fournier, M., Truitomo, S., Sadelman, M. T. and Semah, A. M. (1988) Velocity of tropical peat accumulation in central Kalimantan, Borneo. *International Peat Society*, 1, pp. 90–98.

Siegert, F. and Kuntz, S. (1996) Multitemporal evaluation of ERS-SAR Data for monitoring deforestation in tropical rain forests. *Proceedings of the second ERS 1/2 applications workshop*, London, ESA SP-383, Frascati.

Siegert, F. and Kuntz, S. (1999) Monitoring of deforestation and land use in Indonesia with multitemporal ERS data. *International journal of Remote Sensing*, 20(14), pp. 2835- 2853.

Siegert, F. and Ruecker, G. (2000) Use of multitemporal ERS-2 SAR images for identification of burned scars in south-east Asian tropical rain forest. *International Journal of Remote Sensing*, 21(4), pp. 831 – 837.

Siegert, F., Ruecker, G., Hindrichs, A., Hoffman, A. A. (2001) Increased damage from fires in logged forests during droughts caused by El Nino. *Nature*, 414, pp.437-440.

Smith, G., Dammert, P. B. G., Santoro, M., Fransson, J. E. S., Wegmüller, U. and Askne, J. (1998) Biomass retrieval in boreal forest using ERS and JERS SAR. *2nd International Workshop on Retrieval of Bio- and Geophysical Parameters from SAR data for Land Applications*, pp. 293–300, Noordwijk, The Netherlands.

Smith, G. and Askne, J. (2001) Clear-cut detection using ERS interferometry. *International Journal of Remote Sensing*, 22(18), pp. 3651–3664.

Stebler, O., Pasquali, P., Small, D., Holecz, F. and Nüesch, D. (1996) Analysis of ERS-SAR tandem time-series using coherence and backscattering coefficient. *ESA FRINGE Workshop*, Zurich.

Stephens, J. C., Allen, L. H., Jr. and Chew, E. (1984) Organic soil, subsidence. *American Geological Society Reviews in Engineering Geology*, 1, pp. 107-122.

Strozzi, T., Wegmüller, U., Luckman, A. J. and Balzter, H. (1999) Mapping deforestation in Amazon with ERS SAR interferometry. *IGARSS*, 28 June- 2 July, Hamburg.

Strozzi, T., Dammert, P. B. G., Wegmüller, U., Martinez, J. M., Askne, J. I. H., Beaudin, A. and Hallikainen, M. (2000) Land use mapping with ERS SAR interferometry. *IEEE Transactions on Geoscience and Remote Sensing*, 38, pp. 766–775.

Strozzi, T., Wegmüller, U., Tosi, L., Bitelli, G. and Spreckels, V. (2001) Land subsidence monitoring with differential SAR interferometry. *Photogrammetric engineering and remote sensing*, 67(11), pp. 1261-1270.

Tansey, K., Luckman, A. and Schmullius, C. (1999) Mapping boreal forest in Siberia with ERS SAR interferometry. *Proceedings of the 25th Annual Conference of the Remote Sensing Society (RSS 99)*, 8-10 September, Cardiff, Wales, UK.

Tansey, K., Luckman, A., Skinner, L., Balzter, H., Strozzi, T. and Wagner, W. (2004) Classification of forest volume resources using ERS tandem coherence and JERS intensity data. *International Journal of Remote Sensing*, 25, pp. 751-768.

Tansey, K., Beston, J., Hoscilo, A., Page, S. E. and Paredes Hernández, C. U. (2008) The relationship between MODIS fire hotspot count and burned area in a degraded tropical peat swamp forest in Central Kalimantan, Indonesia. *Journal of Geophysical Research-Atmospheres*, 113, pp. 1-8.

Tarayre, H. and Massonnet, D. (1996) Atmospheric propagation heterogeneities revealed by ERS-1. *Geophysical Research Letters*, 23(9), pp. 989-992.

The World FactBook, 1995. *Indonesia. central intelligence agency (CIA)*. Available at <https://www.cia.gov/library/publications/the-world-factbook/geos/id.html> [Cited 22 November 2007].

Thiel, C., Drezet, P., Weise, E., Quegan, S. and Schmullius, C. (2006) Radar remote sensing for the delineation of forest cover maps and the detection of deforestation. *International Journal of Forest Research*, 79(5), pp. 589-597.

Thiel, C. J., Thiel, C. and Schmullius, C. C. (2009) Operational large-area forest monitoring in Siberia using ALOS PALSAR summer intensities and winter coherence. *Transactions on Geoscience and Remote Sensing*, 47(12), pp. 3993-4000.

Thompson, A.R., Moran, J. M. and Swenson, G. W. (1986) *Interferometry and synthesis in radio astronomy*. Wiley Interscience, New York.

Tsay, J. R. and Lu, H. C. (2001) Quality analysis on height displacement values determined by three-pass method and some test results in urban area in Taiwan. *Proceedings of 22nd Asian Conference on Remote Sensing*, 5-9 November, Singapore, 2, pp. 977-982.

Tsay, J. R. and Chen, H. H. (2001) DEM generation in Taiwan by using InSAR and ERS data. *Proceedings of 22nd Asian Conference on Remote Sensing*, 5-9 November, Singapore, 2, pp. 1061-1066.

Ulaby, F. T., Moore, R. K. and Fung, A. K. (1986) *The backscattering behavior of random surface, microwave remote sensing: active and passive: from theory to application*. pp. 1811-1830, Artech House, Dedham.

Uryu, Y., Mott, C., Foad, N., Yulianto, K., Budiman, A., Setiabudi, Takakai, F., Nursamsu, Sunarto, Fadhli, N., Hutajulu, C. M. B., Jaenicke, J., Hatano, R., Siegert, F. and Stuwe, M. (2008) Deforestation forest degradation, biodiversity loss and CO₂ emission in Riau, Sumarta, Indonesia. *WWWF Indonesia technical report*, Jakarta, Indonesia.

U.S. Geological Survey. (1997) Standards for digital elevation models: part 3–quality control, National mapping programme. *Technical instruction, National Mapping Division*.

U.S. Geological Survey. (1998) SUSGS geospatial data clearinghouse, national mapping and remotely sensed data: digital elevation models (DEMs). *Technical instruction, National Mapping Division*.

Vadon, H. and Sigmundsson, F. (1997) Crustal deformation from 1992 to 1995 at the Mid- Atlantic ridge, southwest Iceland, mapped by satellite radar interferometry. *Science*, 275(5), pp. 193–197.

Wagner, W., Luckman, A., Vietmeier, J., Tansey, K., Balzter, H., Schmullius, C., Davidson, M., Gaveau, D., Gluck, M., Le Toan, T., Quegan, S., Shvidenko, A., Wiesmann, A. and Yu, J. J. (2003) Large-scale mapping of boreal forest in SIBERIA using ERS tandem coherence and JERS backscatter data. *Remote Sensing of Environment*, 85, pp. 125-144.

Walker, A., Muller, J. P., Morley, J. G. Smith, A. and Naden, P. (2000) Multi-pass interferometric SAR DEMs for hydrological network derivation. *Proceedings of the 2nd International Workshop on ERS SAR Interferometry on "Advancing ERS SAR*

Interferometry from Applications towards Operations. Palais des Congrès: Liège, Belgium.

Waring, R., Way, J. B., Hunt, R., Morrissey, L., Ranson, J., Weishampel, J., Oren, R. and Franklin, S. (1995) Remote sensing with synthetic aperture radar in ecosystem studies. *Bioscience*, 45(10), pp. 715–723.

Warren, M., Sowter, A. and Bingley, R. (2006) A DEM-free approach to persistent point scatterer interferometry. *3rd IAG / 12th FIG Symposium*, 22-24 May, Baden.

Wegmüller, U. and Werner, C. L. (1995) SAR interferometric signature of forest. *IEEE Transactions on Geoscience and Remote Sensing*, 33(5), pp. 1153–1161.

Wegmüller, U., Werner, C. L., Nuesch, D. and Borgeaud, M. (1995) Forest mapping using ERS repeat-pass SAR interferometry. *ESA Earth Observation*, Q 49, pp. 4–7.

Wegmüller, U. and Werner, C. (1997a) Retrieval of vegetation parameters with SAR interferometry. *IEEE Transactions on Geoscience and Remote Sensing*, 35(1), pp. 18–24.

Wegmüller, U. and Werner, C. (1997b) GAMMA SAR processor and interferometry software. *3rd ERS Symposium on Space at the service of our Environment*, 14-21 March, Florence, Italy.

Wegmüller, U., Werner, C. and Strozzi, T. (1998) SAR interferometric and differential interferometric processing chain. *IGARRS*, pp. 1106-1108, Seattle, USA.

Wegmüller, U., Strozzi, T. and Bitelli, G. (1999) Validation of ERS differential SAR interferometry for land subsidence mapping: the Bologna case study. *IGARRS*, 2, pp. 1131 – 1133.

Wegmüller, U., Spreckels, V., Werner, C., Strozzi, T. and Wiesmann, A. (2005) Monitoring of mining induced surface deformation using L-band SAR interferometry. *IGARSS*, 3, pp. 2165-2168.

-
- Wells, D. E., Beck, N., Delikaraoglou, D., Kleusberg, E. Krakiwsky, J., Lachapelle, G., Langley, R. B., Nakiboglu, M., Schwarz, K. P. Tranquilla, J. M. and Vanicek, P.(1986) *Guide to GPS positioning*. Canadian GPS Associates, Fredericton.
- Werner, C. L., Hensley, S., Goldstein, R. M., Rosen, P. A. and Zebker, H. A. (1993) Techniques and applications of SAR interferometry for ERS-1: topographic mapping, change detection and slope measurement. *First ERS-1 Symposium*, 4-6 November, Cannes, France, *ESA SP-359*, pp. 205-210.
- Werner, C. L. and Wegmüller, U. (1995) SAR interferometric signatures of forest. *IEEE Transactions on Geoscience and Remote Sensing*, 33, pp. 1153– 1161.
- Werner, C., Wiesmann, A., Siegert, F. and Kuntz, S. (2000) JERS InSAR DEM generation for Borneo. *IGARSS*, 24-28 July, Honolulu, USA.
- Weydahl, D. J. (2001) Analysis of ERS SAR coherence images acquired over vegetated areas and urban features. *International Journal of Remote Sensing*, 22, pp. 2811-2830.
- Wösten, J. M., Ismail, A. B. and van Wijk, A. M. (1997) Peat subsidence and its practical implications: a case study in Malaysia. *Geoderma*, 78, pp. 25-36.
- Wösten, J. M. and Ritzema, H. P. (2001) Land and water management options for peatland development in Sarawak, Malaysia. *International Peat Journal*, 11, pp. 59–66.
- Wösten, H., Rieley, J. and Ritzema, H. (2010) Assessment of risks and vulnerabilities of tropical peatland carbon pools: mitigation and restoration strategies. *CARBOPEAT technical report 3*. University of Leicester and CARBOPEAT partners.
- Wösten, J. H. M., Clymans, E., Page, S. E., Rieley, J. O. and Limin, S. H. (2008) Peat-water interrelationships in a tropical peatland ecosystem in Southeast Asia. *Catena*, 73, pp. 212-224.
- Zebker, H. A. and Goldstein, R. M. (1986) Topographic mapping from interferometric SAR observations. *Journal of Geophysical Research, Solid Earth*, 91(B5), pp. 4993-4999.

Zebker, H. A. and Villasenor, J. (1992) Decorrelation in interferometric radar echoes. *IEEE Transactions on Geoscience and Remote Sensing*, 30(5), pp. 950-959.

Zebker, H. A., Madsen, S. N., Martin, J., Wheeler, K. B., Miller, T., Lou, Y., Alberti, G., Vettorella, S. and Cucci, A. (1992) The TOPSAR interferometric radar topographic mapping instrument. *IEEE Transactions on Geoscience and Remote Sensing*, 30(5), pp. 933–940.

Zebker, H.A., Werner, C. L., Rosen, P. A. and Hensley, S. (1994a) Accuracy of topographic maps derived from ERS-1 radar interferometry. *IEEE Transactions on Geoscience and Remote Sensing*, 32(4), pp. 823-836.

Zebker, H. A., Rosen, P. A., Goldstein, R. M., Gabriel, A. and Werner, C. L. (1994b) On the derivation of coseismic displacement fields using differential radar interferometry: the Landers earthquake. *Journal of Geophysical Research*, 99(B10), pp. 19617–34.

Zebker, H. A., Rosen, P. A., Hensley, S. and Mougini-Mark, P. J. (1996) Analysis of active lava flows on Kilauea volcano, Hawaii, using SIR-C radar correlation measurements. *Geology*, 24(6), pp. 495-498.

Zebker, H. A., Rosen, P. and Earth, J. (1997) Atmospheric artifacts in interferometric SAR surface deformation and topographic maps. *Journal of Geophysical Research, Solid Earth*, 102(B4), pp. 7547–7563.

Zebker, H. A. and Lu, Y. (1998) Phase unwrapping algorithms for radar interferometry: residue-cut, least-squares, and synthesis algorithms. *The Journal of the Optical Society of America A*, 15(3), pp. 586-598.

Zou, W; Li, Y; Li, Z and Ding, X. (2009) Improvement of the accuracy of InSAR image co-registration based on tie points – a review. *Sensors*, 9, pp. 1259-1281.

Appendices

Appendices 1 *Gamma interferometric SAR Processor (ISP) script: intensity method*

```
#!/bin/csh -fe

if ($#argv < 2) then
  echo " "
  echo "**** Process Indonesia ERS SAR DATA ****"
  echo "**** Copyright 2004, Gamma Remote Sensing, v1.4 18-May-2004 ts/uw/clw
****"
  echo " "
  echo "run_ISP_indonesia : To run interferometric processing sequence for Indonesia"
  echo "          and estimate the heights (DEM)."
```

1.1 Prepare slc data and processing parameter files

```
if (0) then
  if (-e "$1.slc.par") rm -f $1.slc.par
  par_ESA_ERS ../$1/LEA_01.001 $1.slc.par ../$1/DAT_01.001 $1.slc
  if (-e "$2.slc.par") rm -f $2.slc.par
  par_ESA_ERS ../$2/LEA_01.001 $2.slc.par ../$2/DAT_01.001 $2.slc
endif
```

1.2 Offset estimation of the slc images

```
if (0) then # Note to flag the method to either 1 (intensity) or 2 (fringe)
  if (-e "$1\_2.off") rm -f $1\_2.off
  create_offset $1.slc.par $2.slc.par $1\_2.off 1 2 10
```

```
###Correlation SNR threshold(default: 7.000),2 10 :multi look
```

```

#init_offset $1.slz $2.slz $1.slz.par $2.slz.par $1\_ $2.off 2 10
# For 19960325_3645_19960326_3645. all fram 3.
#init_offset $1.slz $2.slz $1.slz.par $2.slz.par $1\_ $2.off 1 1
#init_offset_orbit $1.slz.par $2.slz.par $1\_ $2.off
endif

```

NOTE!!!! To be used when using option 1 in create_offset above (intensity)

```

if (0) then
  if (-e "$1\_ $2.off ") rm -f $1\_ $2.off
  if (-e "$1\_ $2.snr ") rm -f $1\_ $2.snr
  if (-e "$1\_ $2.offsets ") rm -f $1\_ $2.offsets
  if (-e "$1\_ $2.coffs ") rm -f $1\_ $2.coffs
  if (-e "$1\_ $2.coffsets ") rm -f $1\_ $2.coffsets
  offset_pwr $1.slz $2.slz $1.slz.par $2.slz.par $1\_ $2.off $1\_ $2.off $1\_ $2.snr - -
  $1\_ $2.offsets 1 - - 7.0
  offset_fit $1\_ $2.off $1\_ $2.snr $1\_ $2.off $1\_ $2.coff $1\_ $2.coffsets - 4 0
endif

```

```

if (0) then
  if (-e "$1.mli") rm -f $1.mli
  if (-e "$1.mli.par") rm -f $1.mli.par
  multi_look $1.slz $1.slz.par $1.mli $1.mli.par 2 10
  if (-e "$2.mli") rm -f $2.mli
  if (-e "$2.mli.par") rm -f $2.mli.par
  multi_look $2.slz $2.slz.par $2.mli $2.mli.par 2 10
endif

```

```

if (0) then
  if (-e "$1.mli.bmp") rm -f $1.mli.bmp
  if (-e "$2.mli.bmp") rm -f $2.mli.bmp
  raspwr $1.mli $interf_width 1 0 1 1 1.0 0.35 $flipping $1.mli.bmp
  raspwr $2.mli $interf_width 1 0 1 1 1.0 0.35 $flipping $2.mli.bmp
endif

```

1.3 Compute interferogram with 2x10 multilooks

```

if (0) then
  if (-e "$1\_ $2.int ") rm -f $1\_ $2.int
  if (-e "$1.pwr ") rm -f $1.pwr
  if (-e "$2.pwr ") rm -f $2.pwr
  interf_SLC $1.slz $2.slz $1.slz.par $2.slz.par $1\_ $2.off $1.pwr $2.pwr $1\_ $2.int 2 10
endif

```

*# Before implementation, need to edit \$interf_width variable above: Look in the file
#*.off file under parameter 'interferogram width'*

```

if (0) then
  if (-e "$1\_ $2.mag_phase.bmp") rm -f $1\_ $2.mag_phase.bmp

```

```

rasmph $1\_ $2.int $interf_width 1 0 1 1 1. 0.35 $flipping $1\_ $2.mag_phase.bmp
if (-e "$1\_ $2.mag_phase_pwr.bmp") rm -f $1\_ $2.mag_phase_pwr.bmp
rasmph_pwr $1\_ $2.int $1.pwr $interf_width 1 1 0 1 1 1.0 0.35 $flipping
$1\_ $2.mag_phase_pwr.bmp
if (-e "$1.pwr.bmp") rm -f $1.pwr.bmp
if (-e "$2.pwr.bmp") rm -f $2.pwr.bmp
raspwr $1.pwr $interf_width 1 0 1 1 1.0 0.35 $flipping $1.pwr.bmp
raspwr $2.pwr $interf_width 1 0 1 1 1.0 0.35 $flipping $2.pwr.bmp
endif

```

1.4 Initial baseline estimation

```

if (0) then # generate baseline file (first remove an eventual first estimate)
if (-e "$1\_ $2.base") rm -f $1\_ $2.base
base_init $1.slc.par $2.slc.par $1\_ $2.off $1\_ $2.int $1\_ $2.base 2 1024 1024
endif

```

1.5 Curved Earth phase trend removal ("flattening") and filter

```

if (0) then
if (-e "$1\_ $2.flt") rm -f $1\_ $2.flt
ph_slope_base $1\_ $2.int $1.slc.par $1\_ $2.off $1\_ $2.base $1\_ $2.flt
if (-e "$1\_ $2.flt_mag_phase.bmp") rm -f $1\_ $2.flt_mag_phase.bmp
rasmph $1\_ $2.flt $interf_width 1 0 1 1 1. 0.35 $flipping $1\_ $2.flt_mag_phase.bmp
if (-e "$1\_ $2.flt_mag_phase_pwr.bmp") rm -f $1\_ $2.flt_mag_phase_pwr.bmp
rasmph_pwr $1\_ $2.flt $1.pwr $interf_width 1 1 0 1 1 1.0 0.35 $flipping
$1\_ $2.flt_mag_phase_pwr.bmp
endif

```

1.6 Coherence estimation and generation of Bitmaps

```

#if (0) then # Coherence estimation and generation of Bitmaps
# if (-e "$1\_ $2.cc") rm -f $1\_ $2.cc
# cc_wave $1\_ $2.flt $1.pwr $2.pwr $1\_ $2.cc $interf_width
# if (-e "$1\_ $2.cc.bmp") rm -f $1\_ $2.cc.bmp
# ras_linear $1\_ $2.cc $interf_width 1 0 1 1 0.0 1.0 -1 $1\_ $2.cc.bmp
# if (-e "$1\_ $2.cc_pwr.bmp") rm -f $1\_ $2.cc_pwr.bmp
# rascc $1\_ $2.cc $1.pwr $interf_width 1 1 0 1 1 0.1 0.9 1.0 0.35 $flipping
$1\_ $2.cc_pwr.bmp
# endif

```

```

if (0) then # Coherence estimation and generation of Bitmaps
if (-e "$1\_ $2.cc") rm -f $1\_ $2.cc
if (-e "$1\_ $2.cc_t") rm -f $1\_ $2.cc_t ### 1: triangular
if (-e "$1\_ $2.cc_g") rm -f $1\_ $2.cc_g ### 2: gaussian
if (-e "$1\_ $2.cc_f") rm -f $1\_ $2.cc_f ###3: none (phase only)
if (-e "$1\_ $2.cc_7_7") rm -f $1\_ $2.cc_7_7
if (-e "$1\_ $2.cc_3_3") rm -f $1\_ $2.cc_3_3
if (-e "$1\_ $2.cc_9_9") rm -f $1\_ $2.cc_9_9
cc_wave $1\_ $2.flt $1.mli $2.mli $1\_ $2.cc $interf_width ##5 x 5

```

```

cc_wave $1\_ $2.flr $1.mli $2.mli $1\_ $2.cc_7_7 $interf_width 7.0 7.0 0.0
cc_wave $1\_ $2.flr $1.mli $2.mli $1\_ $2.cc_3_3 $interf_width 3.0 3.0 0.0
cc_wave $1\_ $2.flr $1.mli $2.mli $1\_ $2.cc_9_9 $interf_width 9.0 9.0 0.0
cc_wave $1\_ $2.flr $1.mli $2.mli $1\_ $2.cc $interf_width
cc_wave $1\_ $2.flr $1.mli $2.mli $1\_ $2.cc_t $interf_width 5.0 5.0 1.0
cc_wave $1\_ $2.flr $1.mli $2.mli $1\_ $2.cc_g $interf_width 5.0 5.0 2.0
cc_wave $1\_ $2.flr $1.mli $2.mli $1\_ $2.cc_f $interf_width 5.0 5.0 3.0
if (-e "$1\_ $2.cc_7_7.bmp") rm -f $1\_ $2.cc_7_7.bmp
if (-e "$1\_ $2.cc_3_3.bmp") rm -f $1\_ $2.cc_3_3.bmp
if (-e "$1\_ $2.cc.bmp") rm -f $1\_ $2.cc.bmp
if (-e "$1\_ $2.cc_9_9.bmp") rm -f $1\_ $2.cc_9_9.bmp
if (-e "$1\_ $2.cc_t.bmp") rm -f $1\_ $2.cc_t.bmp
if (-e "$1\_ $2.cc_g.bmp") rm -f $1\_ $2.cc_g.bmp
if (-e "$1\_ $2.cc_f.bmp") rm -f $1\_ $2.cc_f.bmp
ras_linear $1\_ $2.cc $interf_width 1 0 1 1 0.0 1.0 -1 $1\_ $2.cc.bmp
ras_linear $1\_ $2.cc_7_7 $interf_width 1 0 1 1 0.0 1.0 -1 $1\_ $2.cc_7_7.bmp
ras_linear $1\_ $2.cc_3_3 $interf_width 1 0 1 1 0.0 1.0 -1 $1\_ $2.cc_3_3.bmp
ras_linear $1\_ $2.cc_9_9 $interf_width 1 0 1 1 0.0 1.0 -1 $1\_ $2.cc_9_9.bmp
ras_linear $1\_ $2.cc_t $interf_width 1 0 1 1 0.0 1.0 -1 $1\_ $2.cc_t.bmp
ras_linear $1\_ $2.cc_g $interf_width 1 0 1 1 0.0 1.0 -1 $1\_ $2.cc_g.bmp
ras_linear $1\_ $2.cc_f $interf_width 1 0 1 1 0.0 1.0 -1 $1\_ $2.cc_f.bmp
if (-e "$1\_ $2.cc_7_7_pwr.bmp") rm -f $1\_ $2.cc_7_7_pwr.bmp
if (-e "$1\_ $2.cc_3_3_pwr.bmp") rm -f $1\_ $2.cc_3_3_pwr.bmp
if (-e "$1\_ $2.cc_pwr.bmp") rm -f $1\_ $2.cc_pwr.bmp
if (-e "$1\_ $2.cc_9_9_pwr.bmp") rm -f $1\_ $2.cc_9_9_pwr.bmp
if (-e "$1\_ $2.cc_t_pwr.bmp") rm -f $1\_ $2.cc_t_pwr.bmp
if (-e "$1\_ $2.cc_g_pwr.bmp") rm -f $1\_ $2.cc_g_pwr.bmp
if (-e "$1\_ $2.cc_f_pwr.bmp") rm -f $1\_ $2.cc_f_pwr.bmp
rascc $1\_ $2.cc $1.mli $interf_width 1 1 0 1 1 0.1 0.9 1.0 0.35 $flipping
$1\_ $2.cc_pwr.bmp
rascc $1\_ $2.cc_7_7 $1.mli $interf_width 1 1 0 1 1 0.1 0.9 1.0 0.35 $flipping
$1\_ $2.cc_7_7_pwr.bmp
rascc $1\_ $2.cc_3_3 $1.mli $interf_width 1 1 0 1 1 0.1 0.9 1.0 0.35 $flipping
$1\_ $2.cc_3_3_pwr.bmp
rascc $1\_ $2.cc_9_9 $1.mli $interf_width 1 1 0 1 1 0.1 0.9 1.0 0.35 $flipping
$1\_ $2.cc_9_9_pwr.bmp
rascc $1\_ $2.cc_t $1.mli $interf_width 1 1 0 1 1 0.1 0.9 1.0 0.35 $flipping
$1\_ $2.cc_t_pwr.bmp
rascc $1\_ $2.cc_g $1.mli $interf_width 1 1 0 1 1 0.1 0.9 1.0 0.35 $flipping
$1\_ $2.cc_g_pwr.bmp
rascc $1\_ $2.cc_f $1.mli $interf_width 1 1 0 1 1 0.1 0.9 1.0 0.35 $flipping
$1\_ $2.cc_f_pwr.bmp
endif

```

1.7 Adaptive interferogram filtering and generation of Bitmaps

```

if (0) then
if (-e "$1\_ $2.cc_filt") rm -f $1\_ $2.cc_filt
if (-e "$1\_ $2.flr_filt") rm -f $1\_ $2.flr_filt

```

```

if (-e "$1\_2.flt_filt_mag_phase_pwr.bmp") rm -f
$1\_2.flt_filt_mag_phase_pwr.bmp
if (-e "$1\_2.cc_filt.bmp") rm -f $1\_2.cc_filt.bmp
adf $1\_2.flt $1\_2.flt_filt $1\_2.cc_filt $interf_width .5 ##default 32
rasmp_h_pwr $1\_2.flt_filt $1.mli $interf_width 1 1 0 1 1 1.0 0.35 $flipping
$1\_2.flt_filt_mag_phase_pwr.bmp
rascc $1\_2.cc_filt $1.mli $interf_width 1 1 0 1 1 0.1 0.9 1.0 0.35 $flipping
$1\_2.cc_filt.bmp ###16
endif

if (0) then # adaptive interferogram filtering and generation of Bitmaps
if (-e "$1\_2.cc_filt128") rm -f $1\_2.cc_filt128
if (-e "$1\_2.cc_filt64") rm -f $1\_2.cc_filt64
if (-e "$1\_2.cc_filt32") rm -f $1\_2.cc_filt32
if (-e "$1\_2.cc_filt") rm -f $1\_2.cc_filt
if (-e "$1\_2.flt_filt128") rm -f $1\_2.flt_filt128
if (-e "$1\_2.flt_filt64") rm -f $1\_2.flt_filt64
if (-e "$1\_2.flt_filt32") rm -f $1\_2.flt_filt32
if (-e "$1\_2.flt_filt") rm -f $1\_2.flt_filt
adf $1\_2.flt $1\_2.flt_filt $1\_2.cc_filt $interf_width .5 ##default 32
#adf $1\_2.flt $1\_2.flt128 $1\_2.cc_filt128 $interf_width .5 128
#adf $1\_2.flt128 $1\_2.flt64 $1\_2.cc_filt64 $interf_width .6 64
# adf $1\_2.flt64 $1\_2.flt32 $1\_2.cc_filt32 $interf_width .5 32
#adf $1\_2.flt32 $1\_2.flt_filt $1\_2.cc_filt $interf_width .4 16

if (-e "$1\_2.flt_filt_mag_phase_pwr.bmp") rm -f
$1\_2.flt_filt_mag_phase_pwr.bmp
rasmp_h_pwr $1\_2.flt_filt $1.pwr $interf_width 1 1 0 1 1 1.0 0.35 $flipping
$1\_2.flt_filt_mag_phase_pwr.bmp
endif

if (0) then
# rascc $1\_2.cc_filt128 $1.pwr $interf_width 1 1 0 1 1 0.1 0.9 1.0 0.35 $flipping
$1\_2.cc_filt128.bmp
# rascc $1\_2.cc_filt64 $1.pwr $interf_width 1 1 0 1 1 0.1 0.9 1.0 0.35 $flipping
$1\_2.cc_filt64.bmp
#rascc $1\_2.cc_filt32 $1.pwr $interf_width 1 1 0 1 1 0.1 0.9 1.0 0.35 $flipping
$1\_2.cc_filt32.bmp
rascc $1\_2.cc_filt $1.pwr $interf_width 1 1 0 1 1 0.1 0.9 1.0 0.35 $flipping
$1\_2.cc_filt.bmp ###16
endif

```

1.8 Phase unwrapping

1.8.1 Branch-cut algorithm

```

if (0) then
if (-e "$1\_2.flag") rm -f $1\_2.flag
if (-e "$1\_2.unw") rm -f $1\_2.unw

```

```

corr_flag $1\_ $2.cc_filt $1\_ $2.flag $interf_width 0.25
neutron $1.pwr $1\_ $2.flag $interf_width
residue $1\_ $2.flt_filt $1\_ $2.flag $interf_width
tree_cc $1\_ $2.flag $interf_width 64
grasses $1\_ $2.flt_filt $1\_ $2.flag $1\_ $2.unw $interf_width - - - - 1000
ph_slope_base $1\_ $2.unw $1.slc.par $1\_ $2.off $1\_ $2.base $1\_ $2.int.unw 0 1
if (-e "$1\_ $2.unw.bmp") rm -f $1\_ $2.unw.bmp
rasrmg $1\_ $2.unw $1.pwr $interf_width 1 1 0 1 1 .5 1. .35 0.0 $flipping
$1\_ $2.unw.bmp
if (-e "$1\_ $2.int.unw.bmp") rm -f $1\_ $2.int.unw.bmp
rasmph $1\_ $2.int.unw $interf_width 1 0 1 1 1. 0.35 $flipping $1\_ $2.int.unw.bmp
if (-e "$1\_ $2.int.unw_pwr.bmp") rm -f $1\_ $2.int.unw_pwr.bmp
rasmph_pwr $1\_ $2.int.unw $1.pwr $interf_width 1 1 0 1 1 1.0 0.35 $flipping
$1\_ $2.int.unw_pwr.bmp
endif

```

##Construction of bridges between disconnected regions unwrapped of disconnected #area

```

if (0) then
if (-e "$1\_ $2.unw.tree.ras") rm -f $1\_ $2.unw.tree.ras
if (-e "$1\_ $2.bridges") rm -f $1\_ $2.bridges
rastree $1\_ $2.flag - - $interf_width - - $1\_ $2.flag.ras
#rastree $1\_ $2.flt_filt $1\_ $2.unw $1\_ $2.flag $interf_width - - $1\_ $2.unw.tree.ras
rastree $1\_ $2.flag $1\_ $2.unw $1\_ $2.flt_filt $interf_width 1 0 0.33333
$1\_ $2.unw.tree.ras
disras $1\_ $2.unw.tree.ras
rastree $1\_ $2.flag $1\_ $2.unw $1\_ $2.flt_filt $interf_width 1 0 0.33333
$1\_ $2.unw.tree.bmp
bridge $1\_ $2.flt_filt $1\_ $2.flag $1\_ $2.unw $1\_ $2.bridges $interf_width 0 1 0 1
endif

```

1.8.2 Phase unwrapping with Minimum Cost Flow(MCF) algorithm

1.8.2.1 Generation of phase unwrapping validity mask

```

if (0) then
if (-e "$1\_ $2.mask.ras") rm -f $1\_ $2.mask.ras
if (-e "$1\_ $2.mask_thinned.ras") rm -f $1\_ $2.mask_thinned.ras
rascc_mask $1\_ $2.cc $1.mli $interf_width 1 1 0 1 1 0.3 - - - - $1\_ $2.mask.ras
disras $1\_ $2.mask.ras

```

1.8.2.2 Adaptive sampling reduction for phase unwrapping validity mask

```

rascc_mask_thinning $1\_ $2.mask.ras $1\_ $2.cc $interf_width
$1\_ $2.mask_thinned.ras 3 0.3 0.4 0.5
rascc_mask_thinning $1\_ $2.mask.ras $1\_ $2.cc $interf_width
$1\_ $2.mask_thinned.ras.bmp 5 0.3 0.4 0.5 0.6 0.7
endif

```

1.8.2.3 Phase unwrapping

```
if (0) then
if (-e "$1\_2.flat_filt.mcf.unw0") rm -f $1\_2.flat_filt.mcf.unw0
if (-e "$1\_2.flt_filt.mcf.unw") rm -f $1\_2.flt_filt.mcf.unw
if (-e "$1\_2.flt_filt.mcf.unw.ras.bmp") rm -f $1\_2.flt_filt.mcf.unw.ras.bmp
mcf $1\_2.flt_filt $1\_2.cc $1\_2.mask.ras $1\_2.flat_filt.mcf.unw0 $interf_width
1 0 0 - - 1 1 - - - 0
mcf $1\_2.flt_filt $1\_2.cc - $1\_2.flt_filt.mcf.unw $interf_width 1 0 0 - - 1 1 - - - 0
disrmg $1\_2.flt_filt.mcf.unw $1.mli $interf_width
rasrmg $1\_2.flt_filt.mcf.unw $1.mli $interf_width 1 1 0 1 1 .5 1. .35 0.0 $flipping
$1\_2.flt_filt.mcf.unw.ras.bmp
dis2rmg $1\_2.flt_filt.mcf.unw $1\_2.flat_filt.mcf.unw0 $interf_width $interf_width
endif
```

```
if (0) then
if (-e "$1\_2.int_mcf.unw") rm -f $1\_2.int_mcf.unw
ph_slope_base $1\_2.flt_filt.mcf.unw $1.slc.par $1\_2.off $1\_2.base
$1\_2.int_mcf.unw 0 1 # I add it
endif
```

1.8.2.4 Weighted interpolation of gaps in unwrapped phase data using adaptive window size (32)

```
if (0) then
if (-e "$1\_2.flat_filt.mcf.unw0_interp") rm -f $1\_2.flat_filt.mcf.unw0_interp
if (-e "$1\_2.flat_filt.mcf.unw0_interp.ras") rm -f $1\_2.flat_filt.mcf.unw0_interp.ras
if (-e "$1\_2.flat_filt.mcf.unw0_interp.ras.bmp") rm -f
$1\_2.flat_filt.mcf.unw0_interp.ras.bmp
interp_ad $1\_2.flat_filt.mcf.unw0 $1\_2.flat_filt.mcf.unw0_interp $interf_width 32
8 16 2
disrmg $1\_2.flat_filt.mcf.unw0_interp $1.mli $interf_width
rasrmg $1\_2.flat_filt.mcf.unw0_interp $1.mli $interf_width 1 1 0 1 1 .5 1. .35 0.0
$flipping $1\_2.flat_filt.mcf.unw0_interp.ras
rasrmg $1\_2.flat_filt.mcf.unw0_interp $1.mli $interf_width 1 1 0 1 1 .5 1. .35 0.0
$flipping $1\_2.flat_filt.mcf.unw0_interp.ras.bmp
endif
```

1.8.2.5 Phase unwrapping using model of unwrapped phase

```
if (0) then
if (-e "$1\_2.flat_filt.mcf.unw.ras") rm -f $1\_2.flat_filt.mcf.unw.ras
if (-e "$1\_2.flat_filt.mcf.unw.ras.bmp") rm -f $1\_2.flat_filt.mcf.unw.ras.bmp
unw_model $1\_2.flt_filt $1\_2.flat_filt.mcf.unw0_interp $1\_2.flat_filt.mcf.unw
$interf_width 1200 1500
disrmg $1\_2.flat_filt.mcf.unw $1.mli $interf_width
```

```

rasrmg $1\_$.flat_filt.mcf.unw $1.mli $interf_width - - - 4 4 - - - -
$1\_$.flat_filt.mcf.unw.ras
rasrmg $1\_$.flat_filt.mcf.unw $1.mli $interf_width 1 1 0 1 1 .5 1. .35 0.0 $flipping
$1\_$.flat_filt.mcf.unw.ras.bmp
dis2rmg $1\_$.flat_filt.mcf.unw0 $1\_$.flat_filt.mcf.unw $interf_width
$interf_width
endif

```

1.9 Interferometric estimation of heights and ground ranges

1.9.1 Branch cut unwrapping method

1.9.1.1 Least square estimation of interferometric baseline

```

if (0) then
  if (-e "$1\_$.gcp_ph") rm -f $1\_$.gcp_ph
  if (-e "$1\_$.base") rm -f $1\_$.base
  gcp_phase $1\_$.unw $1\_$.off $1\_$.gcp $1\_$.gcp_ph 7
  base_ls $1.slc.par $1\_$.off $1\_$.gcp_ph $1\_$.base 1 1 1 1 1 1
endif

```

1.9.1.2 Interferometric estimation of heights and ground ranges

```

if (0) then
  if (-e "$1\_$.hgt") rm -f $1\_$.hgt
  if (-e "$1\_$.hgt.bmp") rm -f $1\_$.hgt.bmp
  if (-e "$1\_$.grd") rm -f $1\_$.grd
  hgt_map $1\_$.unw $1.slc.par $1\_$.off $1\_$.base $1\_$.hgt $1\_$.grd
  rashgt $1\_$.hgt $1.pwr $interf_width 1 1 0 1 1 160.0 1. .35 $flipping
  $1\_$.hgt.bmp
endif

```

1.9.1.3 Resample interferometric height map to orthonormal coordinates

```

if (0) then
  if (0) then
    if (-e "$1\_$.rhgt") rm -f $1\_$.rhgt
    if (-e "$1\_$.rpwr") rm -f $1\_$.rpwr
    res_map $1\_$.hgt $1\_$.grd $1.pwr $1.slc.par $1\_$.off $1\_$.rhgt $1.pwr 7 7
  40
  endif

  if (0) then
    set resampled_width = 2478 # Resampled_pixels_per_line
    if (-e "$1\_$.rhgt.bmp") rm -f $1\_$.rhgt.bmp
    rashgt $1\_$.rhgt $1.pwr $resampled_width 1 1 0 1 1 160.0 1. .35 $flipping
    $1\_$.rhgt.bmp
  endif
endif

```

1.9.2 MCF unwrapping method

1.9.2.1 Least square estimation of interferometric baseline

```
if (0) then
  if (-e "$1\_ $2_.gcp_ph") rm -f $1\_ $2_.gcp_ph
  if (-e "$1\_ $2_.base") rm -f $1\_ $2_.base
  gcp_phase $1\_ $2_.flt_filt.mcf.unw $1\_ $2_.off $1\_ $2_.gcp $1\_ $2_.gcp_ph 1
  base_ls $1_.slc.par $1\_ $2_.off $1\_ $2_.gcp_ph $1\_ $2_.base 1 1 1 1 1
endif
```

1.9.2.2 Interferometric estimation of heights and ground ranges

```
if (0)
  if (-e "$1\_ $2_.hgt") rm -f $1\_ $2_.hgt
  if (-e "$1\_ $2_.hgt.bmp") rm -f $1\_ $2_.hgt.bmp
  if (-e "$1\_ $2_.grd") rm -f $1\_ $2_.grd
  hgt_map $1\_ $2_.flt_filt.mcf.unw $1_.slc.par $1\_ $2_.off $1\_ $2_.base $1\_ $2_.hgt
  $1\_ $2_.grd
  rashgt $1\_ $2_.hgt $1_.pwr $interf_width 1 1 0 1 1 160.0 1. .35 $flipping
  $1\_ $2_.hgt.bmp
endif
```

1.9.2.3 Resample interferometric height map to orthonormal coordinates

```
if (0) then
  if (0) then
    if (-e "$1\_ $2_.rhgt") rm -f $1\_ $2_.rhgt
    if (-e "$1\_ $2_.rpwr") rm -f $1\_ $2_.rpwr
    res_map $1\_ $2_.hgt $1\_ $2_.grd $1_.pwr $1_.slc.par $1\_ $2_.off $1\_ $2_.rhgt
    $1\_ $2_.rpwr 7 7 40
  endif
  if (0) then
    set resampled_width = 2476 # Resampled_pixels_per_line
    if (-e "$1\_ $2_.rhgt.bmp") rm -f $1\_ $2_.rhgt.bmp
    rashgt $1\_ $2_.rhgt $1\_ $2_.rpwr $resampled_width 1 1 0 1 1 160.0 1. .35 $flipping
    $1\_ $2_.rhgt.bmp
    rashgt $1\_ $2_.rhgt - $resampled_width 1 1 0 1 1 160.0 1. .35 $flipping
    $1\_ $2_.rhgt.bmp
  endif
endif
cd ..
```

Appendices 2 Gamma interferometric SAR Processor (ISP) script: orbit method

```
#!/bin/csh -fe
if ($#argv < 2) then
  echo " "
  echo "**** Process Indonesia ERS SAR DATA ****"
  echo "**** Copyright 2004, Gamma Remote Sensing, v1.4 18-May-2004 ts/uw/clw
****"

  echo " "
  echo "run_ISP_indonesia : To run interferometric processing sequence for Indonesia"
  echo "          and estimate the heights (DEM)."
```

2.1 Prepare slc data and processing parameter files

```
if (0) then
if (-e "$3.slc.par") rm -f $3.slc.par
par_ESA_ERS ../$3/LEA_01.001 $3.slc.par ../$3/DAT_01.001 $3.slc
if (-e "$4.slc.par") rm -f $4.slc.par
par_ESA_ERS ../$4/LEA_01.001 $4.slc.par ../$4/DAT_01.001 $4.slc
endif
```

2.2 Offset estimation of the slc images

```
if (0) then # Note to flag the method to either 1 (intensity) or 2 (fringe)
if (-e "$3\_ $4.off") rm -f $3\_ $4.off
create_offset $3.slc.par $4.slc.par $3\_ $4.off 1 2 10 ### when we use intensity, search
window 64*64 while when use fringe 16x16
init_offset_orbit $3.slc.par $4.slc.par $3\_ $4.off #I add it
endif
```

```

# NOTE!!!! To be used when using option 1 in create_offset above(intensity)
if (0) then
  if (-e "$3\_4.offfs ") rm -f $3\_4.offfs
  if (-e "$3\_4.snr ") rm -f $3\_4.snr
  if (-e "$3\_4.offsets ") rm -f $3\_4.offsets
  if (-e "$3\_4.cofffs ") rm -f $3\_4.cofffs
  if (-e "$3\_4.coffsets ") rm -f $3\_4.coffsets
  offset_pwr $3.slrc $4.slrc $3.slrc.par $4.slrc.par $3\_4.off $3\_4.offfs $3\_4.snr - -
  $3\_4.offsets 1 - - 7.0
  offset_fit $3\_4.offfs $3\_4.snr $3\_4.off $3\_4.coff $3\_4.coffsets - 4 0
endif

```

2.3 Compute interferogram with 2x10 multilooks

```

if (0) then
  if (-e "$3\_4.int ") rm -f $3\_4.int
  SLC_interp $4.slrc $3.slrc.par $4.slrc.par $3\_4.off $4.rslc $4.rslc.par
  SLC_intf $3.slrc $4.rslc $3.slrc.par $4.rslc.par $3\_4.off $3\_4.int 2 10 - - 1 1
endif

```

```

if (0) then
  if (-e "$3.mli") rm -f $3.mli
  if (-e "$3.mli.par") rm -f $3.mli.par
  multi_look $3.slrc $3.slrc.par $3.mli $3.mli.par 2 10
  if (-e "$4.mli") rm -f $4.mli
  if (-e "$4.mli.par") rm -f $4.mli.par
  multi_look $4.slrc $4.slrc.par $4.mli $4.mli.par 2 10
endif

```

```

if (0) then
  if (-e "$3.mli.bmp") rm -f $3.mli.bmp
  if (-e "$4.mli.bmp") rm -f $4.mli.bmp
  raspwr $3.mli $interf_width 1 0 1 1 1.0 0.35 $flipping $3.mli.bmp
  raspwr $4.mli $interf_width 1 0 1 1 1.0 0.35 $flipping $4.mli.bmp
endif

```

```

if (0) then
  if (-e "$3\_4.mag_phase.bmp") rm -f $3\_4.mag_phase.bmp
  rasmph $3\_4.int $interf_width 1 0 1 1 1.0 0.35 $flipping $3\_4.mag_phase.bmp
  if (-e "$3\_4.mag_phase_pwr.bmp") rm -f $3\_4.mag_phase_pwr.bmp
  rasmph_pwr $3\_4.int $3.mli $interf_width 1 1 0 1 1 1.0 0.35 $flipping
  $3\_4.mag_phase_pwr.bmp
endif

```

2.4 Initial baseline estimation

```

if (0) then
  if (-e "$3\_4.base") rm -f $3\_4.base

```

```

base_init $3.slc.par $4.slc.par $3\_ $4.off $3\_ $4.int $3\_ $4.base 2 1024 1024
endif

```

2.5 Curved Earth phase trend removal ("flattening") and filter

```

if (0) then
  if (-e "$3\_ $4.flt") rm -f $3\_ $4.flt
  ph_slope_base $3\_ $4.int $3.slc.par $3\_ $4.off $3\_ $4.base $3\_ $4.flt
  if (-e "$3\_ $4.flt_mag_phase.bmp") rm -f $3\_ $4.flt_mag_phase.bmp
  rasmp $3\_ $4.flt $interf_width 1 0 1 1 1. 0.35 $flipping $3\_ $4.flt_mag_phase.bmp
  if (-e "$3\_ $4.flt_mag_phase_pwr.bmp") rm -f $3\_ $4.flt_mag_phase_pwr.bmp
  rasmp_pwr $3\_ $4.flt $3.mli $interf_width 1 1 0 1 1 1.0 0.35 $flipping
  $3\_ $4.flt_mag_phase_pwr.bmp
endif

```

2.6 Coherence estimation and generation of Bitmaps

```

if (0) then # Coherence estimation and generation of Bitmaps
  if (-e "$3\_ $4.cc") rm -f $3\_ $4.cc
  cc_wave $3\_ $4.flt $3.mli $4.mli $3\_ $4.cc $interf_width
  if (-e "$3\_ $4.cc.bmp") rm -f $3\_ $4.cc.bmp
  ras_linear $3\_ $4.cc $interf_width 1 0 1 1 0.0 1.0 -1 $3\_ $4.cc.bmp
  if (-e "$3\_ $4.cc_pwr.bmp") rm -f $3\_ $4.cc_pwr.bmp
  rascc $3\_ $4.cc $3.mli $interf_width 1 1 0 1 1 0.1 0.9 1.0 0.35 $flipping
  $3\_ $4.cc_pwr.bmp
endif

```

2.7 Adaptive interferogram filtering and generation of Bitmaps

```

if (0) then # adaptive interferogram filtering and generation of Bitmaps
  if (-e "$3\_ $4.cc_filt") rm -f $3\_ $4.cc_filt
  if (-e "$3\_ $4.flt_filt") rm -f $3\_ $4.flt_filt
  if (-e "$3\_ $4.flt_filt_mag_phase_pwr.bmp") rm -f
  $3\_ $4.flt_filt_mag_phase_pwr.bmp
  if (-e "$3\_ $4.cc_filt.bmp") rm -f $3\_ $4.cc_filt.bmp
  adf $3\_ $4.flt $3\_ $4.flt_filt $3\_ $4.cc_filt $interf_width .5 ##default 32
  rasmp_pwr $3\_ $4.flt_filt $3.mli $interf_width 1 1 0 1 1 1.0 0.35 $flipping
  $3\_ $4.flt_filt_mag_phase_pwr.bmp
  rascc $3\_ $4.cc_filt $3.mli $interf_width 1 1 0 1 1 0.1 0.9 1.0 0.35 $flipping
  $3\_ $4.cc_filt.bmp ###16
endif

```

2.8 Phase unwrapping

2.8.1 Branch-cut algorithm

```

if (0) then
  if (-e "$3\_ $4.flag") rm -f $3\_ $4.flag
  if (-e "$3\_ $4.unw") rm -f $3\_ $4.unw
  corr_flag $3\_ $4.cc_filt $3\_ $4.flag $interf_width 0.25

```

```

neutron $3\_ $4.flag $interf_width
residue $3\_ $4.flt_filt $3\_ $4.flag $interf_width
tree_cc $3\_ $4.flag $interf_width 64
grasses $3\_ $4.flt_filt $3\_ $4.flag $3\_ $4.unw $interf_width - - - - 1000
ph_slope_base $3\_ $4.unw $3.slc.par $3\_ $4.off $3\_ $4.base $3\_ $4.int.unw 0
if (-e "$3\_ $4.unw.bmp") rm -f $3\_ $4.unw.bmp
  rasrmg $3\_ $4.unw $3.mli $interf_width 1 1 0 1 1 .5 1. .35 0.0 $flipping
$3\_ $4.unw.bmp
endif

```

##Construction of bridges between disconnected regions unwrapped of disconnected #area

```

if (0) then
if (-e "$3\_ $4.unw.tree.ras") rm -f $3\_ $4.unw.tree.ras
if (-e "$3\_ $4.bridges") rm -f $3\_ $4.bridges
rastree $3\_ $4.flag - - $interf_width - - $3\_ $4.flag.ras
  rastree $3\_ $4.flag $3\_ $4.unw $3\_ $4.flt_filt $interf_width 1 0 0.33333
$3\_ $4.unw.tree.ras
  disras $3\_ $4.unw.tree.ras
  rastree $3\_ $4.flag $3\_ $4.unw $3\_ $4.flt_filt $interf_width 1 0 0.33333
$3\_ $4.unw.tree.bmp
  bridge $3\_ $4.flt_filt $3\_ $4.flag $3\_ $4.unw $3\_ $4.bridges $interf_width 0 1 0 1
endif

```

2.8.2 Phase unwrapping with Minimum Cost Flow(MCF) algorithm

2.8.2.1 Generation of phase unwrapping validity mask

```

if (0) then
if (-e "$3\_ $4.mask.ras") rm -f $3\_ $4.mask.ras
if (-e "$3\_ $4.mask_thinned.ras") rm -f $3\_ $4.mask_thinned.ras
rascc_mask $3\_ $4.cc $3.mli $interf_width 1 1 0 1 1 0.3 - - - - $3\_ $4.mask.ras
disras $3\_ $4.mask.ras

```

2.8.2.2 Adaptive sampling reduction for phase unwrapping validity mask

```

rascc_mask_thinning $3\_ $4.mask.ras $3\_ $4.cc $interf_width
$3\_ $4.mask_thinned.ras 3 0.3 0.4 0.5
rascc_mask_thinning $3\_ $4.mask.ras $3\_ $4.cc $interf_width
$3\_ $4.mask_thinned.ras.bmp 5 0.3 0.4 0.5 0.6 0.7
endif

```

2.8.2.3 Phase unwrapping

```

if (0) then
if (-e "$3\_ $4.flat_filt.mcf.unw0") rm -f $3\_ $4.flat_filt.mcf.unw0
if (-e "$3\_ $4.flt_filt.mcf.unw") rm -f $3\_ $4.flt_filt.mcf.unw
if (-e "$3\_ $4.flt_filt.mcf.unw.ras.bmp") rm -f $3\_ $4.flt_filt.mcf.unw.ras.bmp

```

```

mcf $3\_ $4.flat_filt $3\_ $4.cc $3\_ $4.mask.ras $3\_ $4.flat_filt.mcf.unw0 $interf_width
1 0 0 - - 1 1 - - - 0
mcf $3\_ $4.flat_filt $3\_ $4.cc - $3\_ $4.flat_filt.mcf.unw $interf_width 1 0 0 - - 1 1 - - - 0
disrmg $3\_ $4.flat_filt.mcf.unw $3.mli $interf_width
rasrmg $3\_ $4.flat_filt.mcf.unw $3.mli $interf_width 1 1 0 1 1 .5 1. .35 0.0 $flipping
$3\_ $4.flat_filt.mcf.unw.ras.bmp
dis2rmg $3\_ $4.flat_filt.mcf.unw $3\_ $4.flat_filt.mcf.unw0 $interf_width $interf_width
endif

```

```

if (0) then
if (-e "$3\_ $4.int_mcf.unw") rm -f $3\_ $4.int_mcf.unw
ph_slope_base $3\_ $4.flat_filt.mcf.unw $3.slc.par $3\_ $4.off $3\_ $4.base
$3\_ $4.int_mcf.unw 0 1 # I add it
endif

```

2.8.2.4 Weighted interpolation of gaps in unwrapped phase data using adaptive window size (32)

```

if (0) then
if (-e "$3\_ $4.flat_filt.mcf.unw0_interp") rm -f $3\_ $4.flat_filt.mcf.unw0_interp
if (-e "$3\_ $4.flat_filt.mcf.unw0_interp.ras") rm -f $3\_ $4.flat_filt.mcf.unw0_interp.ras
if (-e "$3\_ $4.flat_filt.mcf.unw0_interp.ras.bmp") rm -f
$3\_ $4.flat_filt.mcf.unw0_interp.ras.bmp
interp_ad $3\_ $4.flat_filt.mcf.unw0 $3\_ $4.flat_filt.mcf.unw0_interp $interf_width 32
8 16 2
disrmg $3\_ $4.flat_filt.mcf.unw0_interp $3.mli $interf_width
rasrmg $3\_ $4.flat_filt.mcf.unw0_interp $3.mli $interf_width 1 1 0 1 1 .5 1. .35 0.0
$flipping $3\_ $4.flat_filt.mcf.unw0_interp.ras
rasrmg $3\_ $4.flat_filt.mcf.unw0_interp $3.mli $interf_width 1 1 0 1 1 .5 1. .35 0.0
$flipping $3\_ $4.flat_filt.mcf.unw0_interp.ras.bmp
endif

```

1.8.2.5 Phase unwrapping using model of unwrapped phase

```

if (0) then
if (-e "$3\_ $4.flat_filt.mcf.unw.ras") rm -f $3\_ $4.flat_filt.mcf.unw.ras
if (-e "$3\_ $4.flat_filt.mcf.unw.ras.bmp") rm -f $3\_ $4.flat_filt.mcf.unw.ras.bmp
unw_model $3\_ $4.flat_filt $3\_ $4.flat_filt.mcf.unw0_interp $3\_ $4.flat_filt.mcf.unw
$interf_width 1200 1500
disrmg $3\_ $4.flat_filt.mcf.unw $3.mli $interf_width
rasrmg $3\_ $4.flat_filt.mcf.unw $3.mli $interf_width - - - 4 4 - - - -
$3\_ $4.flat_filt.mcf.unw.ras
rasrmg $3\_ $4.flat_filt.mcf.unw $3.mli $interf_width 1 1 0 1 1 .5 1. .35 0.0 $flipping
$3\_ $4.flat_filt.mcf.unw.ras.bmp
dis2rmg $3\_ $4.flat_filt.mcf.unw0 $3\_ $4.flat_filt.mcf.unw $interf_width
$interf_width
endif

```

2.9.2 MCF unwrapping method

2.9.2.1 Least square estimation of interferometric baseline

```
if (0) then
  if (-e "$3\_4_2.gcp_ph") rm -f $3\_4_2.gcp_ph
  if (-e "$3\_4.base") rm -f $3\_4.base
  gcp_phase $3\_4.flt_filt.mcf.unw $3\_4.off $3\_4.gcp $3\_4_2.gcp_ph 1
  base_ls $3.slc.par $3\_4.off $3\_4_2.gcp_ph $3\_4.base 1 1 1 1 1
endif
```

2.9.2.2 Interferometric estimation of heights and ground ranges

```
if (0) then
  if (-e "$3\_4_2.hgt") rm -f $3\_4_2.hgt
  if (-e "$3\_4_2.hgt.bmp") rm -f $3\_4_2.hgt.bmp
  if (-e "$3\_4_2.grd") rm -f $3\_4_2.grd
  hgt_map $3\_4.flt_filt.mcf.unw $3.slc.par $3\_4.off $3\_4.base $3\_4_2.hgt
  $3\_4_2.grd
  rashgt $3\_4_2.hgt $3.mli $interf_width 1 1 0 1 1 160.0 1. .35 $flipping
  $3\_4_2.hgt.bmp
endif
```

2.9.2.3 Resample interferometric height map to orthonormal coordinates

```
if (0) then
  if (0) then
    if (-e "$3\_4_2.rhgt") rm -f $3\_4.rhgt
    if (-e "$3\_4_2.rpwr") rm -f $3\_4.rpwr
    res_map $3\_4_2.hgt $3\_4_2.grd $3.mli $3.slc.par $3\_4.off $3\_4_2.rhgt
    $3_2.rpwr 7 7 40
  endif
  if (0) then
    set resampled_width = 2490 # Resampled_pixels_per_line
    if (-e "$3\_4.rhgt.bmp") rm -f $3\_4.rhgt.bmp
    rashgt $3\_4_2.rhgt $3_2.rpwr $resampled_width 1 1 0 1 1 160.0 1. .35 $flipping
    $3\_4_2.rhgt.bmp
    rashgt $3\_4_2.rhgt - $resampled_width 1 1 0 1 1 160.0 1. .35 $flipping
    $3\_4_2_2.rhgt.bmp
  endif
endif
cd ..
```

Appendices 3 *Gamma Differential Interferometric SAR Processor (DISP) script: 4-pass method*

```
#!/bin/csh -fe
if ($#argv < 2) then
  echo " "
  echo "**** Process Indonesia ERS SAR DATA ****"
  echo "**** Copyright 2004, Gamma Remote Sensing, v1.4 18-May-2004 ts/uw/clw
****"
  echo " "
  echo "run_ISP_diff : To run interferometric processing sequence for Indonesia"
  echo "          and estimate the heights (DEM)."
  echo " "
  echo "usage: run_ISP_indonesia.csh <diff1 dir> <diff2 dir> <diff3 dir> <diff4 dir>"
  echo "   diff1_dir   (input) data directory for diff1"
  echo "   diff2_dir   (input) data directory for diff2"
  echo "   diff3_dir   (input) data directory for diff3"
  echo "   diff4_dir   (input) data directory for diff4"
  echo " "
  exit
endif
set diff1 = $1
set diff2 = $2
set diff3 = $3
set diff4 = $4
set insardir = diff
set interf_width = 2451
set flipping = -1

if( (-e "$insardir" == 0) ) mkdir $insardir
cd $insardir
```

3.1 Generate a parameter file for the differential interferogram

```
if (1) then
  if (-e "$1_$2_$3_$4.off") rm -f $1_$2_$3_$4.off
  create_diff_par $1_$2.off $3_$4.off $1_$2_$3_$4.off
endif
```

3.2 Compute the initial offsets between the geometries of the two interferograms using the correlation between the MLI intensity images

```
if (1) then
```

```

init_offsetm $1.mli $3.mli $1_$2_$3_$4.off 1 1

offset_pwrn $1.mli $3.mli $1_$2_$3_$4.off offs snr 64 64 offsets 1 24 24 7.

offset_fitm offs snr $1_$2_$3_$4.off coffs coffsets 7.0 4 0
endif

```

3.3 Resample any image in the differential pair geometry to the topographic pair geometry.

```

if (1) then
if (-e "$3\_4.unw.reg") rm -f $3\_4.unw.reg
if (-e "$3\_4.int.unw.reg") rm -f $3\_4.int.unw.reg
if (-e "$3.mli.reg") rm -f $3.mli.reg

interp_real $3\_4.unw $1_$2_$3_$4.off $3\_4.unw.reg

interp_real $3\_4.int.unw $1_$2_$3_$4.off $3\_4.int.unw.reg

interp_real $3.mli $1_$2_$3_$4.off $3.mli.reg
endif

```

3.4 Determine the scaling factors for phase and generate the differential interferogram

3.4.1 First method: Least Squares offset fit (LSOF)

```

if (1) then
if (-e "$1_$2_$3_$4.diff_unw") rm -f $1_$2_$3_$4.diff_unw
diff_ls_fit $3\_4.int.unw.reg $1\_2.int.unw $1_$2_$3_$4.off 32 32 -

diff_ls_unw $3\_4.int.unw.reg $1\_2.int.unw $1_$2_$3_$4.off
$1_$2_$3_$4.diff_unw 0

endif

if (1) then
if (-e "$1_$2_$3_$4.diff_unw.ras") rm -f $1_$2_$3_$4.diff_unw.ras
if (-e "$1_$2_$3_$4.diff_unw.ras.bmp") rm -f $1_$2_$3_$4.diff_unw.ras.bmp
disrmg $1_$2_$3_$4.diff_unw $3.mli.reg $interf_width 1 1 0 1
rasrmg $1_$2_$3_$4.diff_unw $3.mli.reg $interf_width 1 1 0 1 1 1. .35 0.0 -1
$1_$2_$3_$4.diff_unw.ras
rashgt $1_$2_$3_$4.diff_unw $3.mli.reg $interf_width 1 1 0 1 1 160 1 .35 $flipping
$1_$2_$3_$4.diff_unw.ras.bmp
endif

```

3.4.1 Second method: Scaling the topographic pair according to baseline information and subtracting this phase from the differential pair

```

if (1) then
  if (-e "$1_$2_$3_$4.diff_unw") rm -f $1_$2_$3_$4.diff_unw

  scale_base $1\_ $2.int.unw $3\_ $4.unw $3\_ $4.base $3.slc.par $3\_ $4.off $1\_ $2.base
  $1.slc.par $1\_ $2.off 0
  sub_phase $3\_ $4.int.unw.reg $3\_ $4.unw $1_$2_$3_$4.off $1_$2_$3_$4.diff_2_unw
  0
endif

```

```

if (1) then
  if (-e "$1_$2_$3_$4.diff_2_unw.ras") rm -f $1_$2_$3_$4.diff_2_unw.ras
  if (-e "$1_$2_$3_$4.diff_2_unw.ras.bmp") rm -f $1_$2_$3_$4.diff_2_unw.ras.bmp
  disrmg $1_$2_$3_$4.diff_2_unw $3.mli.reg $interf_width 1 1 0 1
  rasrmg $1_$2_$3_$4.diff_2_unw $3.mli.reg $interf_width 1 1 0 1 1 1. 1. .35 0.0 -1
  $1_$2_$3_$4.diff_2_unw.ras
  rashgt $1_$2_$3_$4.diff_2_unw $3.mli.reg $interf_width 1 1 0 1 1 160 1 .35 $flipping
  $1_$2_$3_$4.diff_2_unw.ras.bmp
endif

```

3.5 Conversion of differential phase to displacement

```

if (1) then
  if (-e "$1_$2_$3_$4.disp_map") rm -f $1_$2_$3_$4.disp_map
  if (-e "$1_$2_$3_$4.disp_map") rm -f $1_$2_$3_$4.disp_map_without_Hgt
  if (-e "$1_$2_$3_$4.disp_map.bmp") rm -f $1_$2_$3_$4.disp_map.bmp
  if (-e "$1_$2_$3_$4.disp_map.bmp") rm -f
  $1_$2_$3_$4.disp_map_without_Hgt.bmp
  dispmap $1_$2_$3_$4.diff_unw $3_$4.hgt $3.slc.par $3_$4.off
  $1_$2_$3_$4.disp_map 1 ###vertical displacement
  dispmap $1_$2_$3_$4.diff_unw - $3.slc.par $3_$4.off
  $1_$2_$3_$4.disp_map_without_Hgt 1
  dishgt $1_$2_$3_$4.disp_map $3.mli.reg $interf_width 1 1 0 0.02
  rashgt $1_$2_$3_$4.disp_map $3.mli.reg $interf_width 1 1 0 1 1 160 1 .35 $flipping
  $1_$2_$3_$4.disp_map.bmp
  dishgt $1_$2_$3_$4.disp_map_without_Hgt $3.mli.reg $interf_width 1 1 0 0.02
  rashgt $1_$2_$3_$4.disp_map_without_Hgt $3.mli.reg $interf_width 1 1 0 1 1 160 1
  .35 $flipping $1_$2_$3_$4.disp_map_without_Hgt.bmp
endif

```

Appendices 4 *Gamma Differential Interferometric SAR Processor (DISP) script: Complex interferogram combination method*

```
#!/bin/csh -fe
if ($#argv < 2) then
  echo " "
  echo "**** Process Indonesia ERS SAR DATA ****"
  echo "**** Copyright 2004, Gamma Remote Sensing, v1.4 18-May-2004 ts/uw/clw
****"
  echo " "
  echo "run_ISP_diff : To run interferometric processing sequence for Indonesia"
  echo "                and estimate the heights (DEM)."
```

4.1 Generate a parameter file for the differential interferogram

```
if (1) then
  if (-e "$1_$2_$3_$4.off") rm -f $1_$2_$3_$4.off
  create_diff_par $1_$2.off $3_$4.off $1_$2_$3_$4.off
endif
```

4.2 Compute the initial offsets between the geometries of the two interferograms using the correlation between the MLI intensity images

```
if (1) then

init_offsetm $1.mli $3.mli $1_$2_$3_$4.off 1 1
```

```
offset_pwr $1.mli $3.mli $1_$2_$3_$4.off offs snr 64 64 offsets 1 24 24 7.
```

```
offset_fitm offs snr $1_$2_$3_$4.off coeffs coeffs 7.0 4 0
```

```
endif
```

4.3 Resampling differential pair to topographical pair geometry

```
if (1) then
if (-e "$3\_4.int.reg") rm -f $3\_4.int.reg
if (-e "$3.mli.reg") rm -f $3.mli.reg
interp_cpx $3\_4.int $1_$2_$3_$4.off $3\_4.int.reg
interp_real $3.mli $1_$2_$3_$4.off $3.mli.reg
endif
```

4.4 Complex interferogram combination

```
if (1) then # E.4. Complex interferogram combination
if (-e "$1_$2_$3_$4.diff_int") rm -f $1_$2_$3_$4.diff_int
if (-e "$1_$2_$3_$4.base_comb") rm -f $1_$2_$3_$4.base_comb
if (-e "$1_$2_$3_$4.diff_in.bmp") rm -f $1_$2_$3_$4.diff_in.bmp
comb_interfs $3\_4.int.reg $1\_2.int $3\_4.base $1\_2.base 1. -1. $interf_width
$1_$2_$3_$4.diff_int $1_$2_$3_$4.base_comb 1
```

#The differential interferogram contains the differential phase components of the first pair minus two times the differential phase components of the second pair

```
rasmph_pwr $1_$2_$3_$4.diff_int $3.mli.reg $interf_width 1 1 0 1 1 1.0 0.35 $flipping
$1_$2_$3_$4.diff_in.bmp
endif
```

```
if (1) then
if (-e "$1_$2_$3_$4.base_final ") rm -f $1_$2_$3_$4.base_final
if (-e "$1_$2_$3_$4.diff_int_ph") rm -f $1_$2_$3_$4.diff_int_ph
if (-e "$1_$2_$3_$4.diff_int_sm") rm -f $1_$2_$3_$4.diff_int_sm
if (-e "$1_$2_$3_$4.cc_filt2") rm -f $1_$2_$3_$4.cc_filt2
if (-e "$1_$2_$3_$4.diff_int_sm.bmp") rm -f $1_$2_$3_$4.diff_int_sm.bmp
if (-e "$1_$2_$3_$4.diff_int_ph.bmp") rm -f $1_$2_$3_$4.diff_int_ph.bmp
if (-e "$1_$2_$3_$4.diff_int_sm64") rm -f $1_$2_$3_$4.diff_int_sm64
if (-e "$1_$2_$3_$4.diff_int_sm32") rm -f $1_$2_$3_$4.diff_int_sm32
if (-e "$1_$2_$3_$4.cc_filt64") rm -f $1_$2_$3_$4.cc_filt64
if (-e "$1_$2_$3_$4.cc_filt32") rm -f $1_$2_$3_$4.cc_filt32
```

```
base_est_fft $1_$2_$3_$4.diff_int $3.slc.par $3_$4.off $1_$2_$3_$4.base_final
```

4.5 Remove the remaining phase trend

```
ph_slope_base $1_$2_$3_$4.diff_int $3.slc.par $1_$2.off $1_$2_$3_$4.base_comb
$1_$2_$3_$4.diff_int_ph 1 0
```

```

rasmpH $1_$2_$3_$4.diff_int_ph $interf_width 1 0 1 1 1. 0.35 $flipping
$1_$2_$3_$4.diff_int_ph.bmp
adf $1_$2_$3_$4.diff_int_ph $1_$2_$3_$4.diff_int_sm64 $1_$2_$3_$4.cc_filt64
$interf_width .7 64 7 4
adf $1_$2_$3_$4.diff_int_sm64 $1_$2_$3_$4.diff_int_sm32 $1_$2_$3_$4.cc_filt32
$interf_width .5 32 7 4
adf $1_$2_$3_$4.diff_int_sm32 $1_$2_$3_$4.diff_int_sm $1_$2_$3_$4.cc_filt2
$interf_width .5 16 7 4
rashgt $1_$2_$3_$4.diff_int_sm $3.mli.reg $interf_width 1 1 0 1 1 160 1 0.35 $flipping
$1_$2_$3_$4.diff_int_sm.bmp
endif

```

4.6 Phase unwrapping with MCF algorithm

```

if (1) then
if (-e "$1_$2_$3_$4.diff_int.unw") rm -f $1_$2_$3_$4.diff_int.unw
if (-e "$1_$2_$3_$4.diff_int.unw_pwr.bmp") rm -f
$1_$2_$3_$4.diff_int.unw_pwr.bmp
if (-e "$1_$2_$3_$4.diff_int.unw.bmp") rm -f $1_$2_$3_$4.diff_int.unw.bmp
mcf $1_$2_$3_$4.diff_int_sm - - $1_$2_$3_$4.diff_int.unw $interf_width 1 0 0 - - 1 1
- - - 0
rashgt $1_$2_$3_$4.diff_int.unw $3.mli.reg $interf_width 1 1 0 1 1 160 1 0.35
$flipping $1_$2_$3_$4.diff_int.unw_pwr.bmp
rasrmg $1_$2_$3_$4.diff_int.unw $3.mli.reg $interf_width 1 1 0 1 1 .5 1. .35 0.0
$flipping $1_$2_$3_$4.diff_int.unw.bmp
endif

```

4.7 Conversion of differential phase to displacement

```

if (1) then
if (-e "$1_$2_$3_$4.disp_comx_mcf_map") rm -f $1_$2_$3_$4.disp_comx_mcf_map
if (-e "$1_$2_$3_$4.disp_comx_mcf_los_map") rm -f
$1_$2_$3_$4.disp_comx_mcf_los_map
if (-e "$1_$2_$3_$4.disp_comx_mcf_map.bmp") rm -f
$1_$2_$3_$4.disp_comx_mcf_map.bmp
dispmap $1_$2_$3_$4.diff_int.unw - $3.slc.par $3_$4.off
$1_$2_$3_$4.disp_comx_mcf_map 1
rashgt $1_$2_$3_$4.disp_comx_mcf_map $3.mli.reg $interf_width 1 1 0 1 1 160 1 .35
$flipping $1_$2_$3_$4.disp_comx_mcf_map.bmp
endif

```